Accounting for capillary effects in level-set based Finite Elements modelling of impregnation in fibrous media

Loïc Chevalier

N°d'ordre NNT : 2019LYSEM008

THÈSE de DOCTORAT DE L'UNIVERSITÉ DE LYON
opérée au sein de
l'École des Mines de Saint-Étienne

École Doctorale N° 488
Sciences, Ingénierie, Santé

Spécialité de doctorat : Mécanique et Ingénierie

Soutenue publiquement le 11/03/2019, par :
Loïc CHEVALIER

Prise en compte des effets capillaires dans la modélisation par Elements Finis et *level-set* de l'imprégnation dans les milieux fibreux

-

Accounting for capillary effects in level-set based Finite Element modelling of impregnation in fibrous media

---

Devant le jury composé de :

Arquis, Eric	Professeur	Institut de Mécanique et d'Ingénierie, Bordeaux	*Président*
Michaud, Véronique	Professeure	Ecole Polytechnique Fédérale de Lausanne	*Rapporteure*
Legendre, Dominique	Professeur	Institut de Mécanique des Fluides de Toulouse	*Rapporteur*
Comas-Cardona, Sébastien	Professeur	École Centrale Nantes	*Examinateur*
Drapier, Sylvain	Professeur	Mines Saint-Étienne	*Directeur de thèse*
Bruchon, Julien	Professeur	Mines Saint-Étienne	*Co-directeur*
Liotier, Pierre-Jacques	Maître-assistant	Mines Saint-Étienne	*Encadrant*
Maxime, Blais	Ingénieur R&T	Hexcel Reinforcements	*Invité*

Spécialités doctorales	Responsables :	Spécialités doctorales	Responsables
SCIENCES ET GENIE DES MATERIAUX	K. Wolski Directeur de recherche	MATHEMATIQUES APPLIQUEES	O. Roustant, Maître-assistant
MECANIQUE ET INGENIERIE	S. Drapier, professeur	INFORMATIQUE	O. Boissier, Professeur
GENIE DES PROCEDES	F. Gruy, Maître de recherche	SCIENCES DES IMAGES ET DES FORMES	JC. Pinoli, Professeur
SCIENCES DE LA TERRE	B. Guy, Directeur de recherche	GENIE INDUSTRIEL	N. Absi, Maitre de recherche
SCIENCES ET GENIE DE L'ENVIRONNEMENT	D. Graillot, Directeur de recherche	MICROELECTRONIQUE	Ph. Lalevée, Professeur

EMSE : Enseignants-chercheurs et chercheurs autorisés à diriger des thèses de doctorat (titulaires d'un doctorat d'État ou d'une HDR)

ABSI	Nabil	MR	Génie industriel	CMP
AUGUSTO	Vincent	CR	Image, Vision, Signal	CIS
AVRIL	Stéphane	PR2	Mécanique et ingénierie	CIS
BADEL	Pierre	MA(MDC)	Mécanique et ingénierie	CIS
BALBO	Flavien	PR2	Informatique	FAYOL
BASSEREAU	Jean-François	PR	Sciences et génie des matériaux	SMS
BATTON-HUBERT	Mireille	PR2	Sciences et génie de l'environnement	FAYOL
BEIGBEDER	Michel	MA(MDC)	Informatique	FAYOL
BLAYAC	Sylvain	MA(MDC)	Microélectronique	CMP
BOISSIER	Olivier	PR1	Informatique	FAYOL
BONNEFOY	Olivier	PR	Génie des Procédés	SPIN
BORBELY	Andras	MR(DR2)	Sciences et génie des matériaux	SMS
BOUCHER	Xavier	PR2	Génie Industriel	FAYOL
BRODHAG	Christian	DR	Sciences et génie de l'environnement	FAYOL
BRUCHON	Julien	MA(MDC)	Mécanique et ingénierie	SMS
CAMEIRAO	Ana	MA(MDC)	Génie des Procédés	SPIN
CHRISTIEN	Frédéric	PR	Science et génie des matériaux	SMS
DAUZERE-PERES	Stéphane	PR1	Génie Industriel	CMP
DEBAYLE	Johan	MR	Sciences des Images et des Formes	SPIN
DEGEORGE	Jean-Michel	MA(MDC)	Génie industriel	Fayol
DELAFOSSE	David	PR0	Sciences et génie des matériaux	SMS
DELORME	Xavier	MA(MDC)	Génie industriel	FAYOL
DESRAYAUD	Christophe	PR1	Mécanique et ingénierie	SMS
DJENIZIAN	Thierry	PR	Science et génie des matériaux	CMP
BERGER-DOUCE	Sandrine	PR1	Sciences de gestion	FAYOL
DRAPIER	Sylvain	PR1	Mécanique et ingénierie	SMS
DUTERTRE	Jean-Max	MA(MDC)		CMP
EL MRABET	Nadia	MA(MDC)		CMP
FAUCHEU	Jenny	MA(MDC)	Sciences et génie des matériaux	SMS
FAVERGEON	Loïc	CR	Génie des Procédés	SPIN
FEILLET	Dominique	PR1	Génie Industriel	CMP
FOREST	Valérie	MA(MDC)	Génie des Procédés	CIS
FRACZKIEWICZ	Anna	DR	Sciences et génie des matériaux	SMS
GARCIA	Daniel	MR(DR2)	Sciences de la Terre	SPIN
GAVET	Yann	MA(MDC)	Sciences des Images et des Formes	SPIN
GERINGER	Jean	MA(MDC)	Sciences et génie des matériaux	CIS
GOEURIOT	Dominique	DR	Sciences et génie des matériaux	SMS
GONDRAN	Natacha	MA(MDC)	Sciences et génie de l'environnement	FAYOL
GONZALEZ FELIU	Jesus	MA(MDC)	Sciences économiques	FAYOL
GRAILLOT	Didier	DR	Sciences et génie de l'environnement	SPIN
GROSSEAU	Philippe	DR	Génie des Procédés	SPIN
GRUY	Frédéric	PR1	Génie des Procédés	SPIN
HAN	Woo-Suck	MR	Mécanique et ingénierie	SMS
HERRI	Jean Michel	PR1	Génie des Procédés	SPIN
KERMOUCHE	Guillaume	PR2	Mécanique et Ingénierie	SMS
KLOCKER	Helmut	DR	Sciences et génie des matériaux	SMS
LAFOREST	Valérie	MR(DR2)	Sciences et génie de l'environnement	FAYOL
LERICHE	Rodolphe	CR	Mécanique et ingénierie	FAYOL
MALLIARAS	Georges	PR1	Microélectronique	CMP
MOLIMARD	Jérôme	PR2	Mécanique et ingénierie	CIS
MOUTTE	Jacques	CR	Génie des Procédés	SPIN
NAVARRO	Laurent	CR		CIS
NEUBERT	Gilles			FAYOL
NIKOLOVSKI	Jean-Pierre	Ingénieur de recherche	Mécanique et ingénierie	CMP
NORTIER	Patrice	PR1	Génie des Procédés	SPIN
O CONNOR	Rodney Philip	MA(MDC)	Microélectronique	CMP
PICARD	Gauthier	MA(MDC)	Informatique	FAYOL
PINOLI	Jean Charles	PR0	Sciences des Images et des Formes	SPIN
POURCHEZ	Jérémy	MR	Génie des Procédés	CIS
ROUSSY	Agnès	MA(MDC)	Microélectronique	CMP
ROUSTANT	Olivier	MA(MDC)	Mathématiques appliquées	FAYOL
SANAUR	Sébastien	MA(MDC)	Microélectronique	CMP
SERRIS	Eric	IRD		FAYOL
STOLARZ	Jacques	CR	Sciences et génie des matériaux	SMS
TRIA	Assia	Ingénieur de recherche	Microélectronique	CMP
VALDIVIESO	François	PR2	Sciences et génie des matériaux	SMS
VIRICELLE	Jean Paul	DR	Génie des Procédés	SPIN
WOLSKI	Krzystof	DR	Sciences et génie des matériaux	SMS
XIE	Xiaolan	PR0	Génie industriel	CIS
YUGMA	Gallian	CR	Génie industriel	CMP

Mise à jour : 30/08/2018

À ma maman.

“*6accdæ13eff7i3l9n4o4qrr4s8t12ux*[1] ”

Letter from Newton to Leibniz, 1677

1. The anagram expresses, in Newton's terminology, the fundamental theorem of the calculus. The solution of this anagram is probably the following "Data aequatione quotcunque fluentes quantitates involvente, fluxiones invenire; et vice versa"

Remerciements

Le travail présenté dans ce document représente l'aboutissement de trois années de thèse passées au département Mécanique et Procédés d'Élaboration (MPE), au sein de l'école des Mines de Saint-Étienne. Je souhaite exprimer ma gratitude à celles et ceux qui ont participé, de manière directe et indirecte, à ce travail.

Pour commencer, je tiens à remercier mon directeur de thèse Sylvain Drapier, professeur aux Mines de Saint-Étienne, pour m'avoir donné l'opportunité de réaliser cette thèse et la confiance pour mener à bien ce travail de recherche. Je remercie chaleureusement mon co-directeur de thèse Julien Bruchon, professeur aux Mines de Saint-Étienne, pour sa patience dans les explications, la richesse des discussions et sa rigueur à toute épreuve. Mes remerciements vont également à mon encadrant Pierre-Jacques Liotier, pour son approche réaliste de la simulation et à Nicolas Moulin pour m'avoir donné un réel goût à la programmation et aux systèmes distribués.

Je tiens à remercier l'ensemble des membres du jury : Monsieur Eric Arquis qui a fait l'honneur d'accepter la présidence du Jury, Madame Véronique Michaud et Monsieur Dominique Legendre pour avoir accepté d'être rapporteurs de cette thèse et enfin messieurs Sébastien Comas-Cardona et Maxime Blais pour leur participation.

J'adresse mes remerciements à la femme formidable, avec qui j'ai partagé trois années de vie semi-commune entre nos quatre cloisons. Pour avoir été d'une accessibilité totale, avec la possibilité de discuter de tout, je te remercie Koloina Andriamananjara. Mes remerciements à la garde rapprochée, Laure et Marianne pour l'ensemble des moments partagés. Merci aux coureurs du midi pour les ascensions aux alentours de Rochetaillée et plus généralement aux doctorants, post-doctorants et ingénieurs : Arnaud, Greg, Rabih, Bassem, Inès, Baptiste, ... J'adresse toute ma sympathie aux permanents du laboratoire que j'ai côtoyé au travail ou en soirée durant une partie de fléchettes.

Enfin, je tiens à exprimer toute mon affection à ma famille pour leur soutien tout au long de cette thèse.

ÉCOLE NATIONALE SUPÉRIEURE DES MINES DE SAINT-ÉTIENNE

Abstract

Speciality: Mechanics and Engineering

Accounting for capillary effects in level-set based Finite Elements modelling of impregnation in fibrous media

by Loïc CHEVALIER

Keywords: Capillarity, stabilised FE, bi-fluid flow, level-set, discontinuities capturing, surface tension, fibrous composites, numerical permeability, capillary pressure

Accounting for surface tension effects is of major interest in many fields in engineering. More specifically, in the field of LCM composite processing, surface tension driven phenomena control the impregnation of liquid resin into fibrous preforms. In the work described here, a numerical method able to deal with a general bi-fluid model integrating capillary actions is developed and implemented. Firstly, the method relies on a precise computation of the surface tension force. Considering a mathematical transformation of the surface tension virtual work, the regularity required for the solution on the evolving curved interface is weakened, and the mechanical equilibrium of the triple line can be enforced as a natural condition. Consequently, contact angles of the liquid over the solid phase result from this equilibrium. Secondly, for an exhaustive capillary action representation, pressure and pressure gradient jumps across the interface must be accounted for. A pressure enrichment strategy is used to properly compute the discontinuities in both pressure and gradient fields. On top of that, a strong coupling strategy is shown to yield physically sound solutions even for complex solid surfaces. The resulting method is shown to predict accurately static contact angles for several test cases and is evaluated in complex 3D cases. Owing to this methodology, capillary pressure and permeability can be extracted, upscaled from flows computed in both model and more realistic microstructures.

Contents

List of Symbols

General notations

$\boldsymbol{v}$	Velocity
p	Pressure
T	Temperature
E	Energy
ϕ	Level-set function
Ω	Computational domain
Ω_h	Discretised computational domain (mesh)
Ω_h^e	Element e of the discretised computational domain
$\boldsymbol{n}$	Unit normal pointing outward
$\boldsymbol{I}$	Identity tensor
h_e	Element mesh size
$\mathscr{R}e$	Reynolds number
t	Time
t_n	Discretised time
$\boldsymbol{x}$	Point coordinates
θ	Parameter for time discretisation θ-method
dim	Dimension of the computational domain (2D or 3D)

Symbols for the fluid mechanics

μ_j	Dynamic viscosity $j \in \{L, S\}$
ρ_j	Density $j \in \{L, S\}$
λ	Thermal conductivity
γ_i	Surface tensions $i \in \{LV, SV, SL\}$
$\mathscr{C}$	Mean curvature
$\boldsymbol{g}$	Acceleration of gravity
$\boldsymbol{\sigma}$	Cauchy stress tensor
$\dot{\boldsymbol{\epsilon}}(\boldsymbol{v})$	Strain rate tensor
Γ_i	Interfaces $i \in \{LV, SV, SL\}$
θ_c	Contact angle at equilibrium
β	Friction coefficient
$\mathscr{W}$	Velocity space
$\mathscr{Q}$	Pressure space
$\boldsymbol{w}$	Velocity shape function
q	Pressure shape function

τ_v	Velocity stabilisation coefficient for ASGS method
τ_p	Pressure stabilisation coefficient for ASGS method

Symbols for the level-set problem

$\check{\phi}$	Filter level-set
$\mathscr{S}$	Level-set space
ϕ^*	Shape function
$\tilde{\phi}^*$	Stabilised shape function
τ	Re-initialisation time step
$\boldsymbol{v}_r$	Re-initialisation velocity

Operators

$\frac{\partial \bullet}{\partial t}$	Partial derivative with respect to time
$\frac{D \bullet}{Dt} = \frac{\partial \bullet}{\partial t} + \boldsymbol{v} \cdot \nabla \bullet$	Material derivative
$\nabla \bullet$	Gradient
$\nabla_\Gamma \bullet$	Surface gradient
$\nabla \cdot \bullet$	Divergence
$\bullet \otimes \bullet$	Tensorial product

Acronyms

LV	Liquid/Vapour
SV	Solid/Vapour
SL	Solid/Liquid
ASGS	Algebraic Sub-Grid Scale
SUPG	Streamline Upwind/Petrov-Galerkin
SLR	Surface Local Reconstruction

General Introduction - Composite materials

Contents

Introduction

As a part of an industrial chair between the company Hexcel Reinforcements and Mines Saint-Etienne, composite manufacturing through Liquid Composite Molding (LCM) processes are studied and numerically simulated. LCM processes are investigated to produce thin parts for aeronautics, when seeking a cost effective alternative to autoclave processing. Indeed, in most cases, no conditioned storage and no heavily expensive facilities are required. Additionally, a fewer number of steps are needed for producing a part. All these factors reduce the global cost.
In this general introduction, the constituents of the studied composite materials are presented. Then, the motivation of using infusion based processes (namely Liquid Resin Infusion (LRI) [75]) over injection based processes (namely Resin Transfer Molding (RTM) [108]) is explained by the targeted application range. Numerical process simulation is elaborated to minimise the apparition of defects, such as porosities, in the composite materials during the infusion. Additionally, numerical models give an insight into local phenomena which control the overall response but are difficult to assess experimentally. Three scales may be chosen to look at the resin impregnation. The lower scale contains precise and local information, it is the scale chosen in this work.

Composite materials constituents

Composite materials such as considered here are heterogeneous fibrous materials made of at least two immiscible components: a reinforcement and a matrix.

Matrix

The main role of the matrix is to ensure the cohesion of the material. Also, it is used to prevent the composite material from being damaged by external aggressions [33, 53]. The type of matrix is determined by the intended application. Organic matrix composites have an operating range of up to 250 °C. Among the organic matrices, two subcategories may be dissociated:

thermoplastic and thermosetting resins.

— Thermoplastic resins have long molecular chains forming a semi-crystalline structure when cooling down. Then, weak bonds such as Van der Waals interaction or hydrogen bonds are created between the molecules. These bonds can be broken up when temperature increases allowing relative motion between particles which translates into a flow at the upper scale. Therefore, thermoplastic resins may be recycled by applying a thermal cycle. Due to the long molecule chain, the viscosity is above $1\,\mathrm{Pa}\cdot\mathrm{s}$. This high viscosity tends to slow down the flow during infusion/injection, making the reinforcements impregnation a sensitive step.
— Due to short polymer chain, thermosetting resins have a lower viscosity. An exothermic chemical reaction [22, 126, 128] is thermo-activated, leading to irreversibly change from a liquid phase to a solid phase. During the cross-link step, covalent bonds are created between molecules. When the resin has entirely polymerised, the complex geometrical structure formed may be destroyed by an important thermal loading, making the composite hard to recycle. By its structure (geometry and bounds), the thermosetting have high thermo-mechanical properties. More specifically, the use of epoxy resins is a common practice in the field of high-performance composites such as in aeronautics.

Reinforcements

Reinforcements considered in this industrial chair are made of continuous and dry carbon fibres. These carbon fibres have a high tensile modulus (between 240 and 800 GPa) for a low density (between 1.75 and $1.9\,\mathrm{kg}\cdot\mathrm{dm}^{-3}$) [23, 25]. Therefore, composites made with carbon fibres are mainly employed for structural parts. Carbon fibre reinforcements may have a variety of structural architecture depending on the number of fibre orientations: unidirectional (UD), bidirectional or multidirectional and the reinforcements architecture: NCF, woven, interlock, *etc*. This work focuses on unidirectional carbon reinforcements.

In this work, the resin is of epoxy type with an assumed Newtonian behaviour in this liquid state [36]. Unidirectional reinforcements made of continuous dry carbon fibres are considered. Fibres are arranged in tows, which are a group of several thousand of fibres. These fibres have an almost constant diameter and a circular cross-section.

LRI process

Among LCM processes, LRI process is chosen to be studied in the industrial chair. LRI is a promising process since it is cost effective and well adapted for manufacturing thin and large parts. Actually, unlike RTM where the resin is injected in the fibrous preform constrained between rigid moulds, in injection only a lower mould is mandatory, and a vacuum bag isolates the system from atmosphere. The vacuum bag is cheaper than an outer mould and allows to compact the stack of preforms when vacuum is pulled out. The second advantage of LRI is the inlet vents. For the RTM process, the position of the resin inlets impacts greatly the filling time and the flow pattern in the preforms. This limitation does not apply to LRI process since the resin flows in a wetting membrane in the plane before starting to infuse the preforms through

their thickness. Therefore, among LCM processes LRI is studied in this work over RTM since it is the most relevant process for thin and large pieces under industrial context, rate and high quality requirements.

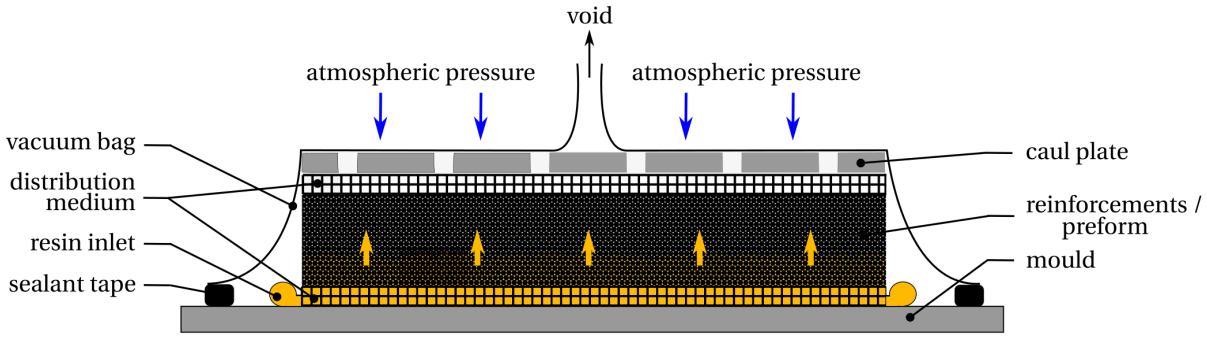

FIGURE 1 – LRI process principle

Infusion strategy (LRI) is shown in Fig. 1. Atmospheric pressure compacts the preform, since air is pumped out. Vacuum is also the driving force for the resin to flow from the injection vent through a highly permeable distribution medium located under the preform. Thus the resin flows preferentially into the distribution medium, forming a homogeneous bed, before infusing into the preforms across their thickness. The challenge in mastering this process lies in obtaining a homogeneous composite part, with the expected dimensions, since the parts undergoes deformations during the infusion [51, 217] and without air entrapments (voids) [140]. Indeed, at the moment, void creation and transport is a challenge on its own [35, 52]. The composite material being a multi-scales structure or at least a dual-scale medium, then a variation of fluid velocity between two scales may cause voids entrapment [139]. The change of velocity is dictated by the capillary effects. They represent the intermolecular forces acting at an interface between two phases. Typically, three interfaces are involved namely fibres/resin, fibres/rarefied-air and resin/rarefied-air interfaces. The global force resulting from each interfaces may be modelled by a capillary pressure (pressure jump p_{cap}) between the resin and air, which helps the fluid to flow in narrow regions such as fibre tows. To understand the voids creation mechanism, the competition between capillary effects and the viscous effect is an important factor to assess [127, 167]. As shown in Fig. 2, if the viscous effect is larger than capillary effect then micro-voids

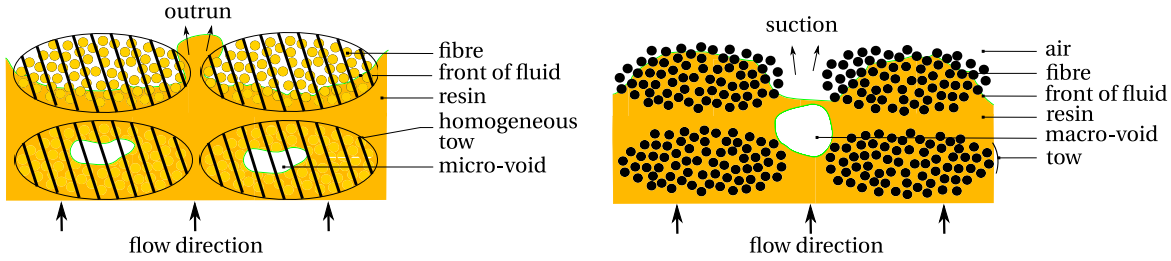

(A) Flow between the tows and micro-voids entrapment (B) Flow inside the tows and macro-voids entrapment

FIGURE 2 – LRI - voids entrapment mechanism

may be entrapped (see (A)), whereas capillary effect higher than viscous effect may lead to entrap macro-voids (see (B)). Voids are harmful to the materials since they can initiate cracks or help in propagating them. They tend to deteriorate the mechanical properties of the composite materials.

LRI process may have another source of void generation: the residual solubilised air. Solubilised air is mostly removed from the resin during an outgassing step. However, the residual solubilised air vapourises when lowering the pressure. Finally, at the end of the process, voids generated by one of the entrapment mechanisms or vapourised, grow during the curing of composite materials [72] due to moisture.
This study is centred on the resin propagation into the micro-structure during the infusion. Therefore, the method has to be able to describe the capillary action in order to recreate the two voids entrapment mechanisms depicted in Fig. 2.
Finally, our study aims at representing the dual-scale flow by reporting the local effects induced by the resin flow into the part scale. So far, studies carried out have shown that filling times are rather poorly predicted from studies at the part scale [36]. Therefore, such models have to be enriched by integrating local information on the micro-structure and local capillary effects.

Capillary flow in fibrous materials at different scales

As a consequence of the structure of the reinforcements, resin flow can be described at three scales, as shown in Fig. 3: the macroscopic scale or part scale, the mesoscopic scale or tow scale, and the microscopic scale or fibre scale. We can briefly describe these different scales and evaluate how capillary effects and the geometric description of the micro-structure can be modelled.

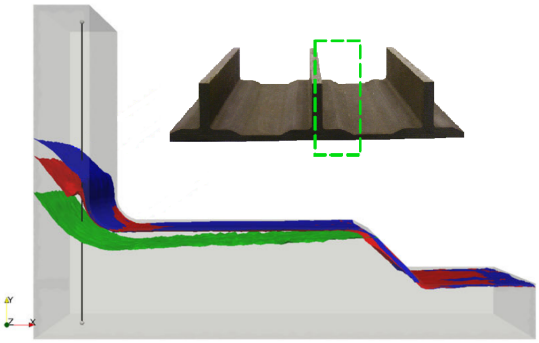

(A) Part scale $\propto$ 1 m

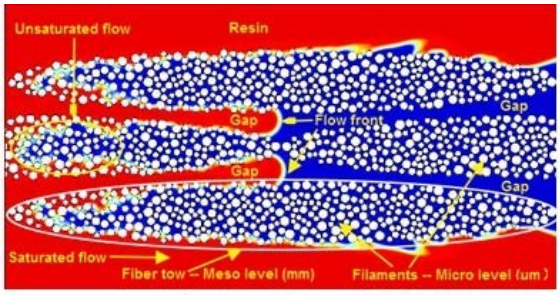

(B) Tow scale $\propto 10^{-3}$ m

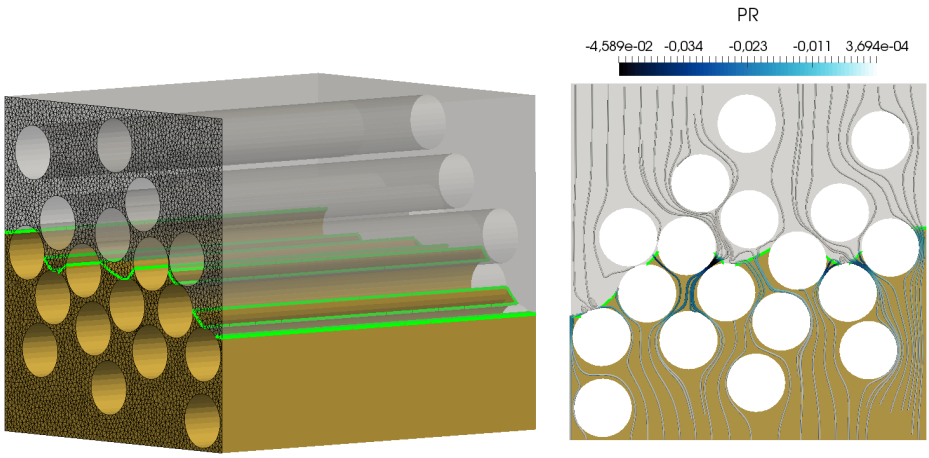

(C) Fibres scale $\propto 10^{-6}$ m

FIGURE 3 – LRI - Process scales from (A) [17], (B) [138], (C)

Part scale

At the part scale, the fibrous reinforcement can be considered as a homogeneous medium characterised by a permeability and a fibre volume fraction. Permeability K is originally defined as the ability of a medium to allow fluids, *i.e.* resin in the scope of this study, to pass through it in a saturated regime. The resin flow can be described by the Darcy's law [69] when the permeability is lower than $10^{-6}\,m^2$. This description has been used within our team so far [36, 74, 3, 166] to study composite manufacturing at the macroscopic scale. In these past studies, Darcy's equations have been solved in the reinforcements while Stokes equations were solved in the distribution medium, during the resin infusion (see Fig. 4). However, Darcy's law has been initially

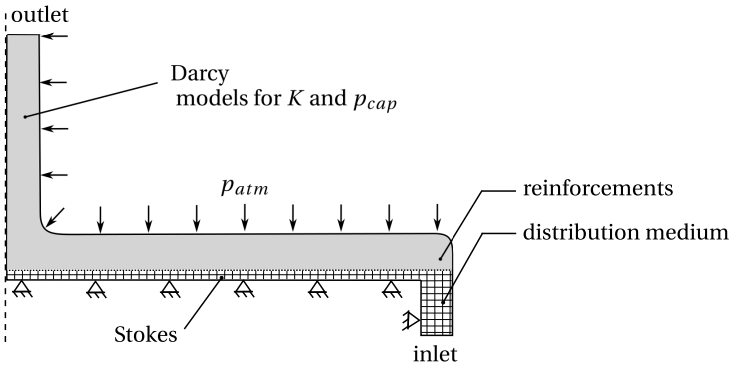

FIGURE 4 – LRI - part scale approach

established for a saturated flow and requires modelling the permeability and capillary action, both depending on the micro-structure and the fluid (resin) travelling inside [76, 176]. At the macroscopic scale and for the infusion modelling, the micro-structure may only be taken into account through empirical laws (*e.g.* Carman-Kozeny [29]) based on morphological descriptors such as the fibre volume fraction, the diameter of the fibers, the spacing between the fibers, ... Furthermore, the capillary effects are represented by a pressure jump at the resin/rarefied air interface. This capillary pressure and the permeability are given by either: phenomenological models [134, 153], micro-mechanical based on a simple micro-structure [93], or experiments. It is possible to overcome these models by extracting the relevant information from the sub-scales.

Tow scale

At the tow scale, the domain of interest contains a set of tows described as equivalent homogeneous media characterized by permeability and volume fraction of fibres. The resin flow between the tows is ruled by the Stokes equations, and by the Darcy equation inside the tows, as shown in Fig. 5. Like at the macroscopic scale, it is possible to take into account a capillary force via a pressure discontinuity at the fluid front. Here too, the value of this jump is given by: a phenomenological law, a micro-mechanical model or experiments, since it depends on the geometry of the fibre network, accessible only by morphological descriptors. However, this capillary force is only taken into account in tows, which implies that the flow depends directly on the geometry of the tows.

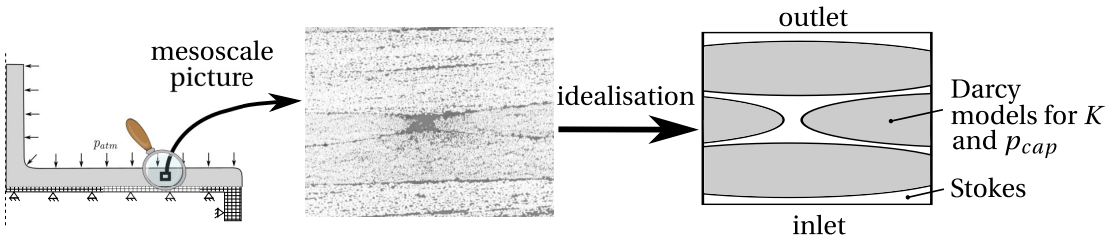

FIGURE 5 – LRI - tow scale approach (picture extracted from [36])

Fibre scale

At the scale of the fibre, the domain of interest corresponds to all the inter-fibre spaces (fibres are impervious) and the flow is described by the Stokes equations, as seen in Fig. 6. The

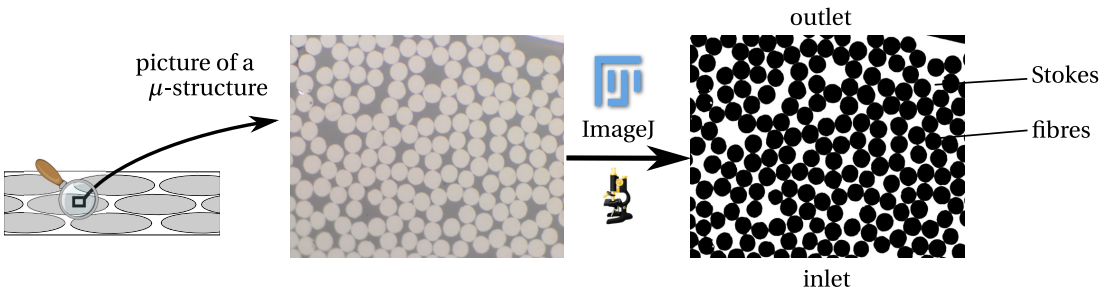

FIGURE 6 – LRI - fibre scale approach

model accuracy comes from the geometrical description of the fibres arrangement which is directly taken into account, unlike in a homogeneous medium approach, as for tow and part scales. Furthermore, no phenomenological law is needed for the capillary action. The capillary force given by the mechanical equilibrium of the triple line is added as a condition to satisfy when solving the Stokes equations. Even at this microscopic scale, the continuum approach does not take into account the motion of the particles (atoms) at the triple line. Therefore, computing the dynamic of the capillary action/force would require a model for the contact angle driven by the molecular scale phenomena.

The study of this scale has the advantage that a capillary pressure and a permeability may be derived through an upscaling step. Computed at the fibre scale, the capillary pressure gives a model for the capillary action to be used at the global scale [136]. Whereas, the permeability models the action of the fibres onto the fluid flow [195]. Both parameters are computed at the fibre scale in order to be used at the part scale.

The capillary pressure can be defined as the average action of the surface tension force, contrary to the permeability, which is defined for a homogeneous medium but has to be computed at the fibre scale. Therefore, this work will focus on presenting a numerical method describing capillary effect. The method will be used to compute permeabilities and capillary pressures in micro-structures.

Research objectives

The aim of this industrial chair with Hexcel and Mines Saint-Etienne is to provide a numerical model to simulate the LRI manufacturing process for aeronautic applications, especially when thin composite parts are considered. In our group, a macroscopic and mesoscopic approach has been developed [17] relying on models and experimental values to account for both the capillary action and permeability. The present work proposes a numerical strategy to describe the resin infusion at the microscopic scale with a surface tension force acting on the fluid front and surface energies of fibres. It is intended to enhance the accuracy and physical description of the macroscopic model but not replace it. Meaningful descriptors of the microstructure such as the permeability and a capillary pressure will be scaled-up to the macroscopic model. The rest of the manuscript is organised in five chapters as follows:

— Chapter 2 presents the physical model used to describe the flow at microscopic scale. The model is able to represent the fluid velocity and the pressure in the microstrucutre. It is given in a general case with three interfaces between three phases (solid, liquid and vapour). Two numerical models called 'solvers' are needed to describe respectively the flow and the interface between the liquid and vapour phase.

— Chapter 3 introduces the numerical model for the fluid computation (in both liquid and vapour phases). Mathematical modelling presented in the previous chapter is numerically solved after highlighting the underlying challenges. A validation of the fluid 'solver' is presented at the end of the chapter

— Chapter 4 focuses on the interface capturing 'solver' based on a level-set function. The level-set 'solver' is tested to verify the numerical implementation. The final test emphasises that the level-set method conserves the mass if numerical parameters are chosen wisely.

— Chapter 5 steps up the global numerical strategy to describe the surface tension force. The level-set solver used to capture the interface gives the interface position. At this position, a force is added into the fluid solver to represent the action of molecular cohesion on an interface. A comparison between two strategies to couple the two solvers (fluid and level-set) is carried out.

— The final chapter, 6, validates the method proposed to compute surface tension action. Furthermore, it presents a strategy to scale-up the two local parameters: surface tension action and fibres arrangement, into two global parameters respectively called capillary pressure and permeability.

Résumé en Français : Introduction générale - les matériaux composites

Les procédés de fabrication par voie liquide sont une technique prometteuse pour réduire les coûts associés à la fabrication de pièces composites. L'étude approfondie des procédés est nécessaire pour en acquérir la maîtrise et les optimiser, afin de réduire les défauts induits tout en maximisant les rendements. Du fait des coûts importants d'une analyse expérimentale par essais / erreurs sur de grandes pièces pour l'aéronautique, la simulation numérique offre une alternative moins onéreuse et complémentaire pour l'étude quantitative des physiques à l'œuvre

et des phénomènes associés. C'est dans ce contexte qu'une chaire industrielle a été créée en 2015 entre l'École des Mines de Saint-Étienne et Hexcel Reinforcements pour simuler les procédés de fabrication. Finalement, le cadre d'étude de cette thèse s'inscrit dans cette collaboration entre un laboratoire et un partenaire industriel, visant plus particulièrement à comprendre et simuler la phase d'infusion du procédé.

Les travaux précédents ont produit des outils numériques pour simuler l'avancée du front de résine pendant l'infusion d'une préforme fibreuse en se basant sur plusieurs hypothèses. Un milieu homogène équivalent a été associé à la préforme dans laquelle l'écoulement est régi par la loi de Darcy. La résine imprègne la préforme fibreuse grâce à un différentiel de pression induit par la mise sous vide du système. Ce type de modélisation est capable de rendre compte de géométries complexes de pièces ainsi que de l'anisotropie de la perméabilité liée aux empilements des fibres de carbone. Enfin, les composites dits de hautes performances se distinguent par un taux volumique de fibre élevé assurant de meilleures propriétés mécaniques. Ce milieu fibreux dense possédant des espaces poreux confinés est propice aux effets capillaires, non représentés dans les travaux antérieurs. Le but de cette thèse est par conséquent de pallier les limitations du modèle développé en calculant l'écoulement de la résine à l'échelle locale des fibres. L'objectif principal de cette thèse est double : premièrement, établir un modèle numérique stable et robuste permettant de prendre en compte les phénomènes capillaires à l'échelle des fibres ; puis dans un second temps, proposer une remontée d'échelle pour retranscrire la richesse des informations locales dans des paramètres globaux tels que la perméabilité et la pression capillaire. L'écoulement dans la préforme est multiéchelle, pouvant être décomposé en trois niveaux (l'échelle de la pièce, du toron et des fibres). L'étude à l'échelle des fibres offre une meilleure représentativité de la force capillaire en se basant sur l'équilibre mécanique d'une interface plutôt que sur des lois empiriques.

La modélisation de l'écoulement de la résine avec effets capillaires est étudiée dans un premier temps. La résolution numérique des équations du modèle nécessite deux outils : le premier permettant de résoudre les équations de la mécanique des fluides avec prise en compte des tensions de surface ; le second permettant la description d'une interface propre à la formulation Eulérienne du problème. Les deux outils (solveurs) seront successivement présentés et validés. Une méthode numérique pour prendre en compte la force de tension de surface sera présentée, basée sur ces deux solveurs. Deux algorithmes de couplage des deux solveurs seront détaillés. Enfin, plusieurs cas tests de validations seront menés avec l'étude de ménisques dans différentes configurations géométriques. Une comparaison à un benchmark numérique permettra de positionner la méthode par rapport à d'autres méthodes issues de groupes de recherche. La dernière partie de la section résultat sera consacrée à l'exploitation d'écoulements dans des microstructures pour en extraire des perméabilités numériques et des pressions capillaires.

Chapter 1

Modelling the flow and capillary action

Contents

Introduction

Composites manufacturing by LRI process has to be studied at the microscopic scale (fibre scale) with all its complexity, if one wants to get a deep understanding of the mechanisms controlling the resin impregnation through fibrous preforms. The first key step, which is developed in this chapter, consists in modelling the resin and air flows at fibre scale. With this model, a local description of geometry (fibres) is possible and mechanical equilibrium of the three interfaces (solid/liquid, solid/vapour and liquid/vapour) may be added in the equations to describe the capillary action. First, conservation equations are given for the fluid and then the equilibrium equations are given for an interface. These equations form the system to be solved in velocity and pressure. This chapter presents a general framework for a bi-fluid flow. Each concept is exposed and systematically simplified based on the LRI process context. Two cases of capillary action against gravity, one against a wall and the second between two walls, are presented at the end of the chapter. They are designed to understand with examples the boundary condition at the triple line where all the three phases (solid, liquid and vapour) are in contact.

1.1 Fluid mechanics equations

Fluid mechanics equations are presented in the following section for the bulk fluid which can be either the vapour or the liquid phase.

1.1.1 Notation

The problem to be solved considers two fluids: a vapour phase and a liquid phase. The fibres or solid phase, are taken into account only through boundary conditions since they are supposed to be fixed. Geometry and notations are given using Fig. 1.1. The bounded domain

$\Omega \subset \mathbb{R}^3$ is subdivided into two sub-regions denoted $\Omega_L(t)$ for the liquid and $\Omega_V(t)$ for the vapour phase with $\Omega = \Omega_V(t) \cup \Omega_L(t)$ as shown in Fig. 1.1. The presence of two phases leads to the creation of an interface, denoted $\Gamma_{LV}(t) = \partial\Omega_V(t) \cap \partial\Omega_L(t)$ the position of which depends on time. Furthermore, the rigid wall (*Solid*) is defined as a boundary of the computational domain and may represent fibres for the composite manufacturing case. The solid interface can be subdivided into two interfaces $\Gamma_{SL} = \Omega_L \cap Solid$ and $\Gamma_{SV} = \Omega_V \cap Solid$. Each of the three interfaces Γ_{int}, for $int \in \{SL, SV, LV\}$, has a unit normal $\boldsymbol{n}_{int}$ and a tangent plane described by two orthogonal vectors $\boldsymbol{t}^1_{int}$ and $\boldsymbol{t}^2_{int}$, along with one in-going tangent $\boldsymbol{T}_{int}$ of the interfaces contour at the triple line (*see* Fig. 1.1). The line at the junction between the three phases (liquid, solid, vapour) is called the triple line and is denoted $L(t) = \Gamma_{SL} \cap \Gamma_{SV} \cap \Gamma_{LV}$.

In the specific case of composite manufacturing, the resin is represented by the liquid phase,

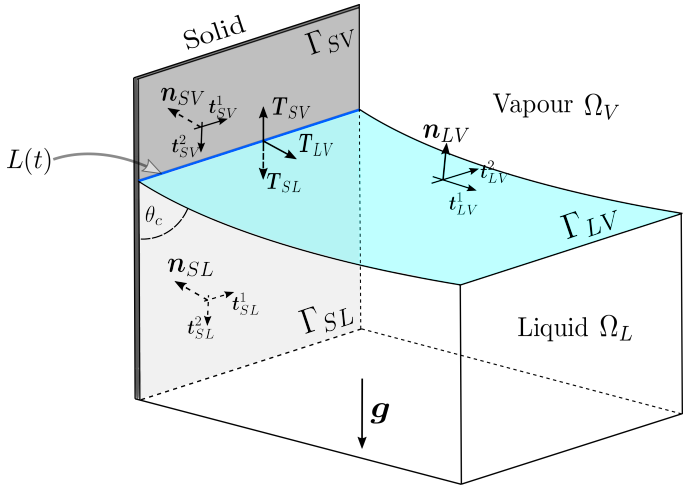

FIGURE 1.1 – Schematic description of notations for a capillary flow - a liquid meniscus against a rigid wall [58]

the rarefied air is the vapour phase and the fibres are the solid phase which is a boundary of the fluid domain. Vectors and tensors are represented in the standard orthonormal basis of $\mathbb{R}^{dim}$ formed of vectors $\boldsymbol{x}^k$, with dim the dimension of the problem.

1.1.2 Bulk fluid conservation laws

The conservation of a quantity ψ in a control volume Ω fix in time reads: at time t, the instantaneous variation of ψ in Ω is due to a convective flux characterized by a velocity $\boldsymbol{v}$ and due to creation/annihilation phenomena, described by two source/sink terms. It can be written as

$$\underbrace{\frac{\partial}{\partial t}\int_\Omega \psi dV}_{\text{variation of quantity } \psi} = \; - \; \underbrace{\int_{\partial\Omega} \psi\, \boldsymbol{v}\cdot\boldsymbol{n} dA}_{\text{convection flux}} \; + \underbrace{\int_{\partial\Omega} \boldsymbol{s}^{surf}\cdot\boldsymbol{n} dS + \int_\Omega s^{vol} dV}_{\text{creation/anihilation rate}} \tag{1.1}$$

with $\boldsymbol{n}$ the outgoing unit vector, normal to the domain boundary $\partial\Omega$. The source/sink term can be defined on the surface ($\boldsymbol{s}^{surf}$) or in the volume (s^{vol}) of the control volume. Using Ostrogradsky's theorem, the local form of Eq. 1.1 is

$$\frac{\partial \psi}{\partial t} + \nabla\cdot(\psi\,\boldsymbol{v}) = \nabla\cdot\boldsymbol{s}^{surf} + s^{vol} \tag{1.2}$$

This equation is known as continuity equation, written in a conservative form. Classically, three quantities are conserved: mass, momentum and energy density E. Five equations have to be established to solve the five unknowns that will be pressure p, velocity $\boldsymbol{v}$, and temperature T resulting from energy conservation.

Mass conservation

Without any change in the matter itself (chemical or thermal reaction for instance), mass is conserved over time. Therefore mass conservation can be derived by replacing ψ by the density, ρ in Eq. 1.2. After removing the source terms, the equation reads

$$\frac{\partial \rho}{\partial t} + \nabla \cdot (\rho \boldsymbol{v}) = 0 \tag{1.3}$$

— For an incompressible fluid, density is constant over time and space. The previous equation 1.3 can be simplified and yields

$$\nabla \cdot \boldsymbol{v} = 0. \tag{1.4}$$

— Otherwise if the fluid is compressible, the system must be closed by a state equation relating the thermodynamic variable ρ to the pressure and temperature T, $\rho = \rho(p,T)$ [107, 111, 110]. A well known equation of state is for example the ideal gas law $p = \rho RT$. Eq. 1.3 can be rewritten as $\frac{D\rho}{Dt} + \rho \nabla \cdot \boldsymbol{v} = 0$, introducing the material derivative $\frac{D}{Dt}$ notation, defined as

$$\frac{D\bullet}{Dt} = \frac{\partial \bullet}{\partial t} + \boldsymbol{v} \cdot \nabla \bullet$$

Next, using the fact that ρ is a function of p and T, from the chain rule it comes that

$$\frac{D\rho}{Dt} = \frac{\partial \rho}{\partial T}\Big|_p \frac{DT}{Dt} + \frac{\partial \rho}{\partial p}\Big|_T \frac{Dp}{Dt}.$$

Then replacing it back into the mass conservation equation, thise equation reads

$$\underbrace{\frac{1}{\rho}\frac{\partial \rho}{\partial T}\Big|_p}_{-\chi_T} \frac{DT}{Dt} + \underbrace{\frac{1}{\rho}\frac{\partial \rho}{\partial p}\Big|_T}_{\chi_p} \frac{Dp}{Dt} + \nabla \cdot \boldsymbol{v} = 0 \tag{1.5}$$

where χ_T and χ_p are respectively the thermal isobaric expansion coefficient and the isothermal compressibility coefficient. For an ideal gas, those coefficients are $\chi_T = 1/T$ and $\chi_p = 1/p$. The global mass conservation in the case of a compressible fluid is

$$\nabla \cdot \boldsymbol{v} + \chi_p \left(\frac{\partial p}{\partial t} + \boldsymbol{v} \cdot \nabla p \right) = \chi_T \left(\frac{\partial T}{\partial t} + \boldsymbol{v} \cdot \nabla T \right) \tag{1.6}$$

From literature, it is not clear whether the compressibility of the surrounding medium (*e.g.* the rarefied air), has an influence on composites manufacturing. Besides, describing the dynamic of the vapour phase is not in the scope of this study. Consequently, due to the Eulerian approach, only a continuous extension of the velocity across the interface Γ_{LV} is sought. Therefore, the vapour phase is considered Newtonian and incompressible. The same choice holds for

the resin in LCM processes and in particular for spontaneous impregnation or infusion driven by low pressure gradient.

Momentum conservation

Starting from equation 1.2 and considering $\psi = \rho v_k$, where the subscript $k \in \{1,2,3\}$ means the k^{th} component of a vector, leads to a conservation of momentum equation

$$\rho\left(\frac{\partial v_k}{\partial t} + \boldsymbol{v}\cdot\nabla v_k\right) + v_k\underbrace{\left(\frac{\partial \rho}{\partial t} + \nabla\cdot(\rho\boldsymbol{v})\right)}_{=0} = (\nabla\cdot\boldsymbol{s}^{surf})_k + s_k^{vol} \tag{1.7}$$

after decomposing the term $\nabla\cdot(\rho v_k\boldsymbol{v})$ in the following way $\nabla\cdot(\rho v_k\boldsymbol{v}) = \rho\boldsymbol{v}\cdot\nabla v_k + v_k\nabla\cdot(\rho\boldsymbol{v})$.

The surface source/sink term describes the molecular cohesive surface forces acting on the surface of an infinitesimal fixed control volume. For each k momentum conservation equations, the surface source/sink is the divergence of the Cauchy stress tensor projected over the face of normal $\boldsymbol{x}^k$ *i.e.* $\boldsymbol{x}^k\cdot\boldsymbol{\sigma}$, thus $(\nabla\cdot\boldsymbol{s}^{surf})_k = \frac{\partial\sigma_{kl}}{\partial x_l}$. The second source/sink term on the volume is the k^{th} vector component of body forces such as $s_k^{vol} = \rho(\boldsymbol{f}_v)_k$. The momentum conservation equations then read

$$\rho\left(\frac{\partial\boldsymbol{v}}{\partial t} + \boldsymbol{v}\cdot\nabla\boldsymbol{v}\right) = \nabla\cdot\boldsymbol{\sigma} + \rho\boldsymbol{f_v} \tag{1.8}$$

Energy conservation

Finally, the energy balance [15] is obtained by considering $\psi = \rho E$ in Eq. 1.2:

$$\frac{\partial\rho E}{\partial t} + \nabla\cdot(\rho E\boldsymbol{v}) = \nabla\cdot\boldsymbol{s}^{surf} + s^{vol}. \tag{1.9}$$

The surface source term is split in two parts: the heat flux entering/exiting the fixed control volume $\boldsymbol{q}$ and the power dissipated by the surface forces $(\boldsymbol{\sigma}\cdot\boldsymbol{n})\cdot\boldsymbol{v}$. Since the Cauchy stress tensor is symmetric $(\boldsymbol{\sigma}\cdot\boldsymbol{n})\cdot\boldsymbol{v} = (\boldsymbol{\sigma}\cdot\boldsymbol{v})\cdot\boldsymbol{n}$ and $\boldsymbol{s}^{surf} = -\boldsymbol{q} + \boldsymbol{\sigma}\cdot\boldsymbol{v}$. Recalling the Fourrier's law, the heat flux is given as $\boldsymbol{q} = -\lambda\nabla T$ with λ is the isotropic thermal conductivity for the sake of simplicity. Therefore $\nabla\cdot\boldsymbol{s}^{surf} = \nabla\cdot(\lambda\nabla T) + \nabla\cdot(\boldsymbol{\sigma}\cdot\boldsymbol{v})$. Like the surface source term, the volumetric source term is broken up into two terms: the first is related to volumetric heat $\rho\dot{r}$, where $\dot{r}$ is the rate of volumetric heat per unit mass, and the second one is the power dissipated by the volume forces $\rho\boldsymbol{f}_v\cdot\boldsymbol{v}$. Hence, the conservation of energy law can be rewritten as

$$\frac{\partial\rho E}{\partial t} + \nabla\cdot(\rho E\boldsymbol{v}) = \underbrace{\rho\dot{q}}_{\text{volumetric heat}} + \underbrace{\nabla\cdot(\lambda\nabla T)}_{\text{thermal conduction}} + \underbrace{\nabla\cdot(\boldsymbol{\sigma}\cdot\boldsymbol{v})}_{\text{surface force}} + \underbrace{\rho\boldsymbol{f}_v\cdot\boldsymbol{v}}_{\text{body force}} \tag{1.10}$$

The total energy density E is composed of an internal energy density e and a kinetic energy density $\frac{1}{2}v^2$ with $v^2 = \boldsymbol{v}\cdot\boldsymbol{v}$, so $E = e + \frac{1}{2}v^2$. The following steps intend to yield an equation of the internal energy per unit mass and then formulating it in temperature. Using the expression for the total energy density, the left-hand side of Eq. 1.10 becomes

$$\frac{\partial\rho E}{\partial t} + \nabla\cdot(\rho E\boldsymbol{v}) = \rho\left(\frac{\partial e}{\partial t} + \boldsymbol{v}\cdot\nabla e\right) + \rho\left[\frac{\partial}{\partial t}\left(\frac{v^2}{2}\right) + \boldsymbol{v}\cdot\nabla\left(\frac{v^2}{2}\right)\right] \tag{1.11}$$

Taking the scalar product of the momentum conservation equation with the velocity it comes

$$\rho\left[\frac{\partial}{\partial t}\left(\frac{v^2}{2}\right)+\boldsymbol{v}\cdot\nabla\left(\frac{v^2}{2}\right)\right]=(\nabla\cdot\boldsymbol{\sigma})\cdot\boldsymbol{v}+\rho\boldsymbol{f_v}\cdot\boldsymbol{v} \tag{1.12}$$

Then subtracting Eq. 1.12 to Eq. 1.10 the final equation for the internal energy per unit mass becomes

$$\rho\left(\frac{\partial e}{\partial t}+\boldsymbol{v}\cdot\nabla e\right)=\boldsymbol{\sigma}:\nabla\boldsymbol{v}+\rho\dot{q}+\nabla\cdot(\lambda\nabla T) \tag{1.13}$$

when using the identity $\nabla\cdot(\boldsymbol{\sigma}\cdot\boldsymbol{v})-(\nabla\cdot\boldsymbol{\sigma})\cdot\boldsymbol{v}=\boldsymbol{\sigma}:\nabla\boldsymbol{v}$. As in the compressible mass conservation equation, a state equation is needed to close the system. Again the internal energy per unit mass may depend on pressure and temperature ($e=e(p,T)$ and particularly for calorically perfect gas $e=c_vT$ with c_v the specific heat at constant volume). Therefore the temperature variation in time is ruled by the convection, the work of molecular cohesion, a volumetric heating and diffusion/conduction, in the same order as in Eq. 1.13.

The three conservation equations are coupled for two reasons. First, the unknowns may appear in all the three conservation equations (like the fluid velocity in the conservation of mass, momentum and energy). Second, conservation equations are coupled by the material parameters and the geometry. Viscosity and surface tension may depend on temperature for example. In order to avoid the cross-linking of the resin, the stage of infusion is thermally controlled in the LRI-like processes. For this reason, we will assume that the temperature remains constant in our simulations, and so will the surface tension.

1.1.3 Constitutive equation

The constitutive equation is, in our case, a law modelling the response of the studied material to an external stimulus. In other words, it expresses the relationship between the stress and strain.

Newtonian fluids

If the fluid is considered Newtonian, *i.e.* with a constant dynamic viscosity μ, the Cauchy stress tensor $\boldsymbol{\sigma}$ is

$$\boldsymbol{\sigma}=\underbrace{-p\boldsymbol{I}}_{\text{isotropic}}+\underbrace{2\mu\dot{\boldsymbol{\varepsilon}}(\boldsymbol{v})}_{\text{deviatoric}} \tag{1.14}$$

with p the pressure, the strain rate tensor $\dot{\boldsymbol{\varepsilon}}(\boldsymbol{v})=\frac{1}{2}(\nabla\boldsymbol{v}+\nabla\boldsymbol{v}^T)$ and $\boldsymbol{I}$ the second order identity tensor. This definition yields a symmetric stress tensor which is a requirement from the conservation of angular momentum.

Non-Newtonian fluids

Polymer resins used in their liquid state composite manufacturing may be non-Newtonian fluids [13]. Molten polymers may be considered as quasi-Newtonian fluids [14, 187], that is to say their viscosities depend on the strain rate $\dot{\gamma}$ usually expressed from the second invariant of the strain rate tensor, *i.e.* $\dot{\gamma}=\sqrt{2\dot{\varepsilon}:\dot{\varepsilon}}$. The simplest model consists in considering a power-law

dependence $\mu(\dot{\gamma}) = \mu_N \dot{\gamma}^{n-1}$ with μ_N and n respectively the consistency and power-law index; value $n = 1$ corresponding to a Newtonian behaviour. In addition to a strain dependent viscosity, a rheological approach may also be used [59], based on a viscoelastic constitutive law [196] to model the behaviour of the non-Newtonian fluid.
In this work, the resin is considered Newtonian in the range of stresses considered, for LRI process and spontaneous impregnation.

1.1.4 Navier-Stokes equations

The response of the fluid is given by the constitutive Eq. 1.14 which can be substituted in the conservation of momentum Eq. 1.8, leading to:

$$\underbrace{\rho\left(\frac{\partial \boldsymbol{v}}{\partial t} + \boldsymbol{v}\cdot\nabla\boldsymbol{v}\right)}_{\text{inertia}} = \underbrace{-\nabla p}_{\text{pressure term}} + \underbrace{\nabla\cdot\left(2\mu\dot{\boldsymbol{\epsilon}}(\boldsymbol{v})\right)}_{\text{viscous term}} + \underbrace{\rho\boldsymbol{f_v}}_{\text{body forces}} \tag{1.15}$$

In the case of an incompressible fluid with constant viscosity, the viscous term may be simplified: $\nabla\cdot(2\mu\dot{\boldsymbol{\epsilon}}(\boldsymbol{v})) = \mu\Delta\boldsymbol{v}$. The inertial term is made of an unsteady term and a convective term. Only the convective term $\boldsymbol{v}\cdot\nabla\boldsymbol{v}$ makes Eq. 1.15 non-linear. This term is computationally expensive since it requires an iterative strategy to solve the nonlinearity. Finally, body forces can be gravity or magnetic forces like Lorentz force [30, 156] for example. In the following study, the only body force is gravity.
The name "Navier-Stokes equations" refers to both mass and momentum conservation including a constitutive equation, particularly for a Newtonian fluid. With the incompressibility constraint, Navier-Stokes equations to be solved are

$$\begin{cases} \rho\left(\dfrac{\partial \boldsymbol{v}}{\partial t} + \boldsymbol{v}\cdot\nabla\boldsymbol{v}\right) = -\nabla p + \nabla\cdot\left(2\mu\dot{\boldsymbol{\epsilon}}(\boldsymbol{v}\right) + \rho\boldsymbol{g} \\ \nabla\cdot\boldsymbol{v} = 0 \end{cases} \tag{1.16}$$

with $\boldsymbol{g}$ the acceleration of gravity. Navier-Stokes equations define a system of four equations with four unknowns, namely velocity and pressure in three dimensions (with one less equation and velocity component in two dimensions).

Dimensionless equations

The Reynolds number [184], defined as

$$\mathscr{R}e = \frac{\text{inertia}}{\text{viscous force}} = \frac{\rho V_0 L_0}{\mu} \tag{1.17}$$

with L_0 a characteristic length and V_0 a characteristic velocity, is the dimensionless number governing the dimensionless Navier-Stokes equations. A flow with a high Reynolds number, above 10^3 is turbulent, whereas it is considered laminar for lower values of $\mathscr{R}e$.

Dimensionless quantities will be noted with a superscript *. The k^{th} component of the dimensionless coordinates, x_k^*, and velocity, v_k^* are defined from the characteristic length L_0 and velocity V_0 as

$$x_k^* = \frac{x_k}{L_0} \qquad v_k^* = \frac{v_k}{V_0}. \tag{1.18}$$

The definition of the characteristic time is straightforward from the characteristic length and velocity: $T_0 = L_0/V_0$. The last dimensionless parameter to be determined is the pressure and two possibilities may be considered:

- For a high Reynolds number: $p^* = \frac{p}{\rho V_0^2}$. The momentum equations become

$$\frac{\partial \boldsymbol{v}^*}{\partial t^*} + \boldsymbol{v}^* \cdot \nabla \boldsymbol{v}^* = -\nabla p^* + \frac{1}{Re}\Delta \boldsymbol{v}^*. \tag{1.19}$$

  In this form, the inertia terms balance the pressure gradient since the viscous term tends to vanish when the Reynolds number increases.
- For a low Reynolds number: $p^* = \frac{pL_0}{\mu V_0}$. Therefore momentum equations are written as

$$\mathscr{R}e\left(\frac{\partial \boldsymbol{v}^*}{\partial t^*} + \boldsymbol{v}^* \cdot \nabla \boldsymbol{v}^*\right) = -\nabla p^* + \Delta \boldsymbol{v}^*. \tag{1.20}$$

  When the Reynolds number tends to zero, the inertial terms tend to disappear on the left-hand side of the equation. Therefore the viscous diffusion term will be balanced only by the pressure gradient.

Stokes equations

Eq. 1.15 may be simplified for some low values of Reynolds number. Neglecting the inertial terms (*cf.* Eq. 1.20) leads to the momentum balance equation

$$\begin{aligned} \mathbf{0} &= -\nabla p + \nabla \cdot (2\mu \dot{\boldsymbol{\epsilon}}(\boldsymbol{v})) + \rho \boldsymbol{g} \\ \nabla \cdot \boldsymbol{v} &= 0 \end{aligned} \tag{1.21}$$

known as Stokes system. A value for the Reynolds number may not be inferred for LRI process, since the characteristic length is not easy to pick. Actually, one may choose the diameter of one fiber, or the length of a fibre tow (if not the length of the part) as the characteristic length, changing significantly the flow regime according to the Reynolds number. The original Reynolds experience was a flow in a straight pipe and not in a complex microstructure. The relevance of the Stokes assumption regime may be tackled by investigating the discrepancy between Stokes and Navier-Stokes flow.

1.1.5 Boundary conditions

Boundary conditions are needed to solve fluid equations. Two types of boundary may be distinguished: boundary at the interface between fluids and the solid Γ_{Sj} with $j \in \{L, V\}$ and fluid boundary.
At a fluid / solid interface, the fluid may stick to the solid (condition (1)) or slip over it (condition (2)).

— (1) A no-slip condition where the fluid sticks to the surface. Thus, the velocity vector is null in that case $\boldsymbol{v} = \boldsymbol{0}$.

— (2) Slip over the surface or symmetric boundary condition, where the normal velocity is vanishing $\boldsymbol{v} \cdot \boldsymbol{n} = 0$ (see Fig. 1.2). A zero normal velocity physically means that no fluid is entering the solid which may represent a impervious wall. The condition on the normal velocity is associated with a condition on the tangent component of the stress vector $\boldsymbol{t}^{\alpha} \cdot \boldsymbol{\sigma} \cdot \boldsymbol{n} = -\beta \boldsymbol{v} \cdot \boldsymbol{t}^{\alpha}$, where $\alpha = 1$ in two dimensions and $\alpha = 1,2$ in three dimensions. The coefficient β is a friction coefficient which may model the roughness of a wall. In the particular case where $\beta = 0$ the fluid slips freely over the surface, whereas it sticks to the solid surface when $\beta \to \infty$.

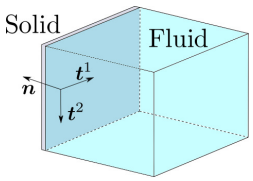

FIGURE 1.2 – Fluid boundary conditions between solid and fluid

For conditions at the purely fluid boundary, the action of an external stress is taken into account with condition (3), whereas a symmetric flow may be represented with condition (4).

— (3) Condition on the stress vector $\boldsymbol{\sigma} \cdot \boldsymbol{n}$ (see Fig. 1.3). The condition reads $\boldsymbol{\sigma} \cdot \boldsymbol{n} = -p_{ext}\boldsymbol{n}$, with p_{ext} the value of the external loading in the normal direction. Nonetheless, conditions on the tangential velocities may be added: $\boldsymbol{t}^{\alpha} \cdot \boldsymbol{v} = 0$, where $\alpha = 1$ in two dimensions and $\alpha = 1,2$ in three dimensions. This condition may represent the action of a pump where the pressure is known but not the velocity distribution of the fluid.

— (4) Symmetric boundary condition. This condition is useful to impose a symmetric flow in order to restrict the computational domain, the condition reads $\boldsymbol{v} \cdot \boldsymbol{n} = 0$ with the tangential components of the stress vector left equal to zero.

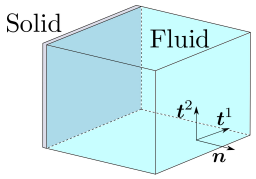

FIGURE 1.3 – Fluid boundary conditions at the fluid boundary

Aside from having boundary conditions in space at the domain boundary, initial fields have to be prescribed as soon as a time derivative is involved in an equation.

1.2 Surface tension force

After studying the bulk, interface mechanics is emphasised as an extension of the derivation presented at the continuum level. Non equilibrated forces are located at each interface between liquid, vapour and solid phases [37, 71, 144]. Those forces are directly linked to the scope of the study since that capillary forces are complementary driving forces for manufacturing composites through LRI process. This force may become prevalent in confined environments, which is involved in a wide range of industrial and natural phenomena [46, 174, 189, 190]. This section recalls concepts of wetting and capillarity involved in capillary flows.

1.2.1 Basic notions

Molecules in a fluid have bonds between them, due either to intermolecular attraction forces such as Van der Waals forces, hydrogen bonds or repulsive forces such as electromagnetic force. In the case of a static liquid drop, such as the one represented in Fig. 1.4, molecules are at equilibrium on average. As it can be seen in figure, molecules at the boundary have fewer interactions than molecules inside the fluid. This creates a disequilibrium. This lack of interactions from the outer side of the liquid surface leads to an extra tension between the molecules acting along the liquid surface. The resulting force on the interface is called surface tension and can be understood as a force per unit length or a surface energy. At equilibrium, the shape of the interface is driven by a minimisation of this surface energy and potential energy.

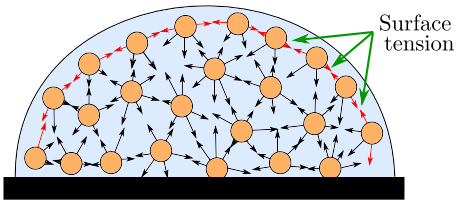

FIGURE 1.4 – Bounds and interactions between molecules in a liquid drop

Surface tension coefficient

Fluid mechanics give a first definition of the surface tension coefficient γ as a force per unit length. Let $\mathrm{d}f$ be the force needed to create an element of length $\mathrm{d}l$, reversibly and isothermally, then γ is defined as

$$\gamma = \left(\frac{\mathrm{d}f}{\mathrm{d}l}\right)_{V,T,n} \tag{1.22}$$

at constant temperature T, volume V, and molecule number n. The force induced by the attraction between molecules is tangent to the interface. For example, a volume with a constant surface tension will modify its shape to become a sphere due to this tangential force. This first definition may be used to describe the surface tension coefficient at the interface Γ_{LV}.
Another equivalent definition for the surface tension coefficient consists in defining it as the work needed to create an element of area $\mathrm{d}A = l\,\mathrm{d}l$ (see Fig. 1.5)

$$\mathrm{d}W = \mathrm{d}\boldsymbol{f}.\mathrm{d}\boldsymbol{l} = 2\gamma\ \mathrm{d}A \tag{1.23}$$

where there are two interfaces Liquid/Vapour since the liquid film has a width. A direct consequence is that the surface tension can be regarded as an energy per square meter.

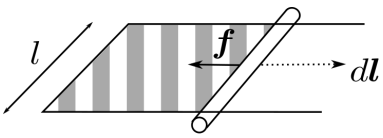

FIGURE 1.5 – Surface tension normal to the tube

Surface energies are coefficients that quantifies the work done to create an interface with solid, in our case Γ_{SL} and Γ_{SV}. The second definition is also known as the thermodynamic approach [97] describing the surface tension as the variation of free energy of a closed system relative to the variation of the interface area. For both approaches, the surface tension is temperature

dependent and tends to decrease as temperature increases. Various methods can be used to measure the surface tension value [5, 32]. Among the common methods, the characterisation used by our team is based on Wilhelmy's method [214, 224]. It consists in measuring, with a tensiometer, the weight of a liquid meniscus formed on a solid of high surface energy. This measured force may be correlated to the surface tension coefficient. In this study, the surface tension and energy coefficients measured are the input data of simulations. These coefficients are usually given in $\mathrm{mN}\cdot\mathrm{m}^{-1}$. For example, the surface tension coefficient value between water and air is $72.8\,\mathrm{mN}\cdot\mathrm{m}^{-1}$ at room temperature. From now on, 'surface tension' refers to the surface tension force and 'surface tension (or energy) coefficient' is the force per unit length. Surface tension is acting on the liquid / vapour interface Γ_{LV} and surface energies are applied on solid / fluid interfaces Γ_j with $j \in \{SV, SL\}$.

1.2.2 Mechanical equilibrium of an interface

The general concept of mechanical equilibrium describing the jump of stress vector at an interface is applied for each interface: Liquid/Vapour, Solid/Liquid and Solid/Vapour. As an extension of the conservation equations presented above, the mechanical balance of the interface is presented. The derivation is given in two dimensions for the sake of clarity but holds in 3D [47]. Force configuration acting on an interface Γ are represented in Fig. 1.6. The curvilinear abscissa is S. The normal $\boldsymbol{n}$ is the outgoing normal and $\boldsymbol{t}$ the only tangent in two dimensions.

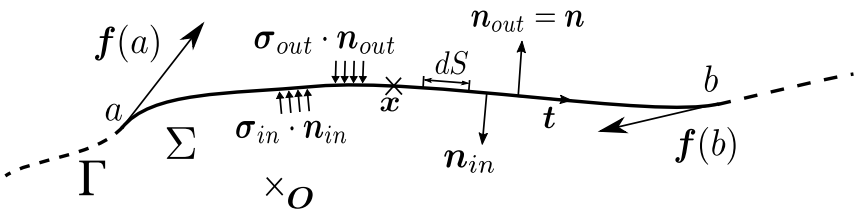

FIGURE 1.6 – Mechanical equilibrium of the interface - Force configuration acting on any $\Sigma \subset \Gamma$

Force and momentum balance equations are derived below for any surface control Σ of interface Γ. These equations imply that surface tension force is acting only in the tangential direction and give the jump of the stress vector across an interface (Laplace's law).

Force balance

A force at the interface, denoted $\boldsymbol{f}(s)$, represents the surface tension. The stress vectors $\boldsymbol{\sigma}\cdot\boldsymbol{n}$ are associated with the interaction of the bulk phases with the interface. Neglecting the inertia of interface, the force equilibrium yields

$$\left[\boldsymbol{f}\right]_a^b + \int_\Sigma (\boldsymbol{\sigma}_{out} - \boldsymbol{\sigma}_{in})\cdot\boldsymbol{n}\, dS = 0 \tag{1.24}$$

where $\left[\boldsymbol{f}\right]_a^b = \boldsymbol{f}(b) - \boldsymbol{f}(a) = \int_\Gamma \frac{d\boldsymbol{f}}{dS} dS$. The jump is noted $[\![\cdot]\!]$ and the jump of stress vector is $[\![\boldsymbol{\sigma}\cdot\boldsymbol{n}]\!]$. Finally, the local force balance equation is

$$\frac{d\boldsymbol{f}}{dS} + [\![\boldsymbol{\sigma}\cdot\boldsymbol{n}]\!] = 0 \tag{1.25}$$

Momentum balance

The equation is written for any vector position $\boldsymbol{x}-\boldsymbol{O}$ where O is an arbitrary origin

$$\left[(\boldsymbol{x}-\boldsymbol{O})\times\boldsymbol{f}\right]_a^b+\int_\Gamma(\boldsymbol{x}-\boldsymbol{O})\times[\![\boldsymbol{\sigma}\cdot\boldsymbol{n}]\!]\,dS=0 \tag{1.26}$$

The first term of the equation may be rewritten in an integral form and further developed

$$\left[(\boldsymbol{x}-\boldsymbol{O})\times\boldsymbol{f}\right]_a^b=\int_\Gamma\left(\boldsymbol{t}\times\boldsymbol{f}+(\boldsymbol{x}-\boldsymbol{O})\times\frac{d\boldsymbol{f}}{dS}\right)dS \tag{1.27}$$

since the derivative of the position vector is the tangent vector $\frac{d(\boldsymbol{x}-\boldsymbol{O})}{dS}=\boldsymbol{t}$. When cancelling terms using the force balance Eq. 1.25, the local momentum equilibrium equation becomes

$$\boldsymbol{t}\times\boldsymbol{f}=0. \tag{1.28}$$

showing that $\boldsymbol{f}$ is colinear to $\boldsymbol{t}$ [89]. Hence, there exists a scalar γ, the surface tension or energy coefficient, such that $\boldsymbol{f}=\gamma\boldsymbol{t}$. The formula for the stress vector jump across an interface is

$$[\![\boldsymbol{\sigma}\cdot\boldsymbol{n}]\!]=-\frac{d(\gamma\boldsymbol{t})}{dS}. \tag{1.29}$$

The formula presented in 2D dimensions is extended in the general case by adding the contribution in the second tangent direction [47]. Therefore, the general equation for the mechanical equilibrium of an interface is

$$[\![\boldsymbol{\sigma}\cdot\boldsymbol{n}]\!]=-\nabla_\alpha(\gamma\boldsymbol{t}^\alpha) \tag{1.30}$$

with ∇_α the derivative with respect to the surface coordinate α with an implicit sum on $\alpha=\{1,2\}$ representing the two tangents.

1.2.3 Mechanical equilibrium of an interface applied to a bi-fluid flow

The complete form of the mechanical equilibrium is given for the Liquid/Vapour interface since it is located inside the domain where a jump of stress vector may be defined. For both interfaces involving a solid interface, a simplification is made.

Liquid/vapour interface mechanical equilibrium

Eq. 1.30 may be applied to the jump of vector stress across the interface Γ_{LV} and reads

$$-(\boldsymbol{\sigma_V}\cdot\boldsymbol{n_V}+\boldsymbol{\sigma_L}\cdot\boldsymbol{n_L})_{\Gamma_{LV}}=[\![\boldsymbol{\sigma}\cdot\boldsymbol{n}]\!]_{\Gamma_{LV}}=-\nabla_\alpha(\gamma_{LV}\boldsymbol{t}_{LV}^\alpha) \tag{1.31}$$

where the jump across the interface Γ_{LV} is denoted $[\![\cdot]\!]_{\Gamma_{LV}}$ and $\boldsymbol{n}=\boldsymbol{n_L}=-\boldsymbol{n_V}$ is the outgoing normal to the liquid domain. Developing Eq. (1.31) yields the more usual expression

$$[\![\boldsymbol{\sigma}\cdot\boldsymbol{n}]\!]_{\Gamma_{LV}}=-\gamma_{LV}\mathscr{C}\boldsymbol{n}-(\nabla_\alpha\gamma_{LV})\boldsymbol{t}_{LV}^\alpha \tag{1.32}$$

where the first right-hand side term expresses the Young-Laplace's law, with $\mathscr{C}$ the mean curvature, while the second term which accounts for surface tension gradient, is the Marangoni term

[143, 149]. In a static case, the jump of stress vector is only the pressure jump across the interface since the strain rate is equal to zero. Taking a constant surface tension value at the interface leads to remove the Marangoni term and then derive the classical Young-Laplace equation [137] $p_{\text{inside}} - p_{\text{outside}} = \gamma\mathscr{C}$. In order to distinguish correctly the inside from the outside, the pressure must always conform to the rule that the higher pressure is in the concave region. This study is based on Eq. (1.31), taking into account both Young-Laplace's law and Marangoni's effect.

Interfaces mechanical equilibrium involving the solid

As shown in Fig. 1.1, the solid can be split in two regions Γ_{SL} and Γ_{SV}, where Γ_{SL} is the solid/liquid interface and Γ_{SV} the solid/vapour interface. As previously, the mechanical equilibrium is written

$$[\![\boldsymbol{\sigma}\cdot\boldsymbol{n}]\!]_{\Gamma_{Sj}} = -\nabla_\alpha\left(\gamma_{Sj}\boldsymbol{t}^\alpha_{Sj}\right) \tag{1.33}$$

with j representing either V or L. The stress vector accounting for the solid side $\boldsymbol{\sigma}_S$ is out of reach since the solid is not represented in the domain. However, in this stress, the stress vector is zero because the solid is considered to be rigid. As explained in Sect. 1.1.5 (1), taking a normal pointing outwards from the fluids to the solid leads to the two conditions on the solid

$$\begin{aligned} &\boldsymbol{v}\cdot\boldsymbol{n}_{SL} = 0 \quad \text{and} \quad \boldsymbol{\sigma}\cdot\boldsymbol{n}_{SL} = -\beta_{SL}\boldsymbol{v} + \nabla_\alpha(\gamma_{SL}\boldsymbol{t}^\alpha_{SL}) \qquad \text{on } \Gamma_{SL} \\ &\boldsymbol{v}\cdot\boldsymbol{n}_{SV} = 0 \quad \text{and} \quad \boldsymbol{\sigma}\cdot\boldsymbol{n}_{SV} = -\beta_{SV}\boldsymbol{v} + \nabla_\alpha(\gamma_{SV}\boldsymbol{t}^\alpha_{SV}) \qquad \text{on } \Gamma_{SV}, \end{aligned} \tag{1.34}$$

The condition of non-penetration on the velocity and a friction law for a fluid slipping on a wall are completed with surface energy by adding a term to the vector stress. Projecting the condition on the unit vectors normal $\boldsymbol{n}$ and tangents $\boldsymbol{t}^\alpha$ to the solid leads to

$$v_n = 0,\ \boldsymbol{t}^\alpha_{Sj}\cdot\boldsymbol{\sigma}\cdot\boldsymbol{n}_{Sj} = -\beta_{SV}\,v_{t^\alpha} + \nabla_\alpha\gamma_{Sj} \text{ and } \boldsymbol{n}_{Sj}\cdot\boldsymbol{\sigma}\cdot\boldsymbol{n}_{Sj} = \gamma_{Sj}\mathscr{C} \quad \text{on } \Gamma_{Sj} \text{ with } j\in\{SL, SV\} \tag{1.35}$$

where velocity is split with $\boldsymbol{v} = v_n\boldsymbol{n} + v_{t^\alpha}\boldsymbol{t}^\alpha$. The coefficient β is a friction coefficient depending on the surrounding fluid ($\beta = \beta_{SL}, \forall \boldsymbol{x}\in\Gamma_{SL}$ and $\beta = \beta_{SV}, \forall \boldsymbol{x}\in\Gamma_{SV}$) aiming at accounting for the dynamic sub-scale effects [200]. Choosing $\beta = 0$ leads to a free slip condition governed only by the capillary effects on the wall. Introducing this friction changes the dynamic but has no effect on the steady-state solution.

1.2.4 Wetting

When three phases are in contact, the contact line is called triple line. In two dimensions, this line is reduced to a point. In addition to the position of the triple line, the contact angle θ_c (see Fig. 1.1) giving the slope of the interface at the contact line is the second major parameter to describe the shape of the interface. This angle is computed from the three surface tension/energy coefficients involved as shown in the following two paragraphs. Therefore, choosing the three surface tension coefficients as input parameters is sufficient to prescribe the equilibrium (static) contact angle θ_c.

Dynamic contact angle

The static contact angle is limited to static cases and hence is not valid in dynamic. Its regime has been experimentally stated [81], that the triple line advances with a "rolling" movement. In order to remove the stress singularity at the contact line due to this no-slip boundary condition (Huh and Scriven's paradox [120], see also [39, 82, 194]), it has been postulated that slip between the liquid and the solid or any other mechanism have to occur very close to the contact line. Several approaches attempt to describe the contact angle in a dynamic case. Some of them focus on molecular simulations of fluid advance and energy dissipation around the triple line [38, 37]. Other approaches are based on hydrodynamic kinetics theories which consider that energy dissipation is generated by viscous flows [66, 67, 94, 114, 205, 213]. In the latter, the dynamic contact angle θ_d depends on the capillary number, which represents the ratio between the viscous effect and the capillary force such as

$$Ca = \frac{\mu_L V_0}{\gamma_{LV}} \tag{1.36}$$

with μ_L the viscosity of the liquid. Although some general theories have attempted to bring those approaches together [172], there is no universal model at the moment. Therefore as a first approximation, no model is added here to represent the dynamic contact angle and only the static contact angle will be considered.

Triple line equilibrium - Static contact angle

At the triple line $L(t)$ (see Fig. 1.1), the mechanical equilibrium reads

$$\gamma_{SL}\boldsymbol{T}_{SL} + \gamma_{SV}\boldsymbol{T}_{SV} + \gamma_{LV}\boldsymbol{T}_{LV} = \boldsymbol{R}_{\text{solid}}. \tag{1.37}$$

It is assumed that the reaction of the solid $\boldsymbol{R}_{\text{solid}}$ has no tangent component ($\boldsymbol{R}_{\text{solid}} = R_{\text{solid}}\boldsymbol{n}_s$ with $\boldsymbol{n}_s$ the normal to the solid which is equal to $\boldsymbol{n}_{SL}$ or $\boldsymbol{n}_{SV}$ at the triple line). Writing the projection of Eq. 1.37 in the tangent direction leads to the Young's relation [229]

$$\gamma_{SV} = \gamma_{SL} + \gamma_{LV}\cos\theta_c. \tag{1.38}$$

In the case of $\theta_c = 0°$, the wetting is named 'total'.

1.3 Summary

In the previous sections, fluid equations have been presented and some assumptions have been made due to the specificity of LRI process. It has been supposed that:

— Fluids are incompressible with a Newtonian behaviour;
— Temperature is constant and then the surface tension coefficient too;
— A surface tension and two surface energies are applied on Γ_{LV}, Γ_{SV} and Γ_{SL} respectively;
— The reaction of the solid is supposed to be in the normal direction in the triple line equilibrium equation;
— A static angle is chosen to model the contact angle at the triple line.
— The solid does not move.

The general framework of bi-fluid flow has many types of boundary conditions as depicted in Fig.1.7 which is a 2D restriction of a meniscus against a vertical wall depicted in Fig. 1.1. Neumann boundary conditions (on Γ_N) and Dirichlet boundary conditions (on Γ_D) are applied, in order to weakly enforce the stress vector $\boldsymbol{\sigma}\cdot\boldsymbol{n}$ or impose a value for the velocity such as $\boldsymbol{v}=\bar{\boldsymbol{v}}$ or one of its components ($\boldsymbol{v}\cdot\boldsymbol{n}$).

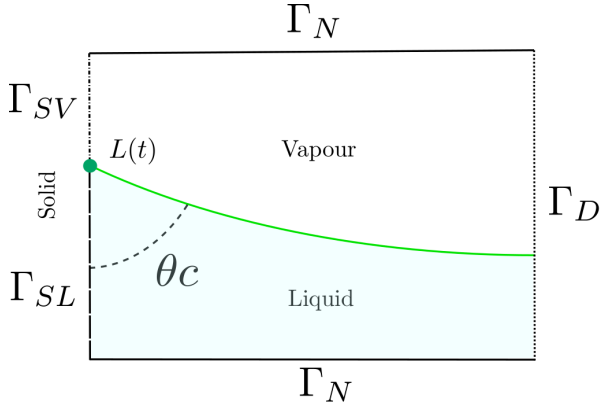

FIGURE 1.7 – Boundary conditions for a bi-fluid flow simulation with capillarity

Combining the Neumann and Dirichlet boundary conditions with those defined in section 1.1.5 and 1.2.3, the problem to solve reads

$$
\begin{aligned}
&\rho\left(\frac{\partial \boldsymbol{v}}{\partial t}+\boldsymbol{v}\cdot\nabla\boldsymbol{v}\right)=-\nabla p+\nabla\cdot\left(2\mu\dot{\boldsymbol{\epsilon}}(\boldsymbol{v})+\rho\boldsymbol{g}\right) && \text{in } \Omega,\\
&\nabla\cdot\boldsymbol{v}=0 && \text{in } \Omega,\\
&\boldsymbol{\sigma}\cdot\boldsymbol{n}=-P_{ext}\boldsymbol{n} && \text{on } \Gamma_N,\\
&[\boldsymbol{\sigma}\cdot\boldsymbol{n}]_{\Gamma_{LV}}=-\nabla_\alpha(\gamma_{LV}\boldsymbol{t}_{LV}^{\alpha}) && \text{on } \Gamma_{LV}(t),\\
&\boldsymbol{v}\cdot\boldsymbol{n}_{SL}=0 \quad\text{and}\quad \boldsymbol{\sigma}\cdot\boldsymbol{n}_{SL}=-\beta_{SL}\boldsymbol{v}+\nabla_\alpha(\gamma_{SL}\boldsymbol{t_{SL}}^{\alpha}) && \text{on } \Gamma_{SL}(t),\\
&\boldsymbol{v}\cdot\boldsymbol{n}_{SV}=0 \quad\text{and}\quad \boldsymbol{\sigma}\cdot\boldsymbol{n}_{SV}=-\beta_{SV}\boldsymbol{v}+\nabla_\alpha(\gamma_{SV}\boldsymbol{t_{SV}}^{\alpha}) && \text{on } \Gamma_{SV}(t),\\
&\gamma_{SL}\boldsymbol{T}_{SL}+\gamma_{SV}\boldsymbol{T}_{SV}+\gamma_{LV}\boldsymbol{T}_{LV}=R_{\text{solid}}\boldsymbol{n}_s \quad\text{and}\quad \boldsymbol{v}\cdot\boldsymbol{n}_s=0 && \text{on } L(t),\\
&\boldsymbol{v}=\overline{\boldsymbol{v}} \text{ or } \boldsymbol{v}\cdot\boldsymbol{n}=0 && \text{on } \Gamma_D.
\end{aligned}
\tag{1.39}
$$

The intersection between the domain where Dirichlet condition is imposed and the domain with a Neumann condition is not zero (in general) $\Gamma_D\cap\Gamma_N\neq 0$. Even if Neumann and Dirichlet conditions are imposed at the same position, they cannot act in the same direction. For example, it is possible to impose the normal velocity equals to zero and at the same position impose a value for the stress vector but only in tangents directions, as shown in Sect. 1.2.3.

1.4 Capillarity and gravity

Capillary effects appear in confined regions where gravity has a negligible effect since it acts upon a very small amount of liquid. The distance from the wall at which the capillary is predominant compared to gravity is called the capillary length [133]. In order to validate our numerical simulations, the analytical solution of a meniscus creeping up against a vertical wall is given and numerical solutions are exhibited for a meniscus between two vertical walls.

1.4.1 Capillary length

κ^{-1} refers to a particular length, called the capillary length, beyond which gravity becomes more important than capillary effect. It can be estimated by comparing the Laplace's pressure γ_{LV}/κ^{-1} and the hydrostatic pressure $\rho_L g\kappa^{-1}$ at a depth κ^{-1}. Equating both pressures leads to the definition of the capillary length

$$\kappa^{-1} = \sqrt{\gamma_{LV}/\rho_L g}. \tag{1.40}$$

For instance, if the diameter of a bubble is smaller than the capillary length, then gravity has a negligible influence compared to Laplace's pressure. In that case, the bubble tends to maintain a spherical shape. Alternatively, if its diameter is longer than the capillary length, the bubble would have a flattened shape due to the effect of gravity.

1.4.2 Equation of a meniscus against a vertical wall

The surface of the meniscus is parametrised by $z(x)$ with z the height and x the distance from the wall. In Fig. 1.8, two types of menisci are represented: $\theta_c < 90°$ (a) and $\theta_c > 90°$ (b). In case (A) curvature is negative whereas it is positive in case (B) of a reverse meniscus, in the Cartesian coordinate system.
The pressure of the vapour phase p_V is higher than the pressure just under the meniscus in

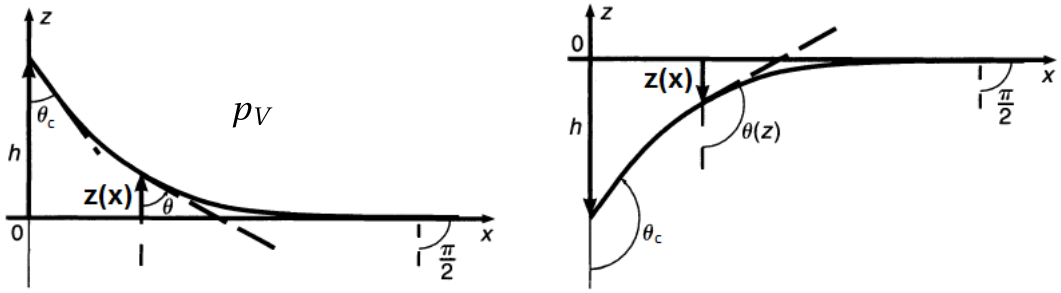

(A) high wettability (B) low wettability

FIGURE 1.8 – Meniscus against a wall [71]

the case (A). The meniscus rises in the first case to verify both the contact angle θ_c and accommodate the pressure pressure jump. This meniscus is constrained by the vapour phase which presses the meniscus and curve it convexly. The pressure drop under the meniscus helps the liquid to rise in the first case while it pushes the fluid down for the second case (B).
The equation for the meniscus is derived by equating the action of the hydrostatic pressure and capillary pressure. The capillary pressure is proportional to the curvature $\mathscr{C}$ which in 2D is

$$\mathscr{C} = -\frac{\dfrac{d^2z}{dx^2}}{\left[1+\left(\dfrac{dz}{dx}\right)^2\right]^{3/2}}. \tag{1.41}$$

In order to evaluate the influence of the capillary length let's assume that far from the wall the first derivative of the position is negligible compared to 1 *i.e.* $\frac{dz}{dx} << 1$. Therefore, the curvature is

approximated by $\mathscr{C} \approx -\frac{d^2z}{dx^2}$ far enough from the wall. Laplace's equation 1.32 gives the pressure under the surface: $p_A = p_{atm} + \gamma\mathscr{C} \approx p_{atm} - \gamma\dfrac{d^2z}{dx^2}$. Furthermore, the pressure must also conform to the laws of hydrostatics: $p_A = p_{atm} - \rho g z$ since at equilibrium $\nabla p = \rho \boldsymbol{g}$. Expressing p_A from the Laplace's law yields

$$-\gamma\mathscr{C} = \rho g z$$

or, equivalently using the first approximation for the curvature $\mathscr{C}$,

$$\kappa^2 z = -\mathscr{C} \approx \frac{d^2z}{dx^2}. \tag{1.42}$$

Using the conditions $z \to 0$ when $x \to +\infty$, the solution is

$$z = z_0 exp\left(-\frac{x}{\kappa^{-1}}\right) \tag{1.43}$$

Consequently, the surface perturbation decays exponentially with distance. Starting from this position and recalling that $exp(-1) \approx 0.37$ and $exp(-2) \approx 0.13$, it can be inferred that the surface tension force has a negligible effect on the shape of the meniscus at a distance greater than the capillary length κ^{-1}. This first part of the derivation helps to understand why the effect of surface tension is larger than gravity when the distance from the solid is smaller than the capillary length. However, the assumption on the curvature does not hold in the immediate vicinity of the wall.

For the complete solution of a meniscus against a wall, curvature does not have to be approximated such as in Eq. 1.42. In this case, an analytical solution is known [71]. The solution can be derived by writing the force balance of the grey dotted surface in Fig. 1.9, made of two forces. The surface tension force is acting at each side of the interface going out of the control dotted volume, x_a and x_m. The second force, the pressure action, is made up of the sum of elementary pressure actions on the striped region, for any height $\bar{z}$ of the striped region between 0 and z.

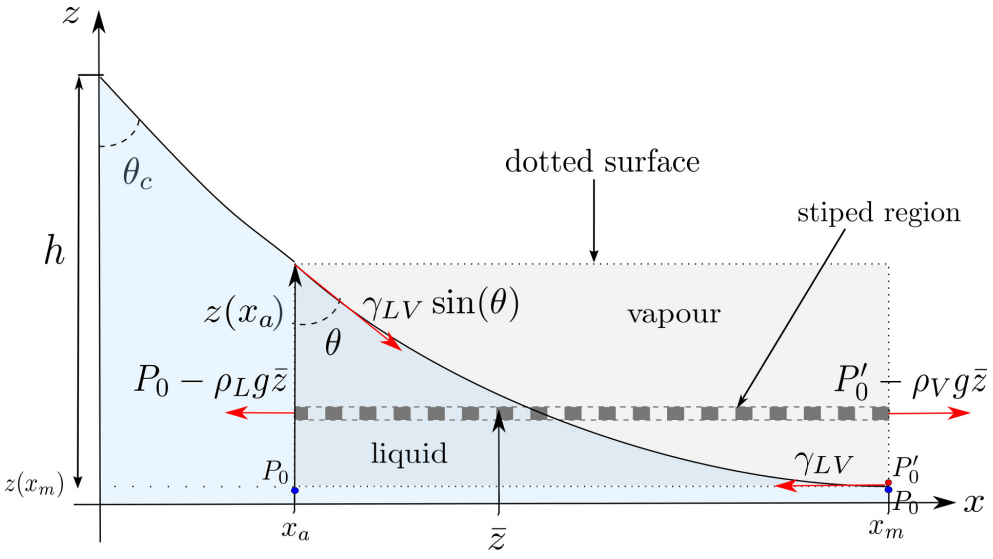

FIGURE 1.9 – Meniscus against a wall - force equilibrium

On the right-hand side of the dotted surface, the tangent to the interface is horizontal, thus the surface tension force is only γ_{LV} in the x direction. Whereas on the left-hand side, the force due to surface tension projected on the x-axis is $\gamma_{LV}\sin(\theta)$ with θ the angle between the meniscus and the z axis at a position x_a. The other contribution to the mechanical equilibrium is brought by the hydrostatic pressure $P_0' - \rho_V g\bar{z}$ in the air and $P_0 - \rho_L g\bar{z}$ in the liquid, with P_0' and P_0 the pressure at each side of the interface at position x_m. The horizontal action of the pressure is derived by integrating the action in the liquid and the vapour phase $\int_0^z P_0' - P_0 + (\rho_L - \rho_V) g\bar{z}\, d\bar{z}$. The relationship between P_0' and P_0 is found at the position $z(x_m)$. Actually, when considering only one wall, the point x_m tends to infinity to recover a horizontal tangent for the meniscus. The curvature is zero precisely in that case since the point x_m is far away from the wall. According to the Young-Laplace's law, the pressure jump is zero and $P_0' = P_0$. In the case of a meniscus between two walls, the relation is $P_0' = P_0 + \gamma_{SL}\mathscr{C}(x_m)$ but the curvature depends on the shape of the meniscus and that is why the equation has no known analytical solution.
Taking $P_0' = P_0$, it comes that the resultant pressure force is $\int_0^z P_0' - P_0 + (\rho_L - \rho_V) g\bar{z}\, d\bar{z} = \frac{1}{2}(\rho_L - \rho_V) g z^2$. The horizontal projection of the force balance yields

$$\sin(\theta) + \frac{1}{2}\kappa_*^2 z^2 = 1 \tag{1.44}$$

with $\kappa_*^{-1} = \sqrt{\dfrac{\gamma_{LV}}{g(\rho_L - \rho_V)}}$ a modified capillary length for this problem. The contribution of the air pressure is taken into account through the air density in the modified capillary length. Yet in most cases, the ratio between liquid and air density is around a thousand. Therefore, the air pressure contribution is negligible, and the equivalent capillary length is very close to the capillary length, $\kappa^{-1} \approx \kappa_*^{-1}$. Eq. 1.44 may be applied to the position against the wall in order to obtain an expression of the height $h = z(x = 0)$ of the meniscus

$$h = \sqrt{2}\kappa^{-1}(1 - \sin\theta_c)^{1/2} \tag{1.45}$$

Noticing that $\sin\theta$ can be rewritten as $\dfrac{1}{\left[1 + \left(\frac{dz}{dx}\right)^2\right]^{1/2}}$ one can integrate one more time the equation 1.44 and yield an implicit relation [71] giving the position x in terms of height z

$$x - x_0 = \kappa^{-1} cosh\left(\frac{2\kappa^{-1}}{z}\right) - 2\kappa^{-1}\left(1 - \frac{z^2}{4\kappa^{-2}}\right)^{1/2} \tag{1.46}$$

where x_0 is a distance to be determined for obtaining $x = 0$ at $z = h$ (*i.e.* at the wall). In this formula again, it is possible to take into account the effect of the pressure of the air by replacing κ by κ_* but it does not significantly change the shape of the meniscus when studying air and water.
In terms of velocity at equilibrium, the velocity field is zero everywhere. From the position of the meniscus, the pressure field can be computed since the pressure under the meniscus is only the hydrostatic pressure balancing Laplace's pressure.

1.4.3 Equation of the meniscus between two vertical walls

The meniscus between two vertical walls is a more challenging case compared to the previous one since the entire meniscus is going up in order to accommodate Laplace's law and hydrostatic pressure constraint at the same time. Two independent numerical methods are used to solve this problem based on the minimisation of global energy [85] and force equilibrium. These numerical methods are considered as semi-analytical to validate the Finite Element (FE) solution.

Method 1: Energy minimisation

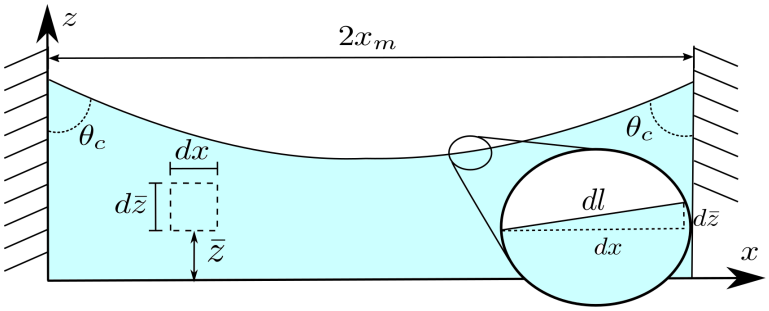

FIGURE 1.10 – Meniscus between two vertical walls - Drawing for energy derivation

Considering $2x_m$ the distance between the two walls and as in Fig. 1.10, the potential energy (E_p) is defined as

$$E_p = \int_0^{2x_m} \int_0^{z(x)} \rho_L g \bar{z} d\bar{z} dx = \int_0^{2x_m} \frac{1}{2} \rho_L g z(x)^2 dx \tag{1.47}$$

representing the sum of potential energy of each column of fluid. As it has been seen for a meniscus against a wall, the contribution of the air pressure may be neglected and this assumption holds for a meniscus between two walls. The second contribution to the energy is the surface tension energy (E_{st})

$$E_{st} = \int_{\Gamma_{LV}} \gamma_{LV} dl = \int_0^{2x_m} \gamma_{LV} \sqrt{1 + z'(x)^2} dx \tag{1.48}$$

where the short notation $z'(x)$ expresses the derivative $z'(x) = \frac{dz}{dx}$. Summing the two energies yields the global energy of the system

$$E(z, z') = E_p + E_{st} = \int_0^{2x_m} \left[\frac{1}{2} \rho_L g z(x)^2 + \gamma_{LV} \sqrt{1 + z'(x)^2} \right] dx \tag{1.49}$$

Finally the problem to be solved is a minimisation of the energy with conditions at the triple points on the left and right walls and it reads

$$\min \left\{ E(z, z') \,;\; z'(0) = -\frac{1}{tan\theta_c} \text{ and } z'(2x_m) = \frac{1}{tan\theta_c} \right\} \tag{1.50}$$

Due to the boundary conditions, the meniscus is going up. Then the surface tension energy is pushing the meniscus up since it does not tolerate a high degree of curvature (*i.e.* meniscus has to be as flat as possible to minimise surface tension energy). It is the value of the contact angle which acts as a driving force in the first instances of the minimisation of energy. The meniscus

keeps going up until the weight of the meniscus balances the energy of the meniscus. Problem 1.50 is solved by an iterative method.

— Problem discretisation
The interval $[0, m_x]$ is divided into $N+1$ points x_k, equally spaced by a distance $h_e = 2x_m/N$ such that $x_k = k \times h$ for $k \in [0, N]$. The $N+1$ heights are computed using a finite difference method at each iteration i. The function $z(x)$ is approximated using the discretised k points for each iteration i

$$Z_k^i \approx z(x_k) \tag{1.51}$$

Therefore the discretised problem reads

$$\min \left\{ E_N^i(\boldsymbol{Z}) \,;\; Z_0^i = \frac{h_e}{tan\theta} + Z_1^i \text{ and } Z_N^i = \frac{h_e}{tan\theta} + Z_{N-1}^i \right\} \tag{1.52}$$

where the energy is discretised using a backward differentiation and the integral is approximated using a rectangular method

$$E_N^i = \sum_{k=0}^{N} \left[\frac{1}{2} \rho g \left(Z_k^i \right)^2 h_e + \gamma \sqrt{h_e^2 + \left(Z_{k+1}^i - Z_k^i \right)^2} \right] \tag{1.53}$$

— Minimisation of energy requires to compute the gradient

$$\frac{\partial E_N^i}{\partial Z_k^i} = \rho g Z_k^i h_e - \gamma \frac{Z_{k+1}^i - Z_k^i}{a_k} + \gamma \frac{Z_k^i - Z_{k-1}^i}{a_{k-1}} \tag{1.54}$$

with $a_k = \sqrt{h_e + \left(Z_{k+1}^i - Z_k^i \right)^2}$. Therefore for each iteration i the new position is

$$\boldsymbol{Z}^{i+1} = \boldsymbol{Z}^i - q \nabla E_N^i \tag{1.55}$$

where q is a penalisation parameter used in the gradient descent method. The procedure is iterated until the norm of the gradient is less than a small value, 1e−18 in this case.

Method 2: Force balance

Energy of the system is still seen as a function of two independent variables, namely z and $z' = dz/dx$. Consequently, the variation of energy is expressed as

$$\begin{aligned} \delta E(z, z') &= \frac{\partial E}{\partial z} \delta z + \frac{\partial E}{\partial z'} \delta z' \\ &= \int_0^{2x_m} \left(\rho_L g z(x) \delta z + \gamma_{LV} \frac{z'(x)}{\sqrt{1 + z'(x)^2}} \delta z' \right) dx \\ &= \int_0^{2x_m} \left(-\frac{d}{dx} \left(\frac{\gamma_{LV} z'(x)}{\sqrt{1 + z'(x)^2}} \right) + \rho_L g z(x) \right) \delta z \, dx + \left[\frac{\gamma_{LV} z'(x)}{\sqrt{1 + z'(x)^2}} \delta z(x) \right]_0^{2x_m} \end{aligned} \tag{1.56}$$

by integration by parts. The equilibrium state is achieved for a minimum of energy $\delta E = 0$, leading to the force balance equation. Actually, the integral term corresponds to the force balance

equation, and the second term is the boundary condition to impose. For the boundary condition at the position $x = 0$ and $x = 2x_m$ it may be possible to impose either the increment of variation δz or $\frac{z'(x)}{\sqrt{1+z'(x)^2}} = \cos\theta_c$. The salient feature of this short derivation is to get a better understanding of the condition at the triple line. The displacement $z(x)$ of the meniscus is the unknown, then it is not a boundary condition. Yet, the condition on $\cos\theta_c$ may be imposed by giving the value of the contact angle θ_c or only by specifying the surface tension and surface energies in the mechanical equilibrium equation of the triple line 1.37. From the force balance strategy, one can be convinced that the problem requires to impose the contact angle. And from the energy minimisation, one can see the strong influence of contact angle on the whole solution. Therefore, even if this condition is only imposed at one point of the domain, it influences the solution on the whole domain.
The force balance is then written:

$$\begin{aligned} & -\frac{d}{dx}\left(\frac{\gamma_{LV} z'(x)}{\sqrt{1+z'(x)^2}}\right) + \rho_L g z(x) = 0 \\ \Leftrightarrow \quad & -\gamma_{LV} \frac{z''(x)}{\left(1+z'(x)^2\right)^{3/2}} + \rho_L g z(x) = 0 \end{aligned} \tag{1.57}$$

representing the surface tension action $\gamma_{LV}\mathscr{C}$ balanced by the weight of the fluid.

— Linearisation of the equation 1.57 is as follows. The expression at iteration $i+1$ may be approximated using

$$\left.\frac{z''(x)}{\left(1+z'(x)^2\right)^{3/2}}\right|_{i+1} \approx \frac{z''(x)\big|_{i+1}}{\left.\left(1+z'(x)^2\right)^{3/2}\right|_i} = z''(x)\big|_{i+1} A_i(x) \tag{1.58}$$

where the symbol $|_{i+1}$ represents the quantity evaluated at iteration $i+1$ and $A^i(x) = \frac{1}{\left.\left(1+z'(x)^2\right)^{3/2}\right|_i}$.

— The equation is discretised using a finite difference method (second order centered in space scheme) like for the minimisation of energy and solved using the boundary condition on the contact angle at each end. The discretised equation reads

$$-\gamma_{LV} A_k^i \frac{Z_{k+1}^{i+1} - 2Z_k^{i+1} + Z_{k-1}^{i+1}}{h_e^2} + \rho_L g Z_k^{i+1} = 0 \tag{1.59}$$

with $A_k^i = \left(1 + \frac{\left(Z_{k+1}^i - Z_{k-1}^i\right)^2}{4h_e^2}\right)^{-3/2}$. The system written in matrix form with boundary conditions is

$$\begin{pmatrix} \frac{2\gamma_{LV}}{h_e^2}A_1^i + \rho_L g & -\frac{\gamma_{LV}}{h_e^2}A_1^i & 0 & \cdots & 0 \\ -\frac{\gamma_{LV}}{h_e^2}A_2^i & \frac{2\gamma_{LV}}{h_e^2}A_2^i + \rho_L g & -\frac{\gamma_{LV}}{h_e^2}A_2^i & 0 & \vdots \\ 0 & \ddots & \ddots & \ddots & 0 \\ \vdots & & -\frac{\gamma_{LV}}{h_e^2}A_{N-2}^i & \frac{2\gamma_{LV}}{h_e^2}A_{N-2}^i + \rho_L g & -\frac{\gamma_{LV}}{h_e^2}A_{N-2}^i \\ 0 & \cdots & 0 & -\frac{\gamma_{LV}}{h_e^2}A_{N-1}^i & \frac{2\gamma_{LV}}{h_e^2}A_{N-1}^i + \rho_L g \end{pmatrix} \begin{pmatrix} Z_1^{i+1} \\ Z_2^{i+1} \\ \vdots \\ Z_{N-2}^{i+1} \\ Z_{N-1}^{i+1} \end{pmatrix} = \begin{pmatrix} \frac{\gamma_{LV}A_1^i}{h_e \tan\theta_c} \\ 0 \\ \vdots \\ 0 \\ \frac{\gamma_{LV}A_{N-1}^i}{h_e \tan\theta_c} \end{pmatrix} \tag{1.60}$$

with boundary conditions in the right-hand side term.

Convergence

The numerical solution describing the shape of the meniscus tends to a limit when refining the spacial discretisation (*i.e.* the number of points) as it can be seen in Fig. 1.11. The asymptote is only assessed for the force balance method since it is shown to be more robust than the energy minimisation method. The contact angle used is 55.5°, surface tension parameter $\gamma_{LV} = 50.8\,\mathrm{mN\cdot m^{-1}}$, the liquid density $\rho_L = 3325\,\mathrm{kg\cdot m^{-3}}$ and the distance between the two walls $2x_m = 0.1\,\mathrm{cm}$ (representing diiodomethane and cellulose [180]). Fig. 1.12 depicts the discrepancy between results from the minimisation of energy and the force equilibrium method, when method 1 converges.

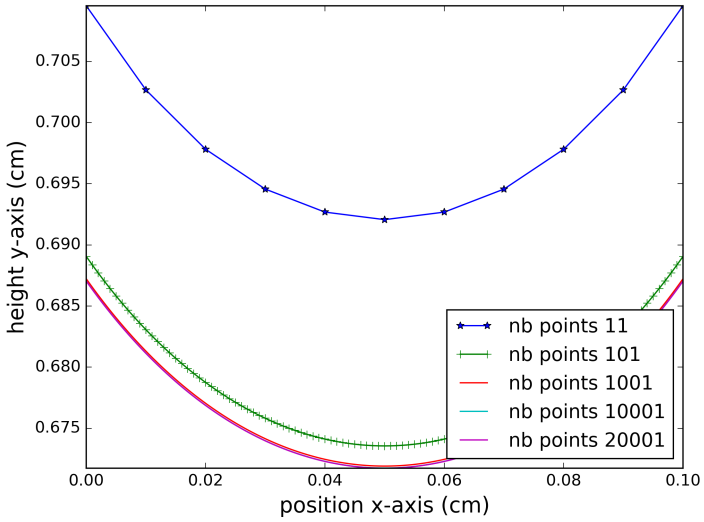

FIGURE 1.11 – Meniscus between two walls - convergence of the shape of the meniscus when increasing the number of points (force balance equation)

Conclusion

Within the context of LRI process, this chapter has introduced the modelling of capillary-driven flows. These equations have three unknowns: the velocity, the pressure and interface position. The two following chapters intend to set-up a solver for fluid equations and a solver to represent the interface position.

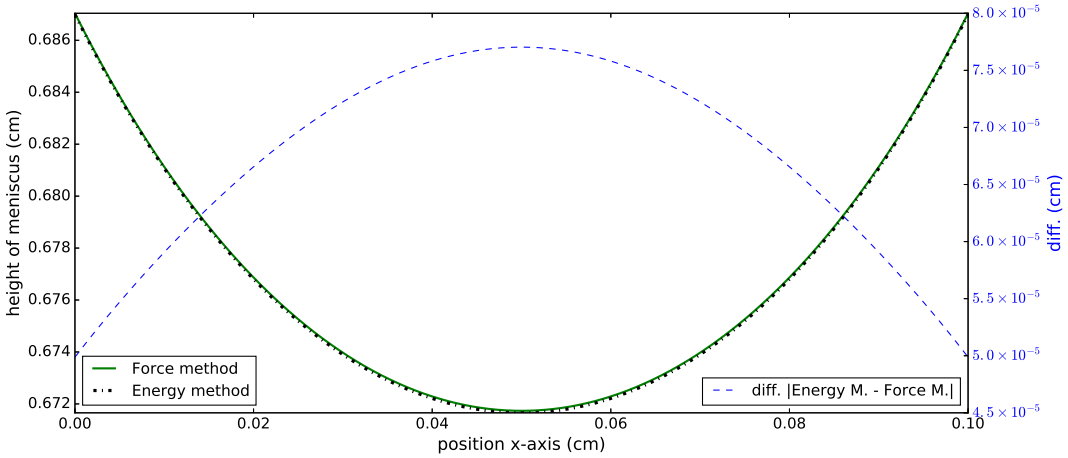

FIGURE 1.12 – Meniscus between two walls - comparison between energy minimisation method (with 1001 points) and force equilibrium method (200001 points)

Résumé en Français : Modélisation de l'écoulement et de l'action capillaire

L'écoulement bifluide est régi par les équations de conservation de la mécanique des milieux continus. Notre étude se place dans un cadre isotherme, car l'infusion de la préforme se fait à température contrôlée. Par conséquent, les équations de conservation de la quantité de mouvement et de conservation de la masse, réduites ici à la contrainte d'incompressibilité ou encore Navier-Stokes ou Stokes, sont résolues pour déterminer le champ de vitesse et de pression. Trois interfaces sont considérées dans cette étude, l'interface entre les fibres et la résine, les fibres et l'air raréfié ainsi que la résine et l'air ; une contrainte surfacique agissant sur chacune d'elles. Chaque interface vérifie l'équilibre mécanique exprimant le saut du vecteur contrainte de part et d'autre de l'interface. Cet équilibre décrit le saut de pression de Laplace et les effets Marangoni. Le second et dernier équilibre mécanique pour les problèmes de capillarité est celui de la ligne triple, s'exprimant comme la somme des contraintes surfaciques de chaque interface équilibrée par la réaction du solide. La projection de cette dernière relation dans une des directions tangentes à l'interface donne l'angle de contact statique de la ligne triple lorsque la réaction du solide est portée par la normale. L'étude d'un ménisque s'appuyant contre un mur permet d'introduire la longueur capillaire. Dans la zone allant de la paroi solide jusqu'à cette longueur critique, l'action capillaire est prédominante par rapport à la gravité. À l'inverse, l'action capillaire est négligeable devant la gravité à une distance supérieure de la paroi. De ce fait, le positionnement de deux plaques à une distance inférieure à la longueur capillaire permet d'obtenir une ascension du liquide entre ces plaques et retrouver à l'équilibre l'angle de contact statique.

Chapter 2

Numerical strategy for solving Navier-Stokes equations

Contents

Introduction

This chapter exposes the numerical strategy for solving the previously established equations describing capillary-driven flows. The first step consists in setting-up a Finite Element formulation for discretising the Navier-Stokes equations. These equations are not linear, because of the convective term $\boldsymbol{v} \cdot \nabla \boldsymbol{v}$, and consequently require the use of an iterative scheme, such as Picard's or Newton-Raphson's schemes. Furthermore, both velocity and pressure fields will be approximated by continuous and piecewise linear discrete fields. Such a discretisation of the Navier-Stokes equations, is known to be unstable. Therefore, a Variational MultiScale method is presented in order to ensure the existence and the uniqueness of the computed numerical solution. This computational strategy will be validated in the last section of this chapter. Noting that resin flow is not turbulent in LRI process, thus no turbulent model is investigated.

2.1 Weak formulation

The nonlinearity of the Navier-Stokes equations results from the convective term $\boldsymbol{v} \cdot \nabla \boldsymbol{v}$. First of all, the weak formulation is given in this subsection. Then a standard time discretisation of the unsteady term and a linearisation of the convective term will be presented. The system of equations will be given as a saddle point minimisation problem requiring a stabilisation technique.

In order to solve the previous system of equations Eq. 1.39 using a Finite Element Method (FEM), the weak integral form of this system has first to be established. Let's first define function spaces, $\mathscr{L}^2$ and $\mathscr{H}^1$ corresponding respectively to the Lebesgues space of square-integrable

functions and the first type Sobolev's space:

$$\begin{aligned}\mathscr{L}^2(\Omega) &= \left\{ u : \Omega \to \mathbb{R} \mid \int_\Omega u^2 \, dV < \infty \right\} \\ \mathscr{H}^1(\Omega) &= \left\{ \boldsymbol{u} \in \mathscr{L}^2(\Omega) \mid \forall i, j \in \mathbb{N} \cap [1, dim], \ \frac{\partial u_i}{\partial x_j} \in \mathscr{L}^2(\Omega) \right\}\end{aligned} \tag{2.1}$$

with dim the space dimension. The functional spaces based on the Lesbesgues $\mathscr{L}^2(\Omega)$ and Sobolev $\mathscr{H}^1(\Omega)$ spaces are defined as

$$\begin{aligned}\mathscr{W}^0 &= \left\{ \boldsymbol{\xi} \in \left(\mathscr{H}^1(\Omega)\right)^{dim} \ \middle| \ \forall \boldsymbol{x} \in \Gamma_D \quad \boldsymbol{\xi} = \boldsymbol{0} \right\} \\ \mathscr{W} &= \left\{ \boldsymbol{\xi} \in \left(\mathscr{H}^1(\Omega)\right)^{dim} \ \middle| \ \forall \boldsymbol{x} \in \Gamma_D \quad \boldsymbol{\xi} = \bar{\boldsymbol{v}} \right\} \\ \mathscr{Q} &= \left\{ \zeta \in \mathscr{L}^2(\Omega) \ \middle| \ \int_\Omega \zeta \, dV = 0 \right\}\end{aligned} \tag{2.2}$$

Following the Galerkin approach, Dirichlet boundary conditions are included in the definition of the approximation space $\mathscr{W}$ (essential boundary condition). Weighting the Navier-Stokes equations Eq. 1.16 with the test functions $\boldsymbol{w}$ and q, and after integrations by parts on the viscous and pressure gradient terms, the problem reads:
find $\boldsymbol{v} \in \mathscr{W}$, $p \in \mathscr{Q}$ such that

$$\begin{aligned}&\int_\Omega \rho \frac{\partial \boldsymbol{v}}{\partial t} \cdot \boldsymbol{w} \, dV + \int_\Omega \rho (\boldsymbol{v} \cdot \nabla) \boldsymbol{v} \cdot \boldsymbol{w} \, dV + \int_\Omega 2\mu \dot{\boldsymbol{\epsilon}}(\boldsymbol{v}) : \dot{\boldsymbol{\epsilon}}(\boldsymbol{w}) \, dV - \int_\Omega p \nabla \cdot \boldsymbol{w} \, dV \\ &\quad + \int_\Omega q \nabla \cdot \boldsymbol{v} \, dV = \int_\Omega \rho \boldsymbol{g} \cdot \boldsymbol{w} \, dV - \int_{\Gamma_N} p_{ext} \boldsymbol{n} \cdot \boldsymbol{w} \, dV + \int_{(\partial\Omega_L \cup \partial\Omega_V) \setminus (\Gamma_N)} \boldsymbol{\sigma} \cdot \boldsymbol{n} \cdot \boldsymbol{w} \, dV\end{aligned} \tag{2.3}$$

for all test functions $(\boldsymbol{w}, q) \in \mathscr{W}^0 \times \mathscr{Q}$. It may be possible to subtract the incompressibility equation $\nabla \cdot \boldsymbol{v} = 0$ to the momentum balance equation which would change the sign of the $q \nabla \cdot \boldsymbol{v}$ term. This has the advantage to yield a symmetric matrix in the case of a Stokes flow. Yet, for the Navier-Stokes equations, this gambit is not needed, since the symmetry of the elementary rigidity matrix is broken by the convective term. In this chapter, the virtual work at the interfaces $\int_{(\partial\Omega_L \cup \partial\Omega_V) \setminus (\Gamma_N)} \boldsymbol{\sigma} \cdot \boldsymbol{n} \cdot \boldsymbol{w} \, dV$ is taken equal to zero since a single fluid is considered.

2.2 Linearisation and discretisation

The linearisation of the convective term can be performed in the weak or strong formulation indistinctly. It can be understood as linearising the unknown velocity $\boldsymbol{v}^{it+1}$ at iteration $it+1$ with the velocity evaluated at the previous iteration $\boldsymbol{v}^{it}$, incremented by a variation $\delta\boldsymbol{v}$ ($\boldsymbol{v}^{it+1} = \boldsymbol{v}^{it} + \delta\boldsymbol{v}$). The convective term from Navier-Stokes equation reads

$$\begin{aligned}(\boldsymbol{v}^{it+1} \cdot \nabla) \boldsymbol{v}^{it+1} &= \left(\boldsymbol{v}^{it} \cdot \nabla \right) \boldsymbol{v}^{it+1} + (\delta\boldsymbol{v} \cdot \nabla) \boldsymbol{v}^{it+1} \\ &= \left(\boldsymbol{v}^{it} \cdot \nabla \right) \boldsymbol{v}^{it+1} + (\delta\boldsymbol{v} \cdot \nabla) \boldsymbol{v}^{it} + (\delta\boldsymbol{v} \cdot \nabla) \delta\boldsymbol{v}\end{aligned} \tag{2.4}$$

Neglecting the second order term $(\delta\boldsymbol{v} \cdot \nabla)\delta\boldsymbol{v}$ and developing the $\delta\boldsymbol{v}$ term in the previous equation, it comes

$$(\boldsymbol{v}^{it+1} \cdot \nabla) \boldsymbol{v}^{it+1} = \left(\boldsymbol{v}^{it} \cdot \nabla \right) \boldsymbol{v}^{it+1} + \left(\boldsymbol{v}^{it+1} \cdot \nabla \right) \boldsymbol{v}^{it} - \left(\boldsymbol{v}^{it} \cdot \nabla \right) \boldsymbol{v}^{it} \tag{2.5}$$

By introducing a numerical parameter α, we obtain the linearisation:

$$(\boldsymbol{v}^{it+1}\cdot\nabla)\boldsymbol{v}^{it+1} \approx (\boldsymbol{v}^{it}\cdot\nabla)\boldsymbol{v}^{it+1} + \alpha(\boldsymbol{v}^{it+1}\cdot\nabla)\boldsymbol{v}^{it} - \alpha(\boldsymbol{v}^{it}\cdot\nabla)\boldsymbol{v}^{it} \tag{2.6}$$

This is known as Picard's linearisation for $\alpha = 0$ and Newton-Raphson's linearisation when $\alpha = 1$. The Picard linearisation is commonly implemented in a FE code, because involving only one term. Additionally, a linear convergence is expected if the convection, or nonlinearity, is not too high [164]. In contrast, the Newton-Raphson method is known to exhibit a quadratic convergence, but only if the initial guess is close enough to the solution [65]. For the sake of robustness and efficiency scheme, both approaches can be combined: Picard linearisation is used during the first iterations in order to approach the solution, and then the scheme is switched to the Newton-Raphson linearisation to accelerate the convergence.

Let $[0, t_f]$ be the computation time interval, $t_f > 0$. This interval is discretised by a set of times $\{t^n\}_{n=0,\cdots,N}$ satisfying $t^0 = 0$, $t^N = t_f$ and $t^{n+1} > t^n$. In the simulations, these times are assumed to be uniformly distributed. The time step is then defined as $\Delta t = t^{n+1} - t^n$. Here, the superscripts n and $n+1$ denote, respectively, quantities evaluated at time t^n and t^{n+1}. The unsteady term of the Navier-Stokes equations is discretised using a first order Euler backward differentiation

$$\frac{\partial \boldsymbol{v}}{\partial t} \approx \frac{\boldsymbol{v}^{n+1} - \boldsymbol{v}^n}{\Delta t} \tag{2.7}$$

The Navier-Stokes equations are written in a time implicit form, and the problem reads:
at time t^{n+1} and iteration $it+1$, find $\boldsymbol{v}^{n+1,it+1} \in \mathcal{W}$, $p^{n+1,it+1} \in \mathcal{Q}$ such that

$$\begin{aligned}
&\int_\Omega \rho \frac{\boldsymbol{v}^{n+1,it+1} - \boldsymbol{v}^n}{\Delta t}\cdot\boldsymbol{w}\,dV + \int_\Omega \rho(\boldsymbol{v}^{n+1,it}\cdot\nabla)\boldsymbol{v}^{n+1,it+1}\cdot\boldsymbol{w}\,dV \\
&+ \alpha\int_\Omega \rho(\boldsymbol{v}^{n+1,it+1}\cdot\nabla)\boldsymbol{v}^{n+1,it}\cdot\boldsymbol{w}\,dV + \int_\Omega 2\mu\dot{\boldsymbol{\epsilon}}(\boldsymbol{v}^{n+1,it+1}) : \dot{\boldsymbol{\epsilon}}(\boldsymbol{w})\,dV - \int_\Omega p^{n+1,it+1}\nabla\cdot\boldsymbol{w}\,dV \\
&+ \int_\Omega q\nabla\cdot\boldsymbol{v}^{n+1,it+1}\,dV = \int_\Omega \rho\boldsymbol{g}\cdot\boldsymbol{w}\,dV + \alpha\int_\Omega \rho(\boldsymbol{v}^{n+1,it}\cdot\nabla)\boldsymbol{v}^{n+1,it}\cdot\boldsymbol{w}\,dV - \int_{\Gamma_N} p_{ext}\boldsymbol{n}\cdot\boldsymbol{w}\,dV
\end{aligned} \tag{2.8}$$

for all $(\boldsymbol{w}, q) \in \mathcal{W}^0 \times \mathcal{Q}$ and with $\boldsymbol{v}(t=0) = \boldsymbol{0}$ the initial velocity. The iterative procedure is carried out until the velocity is solution of the non linearised Navier-Stokes equations. This condition is assessed by looking at the finite element residual, which is defined as the internal forces minus the external loadings. Thus the FE residual tends to zero when the solution converges, else it diverges. During the first iterations (usually 5) the Picard linearisation scheme ($\alpha = 0$) is executed, after which, it switches to the Newton-Raphson scheme ($\alpha = 1$). An improved condition could also be based on a minimum relative residual in order to be close enough to the solution, before starting to converge faster to it. Finally, by its structure, the linearised Navier-Stokes equations can be classified as a saddle point minimisation.

The final step is to approximate the spaces $\mathcal{W}$ and $\mathcal{Q}$ which are of infinite dimension with functional spaces $\mathcal{W}_h$ and $\mathcal{Q}_h$ of finite dimension [41]. Therefore the solution $(\boldsymbol{v}^{n+1,i+1}, p^{n+1,i+1}) \in \mathcal{W}\times\mathcal{Q}$ is approximated by $(\boldsymbol{v}_h^{n+1,i+1}, p_h^{n+1,i+1}) \in \mathcal{W}_h \times \mathcal{Q}_h$. The domain Ω is discretised by a mesh $\mathcal{T}_h(\Omega)$, made up of simplexes Ω^e, triangles in 2D or tetrahedrons in 3D. The discretised domain

Ω_h is such that $\Omega_h = \bigcup_{e=1}^{n_{el}} \Omega^e$ with n_{el} the number of elements. The Navier-Stokes discrete problem may be written with the bilinear operator B and linear operator L. The operators are defined as follow

$$\begin{aligned} B_h([\boldsymbol{v}_h^{n+1,i+1}, p_h^{n+1,i+1}], [\boldsymbol{w}_h, q_h]) &= \int_\Omega \rho \frac{\boldsymbol{v}^{n+1,it+1} - \boldsymbol{v}^n}{\Delta t} \cdot \boldsymbol{w}\, dV + \int_\Omega \rho(\boldsymbol{v}^{n+1,it} \cdot \nabla)\boldsymbol{v}^{n+1,it+1} \cdot \boldsymbol{w}\, dV \\ &+ \alpha \int_\Omega \rho(\boldsymbol{v}^{n+1,it+1} \cdot \nabla)\boldsymbol{v}^{n+1,it} \cdot \boldsymbol{w}\, dV + \int_\Omega 2\mu \dot{\boldsymbol{\epsilon}}(\boldsymbol{v}^{n+1,it+1}) : \dot{\boldsymbol{\epsilon}}(\boldsymbol{w})\, dV - \int_\Omega p^{n+1,it+1} \nabla \cdot \boldsymbol{w}\, dV \\ &+ \int_\Omega q \nabla \cdot \boldsymbol{v}^{n+1,it+1}\, dV \end{aligned} \tag{2.9}$$

and

$$L_h([\boldsymbol{w}_h, q_h]) = \int_\Omega \rho \boldsymbol{g} \cdot \boldsymbol{w}\, dV + \alpha \int_\Omega \rho(\boldsymbol{v}^{n+1,it} \cdot \nabla)\boldsymbol{v}^{n+1,it} \cdot \boldsymbol{w}\, dV - \int_{\Gamma_N} p_{ext} \boldsymbol{n} \cdot \boldsymbol{w}\, dV \tag{2.10}$$

The Navier-Stokes equation written with bilinear and linear operators reads:
Find $\boldsymbol{v}_h \in \mathscr{W}_h$ and $p_h \in \mathscr{Q}_h$ such as

$$B_h([\boldsymbol{v}_h^{n+1,i+1}, p_h^{n+1,i+1}], [\boldsymbol{w}_h, q_h]) = L_h([\boldsymbol{w}_h, q_h]) \qquad \forall\, (\boldsymbol{w}_h, q_h) \in \mathscr{W}_h^0 \times \mathscr{Q}_h. \tag{2.11}$$

In this work, the same approximation is used for both pressure and velocity: a continuous and piecewise linear approximation. This type of finite element is called P1/P1 in velocity and pressure. Among many other combinations, the P2/P1 configuration, or Taylor-Hood element, is well-known for its inherent stability with quadratic/linear approximations. The finite element formulation resulting from the P1/P1 discretisation of NS equations is not stable, and consequently requires a stabilisation technique. On the contrary, the explanation for the choice of a linear approximation and the resulting stabilisation are the subjects of next section.

2.3 Stabilised finite element formulation

Usually, the velocity-pressure mixed discrete formulation Eq. 2.11 has to satisfy the Ladysenskaya-Brezzi-Babuska (LBB) conditions [41], which ensure the existence and uniqueness, or equivalently the stability, of the discrete solution. This restricts the choice of the approximation spaces $\mathscr{W}_h$ and $\mathscr{Q}_h$. From that point, three possibilities arise. The first method developed by the scientific community was based on the fact that pressure can be viewed as the Lagrange multiplier associated with the incompressibility constraint. The equations can then be formulated only in velocity, while pressure is computed via an Uzawa algorithm [186]. This strategy is limited because it requires iterations to solve the linearised problem. The second option is to choose a stable element according to the LBB theory. For example, P2/P1, or P1+/P1 approximations are stable [88]. For these elements, the number of degrees of freedom in velocity is systemically higher than the one in pressure. Intuitively, this may be attributed to the fact that the second order derivatives of the velocity are involved in the Navier-Stokes equations, but only the first order derivative of the pressure. Consequently, approximated velocity has to be smoother than pressure. The last possibility is to use a stabilisation technique to circumvent the LBB condition. Here, a Variational Multiscale Method (VMS) framework, formalised by Hughes [116, 117],

is considered. Such a VMS approach seems relevant for the simulation of capillary-driven flow, for many reasons. Hence, the pressure enrichment strategy, presented later on, and needed to capture the pressure discontinuities, is built and works well in the VMS stabilisation context, and not with Taylor-Hood element P2/P1. Additionally, VMS methods can also be formulated to stabilise the convection-dominated flows. And last but not least, VMS stabilisations may be implemented with ease in a FE code since they consist of adding additional terms in the standard formulation.

The VMS approach is based on the fact that the lost of stability between the continuous and the discrete problems, is due to the unresolved subgrid components, here $\boldsymbol{v}'$ and p' [42]. Both velocity and pressure field are divided into a computable component, the finite element solution, and these subgrid components:

$$\boldsymbol{v} = \boldsymbol{v}_h^{n+1,i+1} + \boldsymbol{v}' \text{ and } p = p_h^{n+1,i+1} + p'.$$

The test function are split accordingly:

$$\boldsymbol{w} = \boldsymbol{w}_h + \boldsymbol{w}', \text{ and } q = q_h + q'.$$

The subgrid components $\boldsymbol{v}'$ and p' belong, respectively, to $\mathcal{W}'$ and $\mathcal{Q}'$, defined such that $\mathcal{W} = \mathcal{W}_h \oplus \mathcal{W}'$ and $\mathcal{Q} = \mathcal{Q}_h \oplus \mathcal{Q}'$. Using the scale decomposition for pressure and velocity, the stabilised bilinear form of the Navier-Stokes equations reads

$$B_h([\boldsymbol{v}_h^{n+1,i+1} + \boldsymbol{v}', p_h^{n+1,i+1} + p'], [\boldsymbol{w}_h + \boldsymbol{w}', q_h + q']) = L_h([\boldsymbol{w}_h + \boldsymbol{w}', q_h + q']) \tag{2.12}$$

$\forall\, (\boldsymbol{w}_h, q_h) \in \mathcal{W}_h^0 \times \mathcal{Q}_h$. The problem can be split into two subproblems, one at the Finite Elements (FE) scale and one at the sub-grid scale. The FE problem reads:

$$B_h([\boldsymbol{v}_h^{n+1,i+1}, p_h^{n+1,i+1}], [\boldsymbol{w}_h, q_h]) + B_h([\boldsymbol{v}', p'][\boldsymbol{w}_h, q_h]) = L_h([\boldsymbol{w}_h, q_h]) \tag{2.13}$$

and the sub-grid problem is:

$$B_h([\boldsymbol{v}_h^{n+1,i+1}, p_h^{n+1,i+1}], [\boldsymbol{w}', q']) + B_h([\boldsymbol{v}', p'][\boldsymbol{w}', q']) = L_h([\boldsymbol{w}', q']) \tag{2.14}$$

Eq. 2.13 may be rewritten as follows, making the sub-grid component terms appear clearly

$$\begin{aligned} &B_h([\boldsymbol{v}_h^{n+1,i+1}, p_h^{n+1,i+1}], [\boldsymbol{w}_h, q_h]) + \sum_{e=1}^{n_{el}} \int_{\Omega^e} 2\mu \dot{\boldsymbol{\epsilon}}(\boldsymbol{v}') : \dot{\boldsymbol{\epsilon}}(\boldsymbol{w}_h)\, dV + \sum_{e=1}^{n_{el}} \int_{\Omega^e} \rho(\boldsymbol{v}_h^{n+1,it} \cdot \nabla \boldsymbol{v}') \cdot \boldsymbol{w}_h\, dV \\ &+ \sum_{e=1}^{n_{el}} \int_{\Omega^e} q_h \nabla \cdot \boldsymbol{v}'\, dV - \sum_{e=1}^{n_{el}} \int_{\Omega^e} p' \nabla \cdot \boldsymbol{w}_h\, dV = L_h([\boldsymbol{w}_h, q_h]) \end{aligned} \tag{2.15}$$

Each stabilisation term involving the sub-grid velocity is integrated by parts. The functions belonging to the space $\mathcal{W}'$ are localised into the mesh elements and consequently vanish on the element boundary. Consequently, the boundary terms at the element level resulting from the

integrations by parts are equal to zero. Therefore the finite element formulation becomes

$$\begin{aligned} &B_h([\boldsymbol{v}_h^{n+1,i+1}, p_h^{n+1,i+1}][\boldsymbol{w}_h, q_h]) - \sum_{e=1}^{n_{el}} \int_{\Omega^e} p' \nabla \cdot \boldsymbol{w}_h \, dV \\ &- \sum_{e=1}^{n_{el}} \int_{\Omega^e} \boldsymbol{v}' \cdot \left[\mu \Delta_h \boldsymbol{w}_h + \rho \boldsymbol{v}_h^{n+1,it} \cdot \nabla \boldsymbol{w}_h + \nabla q_h \right] dV = L_h([\boldsymbol{w}_h, q_h]) \end{aligned} \tag{2.16}$$

$\forall\, (\boldsymbol{w}_h, q_h) \in \mathscr{W}_h^0 \times \mathscr{Q}_h$.

This system is closed once $\boldsymbol{v}'$ and p' are approximated using the subgrid scale problem. This approximation is done by using a VMS-type method called Algebraic SubGrid Scale (ASGS) method, derived by Codina [62]. This method was implemented in the Z-Set (Zebulon) [34] FE code in previous works performed in our laboratory [4, 36, 175] for solving Stokes, Darcy's, and Stokes-Darcy's equations. In this work, the full version of the ASGS method, dedicated to Navier-Stokes equations, was implemented. Using ASGS method, subgrid velocity $\boldsymbol{v}'$ is chosen proportional to the finite element residual $\boldsymbol{R}_h^{n+1,it+1}$ of the momentum balance equation (see Eq. 2.17). Whereas subgrid pressure p' is proportional to the finite element residual of the mass conservation equation (see Eq. 2.19), with specific proportionality coefficients [21, 62]. Hence,

$$\boldsymbol{v}' = -\tau_v \boldsymbol{R}_h^{n+1,it+1} \tag{2.17}$$

with τ_v a stabilisation parameter and the FE residual $\boldsymbol{R}_h^{n+1,it+1}$ defined as

$$\boldsymbol{R}_h^{n+1,it+1} = \rho \frac{\boldsymbol{v}_h^{n+1,it+1} - \boldsymbol{v}_h^n}{\Delta t} + \rho \boldsymbol{v}_h^{n+1,it} \cdot \nabla \boldsymbol{v}_h^{n+1,it+1} - \mu \Delta_h \boldsymbol{v}^{n+1,it+1} + \nabla p_h^{n+1,it+1} - \rho \boldsymbol{g} \tag{2.18}$$

and

$$p' = -\tau_p \nabla \cdot \boldsymbol{v}_h^{n+1,it+1} \tag{2.19}$$

with τ_p a second stabilisation parameter.

Substituting these expression in Eq. 2.16 leads to the finite element formulation of the Navier-Stokes equations discretised and stabilised with the ASGS method. This reads:
find for the time $n+1$ and the iteration $it+1$, $\boldsymbol{v}_h^{n+1,it+1} \in \mathscr{W}_h$ and $p^{n+1,it+1} \in \mathscr{Q}_h$, with the initial

condition $\boldsymbol{v}_h(t=0)=\boldsymbol{v}_0$ such as

$$\begin{aligned}
&\int_{\Omega_h}\rho\frac{\boldsymbol{v}_h^{n+1,it+1}-\boldsymbol{v}_h^{n}}{\Delta t}\cdot\boldsymbol{w}_h\,dV+\int_{\Omega_h}\rho(\boldsymbol{v}_h^{n+1,it}\cdot\nabla)\boldsymbol{v}_h^{n+1,it+1}\cdot\boldsymbol{w}_h\,dV\\
&\qquad+\int_{\Omega_h}2\mu\dot{\boldsymbol{\epsilon}}(\boldsymbol{v}_h^{n+1,it+1}):\dot{\boldsymbol{\epsilon}}(\boldsymbol{w}_h)\,dV-\int_{\Omega_h}p_h^{n+1,it+1}\nabla\cdot\boldsymbol{w}_h\,dV\\
&\qquad+\int_{\Omega_h}q_h\nabla\cdot\boldsymbol{v}_h^{n+1,it+1}\,dV-\int_{\Omega_h}\rho\boldsymbol{g}\cdot\boldsymbol{w}_h\,dV+\int_{\Gamma_N}p_{ext}\boldsymbol{n}\cdot\boldsymbol{w}_h\,dV\\
&+\sum_{e=1}^{n_{el}}\int_{\Omega^e}\tau_v^{n+1,it}\left[\rho\boldsymbol{v}_h^{n+1,it}\cdot\nabla\boldsymbol{w}_h+\nabla q_h\right]\cdot\\
&\qquad\left[\rho\frac{\boldsymbol{v}_h^{n+1,it+1}-\boldsymbol{v}_h^{n}}{\Delta t}+\rho\boldsymbol{v}_h^{n+1,it}\cdot\nabla\boldsymbol{v}_h^{n+1,it+1}+\nabla p_h^{n+1,it+1}-\rho\boldsymbol{g}\right]dV\\
&+\sum_{e=1}^{n_{el}}\int_{\Omega^e}\tau_p^{n+1,it}(\nabla\cdot\boldsymbol{v}_h^{n+1,it+1})(\nabla\cdot\boldsymbol{w}_h)\,dV\;=\;0\qquad\forall(\boldsymbol{w}_h,q_h)\in\mathcal{W}_h^0\times\mathcal{Q}_h
\end{aligned}\tag{2.20}$$

for a Picard's linearisation ($\alpha=0$ as seen in Eq. 2.6). In this work, the velocity $\boldsymbol{v}_h$ is piecewise linear, its second-order derivatives are null in an element, and consequently were removed from this expression. The stabilisation parameters τ_v and τ_p on an element Ω^e are defined using a Fourier analysis [63, 64] as

$$\begin{aligned}
\tau_v&=\left[\frac{4\mu}{(h^e)^2}+\frac{2\rho\|\boldsymbol{v}^e\|}{h^e}\right]^{-1}\\
\tau_p&=\frac{(h^e)^2}{\tau_v}
\end{aligned}\tag{2.21}$$

where h^e and $\|\boldsymbol{v}^e\|$ are respectively the mesh size (sum of all sides divided by the number of sides) and the norm of the arithmetic average velocity on element.

2.4 Implementation validation

The validation of the implementation in the Zebulon FE code of the Navier-Stokes ASGS-stabilized equations is achieved by performing an error analysis in a steady-state case. Moreover, two additional cases will be subsequently considered to assess the efficiency of the strategy applied to 3D Navier-Stokes and Stokes flows. The enforcement of Neumann and friction boundary conditions will be specifically evaluated. Finally, the renowned case of Von Karman vortexes will be used to assess the full 3D Navier-Stokes ASGS solver. In this assessment section no units are given for numerical values, since all type of metric system can be used, as long as it remains homogeneous. The numerical simulation relies on four main steps: meshing the geometry made with GMSH [95], the numerical model implemented in Zebulon [34], solving the linear system of equations with MUMPS solver [10, 11] and visualisation with ParaView [8].

2.4.1 Error analysis in a steady-state case - polynomial manufactured solution

The polynomial manufactured solution of the steady Navier Stokes equations inside a square of unit length $\Omega = [0,1] \times [0,1]$ has been presented and solved several times in [98, 106, 112] in order to assess the efficiency of the Navier-Stokes solver. This analysis is performed by calculating the convergence rate of the stabilised Navier-Stokes equations and comparing it to the error obtained with the naturally stable P2/P1 Navier-Stokes element. The problem consists of a jet impinging upon a wall with a controlled body force $\boldsymbol{f}$ given by

$$\begin{aligned} f_x &= 5\rho x y^8 + 10\rho x y^3 + 60\mu x y^2 \\ f_y &= 0 \end{aligned} \tag{2.22}$$

This body force is acting as an external force like the gravity and is consequently added to the right-hand side of the linear system. The velocity and the pressure fields solutions of the steady Navier-Stokes equations with the external force given in Eq. 2.22 are

$$\begin{aligned} v_x &= -5xy^4 \qquad\qquad v_y = -\frac{1}{2} + y^5 \\ p &= \frac{1}{2}\rho(y^5 - y^{10}) + 5\mu y^4 \end{aligned} \tag{2.23}$$

Fig. 2.1 shows respectively, from left to right and top to down, the boundary conditions, the velocity field, the pressure field with a low Reynold number and pressure field with a higher Reynold number. A specificity of these boundary conditions is to prescribe the pressure at the bottom left corner, since pressure is defined up to an additive constant. Looking at the velocity, the fluid is injected from the upper right-hand side of the domain and is flowing out through the bottom and upper sides after impinging upon the left-hand side wall.
Contrary to the velocity, the pressure field, the analytical expression which is given in Eq. 2.23, depends on the flow regime, *i.e.* on density and viscosity. Actually, Fig. 2.1 (C) represents the pressure field in the case of a laminar flow with a low Reynolds number $\mathscr{R}e = 0.5025$ and the flow is said to be diffusion dominated. Density and viscosity are then $\rho = 0.1$ and $\mu = 1$. In the second case depicted in Fig. 2.1 (D), those parameters are $\rho = 1000$ and $\mu = 1$, yielding a turbulent flow (or convection dominated flow) with a Reynolds number $\mathscr{R}e = 5025$.

For the purpose of studying the convergence order, the norms $\mathscr{L}^2(\Omega)$, $\|\cdot\|_{0,\Omega}$ and $\mathscr{H}^1$, $\|\cdot\|_{1,\Omega}$, are defined:

$$\|\boldsymbol{u}\|_{0,\Omega} = \left(\int_\Omega \boldsymbol{u}^2\, dV\right)^{\frac{1}{2}} \tag{2.24}$$

$$\|\boldsymbol{u}\|_{1,\Omega} = \left(\int_\Omega \boldsymbol{u}^2\, dV + \sum_{j=1}^{dim} \left\| \frac{\partial \boldsymbol{u}}{\partial x_j} \right\|_{0,\Omega}^2\right)^{\frac{1}{2}} \tag{2.25}$$

where dim is the spatial dimension.

As represented in Fig. 2.2, convergence orders are given for the naturally stable P2/P1 element in sub-figure (A) and for the ASGS-P1/P1 element in sub-figure (B), both for the low

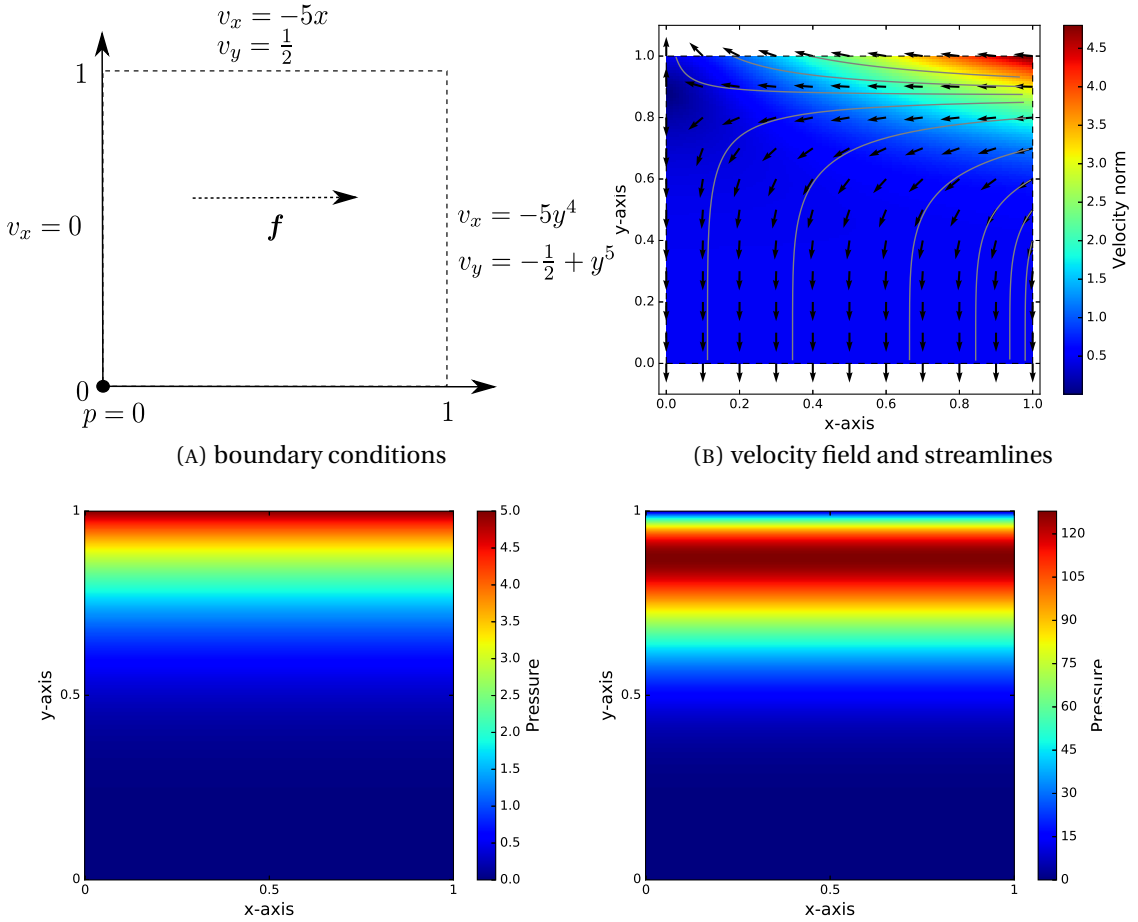

(A) boundary conditions

(B) velocity field and streamlines

(C) Pressure field with $\mathscr{R}e = 0.5025$, $\rho = 0.1$ and $\mu = 1$

(D) Pressure field with $\mathscr{R}e = 5025$, $\rho = 1000$ and $\mu = 1$

FIGURE 2.1 – Manufactured Solution for steady Navier Stokes

Reynolds number $\mathscr{R}e = 0.5025$. Convergence orders are computed using 6 (for P2/P1 element) or 7 (for P1/P1) structured meshes with the number of elements per side ranging from 20 to 400. The P2/P1 element matches the three theoretical convergence orders. The theoretical convergence orders are 2 for both pressure with the norm $\mathscr{L}^2$ and velocity with the norm $\mathscr{H}^1$, and a convergence order of 3 for the velocity with the norm $\mathscr{L}^2$. The numerical values are: 2.04 for the pressure, exactly as anticipated from the theory, 2 and 3 for the velocity with the norms $\mathscr{H}^1$ and $\mathscr{L}^2$ respectively.

The element stabilised with ASGS shows a stronger convergence for the norm $\mathscr{L}^2$ in pressure since the theoretical value is 1 and the computed convergence order is 1.37, but with a lower accuracy compared to the error value of the P2/P1 with the same number of velocity unknowns. Computed convergence orders are consistent with theoretical values for the velocity, 1 and 2 for the norm $\mathscr{H}^1$ and $\mathscr{L}^2$ respectively. This comparison enables to verify that one order of convergence is lost for the velocity between P1/P1 and P2/P1 element, but the stiffness matrix is smaller with linear approximation for a fix mesh size.

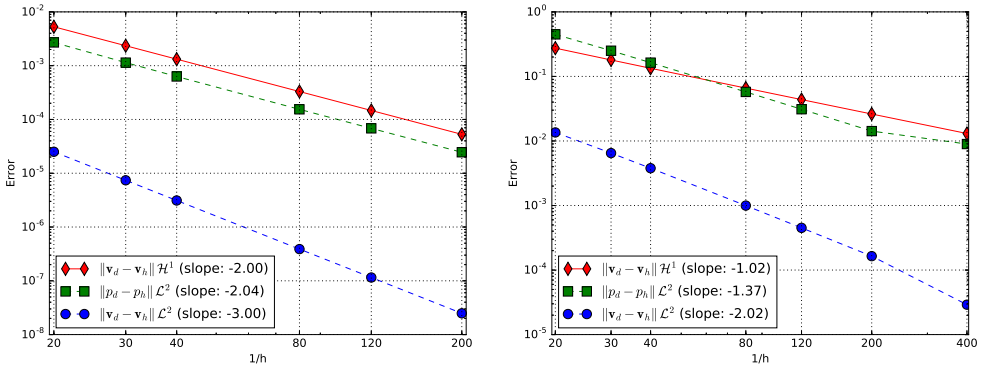

(A) P2/P1 element (B) ASGS stabilisation

FIGURE 2.2 – Manufactured Solution for steady Navier Stokes - Convergence orders in the case of a laminar flow with $\mathscr{R}e = 0.5025$

In the second case of a convection dominated flow ($\mathscr{R}e = 5025$), the convergence orders are plotted using the same structured meshes. As shown in Fig. 2.3, both naturally stable or stabilised elements exhibit a better convergence than expected compared to the theoretical values, stated above. For a fixed mesh size, the error is greater for the turbulent case compared to the laminar case for both types of elements. Here, the pressure convergence order is the same for P1/P1 than P2/P1 element.

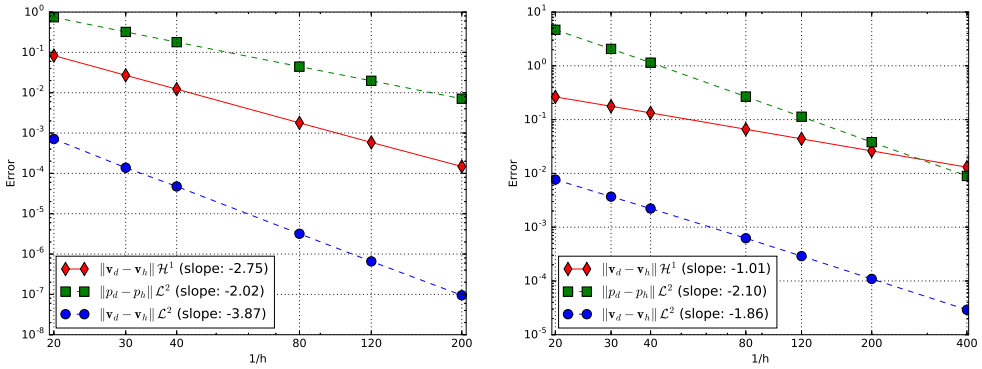

(A) P2/P1 element (B) ASGS stabilisation

FIGURE 2.3 – Manufactured Solution for steady Navier Stokes- Convergence orders in the case of a turbulent flow with $\mathscr{R}e = 5025$

For the presented cases and stationary solution flows, the non linear convective term is not neglected. The non linearity has been managed for the convergence order only with a Picard's scheme (α alawys null) so far, which is iterated until a convergence criterion is reached. The convergence criterion is based on the relative residual, defined as the maximum value of the residual vector divided by the norm of the external force vector. The iterative procedure stops when the relative residual reaches a value below 10^{-12}. The rest of the paragraph will investigate how to reduce the number of iterations to reach the same solution.

As presented previously, an improvement possibility consists in using a Newton-Raphson linearisation ($\alpha = 1$ in Eq. 2.8) instead of the Picard scheme ($\alpha = 0$). To assess the iterative procedure efficiency, the turbulent case ($\mathscr{R}e = 5025$) is solved instead of the laminar case ($\mathscr{R}e = 0.5025$) since in the latter more iterations are added up. Actually, 33 Picard's iterations are necessary to reach a residual value below 10^{-12} for the convective dominated flow, whereas only

6 iterations are required in the case of a laminar flow. Furthermore, no discrepancy has been noted between P2/P1 or P1/P1 stabilised ASGS elements for the residual convergence in either laminar or turbulent case.

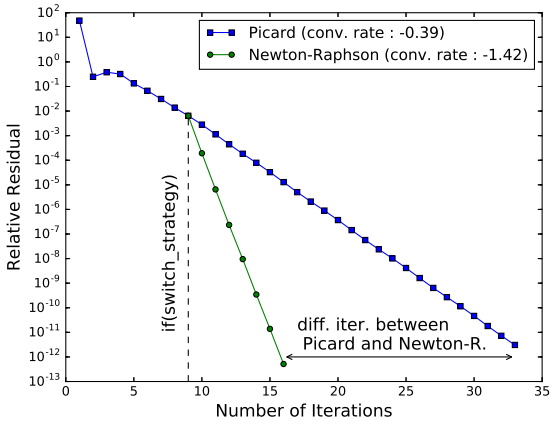

FIGURE 2.4 – Manufactured Solution for steady Navier Stokes - Rate of convergence using ASGS stabilisation, mesh size $1/h^e = 120$, and $\mathscr{R}e = 5025$

The relative residual is plotted in Fig. 2.4 for the fifth refinement mesh corresponding to a mesh size of $1/h^e = 120$ in the case of a turbulent flow ($\mathscr{R}e = 5025$) when using the ASGS-P1/P1 element. The Navier-Stokes solver does only a fixed number of Picard's iterations and will whether or not, based on a 'switch_strategy' condition use a Newton-Raphson's scheme or continue with the Picard's scheme as depicted in Fig 2.4. The blue curve with square markers represents the relative residual evolution during the iterations with a Picard scheme. Whereas the green dotted curve embodies the Newton-Raphson scheme adopted if the 'switch_strategy' is turned in. The 'switch_strategy' condition may be a simple fixed number of iterations for instance. In the presented case, the switch condition is activated after nine Picard iterations. An improved condition could also be based on a minimum relative residual in order to be close enough to the solution, before starting to converge faster to it. As shown in the figure, the relative residual is divided by 2.5 between two successive iterations in the case of the Picard linearisation and by 27 for the Newton-Raphson on average.

2.4.2 Flow between two walls

This 3D case is designed to investigate a Neumann condition imposition when using the ASGS stabilisation and validate the implementation of a frictional boundary condition. Only for this particular case, the Navier-Stokes equations are reduced to the Stokes equations since the focus is not on the inertia terms, contrary to the previous manufactured solution. The domain is an unit square extruded in the y-direction (see Fig. 2.5), $\Omega = [0,1] \times [0,5] \times [0,1]$. On the inlet $\{y = 0\}$, as well as on the outlet $\{y = 5\}$, the fluid is not sheared since the velocity in the x and z directions is imposed to zero. On the bottom $\{z = 0\}$ boundary, a no-slip condition is considered: $\boldsymbol{v} = \mathbf{0}$.

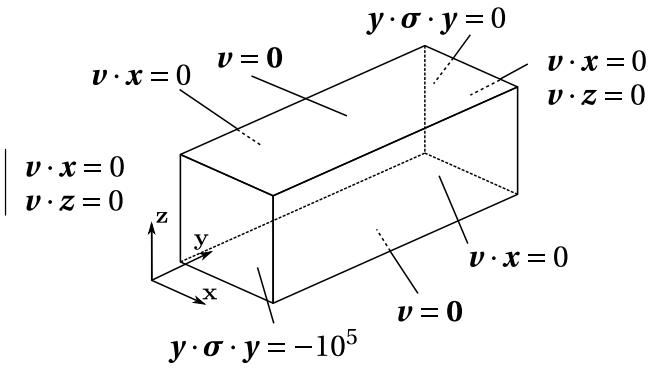

FIGURE 2.5 – Flow between two walls - Boundary conditions

On the right $\{x=1\}$ and left $\{x=0\}$ hand sides boundaries, the normal velocity $\boldsymbol{v}\cdot\boldsymbol{x}$ is set to zero. This condition is a symmetry condition. Neumann conditions are prescribed at the inlet and outlet of the domain of normal $\boldsymbol{n}=+/-\boldsymbol{y}$, *i.e.* $\boldsymbol{y}\cdot\boldsymbol{\sigma}\cdot\boldsymbol{y}=-10^5$ and $\boldsymbol{y}\cdot\boldsymbol{\sigma}\cdot\boldsymbol{y}=0$ respectively. Only the normal component of the stress vector is prescribed since the tangential velocities are imposed with a Dirichlet condition. In the case of no-shear flow at the inlet and outlet, using the definition of the stress tensor Eq. 1.14, the pressure can be derived analytically. More specifically the condition at the inlet reads $p|_{\text{inlet}}=10^5+2\frac{\partial v_y}{\partial y}$. As long as the velocity does not depend on y, the first derivative in the y direction is zero. Therefore, imposing at the inlet and outlet the value for the normal stress is equivalent to enforce the pressure. Below, two types of conditions are investigated at the upper wall: a no-slip condition and a Navier slip condition.

No-slip condition

A no-slip condition is first imposed at the upper wall $\{z=1\}$: $\boldsymbol{v}=0$ (see Fig. 2.5). The analytical solution given in Appendix A Eq. A.8 is a velocity quadratic with respect to z, while pressure is linear along the y-axis. This pressure is plotted in Fig. 2.6 with the dotted line. A numerical experiment has been carried out with six mesh refinement levels. The initial constant mesh size is 0.1 in the entire domain and corresponds to the refinement level 0. For each refinement level, the mesh size is divided by two each time at the inlet and at the outlet where the solution field varies mostly. The mesh is only locally refined otherwise solving the system would become computationally CPU and memory intensive. For the six refinement levels, the pressure profile is plotted along a line passing through points of coordinates (0.5,0,0.5) and (0.5,5,0.5), which are placed at the center of the inlet and outlet faces. The gravity is not considered in this case and viscosity is unitary $\mu=1$.
As seen in Fig.2.6, the pressure values at position $y=0$ and $y=5$ do not match the values imposed through the Neumann condition on the normal stress. The issue comes from the first derivative of the velocity in the y-direction. The stabilisation inside the domain modifies the velocity field and does not recover the analytical solution. In fact, the flow speeds up locally at the inlet and at the outlet, even though the fluid is incompressible. This spurious acceleration results from the relaxation of the mass conservation equation by the ASGS stabilisation $\int_{\Omega^e}\tau_v^{n+1,it}\nabla p_h\cdot\nabla q_h\,dV$. One solution to deal with this adverse impact of the stabilisation is to use multiple refinement levels since the effect of the stabilisation smooths out progressively when refining the mesh size. As seen in the close-ups of Fig. 2.6, the pressure at the inlet and outlet converges towards the analytical value. Refining the mesh relaxes the stabilisation terms influence in the weak formulation, since the stabilisation coefficients depend on the mesh size.

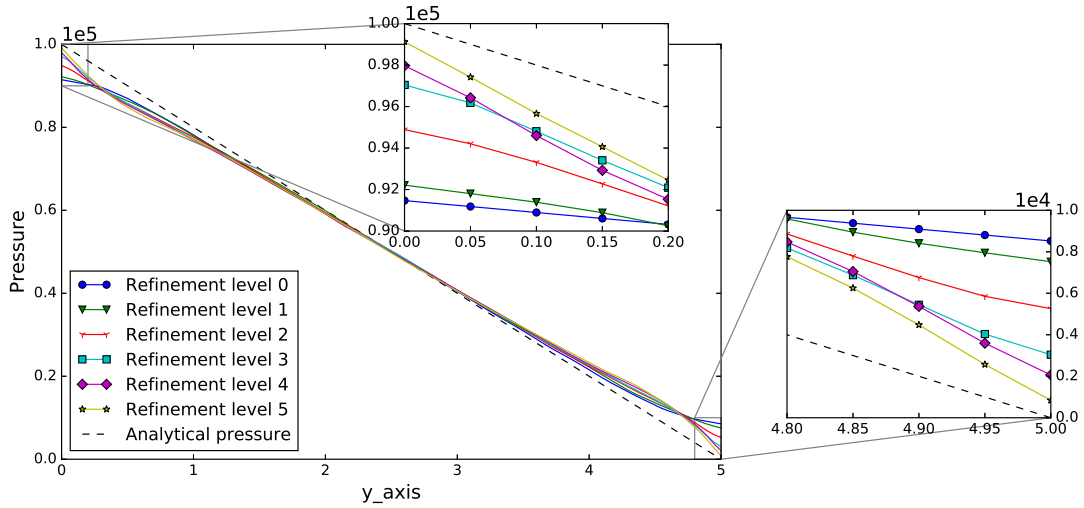

FIGURE 2.6 – Flow between two walls - Pressure field when refining the boundary mesh

A 8.4% error is reported for the pressure at the inlet with a coarser mesh (refinement level 0), this error decreases to 1% for the most refined mesh (refinement level 5).
The refinement is local at the boundary and therefore not all the numerical solution converges

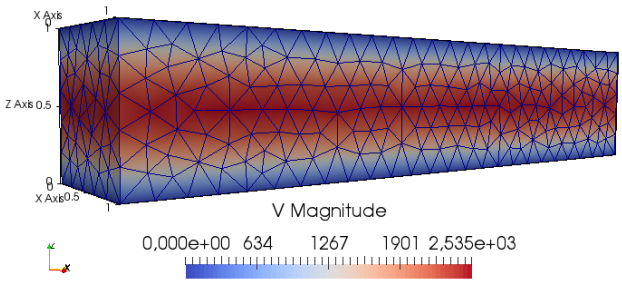

(A) Velocity magnitude with Dirichlet condition

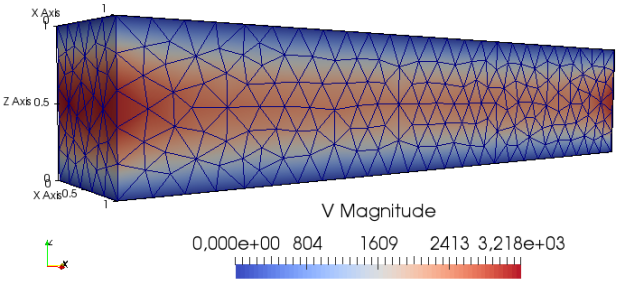

(B) Velocity magnitude without Dirichlet condition

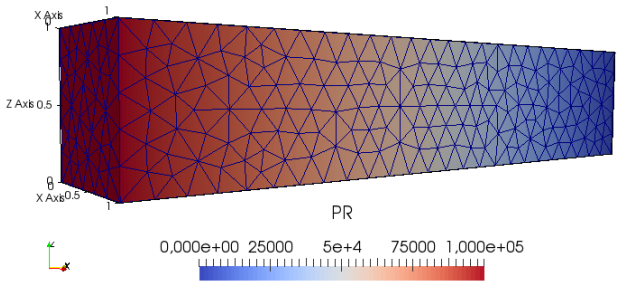

(C) Pressure with Dirichlet condition

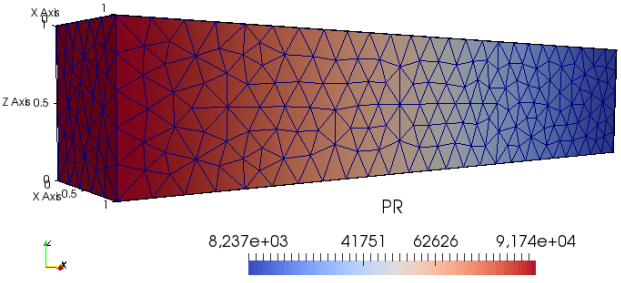

(D) Pressure without Dirichlet condition

FIGURE 2.7 – Flow between two walls - Comparison of velocity and pressure field with (A and C) and without (B and D) over-constrained Dirichlet boundary condition for the pressure at the inlet and outlet - refinement level 0

but only the pressure at the ends of the domain. To our best knowledge, no systematic improvement is known for this problem, except refining the mesh size. It has been also noticed in this work that imposing directly the pressure as a Dirichlet condition helps to improve the accuracy of the result, but only when the flow is oriented in the normal direction. In other terms, the over-constrained problem with Dirichlet boundary condition on the pressure at the inlet and outlet

has a solution closer to the analytical solution. Particularly, for the maximum velocity located at the mid-plane $\{z = 0.5\}$ which has a theoretical value of 2500 (with arbitrarily length unit over time unit). When imposing Dirichlet boundary conditions, the relative error drops from 28.7% to 1.4% for this maximum value, as can be seen in Fig. 2.7 with mesh refinement level 0.

Slip condition on the upper wall

The previous configuration is now extended to test the slip condition. The same boundary conditions as in Fig. 2.5 are still considered, except at the upper wall $\{z = 1\}$ where only the normal velocity $\boldsymbol{v} \cdot \boldsymbol{z}$ is set to zero. This no-penetration condition is completed by a Navier condition relating shear stress to the (tangential) velocity. The simplest relation is the following linear expression

$$f_{\text{Navier}} = \int_{\text{upper wall (uw)}} \boldsymbol{\sigma} \cdot \boldsymbol{n} \cdot \boldsymbol{w}\, dS = \int_{uw} \underbrace{[\boldsymbol{\sigma} \cdot \boldsymbol{n} - (\boldsymbol{\sigma} \cdot \boldsymbol{n} \cdot \boldsymbol{n})\, \boldsymbol{n}]}_{\text{shear stress}} \cdot \boldsymbol{w}\, dS + \int_{uw} \underbrace{(\boldsymbol{\sigma} \cdot \boldsymbol{n} \cdot \boldsymbol{n})\, \boldsymbol{n} \cdot \boldsymbol{w}}_{=0}\, dS$$
$$= -\int_{uw} \beta \boldsymbol{v} \cdot \boldsymbol{w} dS \tag{2.26}$$

The normal component of the test function $\boldsymbol{w}$ is equal to zero since a no-penetration condition is used for the velocity. This leads to remove the normal component of the stress vector in Eq. 2.26 and restrict the velocity vector to its tangential components. The Navier boundary condition [148, 157] represents the fluid behaviour on a solid surface and may model the roughness of the wall for example. The ratio μ/β is the slip length, which can be seen as the depth (inside the solid) where the linear extrapolation of the velocity is equal to zero. Therefore, the no-slip condition is reached when the ratio is equal to zero, that happens when the coefficient β tends to infinity, or, at least, from a computational point of view, when $\beta >> \mu$.

This slip condition is applied on the upper wall and thus the magnitude of the velocity is

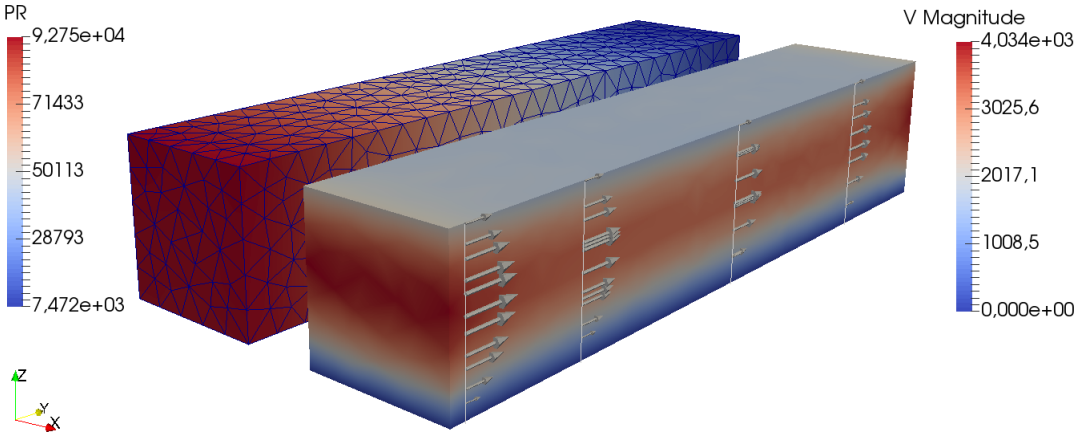

FIGURE 2.8 – Flow between two walls - Pressure and velocity fields

not zero on this wall as seen in Fig. 2.8. The domain with the mesh drawn is colored with the pressure isovalues. This mesh corresponds to the refinement called level 0 in the previous test, which has a mesh size of 0.1. Simulation is run with a viscosity $\mu = 1$ and a friction coefficient $\beta = 5$. An analytical solution is given in Appendix A Eq. A.12. The numerical error with respect

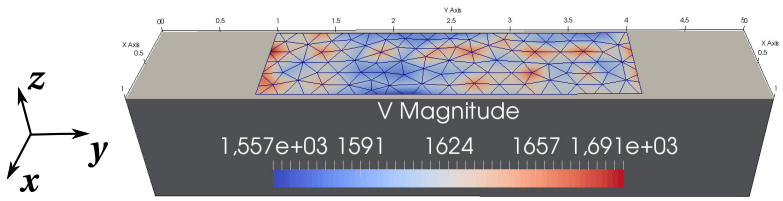

FIGURE 2.9 – Flow between two walls - Velocity field on the upper wall with slip condition

to the analytical solution is bounded between -3.7% and 4.6% (theoretical value $5./3. \times 10^3$), for velocity values on the upper wall at the position $y \in [1,4]$ (see Fig. 2.9). The relative error is reasonable since the computation is run with an unrefined mesh.

2.4.3 Vortex shedding

This example is the well studied [154, 168, 209, 215] vortex shedding behind a cylinder. The computational domain is $\Omega = [0,19] \times [0,8] \times [0,0.2] \setminus D$ with D the cylinder of diameter 1 centered at a point $(x = 4, y = 4, \forall z \in [0,0.2])$. The boundary conditions are shown in Fig. 2.10 which is the same setting as presented in the work of Owen [164]. The inlet velocity is prescribed, and a zero normal stress condition is imposed at the outlet. Symmetrical boundary conditions are prescribed on the other faces, while the velocity on the cylinder is zero, *i.e.* the fluid sticks to the cylinder otherwise no vortex would be generated. Even though the vortex shedding problem

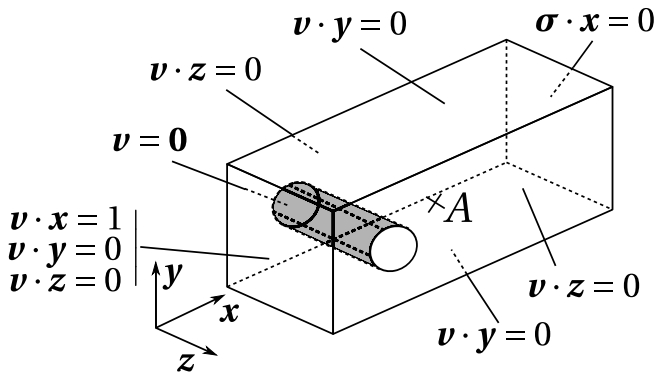

FIGURE 2.10 – Vortex shedding - Boundary conditions with slip on the top boundary

may be simplified to a 2D problem, the complete 3D is computed to demonstrate the ability of the code to cope with complex problems. The mesh presented in Fig. 2.11 is made up of 22564 tetrahedrons with 6762 nodes (*i.e* 27048 unknowns). The inlet face has only one layer of element in the extrusion direction z normal to the slice plan shown in Fig. 2.11. In the cylinder vicinity, the mesh is refined in every space direction, in particular, it has 8 layers in the z-direction, with a mesh size of 0.025. Elsewhere, the mesh size is of 0.5. This coarse mesh is already good enough to predict accurately physical quantities like the Strouhal number, as defined and shown at the end of this paragraph. The Reynolds number is $\mathscr{R}e = 125$, calculated with a viscosity $\mu = 1$, a density $\rho = 125$, a unit characteristic length (the cylinder diameter), and a unit characteristic velocity (inlet velocity). The simulation is run from time $t_0 = 0$ until $t_f = 100$ with a time step of $\Delta t = 0.02$. The flow regime depends on the Reynolds number. The different regimes, from [192, 226] are summarized in Tab. 2.1. As expected for a Reynolds number of 125 (see the fourth line

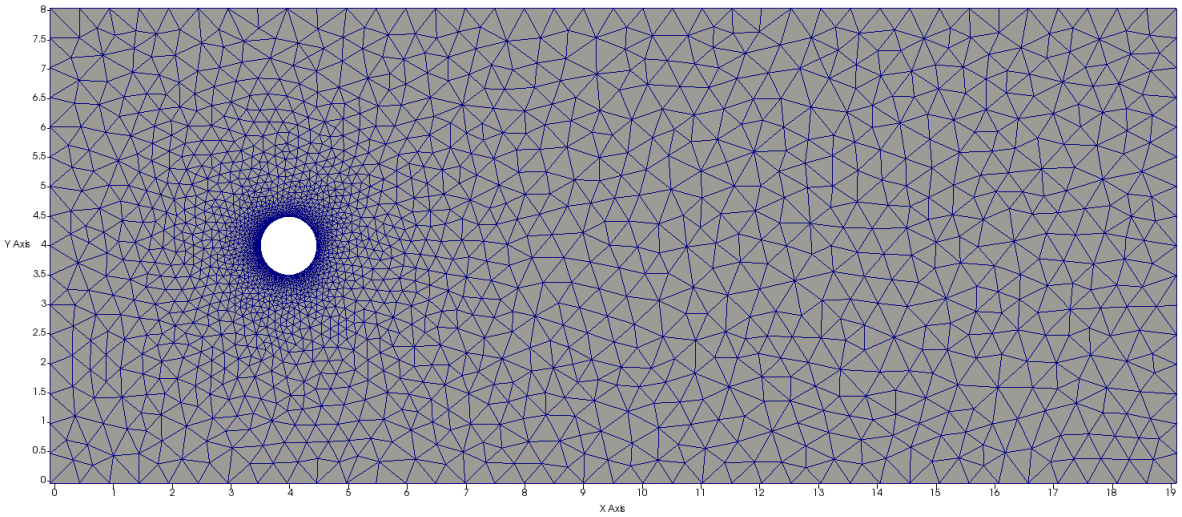

FIGURE 2.11 – Vortex shedding - view of the 3D mesh in the x-y plane

Reynolds number regime	Flow regime	Flow characteristics
$\mathscr{R}e \to 0$	Laminar Creeping Flow	Steady - No wake
$\mathscr{R}e < 49$	Laminar Vortex pairs in wake	Steady symmetric separation
$49 < \mathscr{R}e < 80-90$	Laminar Onset of Karman vortex street	Laminar unstable wake
$80-90 < \mathscr{R}e < [150;300]$	Laminar Pure Karman vortex street	Karman vortex street
$[150;300] < \mathscr{R}e < [10^5;1.3\cdot 10^5]$	Subcritical regime	Vortex street (turbulent instabilities)
$[10^5;1.3\cdot 10^5] < \mathscr{R}e < 3.5\cdot 10^5$	Critical regime	Laminar separation Turbulent reattachment Turbulent separation Turbulent wake
$3.5\cdot 10^5 < \mathscr{R}e$	Supercritical regime	Turbulent separation

TABLE 2.1 – Vortex Shedding - Flow regimes depending on the Reynolds number extracted from [192, 226]

of Tab. 2.1), the Karman vortex street is predicted by the simulation (see Fig. 2.12). The top subplot in Fig. 2.12 represents the pressure field and the bottom one, the magnitude of the velocity at $z = 0.2$ and at time $t = 100$.

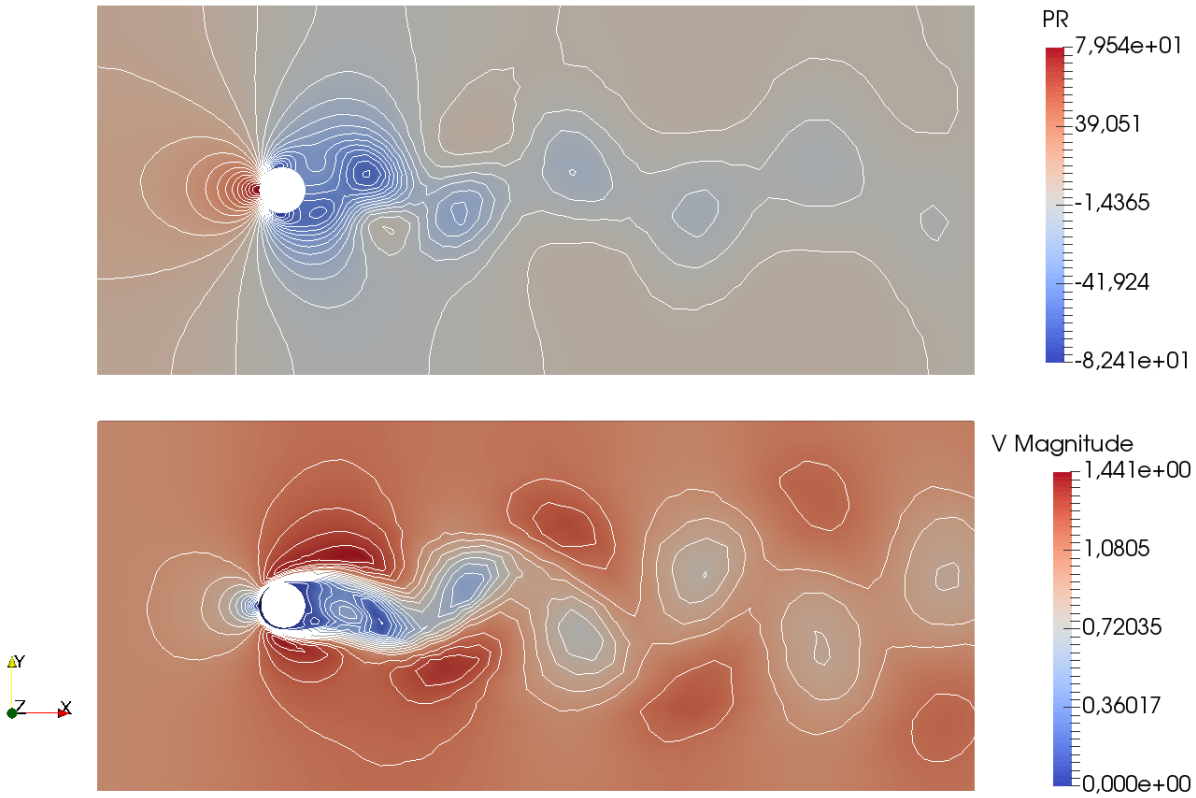

FIGURE 2.12 – Vortex shedding - Pressure and velocity fields at $t = 100$

As in literature [106], pressure and velocities in x and y directions are represented over time for point $A = (6.15, 4, 0.2)$ behind the cylinder in Fig. 2.13. The periodic flow regime is established gradually during the first half of the simulation. At $t = 20$, pressure and velocities components start to oscillate. After $t = 50$ in the second half, it features stabilised periodic oscillations. The oscillations amplitudes and mean values are similar (same first significant figure) with the results obtained in [106] for both velocities and pressure.

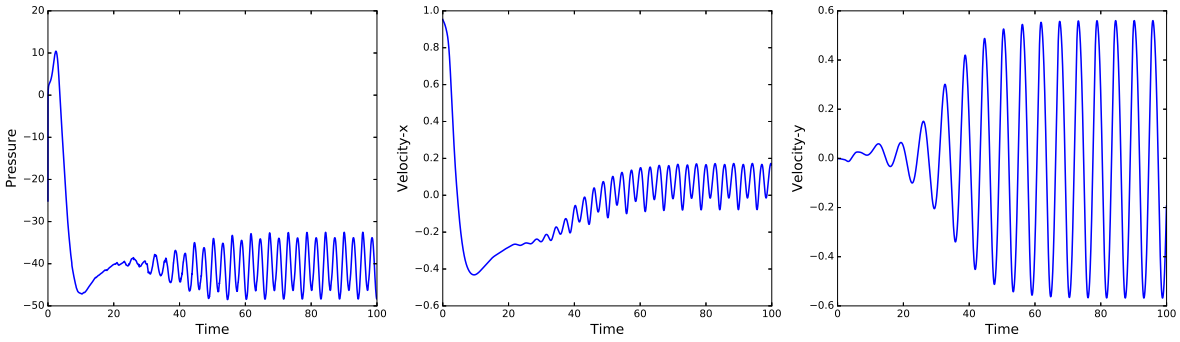

FIGURE 2.13 – Vortex shedding - Pressure and velocity components at point $A = (6.15, 4, 0.2)$

The transitory state in the first half of the simulation is also reflected through drag and lift forces on the cylinder. Since there is a no-slip condition at the cylinder, lift and drag forces are mainly generated by the action of the pressure on the cylinder. The former (lift) is the sum of all stress vector action on the cylinder in the y-direction (normal to the flow) whereas the latter force (the drag) is projected in the flow x-direction. Both forces on the cylinder over time are drawn in Fig. 2.14,where one can verify that, the lift force is smaller in magnitude than the drag one but it covers a higher range when starting to oscillate. The spherical component of the stress vector $-p\boldsymbol{I}$ accounts for almost all the lift whereas it accounts for approximately 80% of the drag.

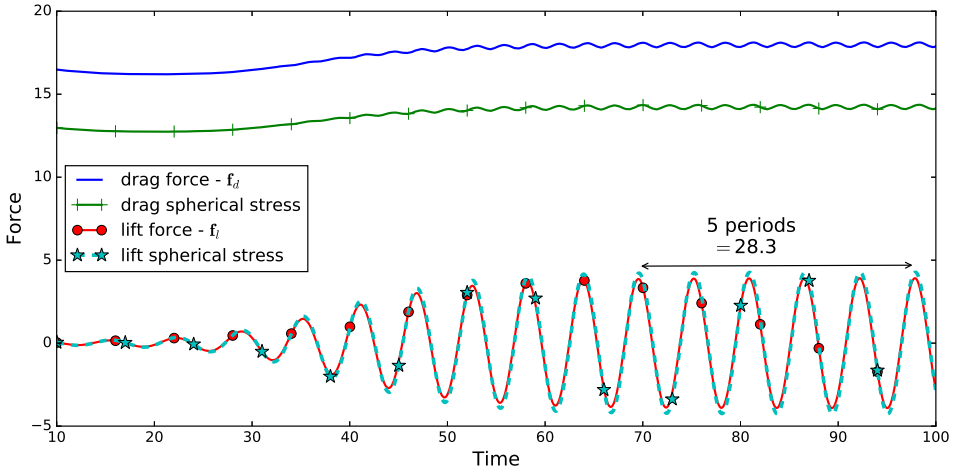

FIGURE 2.14 – Vortex shedding - Drag and lift forces

From the vortex shedding period, one can compute the Strouhal number giving useful insight when describing oscillating flow mechanisms, $St = f_{req}D/\|v_{inlet}\|$, with D the diameter of the cylinder. A vortex is detached each time a peak of velocity in the y-direction or a peak of lift force is reached. On Fig. 2.14, five periods are isolated when the flow is established. Thus, vortices are generated with the frequency: $f_{req} = 5./28.3 \approx 0.177$. Some experiments [227] have explained that the Strouhal number can be given as power expansion of $1/\sqrt{\mathscr{R}e}$ for the exact same case of a flow past a circular cylinder. Fey *et al.* [87] prove that the two first powers give satisfactory fit with experiments. In that case, the Strouhal number is given by

$$St = St^* + A/\sqrt{\mathscr{R}e}$$

with $St^* = 0.2684$ and $A = -1.0356$ which is valid for all Reynolds number between 45 and 2×10^5. The ability to correctly predict the Strouhal number (see Tab. 2.2) has been already no-

Numerical St nb.	Experimental St nb.
0.177	0.176

TABLE 2.2 – Vortex Shedding - Comparison Strouhal number between numerical and experimental values

ticed in the literature [44, 63, 106]. As given in [99], one explanation may be that the backward Euler scheme introduces numerical viscosity, giving satisfactory results. Here also, the numerical Strouhal number is in good agreement with the experimental one.

Conclusion

This chapter focuses on the fluid solver for both Stokes and Navier-Stokes equations for one phase flow. The Navier-Stokes equations have been first linearised (Picard and Newton-Raphson methods) and then discretised using a FE method, piecewise linear both in velocity and pressure. A VMS method has been described to stabilise this discrete formulation. Three kinds of numerical simulations have been carried out to highlight: the convergence rate of the chosen method, the imposition of the natural boundary condition and finally the ability to compute a flow with features of the turbulence such as vortices.
Incrementally, every tool to compute bi-fluid flows are introduced at each chapter. The next chapter intends to give a stand-alone method to capture an interface. The two methods (*i.e.* the presented fluid solver and the one to be defined for capturing interface method) will be coupled next to represent the front of resin in the fibres reinforcement during the LRI process.

Résumé en Français : Stratégie numérique pour résoudre les équations de Navier-Stokes

Le solveur bi-fluide se base sur la méthode des éléments finis pour résoudre les équations de Navier-Stokes en supposant un comportement Newtonien des fluides. Une formulation mixte en vitesse et pression avec une approximation linéaire des deux champs a été implémentée. La stabilisation ASGS est utilisée, afin d'assurer l'existence et l'unicité de la solution. La non-linéarité des équations de Navier-Stokes est traitée par deux schémas itératifs : Newton-Raphson ou Picard, qui peuvent être utilisés séparément ou combinés. La preuve du bon fonctionnement du solveur itératif est donnée par une étude de convergence jusqu'à un Reynolds de 5000, suffisant pour notre étude. De plus, une attention particulière doit être prêtée à l'interaction entre la stabilisation ASGS et les conditions aux bords imposées faiblement. Il a été noté que la stabilisation pouvait biaiser la valeur de la pression imposée faiblement, indirectement. Une taille de maille adaptée ou raffinée permet toutefois de diminuer le poids de la stabilisation et donc du biais sans compromettre la stabilité. La robustesse et la simplicité de mise en œuvre de la stratégie numérique développée en sont les atouts majeurs. Enfin, l'étude des allées de tourbillons de Karman montre une bonne corrélation avec la littérature.

Chapter 3

Level-set method

Contents

Introduction

After setting up the flow solver, a description of the moving interface between resin and air during composites manufacturing must be given and is the purpose of this chapter. Indeed, a method to represent the moving interface between the resin and the air is required to be able, in the next chapter, to numerically integrate the surface tension in the fluid solver. First of all, the method describing the interface must comply with some requirements. Actually, numerical simulation of the LRI manufacturing process must be able to account for drastic topological changes. A detailed approach must give the position of the fluid front between both liquid (the resin) and vapour phases (the air).

Interface tracking and capturing is an active field of research and at least two main types of methods have been developed to deal with this challenging issue. A classification can be made depending on the nature of the computational grid for spatial discretisation: (1) Lagrangian description (2) Eulerian description. In the case of a Lagrangian description the mesh is moving with the flow velocity, therefore, boundaries of the domain describe the interface of the fluid. Unfortunately, large deformation of the grid requires to use a re-meshing strategy which will increase the computational cost. In an Eulerian description, the interface passes through a fixed mesh, dealing naturally with topological changes. Some specific methods give the position of the domains separated by the interface, here liquid and air, while others capture the position of the interface.

Among Eulerian description, one of these methods is the **Volume tracking** method, developed by Harlow and Welch [109] in which markers are placed in the fluid and are moved at each time increment with the velocity field. Similarly, Daly *et al.* [68] placed the markers on the interface creating the **Surface tracking** method. In this second method, the markers are also convected with the velocity field. The main drawback of these methods is the shortage of these weightless markers that may happen locally, decreasing the homogeneity of the geometry representation accuracy throughout the computational domain. Volume tracking and Surface tracking belong

to the group of front tracking methods which represents the interface explicitly.
Opposite approaches are the front capturing methods with an implicit representation of the interface. Such methods introduce a real-valued function ϕ defined on the computational domain, whose value at a point indicates in which domain we are (resin or air). A change of value between two nodes implicitly represent the interface which may be convected with a velocity field. Two subcategories can be distinguished among front-capturing methods, the first one is the **Volume of Fluid** (VoF) method introduced by Hirt and Nichols [113] where the function ϕ is an indicator function, taking only two values: 1 or 0. The VoF method naturally ensures the volume conservation, however the standard continuous Galerkin approximation is not adequate here, since indicator functions are discontinuous. Moreover, even with a discontinuous Galerkin technique [27], one faces the numerical diffusion issues: ϕ_h, the approximation of ϕ, takes its values throughout the interval $[0,1]$, which makes it difficult to locate the interface precisely. Additionally, the geometric descriptors of the interface, such as the normal vectors or the curvature, are not straightforward to compute with a VoF method. The second class of front capturing methods, is constituted by the **level-set** method originally developed by Osher *et al.* [162, 163], which consists in choosing ϕ as a continuous function. Each side of the interface is characterised by the sign of ϕ. Consequently, the interface is described as the zero-isosurface of the field ϕ. Contrary to the VoF method, the interface is not diffuse: a point is either on one side or on the other side of the interface. Besides, the geometrical quantities of the interface (normal and curvature) can be directly computed.
Capturing methods deal implicitly with topological changes (void formation or annihilation), since these changes are automatically taken into account by the value of ϕ. That is why the method employed in this work is an interface capturing method, and more specifically a level-set method, since capillary effects require the geometrical description of the interface. The level-set features, ranging from time discretisation to space discretisation with stabilisation strategy and a reinitialisation strategy will be presented. The question of the inherent mass loss will be the common thread for the validation examples. It will be numerically assessed that mass is conserved when refining the mesh and the time step. Finally, the last section of this chapter will focus on how to perform an integration of a surface tension force on the level-set interface.

3.1 Level-set features

Level-set definition and its convection with a given velocity field are presented first. Second, time and space discretisations are detailed. Finally, the level-set has to be periodically reinitialised in order to keep the metric distance property throughout the computation.

3.1.1 Level-Set function

The level-set function ϕ is a continuous function, chosen positive on one side of the interface to be captured, and negative on the other side. Consequently, the interface $\Gamma_{LV}(t)$ is described as the zero-isosurface of ϕ:

$$\Gamma_{LV}(t) = \{\boldsymbol{x} \in \Omega, \quad \phi(\boldsymbol{x}, t) = 0\} \tag{3.1}$$

where Ω is the computational domain for the level-set which is commonly the same as for the fluid (see Fig. 3.1). The level-set method allows for the straightforward definition of geometrical

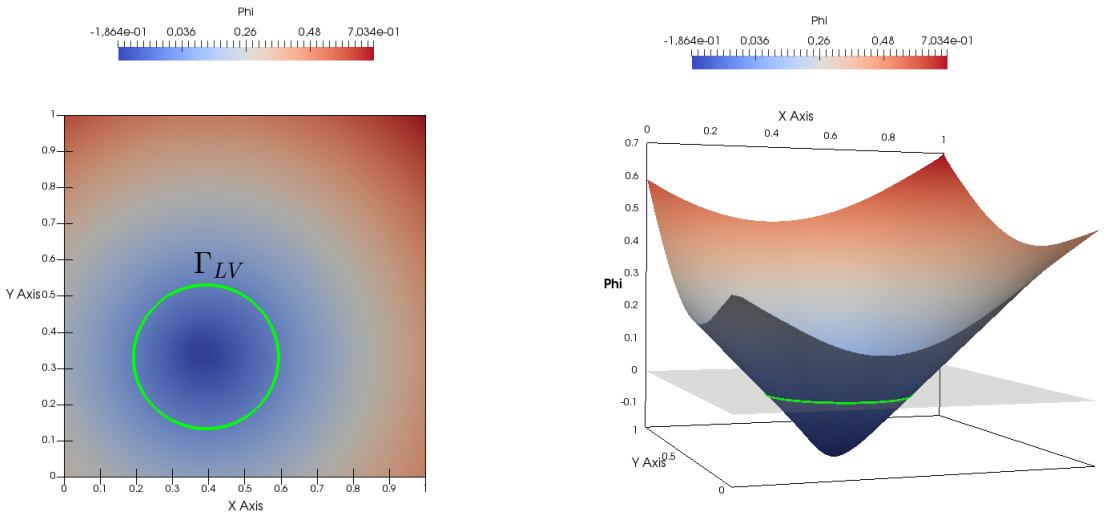

FIGURE 3.1 – Level-set definition - green circle representing the iso-surface zero (interface) of the level-set field ϕ

quantities of the interface such as the vector normal $\boldsymbol{n}$ and the curvature $\mathscr{C}$. The normal is obtained by taking the gradient of ϕ

$$\boldsymbol{n} = \frac{\nabla\phi}{||\nabla\phi||} \tag{3.2}$$

while the curvature, the divergence of this vector

$$\mathscr{C} = \nabla \cdot \boldsymbol{n}. \tag{3.3}$$

3.1.2 Transport equation

To capture the interface, the level-set function $\phi(\boldsymbol{x}, t)$ is advected using a transport equation [161] with a velocity $\boldsymbol{v}$ coming from the physical problem Eq. 2.20. The transport equation is not a conservation equation applied to ϕ but describe the constant variation of a flow particle along a streamline: $D\phi/Dt = cst$. This transport equation may be given as

$$\frac{\partial\phi}{\partial t} + \boldsymbol{v} \cdot \nabla\phi = 0. \tag{3.4}$$

A source or sink term may be added on the right-hand side of the transport equation. In our case of pure advection, this source / sink term is 0. In order to solve the above first-order hyperbolic equation, boundary conditions are considered and the problem to be solved reads

$$\begin{cases} \frac{\partial\phi}{\partial t} + \boldsymbol{v} \cdot \nabla\phi &= 0 & \forall (\boldsymbol{x}, t) \in \Omega \times [0, T] \\ \phi(\boldsymbol{x}, t = 0) &= \phi_0(\boldsymbol{x}) & \forall \boldsymbol{x} \in \Omega \\ \phi(\boldsymbol{x}, t) &= g(\boldsymbol{x}, t) & \forall \boldsymbol{x} \in \partial\Omega_{in}, \forall t \in [0, T] \end{cases} \tag{3.5}$$

where $\partial\Omega_{in} = \{\boldsymbol{x} \in \partial\Omega \mid \boldsymbol{v} \cdot \boldsymbol{n} < 0\}$ corresponds to the inflow boundary. For instance, the inflow boundary is represented by the right-hand side of the domain in Fig. 3.2. The boundary has a velocity in the $-x$ direction whereas the normal is pointing outwards in the x direction. The

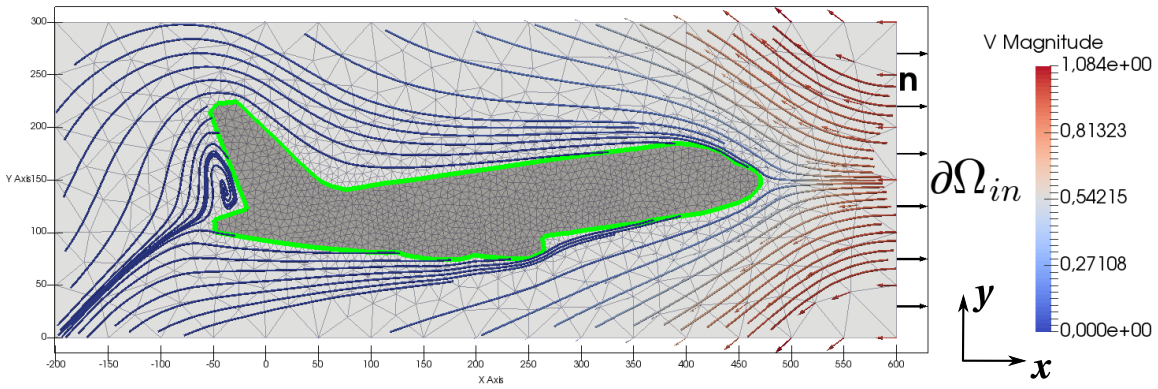

FIGURE 3.2 – Level-set definition - inflow condition on the right-hand side of the domain

level-set method enables to represent complex geometries such as an aircraft without an explicit description of the contour by the mesh.

3.1.3 Time discretisation

Evaluating the transport equation at time $t^{n+\theta}$ with $\theta \in [0,1]$ leads to

$$\left.\frac{\partial \phi}{\partial t}\right|_{n+\theta} + \left.\boldsymbol{v}\cdot\nabla\phi\right|_{n+\theta} = 0 \tag{3.6}$$

where the symbol $\bullet\big|_{n+\theta}$ represents the quantity computed at time $t^{n+\theta}$. Two Taylor expansions, written at time $t^{n+\theta}$, approximating the quantities ϕ^{n+1} and ϕ^n, read

$$\phi^{n+1} = \phi^{n+\theta} + (1-\theta)\Delta t \left.\frac{\partial \phi}{\partial t}\right|_{n+\theta} + (1-\theta)^2 \frac{\Delta t^2}{2} \left.\frac{\partial^2 \phi}{\partial t^2}\right|_{n+\theta} + o(\Delta t^3) \tag{3.7}$$

$$\phi^{n} = \phi^{n+\theta} - \theta\Delta t \left.\frac{\partial \phi}{\partial t}\right|_{n+\theta} + \theta^2 \frac{\Delta t^2}{2} \left.\frac{\partial^2 \phi}{\partial t^2}\right|_{n+\theta} + o(\Delta t^3) \tag{3.8}$$

Subtracting 3.8 to 3.7 leads to an approximation of the first derivate of ϕ at $n+\theta$

$$\left.\frac{\partial \phi}{\partial t}\right|_{n+\theta} = \frac{\phi^{n+1}-\phi^n}{\Delta t} + (2\theta-1)\frac{\Delta t}{2}\left.\frac{\partial^2 \phi}{\partial t^2}\right|_{n+\theta} + o(\Delta t^2). \tag{3.9}$$

Finally, an approximation of the convective term is given by weighting the values at the two time steps as follows

$$\left.\boldsymbol{v}\cdot\nabla\phi\right|_{n+\theta} \approx (1-\theta)\left.\boldsymbol{v}\cdot\nabla\phi\right|_{n} + \theta\left.\boldsymbol{v}\cdot\nabla\phi\right|_{n+1}. \tag{3.10}$$

Thus at the first order, equation 3.6 becomes

$$\frac{\phi^{n+1}-\phi^n}{\Delta t} + \theta\,\boldsymbol{v}^{n+1}\cdot\nabla\phi^{n+1} = (\theta-1)\,\boldsymbol{v}^n\cdot\nabla\phi^n \tag{3.11}$$

For $\theta = 0$, the scheme is an explicit Euler scheme. This common scheme has the advantage to be easy to implement and can be used at a low computation cost because no stiffness matrix has to be inverted during the simulation. As a matter of fact, the explicit Euler scheme requires a small time step Δt to ensure its stability. The condition on the time step is given by the Courant-Friedrichs-Lewy (CFL) condition $\Delta t < \frac{min(h)}{max(\boldsymbol{v})}$. Therefore the interface should move less than one

mesh size to verify the CFL condition. Instead, if $\theta \neq 0$ the scheme is implicit and the discretisation scheme is unconditionally stable if $\theta \in [0.5, 1]$. More specifically for $\theta = 1$ the scheme is an implicit Euler scheme with an order of convergence equal to 1 whereas it is in $O(\Delta t^2)$ for the Crank-Nicolson scheme, as shown in Eq. 3.9. Indeed, the second-order time derivative is not neglected when $\theta = 1/2$, but is directly equal to 0, as shown in Eq. 3.9. Hence, the choice for the rest of the study is to use a Crank-Nicolson scheme which requires to store velocities at the current time step and at the previous time step ($\boldsymbol{v}^{n+1}$ and $\boldsymbol{v}^n$).

3.1.4 Finite element approximation

Let's first define the function spaces $\mathscr{S}^g$ and $\mathscr{S}^0$, based on the Sobolev's space $\mathscr{H}^1$ as

$$\begin{aligned} \mathscr{S}^g &= \left\{\xi \in \mathscr{H}^1(\Omega) \mid \forall \boldsymbol{x} \in \partial\Omega_{in} \quad \xi = g\right\} \\ \mathscr{S}^0 &= \left\{\xi \in \mathscr{H}^1(\Omega) \mid \forall \boldsymbol{x} \in \partial\Omega_{in} \quad \xi = 0\right\} \end{aligned} \tag{3.12}$$

The integral weak form of the equation 3.4 is first obtained by multiplying the equation with a test function $\phi^* \in \mathscr{S}^0$ and then taking the integral over the whole domain. Finally, the problem reads:
find $\phi \in \mathscr{S}^g$ such that

$$\int_\Omega \frac{\phi^{n+1} - \phi^n}{\Delta t}\phi^* \, dV + \int_\Omega \theta \boldsymbol{v}^{n+1} \cdot \nabla\phi^{n+1}\phi^* \, dV = \int_\Omega (\theta - 1)\boldsymbol{v}^n \cdot \nabla\phi^n \, dV, \quad \forall \phi^* \in \mathscr{S}^0 \tag{3.13}$$

Within our FE framework, the domain Ω is discretised Ω_h by a mesh made of simplexes Ω^e such that $\Omega_h = \bigcup_{e=1}^{n_{el}} \Omega^e$. Fluid and level-set have the same discretised domain. The level-set function is approximated by ϕ_h, searched in $\mathscr{S}_h^g$ the space of the continuous and piecewise linear functions. The discrete form of previous equation 3.13 is

$$\begin{aligned} &\frac{1}{\Delta t}\int_{\Omega_h} \phi_h^{n+1}\phi_h^* \, dV + \theta \int_{\Omega_h} \boldsymbol{v}_h^{n+1} \cdot \nabla\phi_h^{n+1}\phi_h^* \, dV = \\ &\frac{1}{\Delta t}\int_{\Omega_h} \phi_h^n\phi_h^* \, dV + (\theta - 1)\int_{\Omega_h} \boldsymbol{v}_h^n \cdot \nabla\phi_h^n\phi_h^* \, dV, \qquad \forall \phi_h^* \in \mathscr{S}_h^0 \end{aligned} \tag{3.14}$$

SUPG stabilisation

The standard Galerkin method, consisting in choosing ϕ_h and ϕ_h^* in the same approximation space, is not stable for hyperbolic problems such as Eq. 3.4. A technique for stabilising the discrete formulation is thus needed. The chosen method is the StreamLine Upwind Petrov-Galerkin (SUPG) method. The SUPG stabilisation [44] creates an 'upwind' effect by adding diffusion in the direction of the convective velocity $\boldsymbol{v}^{n+1}$. Computed using the following formula, the new test functions introduced belongs to the space $\tilde{\mathscr{S}}_h^0$, which has the same dimension as $\mathscr{S}_h^0$. They are defined as

$$\tilde{\phi}_h^* = \phi_h^* + \tau_k^e \boldsymbol{v}^{n+1} \cdot \nabla\phi_h^* \tag{3.15}$$

on a mesh element Ω^e and at time t^{n+1}. The stabilisation parameter τ_k^e is computed from

$$\tau_k^e = \frac{1}{2}\frac{h_e}{||\boldsymbol{v}_{|e}^{n+1}||} \tag{3.16}$$

and it regulates the amount of diffusion needed to compute the solution. $||\boldsymbol{v}_{|e}^{n+1}||$ is the average velocity on the element e and h_e is the mesh size defined for the case of triangles or tetrahedrons as the sum of each edge divided by the number of edges. This stabilisation parameter decreases when refining the mesh and vanishes at the limit $h_e \to 0$. Hence this methods remains consistent with the original transport equation. Therefore, the final stable FE formulation, obtained with the θ-method for time-discretisation and SUPG method for stabilisation, reads:
Find $\phi_h^{n+1} \in \tilde{\mathscr{S}}_h^g$, such that

$$\begin{aligned} &\frac{1}{\Delta t}\int_{\Omega_h} \phi_h^{n+1}\tilde{\phi}_h^* \, dV + \theta \int_{\Omega_h} \boldsymbol{v}_h^{n+1}\cdot\nabla\phi_h^{n+1}\tilde{\phi}_h^* \, dV = \\ &\frac{1}{\Delta t}\int_{\Omega_h} \phi_h^{n+1}\tilde{\phi}_h^* \, dV + (\theta-1)\int_{\Omega_h} \boldsymbol{v}_h^{n}\cdot\nabla\phi_h^{n}\tilde{\phi}_h^* \, dV, \qquad \forall\tilde{\phi}_h^* \in \tilde{\mathscr{S}}_h^0. \end{aligned} \tag{3.17}$$

Choice of the level-set function

Originally, the level-set was defined as the signed distance function to the interface (*cf.* Fig. 3.1). Yet, the information of interest to construct the interface is located in a narrow-band around the zero isosurface whereas outside this region, only the sign of ϕ counts. For this reason, the second possibility consists in filtering the initial distance function [212]. In this way, the level-set function tends quickly to a constant value when moving away from the interface, as seen in Fig. 3.3. This technique avoids, or at least limits, the numerical problems which may occur due to the convective term of the transport equation 3.4 even with the SUPG method. Indeed, the transport equation 3.4 is reduced to $d\phi/dt = 0$ where ϕ is constant.
In this work, an hyperbolic tangent filter is applied to get a smooth truncation far from the interface. The definition leads to the new distance function

$$\check{\phi} = \check{e}\tanh\frac{d}{\check{e}} \tag{3.18}$$

where $\check{e}$ is the bandwidth of the interface and d the signed distance function. Not only the fil-

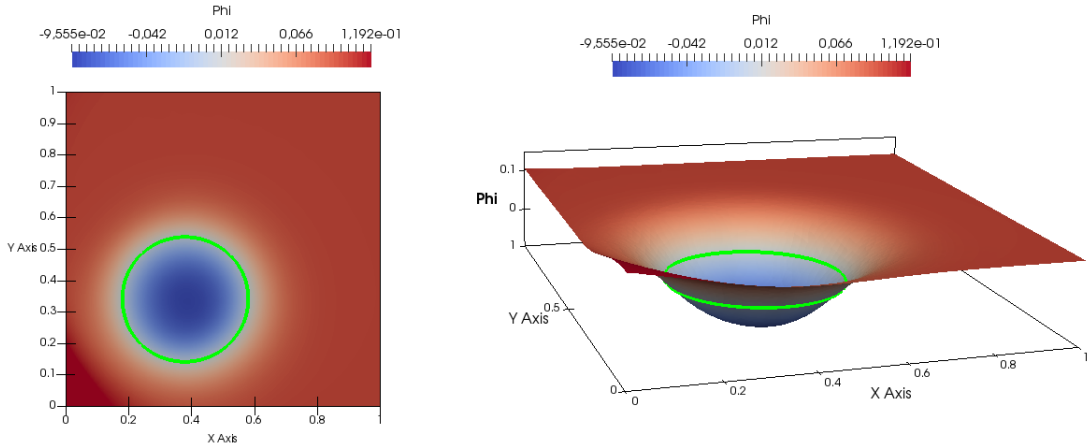

FIGURE 3.3 – Level-set definition - green circle representing the interface of the filtered level-set field ϕ

tering step does not change the convection of the level-set but also does not require additional computation time since it is a mathematical function. The filter is applied only at the initial time

or after a step of direct reinitialisation (see below). Subsequently, the filtered level-set function is transported by using Eq. 3.17, which remains unchanged.

3.1.5 Reinitialisation

The initial property of the level-set function, to be a distance function or a *tanh* function, is not automatically preserved during the resolution of the transport equation, since the convection velocity may be anything. More specifically, the jump of material parameters at the interface induces a discontinuity in the velocity gradient, which leads to strong gradients of the level-set function that develop around the interface. Thus, the weight of the convective term $\boldsymbol{v} \cdot \nabla \phi$ increases in the transport equation 3.4, and the SUPG stabilisation may become insufficient at some point. The property of being a distance function is expressed by $\|\boldsymbol{\phi}\| = 1$. Thus, by regularly reconstructing the level-set to respect this property without changing the position of the zero iso-surface, the gradient is kept under control. This is called the reinitialisation step. Two approaches are possible: direct reinitialisation, implemented in this thesis, or an iterative method based on the Hamilton-Jacobi equation [26]. At the end of this section we will see how to extend these techniques to *tanh* cases.

Direct reinitialisation

The direct reinitialisation is a promising route made possible by an increase of computational power. This technique rebuilds the level-set function by computing the projection of each mesh node on the interface *i.e.* the shortest distance to the interface (see node_0 in Fig. 3.4). It also guarantees optimal accuracy compared to others reinitialisation methods such as the Hamilton-Jacobi's. The actual barrier is the computational cost, which can be overcome by using a $k-d$imensional tree for partitioning the space and improve the search of the projection [193]. Additionally, the domain in which the direct reinitialisation is performed can be restricted to a narrow region around the interface, especially in the case of a filtered level-set [158]. In the present work, the direct reinitialisation is simply benefiting from multi-threading strategy since the step of finding the shortest distance to the interface is independent from node to node.
One shortcoming of this approach comes for nodes for which the shortest distance is located outside the domain (as illustrated in Fig. 3.4). This case occurs for a curved surface close to a

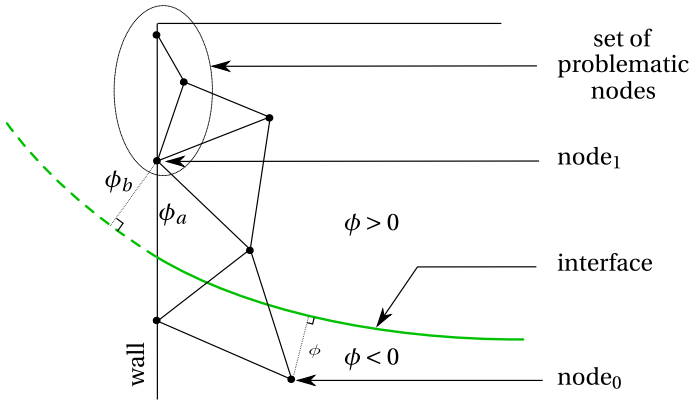

FIGURE 3.4 – Direct reinitialisation - problematic set of nodes

mesh boundary, like a meniscus against a wall in our case. In Fig. 3.4, node_0 may be correctly

reinitialised without changing the interface position. Node_1 has a value ϕ_b before the reinitialisation giving information on the interface outside the domain. After the reinitialisation, the shortest distance to the interface is ϕ_a changing the interface position. In that case, node_1 is not the only node without a projection located on the interface but all the nodes circled are hard to reinitialised. For those points, after the direct reinitialisation, the shortest distance is the distance to the point on the interface against the wall whereas their projections should be located outside the domain by a continuous extension of the interface outside the computational domain. This unsolved problem motivates to choose a Hamilton-Jacobi reinitialisation if not all the points have their projections on the interface within the computational domain and to choose a direct reinitialisation otherwise. Although the efficiency of the multi-threading in two dimensions is verified, this improvement falls short in three dimensions to tackle the computational cost issue.

Principle of the Hamilton-Jacobi reinitialisation

To recover the mathematical property of a unitary gradient $\|\nabla\cdot\phi\| = 1$, the non linear Hamilton-Jacobi equation can be solved [26]

$$\begin{cases} \dfrac{\partial\varphi}{\partial\tau} + sign(\varphi_0)(\|\nabla\varphi\| - 1) = 0 \\ \varphi_0 = \varphi(x, \tau = 0) = \phi(x, t) \end{cases} \tag{3.19}$$

until reaching the steady state, with τ a fictive time and $sign(\phi)$ a sign function that could be defined as

$$sign(\varphi_0) = \begin{cases} 1 & \text{if} \quad \varphi_0 > 0 \\ 0 & \text{if} \quad \varphi_0 = 0 \\ -1 & \text{if} \quad \varphi_0 < 0 \end{cases} \tag{3.20}$$

First of all, it should be noted that when the steady-state is reached $\partial\varphi/\partial\tau = 0$ and consequently $\|\nabla\varphi\| = 1$ as it can be seen in Eq. 3.19. The variation in fictitious time enables to fix the initial state from which computing a unit gradient. This term allows to spanned the complexity of recovering a unit gradient through virtual time steps. Secondly, the interface does not move during the reinitialisation. Indeed, the signed function is null at the interface at the position where $\phi = 0$. This property implies that the variation during the fictitious time is zero $\frac{\partial\varphi}{\partial\tau} = 0$ at the interface. That is why, the interface (the zero iso-surface) does not move during the fictitious reinitialisation time steps.

From a numerical point of view, it is preferable to have a continuous sign function. The first one comes from Sussman *et al.* [204] and reads

$$sign_1(\varphi_0) = \frac{\varphi_0}{\sqrt{\varphi_0^2 + h_e^2}} \tag{3.21}$$

According to Basset [26] the $sign_1$ function works well if ϕ is not too flat or too abrupt close to the interface. To address this issue, another definition from [169] could be used

$$sign_2(\varphi_0) = \frac{\varphi_0}{\sqrt{\varphi_0^2 + ||\nabla\varphi_0||^2 h_e^2}} \tag{3.22}$$

The last sign function has a better conservation of the initial interface [211]. In fact for a steep gradient, $sign_2$ is smaller than $sign_1$ and it will decrease the reinitialisation velocity coming from the linearisation detailed in the following equation. Introducing the convective velocity as $\boldsymbol{v}_r = sign(\varphi_0)\frac{\nabla\varphi}{||\nabla\varphi||}$ and $F = sign(\varphi_0)$ makes possible to write the Hamilton-Jacobi equation 3.19 under the form

$$\frac{\partial\varphi}{\partial\tau}\Big|_{n+1} + \boldsymbol{v}_r(\varphi)\cdot\nabla\varphi\Big|_{n+1} = F \tag{3.23}$$

where the symbol $\bullet\big|_{n+1}$ represents the quantity computed at fictitious time τ^{n+1}. The convective term is still highly non-linear since the reinitialisation velocity depends on the reinitialised function. A fixed-point method is used to remove the non-linearity from the implicit convective term and, it comes

$$\boldsymbol{v}_r(\varphi^{n+1,it+1})\cdot\nabla\varphi^{n+1,it+1} \approx \boldsymbol{v}_r(\varphi^{n+1,it})\cdot\nabla\varphi^{n+1,it+1} \tag{3.24}$$

with it the iteration number. The Hamilton-Jacobi is solved only to recover the sign distance function at static equilibrium. Therefore, at each time step, an exact solution does not need to be computed. More precisely, iterations can be mixed with time increments in order to optimize computational effort. Using this approach, the reinitialisation velocity becomes $\boldsymbol{v}_r(\varphi^{n+1,it}) \approx \boldsymbol{v}_r(\varphi^n)$ removing completely the iterative steps. The final equation to solve after linearisation is

$$\frac{\partial\varphi}{\partial\tau}\Big|_{n+1} + \boldsymbol{v}_r(\varphi^n)\cdot\nabla\varphi^{n+1} = F \tag{3.25}$$

At steady state, $\varphi^{n+1} \approx \varphi^n$ and thus the unit gradient property will be recovered. The reinitialisation equation has the same form than the convection equation of the level-set Eq. 3.4. Hence, the SUPG stabilisation is exactly the same.

Note that by linearisation, the initial problem is rewritten as a convection equation without boundary condition on the incoming flow. One may find examples when the reinitialisation velocity is going inside the domain. The 'set of problematic nodes' in Fig. 3.4 has an inflow for instance. This is also precisely where the direct reinitialisation has problematic nodes. However, from experience, it seems that the calculation succeeds without the condition on the inflow boundary for the Hamilton-Jacobi equation 3.25. One explanation is that the SUPG stabilisation brings diffusion and changes slightly but enough the form of the equation. The SUPG stabilisation transforms the first order Hamilton-Jacobi equation into a second order equation. Finally, for the sake of saving computational time, the reinitialisation step is computed 3 times with the virtual time step value has to same value than the mesh size. In general, this is sufficient to reinitialise the level-set through a narrow-band.

Reinitialisation when using filtered level-set

When applying the *tanh* filter (see Sec. 3.1.4), the convection step remains unchanged. However, the property to be recovered is no longer the unit gradient property, but:

$$\|\nabla\breve{\varphi}\| = 1 - \left(\frac{\breve{\varphi}}{\breve{e}}\right)^2.$$

This property comes from the fact that $tanh'(x) = 1 - tanh^2(x)$. Consequently, the Hamilton-Jacobi system (Eq. 3.19) is replaced by

$$\begin{cases} \dfrac{\partial \breve{\varphi}}{\partial \tau} + sign(\breve{\varphi}_0)\left(\|\nabla \breve{\varphi}\| - \left(1 - \left(\dfrac{\breve{\varphi}}{\breve{e}}\right)^2\right)\right) = 0 \\ \breve{\varphi}_0 = \breve{\varphi}(x, \tau = 0) = \breve{\phi}(x, t) \end{cases} . \tag{3.26}$$

As for the reinitialisation without filtering step, the equation can be linearised and rewritten under the form of a convection equation

$$\frac{\partial \breve{\varphi}^{n+1}}{\partial \tau} + \breve{\boldsymbol{v}}_r(\breve{\varphi}^n) \cdot \nabla \breve{\varphi}^{n+1} = \breve{F}(\breve{\varphi}^n) \tag{3.27}$$

with $\breve{\boldsymbol{v}}_r(\breve{\varphi}^n) = sign(\breve{\varphi}_0)\dfrac{\nabla \breve{\varphi}^n}{\|\nabla \breve{\varphi}^n\|}$ and $\breve{F}(\breve{\varphi}^n) = sign(\breve{\varphi}_0)\left(1 - \left(\dfrac{\breve{\varphi}^n}{\breve{e}}\right)^2\right)$. Away from the interface, in the filtered region, the reinitialised velocity is set to 0 to avoid any singularity. Therefore, the level-set field will not change in the filtered region.

3.1.6 Inflow condition

The function $g(\boldsymbol{x}, t)$ represents the inflow boundary condition. In one case, the value may be chosen as the previous time value, reading $g(\boldsymbol{x}, t) = \phi^n$, with ϕ^n the value previous value of ϕ at the inflow boundary. This condition is not consistent with the signed distance property. Actually, a constant value of the level-set is placed at the inflow boundary and then convected. Therefore, after some time increments, the level-set has the same constant value near the inflow boundary. However, this will not change the interface position if the interface is far from the inflow boundary. In the second case when using a filtering strategy, the inflow boundary value $g(\boldsymbol{x}, t)$ is set as the value in the filtered region. This case works well, if the initial interface is chosen cautiously. The initial interface has to placed further away than the filter width from the inflow boundary.

3.2 Error bound

Discretisation error

According to literature [48] the error for a *level-set* convection, with a Crank-Nicolson scheme and SUPG stabilisation is bounded by:

$$\|\phi_h^n - \phi(\bullet, t_n)\|_{\mathscr{L}^2} \leq c\, t_n \left(h^{\frac{3}{2}} + \Delta t^2\right) + \epsilon_0 \tag{3.28}$$

with c a constant depending on the smoothness of ϕ and ϵ_0 the initial discretisation error. For a fixed time step and mesh size, the error estimate of the level-set is growing with time. A special attention should be paid to the sum of errors coming from errors from time step and mesh size, since they give the linear pace at which the error estimate growths. Therefore, these two discretisation errors (in space and time) should be small enough to keep the bounded error on the level-set reasonable when running long simulations. Choosing independently the time step

and mesh size may rise the weight of one source of error compared to the other and will not minimise the error estimate. Also, in the case of an error mainly conditioned by the time step, a refinement strategy on the mesh size would be vain. Still not mandatory, the best practical choice would be to equilibrate error sources and then take $\Delta t \sim h^{\frac{3}{4}}$. A crucial feature using this relation is that a mesh refinement should always be associated with a decreasing time step. But, this is generally not applicable in practice. Most of the time, the error is driven by the mesh size, and a refinement is used in order to improve the result without changing the time step.

Volume loss

It is well known that conserving the volume with the level-set is challenging [129]. The example presented in Fig. 3.5 transforms a square interface into a circle in a domain Ω with 0 velocity on the boundary of the domain. Taking the volume integral of the level-set transport equation (Eq.

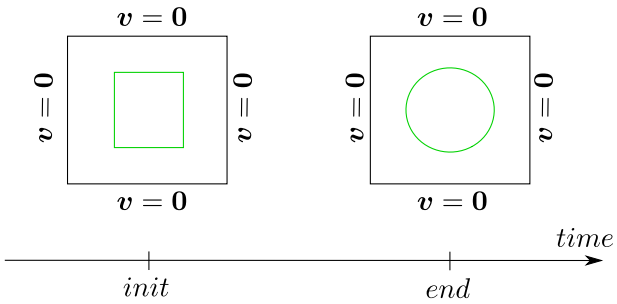

FIGURE 3.5 – Volume loss - evolving interface from a square to a circle

3.4), it comes, in the case of an incompressible fluid :

$$\begin{aligned} &\int_\Omega \frac{\partial \phi}{\partial t}\, dV + \int_\Omega \boldsymbol{v} \cdot \nabla \phi \, dV = 0 \\ &\implies \frac{d}{dt} \int_\Omega \phi(\boldsymbol{x}, t)\, dV = 0 \end{aligned} \tag{3.29}$$

with impermeable boundaries and a fixed domain. The volume of each phase should be constant in time, implying that the volume variation should be zero. As seen with Eq. 3.29, the conservation of volume is verified as long as $\phi(\boldsymbol{x}, t)$ is constant in each phase, which is the case for the Volume of Fluid (VoF) method but not for the level-set method. One can verify that the conservation of the quantity $\int_\Omega \phi \, dV$ between a square and a circle does not imply a conservation of volume. From the previous equation, it can be inferred that the filter around the interface tends to have a better volume conservation, since the method loses volume only within the bandwidth.

Even if the level-set does not strictly conserve the volume Reusken *et al.* [182] have shown that error on the volume is bounded by

$$|V - V_h| \leq c' t_n h \tag{3.30}$$

for linear approximation in space and a θ-method in time. Therefore, refining the mesh tends to improve the volume conservation.

3.3 Validation of level-set implementation

The level-set method has been implemented in the Zebulon [34] FE code. The first test case is shown to demonstrate the implementation validity and the limit of the method. The rotating circle permits to verify the volume of fluid lost during the computation.

3.3.1 Rotating and stretching circle - reinitialisation validation

This test corresponds to the rotation combined with the streching of a circle, and aims at discriminating between the reinitialisation strategies. The input velocity field is divergence free and has a zero value on the boundary of the domain $\Omega = [0,1] \times [0,1]$. It is defined by

$$\begin{cases} v_x = -2\sin^2(\pi x)\sin(\pi y)\cos(\pi y) \times (-1)^p \\ v_y = 2\sin^2(\pi y)\sin(\pi x)\cos(\pi x) \times (-1)^p \end{cases} \tag{3.31}$$

with $p = 0$ if $t \in [0,1]$, $p = 1$ else (*cf.* background velocity field in Fig. 3.6 (B)). The circle is rotated and stretched in the clockwise direction during the first half of the simulation and counter-clockwise in the second half. At the end at $t = 2$ the interface should come back to the initial position. A visual assessment of the circularity at the end of the simulation will give a first hint on how the reinitialisation behaves.

Parameters	Value
Mesh size	0.02
Unstructured mesh	50 × 50
Center of circle	(0.5,0.7)
Circle radius	0.2
Final time	2
Number of time increments	200
Time step	0.01
θ for theta method	0.5
Number of reinitialisation steps	3
Reinitialisation time steps	0.02
Frequency direct reinitialisation	1

TABLE 3.1 – Rotating and stretching circle - model entries.

The model entries are given in the Tab. 3.1. No filter is used in that case to discriminate more easily the effect of the reinitialisation. Fig. 3.6 (A) shows the interface shape at the first half of the computation, at $t = 1$. Both reinitialisation methods give a similar result with a longer tail than without reinitialisation. In Fig. 3.6 (B) the red circle represents the theoretical position of the interface at the end of the simulation, at $t = 2$. The position of the final interface has a more circular shape with the direct reinitialisation compared to the Hamilton-Jacobi's. Whereas, the interface without reinitialisation is the closest to the theoretical interface. This highlights the trade-off between the accuracy on the position of the interface at the final time step and the robustness of the computation by keeping the norm of the gradient of the level-set as close as possible to 1. Norms of the level-set gradients are plotted in Fig. 3.7. The level-set gradient has

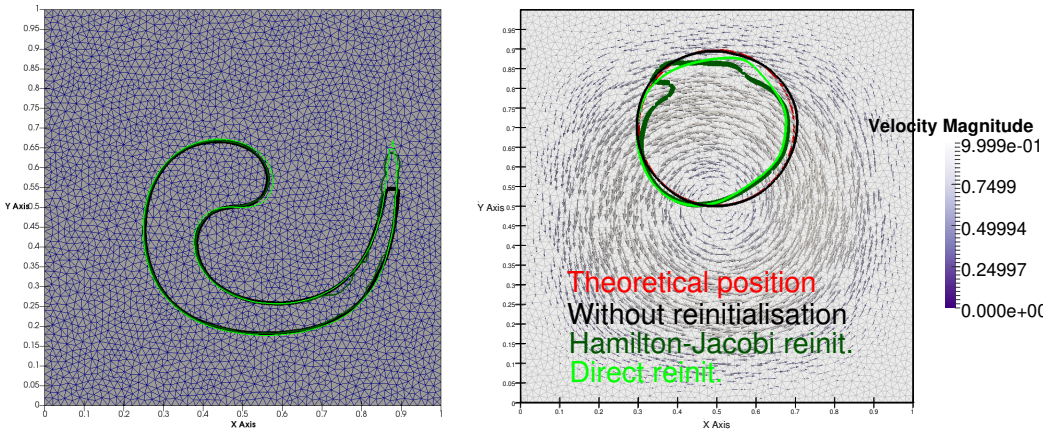

(A) t=1 Half time (B) t=2 Final position

FIGURE 3.6 – Rotating and stretching circle for unfiltered level-set - position of the interface

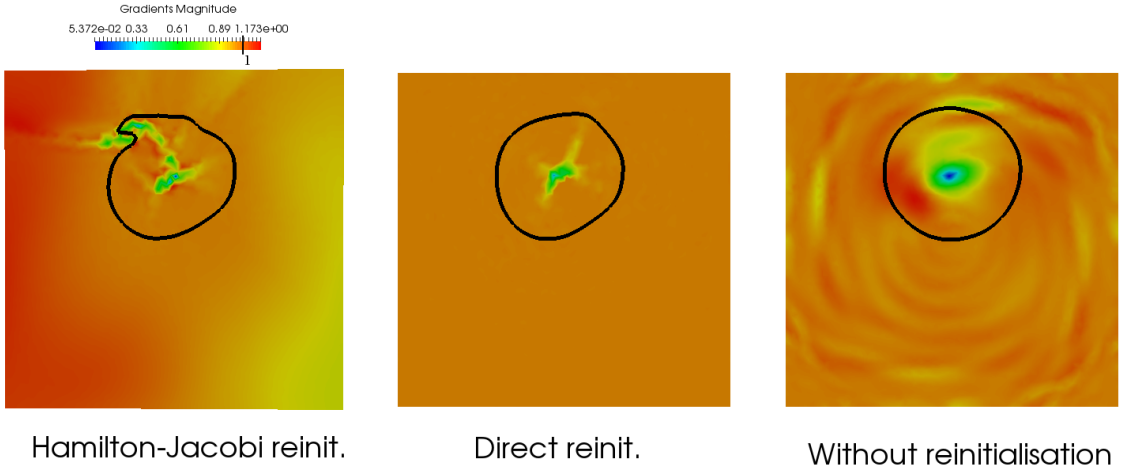

FIGURE 3.7 – Rotating and stretching circle - Norm of the unfiltered level-set gradient at the end of the computation with different reinitialisation strategy.

a singular point at the centre of the circle as shown in each subplot. This particular point does not depend on the reinitialisation strategy but is due to the particular shape of the interface. Besides, the norm of the level-set is more regular when using a reinitialisation strategy as expected. This feature for the level-set will bring robustness since issues on the interface crumbling are directly related to an unphysical local strong convection. The Hamilton-Jacobi reinitialisation is not as good as the direct reinitialisation since only three increments are used for the reinitialisation which tends to be reinitialised only around the interface. But increasing the number of reinitialisation would lead to recover the same result that the direct reinitialisation. Therefore, as expected for this case with only three increments, the direct reintialisation gives better results compared to Hamilton-Jacobi. The improvement comes at the price of a higher computational cost and only in cases where all the projections are well defined in the computational domain (as it was discussed in 3.1.5).

Simulation are run on a Intel(R) Core(TM) i5-4590 processor with a speed of 3302 Hz on one thread. It takes 47.3 s in the case without reinitialisation, 126 s with direct reinitialisation and 155.7 s with Hamilton-Jacobi's method.

Finally, in order to conserve a unit gradient, a reinitialisation strategy should be used during the

convection of the level-set. In a similar case where the shortest distance is inside the computation domain, the direct reintialisation performs well in 2D compared to the Hamilton-Jacobi. However, for interfaces intersecting domain boundary and in 3D, Hamilton-Jacobi may be used over the direct reinitialisation.

3.3.2 Rotation of a circle - volume loss

This cases studies the rotation of a circle around the point $(0.5, 0.5)$ in a domaine $\Omega = [0,1] \times [0,1]$, without deformation [45],[26]. The corresponding velocity, which of course if divergence-free, is expressed as:

$$\begin{cases} v_x(x,y) = -\frac{\pi}{2}(y - \frac{1}{2}) \\ v_y(x,y) = \frac{\pi}{2}(x - \frac{1}{2}). \end{cases} \tag{3.32}$$

With this velocity, the period of rotation is $T = 4\,s$. In this case, it is intended to evaluate the volume loss depending on the average mesh size which successively takes the values $h_e = 0.1, 0.04, 0.02, 0.01$ with an unstructured mesh and the time step which successively takes the values $\Delta t = 0.28, 0.23, 0.18, 0.14, 0.01, 0.02$. The other values are recalled in Tab. 3.2. Note that the final time corresponds to 4 complete rotations. In addition, no reinitialisation is made to discriminate only the influence of the mesh size and time step on the volume loss. The volume

Parameters	Value
Mesh size	[0.01;0.1]
Unstructured mesh	True
Center of circle	(0.5,0.7)
Circle radius	0.2
Final time	16
Number of time increments	[57,1600]
Time step	[0.01, 0.28]
θ for theta method	0.5
Reinitialisation	False

TABLE 3.2 – Rotation of a circle and volume loss - model entries.

lost by the level-set during the convection step is plotted over time in Fig. 3.8. The first four thick curves (blue, red, green and black) describe the volume loss for one fixed time step using four mesh refinements. More specifically, for a time step of $\Delta t = 0.02$, the time discretisation error is proportional to $\Delta t^2 = 4 \times 10^{-4}$ according to Eq. 3.28. For the smallest mesh size, $h_e = 0.01$, the error due to the space discretisation is proportional to the mesh size to the power $3/2$, $h_e^{\frac{3}{2}} = 10^{-3}$. Therefore, for the first four curves, the error is mainly dominated by the space discretisation error. That is why four mesh sizes have been considered. As it can be seen in Fig. 3.8 each mesh refinement leads to a better volume conservation. So far, it shows numerically that if the error is mainly due to the space discretisation then refining the mesh size tends to improve the volume conservation.

Now, reciprocally, if the error is mainly due to the mesh size then refining the time step is somehow ineffective. On Fig. 3.8, the blue curves with markers prove that refining the time step does not improve significantly the volume conservation when the error comes from the spatial discretisation. As shown with the closeup on the centre of the figure, a two times smaller time step,

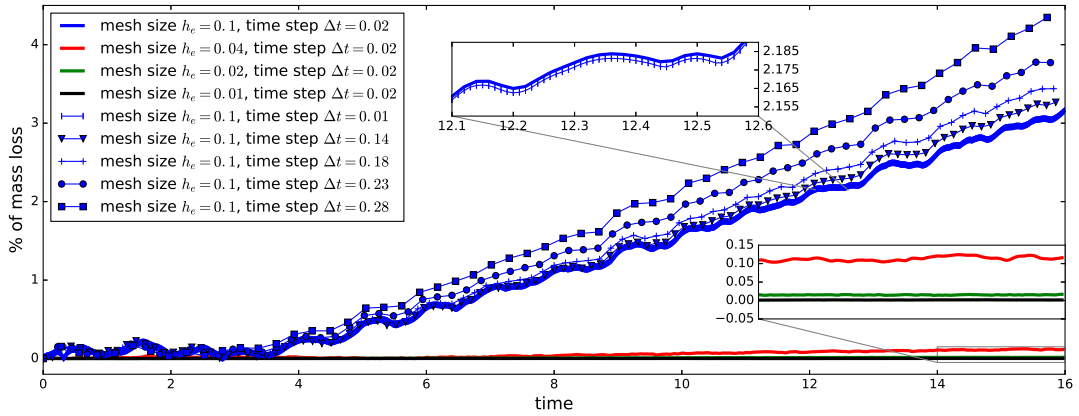

FIGURE 3.8 – Rotation circle - Variation of volume during the simulation with variation of mesh size and time step

does not improve significantly the solution. Among the other curves, the particular blue curve is the one with cross markers and a time step $\Delta t = 0.18$. This time step value with a mesh size of $h_e = 0.1$ should give a well-balanced error between spacial and time discretisation error.
As expected the central close-up shows that refining the time step further does not improve significantly the conservation of volume. The time step is divided by two from $\Delta t = 0.02$ to $\Delta t = 0.01$ and still the volume continue to be lost since the error will come mainly from the space discretisation. This concludes the numerical assessment of the discussion on mesh size and time step refinements. Besides, let's notice that the volume loss is linear in time after $t = 4$ and for the coarser grid does not exceed more than 5% of the initial value. It has already been shown that the Crank-Nicholson scheme is more conservative than the implicit Euler scheme [3]. This explains that even for a coarse grid, the volume lost during the simulation is acceptable.
In conclusion, the non naturally conservative level-set characteristic can be overcome by a thorough control of the time step and mesh size. A joined refinement in space and time converges to the solution.

3.3.3 Zalesak slotted disk - filter influence

The Zalesak slotted disk [230] is investigated in order to assess the effect of the filter on the volume loss. Recalling that the level-set method does not intrinsically conserve the mass due to its signed distance function, the filter may help to remove this constraint far from the interface by taking a constant value.
The Zalesak circle is initialised using topological operators mixing distance functions from lines and circle implemented in our Z-set environment. The circle is convected using the velocity field given in the previous case using Eq. 3.32 and the parameters for the simulation are summarised in the Tab. 3.3 and Fig. 3.9.

Parameters	Value
Unstructured mesh	100 x 100
Centre of circle	(0.5,0.7)
Circle radius	0.175
Final time	4
Number of time increments	40
θ for theta method	0.5
Reinitialisation	False
Filtering function	tanh

TABLE 3.3 – Zalesak slotted disk - model entries

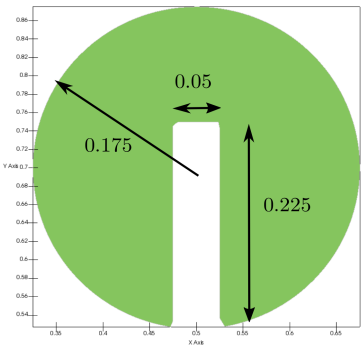

FIGURE 3.9 – Zalesak slotted disk - geometrical entries

In Fig. 3.10 the variation of volume is plotted over time for different values of filter width. Without filter, the blue curve, the variation of volume is the biggest whereas for every filter width value the level-set will be more conservative. A filter width three times the mesh size appears to be a good empirical practice. Following this rule of thumb, the best practice filter width value is 0.03 (the red curve with triangles). As it can be seen in the figure, this value for the level-set width yields the smallest variation of volume at the end of the simulation. Therefore, according to this test, the ability to improve mass conservation should be added to the advantages of the filter. Among the other advantages, the filter is able to remove convection difficulties, such as strong gradient, outside a narrow region around the interface. It also avoids specifying unknown boundary values on the boundary with an inflow because it takes a constant value in the filter region. Finally, it helps to prevent mass loss.

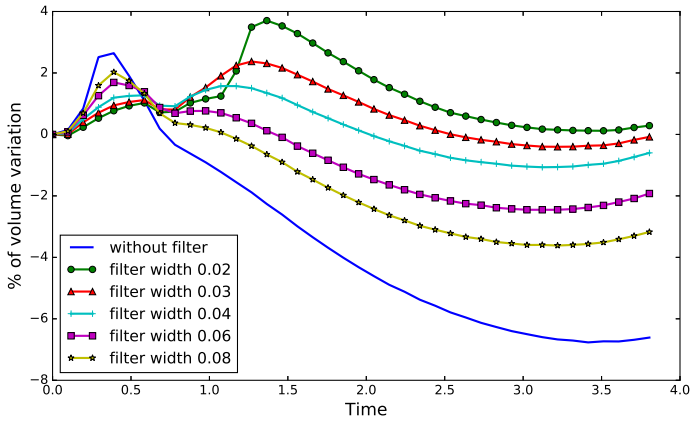

FIGURE 3.10 – Zalesak circle - Variation of volume during the simulation with variation of filter width.

3.3.4 Conclusion

Thanks to the three cases of level-set convection problems, the influence of the reinitialisation, the mesh size, time step and filter have been investigated. The main disadvantage of the level-set is that the method does not conserve intrinsically the volume since it is not a equation of conservation. However, it has been shown that mass/volume loss may be minimised under

certain conditions. The advantages of the level-set method will be exploited in the following paragraphs to precisely represent the interface.

3.4 Quadrature rules and interfaces

Naturally, the level-set sign gives the information on the liquid phase location in the domain. In the case of surface tension force, it is also required to compute a surface integral which may not coincide with the faces of the elements. The surface described by the level-set function separates two different fluids, here resin and air, distinguished with their own material properties:

$$\begin{aligned} \mu(\boldsymbol{x}) &= \mu_V H_{eaviside}(\phi(\boldsymbol{x})) + \mu_L \left(1 - H_{eaviside}(\phi(\boldsymbol{x}))\right) \\ \rho(\boldsymbol{x}) &= \rho_V H_{eaviside}(\phi(\boldsymbol{x})) + \rho_L \left(1 - H_{eaviside}(\phi(\boldsymbol{x}))\right) \end{aligned} \tag{3.33}$$

with $H_{eaviside}$ a transition function to define. This interface passes through some elements of the mesh, but does not coincide with a set of faces or edges. At the numerical level, on the one hand, it is necessary to manage the transition between the two media, (*e.g.* a transition of material properties). On the other hand to evaluate the integrals of the FE problem defined on the interface, such as the integral related to surface tension phenomena. For both issues, which are ideally connected, two strategies are possible: either consider a Continuum Stress Force (CSF) method for a smooth transition (smooth $H_{eaviside}$) or a Surface Local Reconstruction (SLR) method with a sharp transition ($H_{eaviside} = 0$ or 1).

3.4.1 Continuum Stress Force

The main idea is to consider a smooth variation of parameters across the interface. The Continuum Stress Force (CFS) [40] is widely used ([166], [179], [96]) and easy to implement. The performances of this method largely depend on the smoothed Heaviside function $H_{eaviside}$, used to perform the transition. Two functions are usually used [166]

$$H_{lin}(\phi,\epsilon) = \begin{cases} 0 & if\ \phi < -\epsilon \\ \frac{1}{2}\left(1 + \frac{\phi}{\epsilon}\right) & if\ -\epsilon < \phi < \epsilon \\ 1 & if\ \phi > \epsilon \end{cases} \tag{3.34}$$

$$H_{sin}(\phi,\epsilon) = \begin{cases} 0 & if\ \phi < -\epsilon \\ \frac{1}{2}\left(1 + \frac{\phi}{\epsilon} + \frac{1}{\pi}\sin\frac{\pi\phi}{\epsilon}\right) & if\ -\epsilon < \phi < \epsilon \\ 1 & if\ \phi > \epsilon \end{cases} \tag{3.35}$$

where $\epsilon \approx 2h$. A representation is given in Fig. 3.11.

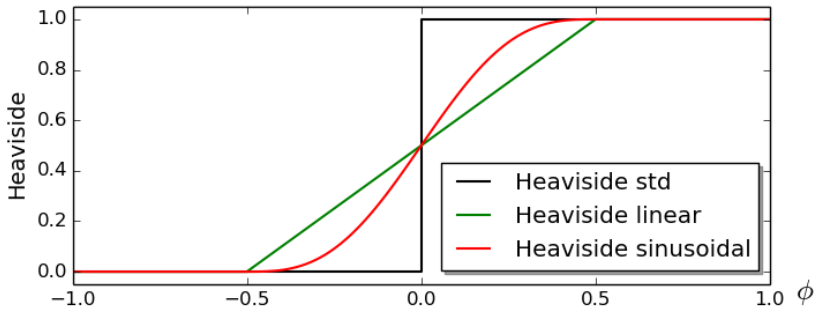

FIGURE 3.11 – Representation of Heaviside and smoothed Heaviside functions with $\epsilon = 0.5$.

The sinusoidal Heaviside has the advantage to avoid a singularity in the derivatives at the two junctions, $\phi = -\epsilon$ and $\phi = \epsilon$, giving better results [225] due to the smoother transition. The width of the interface should be large enough for a smooth transition of parameters such as density or viscosity. But the transition region should not be too large so that it remains a transition zone, *i.e.* with no physical existence. The CSF method, accounting for changing parameters, introduces another parameter ϵ into the numerical simulation, a sort of interface width.
A Dirac function is defined as the derivative of the Heaviside function $\delta(\phi) = \frac{dH}{d\phi}$. It is known that a surface integral can be transformed into a volume integral as long as the condition that the sum of Dirac is unitary: $\int_\Omega \frac{dH_{eaviside}}{d\phi} dV = 1$ is verified. Then it is possible to transform the integral on the interface Γ in the following way

$$\int_\Gamma f\, ds \approx \int_V f\delta(\phi) dV \tag{3.36}$$

with $\delta(\phi) = \frac{dH_{eaviside}}{d\phi}$ a regularised Dirac function and, in the specific case of H_{sin}

$$\delta(\phi) = \begin{cases} \frac{1}{2\epsilon}\left(1 + \cos\frac{\pi\phi}{\epsilon}\right) & \text{if} \quad \phi \in [-\epsilon, \epsilon] \\ 0 & \text{else.} \end{cases} \tag{3.37}$$

Therefore, the surface integral can be easily computed when turned into a volume integral. This strategy may be efficient in the case of a local refinement around the interface [105], since in this case the width of the smooth Heaviside is is reduced due to the element size which is down-sized to capture the interface. Furthermore, this strategy does not take into account the advantage to know the position of the interface with the level-set method. This CSF method can consequently be a solution in the case of a VoF method where the interface position is not defined in an element. On the contrary, the level-set method, used here for the various advantages exposed previously, allows an accurate representation of the interface inside an element. Therefore, a Surface Local Reconstruction integration method is preferred in this work to accurately integrate on the moving interface Γ_{LV}.

3.4.2 Surface Local Reconstruction

The Surface Local Reconstruction (SLR) [175] is another technique which aims at computing exactly each quantity across an interface, but also surface integrals. The Heaviside function in

the SLR case is stated as the standard Heaviside

$$H_{SLR}(\phi) = \begin{cases} 0 & if\ \phi < 0 \\ 1 & if\ \phi > 0 \end{cases} \tag{3.38}$$

form the level-set function. Since the position of the interface is known, one would integrate exactly the contribution of density and viscosity on each side of the interface by changing the quadrature rule, as represented in Fig. 3.12. For example in two dimensions, the element is sub-divided into three elements in order to add further integration points (or Gauss points). No nodes are added contrary to X-FEM but only integration points. Thus, the size of the stiffness matrix remains unchanged. Using these added integration points, the term involving the fluid parameter, such as the term of virtual power of the internal actions in Navier-Stokes and Stokes equations (Eq. 2.3), is integrated without smoothing the interface in the following way

$$\int_{elem} \mu(\boldsymbol{x})\dot{\boldsymbol{\epsilon}}(\boldsymbol{v}) : \dot{\boldsymbol{\epsilon}}(\boldsymbol{w})\, dV = \int_{blue} \mu_{blue}\dot{\boldsymbol{\epsilon}}(\boldsymbol{v}) : \dot{\boldsymbol{\epsilon}}(\boldsymbol{w})\, dV + \int_{black} \mu_{black}\dot{\boldsymbol{\epsilon}}(\boldsymbol{v}) : \dot{\boldsymbol{\epsilon}}(\boldsymbol{w})\, dV \tag{3.39}$$

where the color blue and black refers to Fig 3.12 as the part under and above the interface.

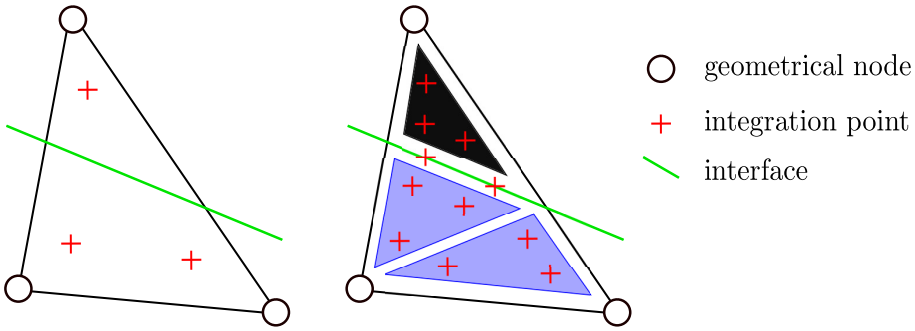

a) P1 element b) P1 element with SLR

FIGURE 3.12 – Intersection between the interface Γ and an element in 2D

Furthermore, to compute a surface integral, one or more integrations points may be added on the interface depending on the order of interpolation. Unlike CSF case, the surface integral does not have to be transformed into a volume integral. Thus, the SLR method has the advantage to be more accurate than CSF method. In addition, SLR method does not require to choose any tunable numerical parameter contrary to CSF method.
Each element cut by the interface is split depending on how it intersects with the interface. The most common case in 2D is the one described in Fig. 3.12. When the element is fully cut by the interface, three integration points are added on the top remaining triangle and the quadrilateral is split into two triangles with three integration points each. In the case of an element cut on the edge, integration points are added on the interface without sub-dividing the element. And in the last case of an element cut at a node, nothing is changed. In three dimensions, the distinction between the cases has to be broadened. Its implementation becomes somehow cumbersome but it is robust, and with the same complexity level as in 2D [36].

Conclusion

In the case of numerical simulation of bi-fluid flow, three interfaces have to be represented. Because only the fluid equations are solved in the domain, boundaries between the solid and the two fluids are represented and captured by mesh boundaries (*i.e.* Γ_{SL} and Γ_{SV}). The third interface between the two fluids Γ_{LV} is captured with a level-set method. This method has the advantage to give a precise description of the fluid front and therefore to be able to integrate exactly physical parameters and surface tension forces. Even though the level-set is not naturally conservative, the method converges when refining the time step and mesh size.
The input of the level-set problem is the convective velocity which is the velocity from the fluid problem, and its output is the position of the interface. The next chapter will investigate how to couple fluid and level-set solvers to numerically take into account capillarity effects.

Résumé en Français : Méthode *level-set*

La description de l'interface mobile entre la phase liquide et la phase vapeur se fait par une méthode *level-set* et résolution d'une équation de transport. Cette résolution se base aussi sur des éléments finis linéaires, stabilisés par la méthode SUPG. Plusieurs méthodes sont évaluées pour maîtriser, voire réduire, la dégradation de l'interface ainsi que les pertes de volume lors de l'étape de transport. Un raffinement conjoint des pas de temps et d'espace permet de maîtriser l'erreur numérique et son accumulation lors des incréments en temps. Tout comme la stratégie de réinitialisation utilisée, le filtre permettant d'avoir une fonction leve-set quasiment constante en dehors d'un certain voisinage autour de l'interface, améliore encore la robustesse du calcul. L'ensemble de ces méthodes participe à la précision de la représentation de l'interface liquide/gaz qui est un point crucial pour ensuite y appliquer la contrainte associée à la tension superficielle. À cet effet, chaque élément du maillage traversé par l'interface bénéficie d'un enrichissement de l'intégration par un découpage en sous-éléments. Ceci permet d'intégrer exactement les termes volumiques de l'équation de la mécanique des fluides, mais aussi de pouvoir calculer numériquement le terme décrivant la tension de surface sur l'interface décrite par la *level-set* ainsi localement reconstruite.

Chapter 4

Numerical strategy for capillary action

Contents

Introduction

After presenting a numerical strategy for solving fluid mechanics equations and an interface capturing method, this chapter presents the different key points for integrating capillary effects in numerical simulation at the fluid-solid scale. First, pressure enrichment of the fluid problem is needed to accurately describe the underlying physics of surface tensions. Next, emphasis is placed on the global finite element formulation for surface tension and surface energies. Finally, the non-linearity intrinsic to the surface tension force will be treated by two coupling strategies between the level-set and the fluid solvers. The corresponding numerical methods have been implemented in Z-Set (Zebulon) [34] FE code, at Mines Saint-Etienne. Validation cases are described on an ongoing basis in this chapter.

4.1 Pressure and pressure gradient jumps

Multiphase flow exhibits strong and weak discontinuities, that is to say, a discontinuity of the field and a discontinuity of its gradient respectively. In a general setting, discontinuities may arise in highly advective compressible flows such as shock in air for example [61, 119, 170, 206]. But also, discontinuities of velocity or pressure may be induced by steep variation in material properties or by surface tension flows of immiscible fluids [56, 77, 102, 125, 152, 185]. Indeed, simply consider two columns of fluid one lying on top of the other. A contrast of densities leads to a jump of pressure gradient, since the momentum equation is written as $-\nabla p+\rho \boldsymbol{g} = 0$. A pressure jump may be also the result of the viscosity jump in a sheared flow or the surface tension on a curved surface. This is the classical Young-Laplace equation [130, 141]. A consequence of the continuous approximation of both pressure and velocity is that classical Galerkin-based FEs are not able to capture a discontinuous solution. Yet, it is of the utmost importance to correctly compute these jumps in the numerical simulation to carry out accurate numerical simulations.

Otherwise, continuous approximation of a discontinuous field generate oscillations in the solution, in particular in the velocity field which degenerates the front of fluid, regardless of the front capturing method.
Many strategies are proposed in the literature to overcome the inability of continuous Galerkin-based FEs to represent discontinuous fields. On one hand, in the case of a multiphase flow, a common method is based on smoothing the discontinuities over the interface [40, 223]. The material parameters are regularised in a region around the interface. Unfortunately, determining the width of the region and the form of this kind of mixture law is problem dependent [130] and requires local refinement of the mesh. On the other hand, some approaches attempt to properly capture the discontinuities instead of smoothing them. Discontinuity Capturing (DC) techniques have been used to compute high-speed flow where the stabilisation SUPG [61, 119, 206] or Galerkin Least-Squares (GLS) [118] are enhanced to capture the discontinuities by adding a discontinuity-capturing operator or discontinuous approximation. The X-FEM, for their part, consider additional nodes on the interface to accurately capture the interface by increasing the pressure space dimension [57, 151, 199]. However, the previous X-FEM method increases the size of the system and changes the mesh connectivity. Consequently, the matrix-graph is permanently changing in a time-dependent problem, reducing the efficiency of the solver. All this leads to a global increase in the computation cost. In addition, a special treatment has to be used to circumvent the problem of the ill-conditioning of the system [191]. A Discontinuous Galerkin (DG) formulation [1, 159, 232] is another way to deal with strong and weak discontinuities at the same time, with an interface corresponding to elements edges. However, like the X-FEM method, this requires a remeshing strategy for bi-fluid flows.
The strategy used and implemented during this work is the Enriched-FEM (E-FEM) [18], where the added degrees of freedom are condensed prior to the assembly of the global matrix. Therefore, the computational cost remains unchanged. Following Ausas *et al.* [20] [19], two degrees of freedom are added to capture pressure jumps. A second enrichment from Owen [165] permits to capture gradient pressure jumps, leading to add a third degree of freedom. In a nutshell, it requires two further shape functions to describe a jump over an interface but only one to capture a jump of gradient. Recently, an enrichment which does verify the partition of unity condition (PUC), recalling that the sum of the shape functions shall equate to 1, has been proposed [123]. This condition is not satisfied by the three degrees of freedom considered in this work. A second recent promising technique consists in endowing subscale space with discontinuous capturing feature in the variational multiscale method [146]. However, results presented in the paper [146] show better accuracy compared to most of discontinuous capturing techniques and the same order of convergence than for Ausas' method [19], considered here. Enforcing the weak and strong discontinuities at the sub-grid scale and not only at the FEM scale, may also help in imposing Neumann condition on an immersed boundary [171]. Actually, the stabilisation terms do not vanish on the interface since the interface cut the elements, in the case of an immersed boundary. Therefore, the Neumann condition is not automatically enforced but several methods may be used such as Nitsche's method [228]. Despite constant improvements in the field of discontinuities capturing, the three added degrees of freedom presented in the next sub-section give good results for the considered problems.

4.1.1 E-FEM and the three added degrees of freedom

The moving interface between liquid and vapour phases is described by a level-set function. Each element cut by the interface has to be enriched in order to capture weak and strong pressure discontinuities. Fig. 4.1 shows in red the enriched elements cut by the interface.

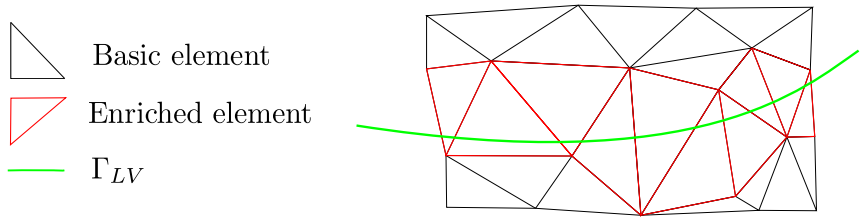

FIGURE 4.1 – Enriched-FEM - Enrichment strategy when elements are cut by the front of fluid

In every enriched element, two degrees of freedom are added to capture pressure jumps [19] and one for pressure gradient discontinuities. The pressure approximation in an enriched element reads

$$p_h = \sum_{I \in \mathscr{I}_e} N_e^I P_e^I + \sum_{J \in \mathscr{J}_e} M_e^J P_{enr}^J \quad \text{on } \Omega_e \tag{4.1}$$

where $\mathscr{I}_e$ is the set of indices accounting for the number of nodes. N_e^I and P_e^I are the shape function and nodal unknown associated with the node I. The set of indices $\mathscr{J}_e = \{0,1,2\}$ accounts for the three added degrees of freedom and P_{enr}^J the associated degrees of freedom. The general form of the system to solve for a cut element is written as

$$\begin{pmatrix} \boldsymbol{K}_{e/e} & \boldsymbol{K}_{e/enr} \\ \boldsymbol{K}_{enr/e} & \boldsymbol{K}_{enr/enr} \end{pmatrix} \begin{pmatrix} d\boldsymbol{U}_e \\ d\boldsymbol{P}_{enr} \end{pmatrix} = - \begin{pmatrix} \boldsymbol{R}_e \\ \boldsymbol{R}_{enr} \end{pmatrix} \tag{4.2}$$

where $\boldsymbol{K}_{e/e}$ is the stiffness matrix and $\boldsymbol{R}_e$ the residual for a standard element. The unknowns are incremental unknowns $d\boldsymbol{U}_e$ because a Newton algorithm is used. The shape functions for the additional degrees of freedom are drawn in Fig. 4.2. The geometrical elements are drawn in two dimensions with the vertices of the triangle represented by dark blue dots. The two first shape functions M_0 and M_1 [19] are required to capture a pressure jump. Actually, M_0 has a positive value on the left-hand side of the interface Γ_{LV} while M_1 is positive on the other side. Therefore, the pressure field may have a value on the left brought by M_0 and another value on the right corresponding to M_1 shape function. Finally, the M_2 shape function has a discontinuous slope across the interface Γ_{LV}. The three shape functions are easy to construct because they are based on the primitive shape functions, allowing a direct implementation.

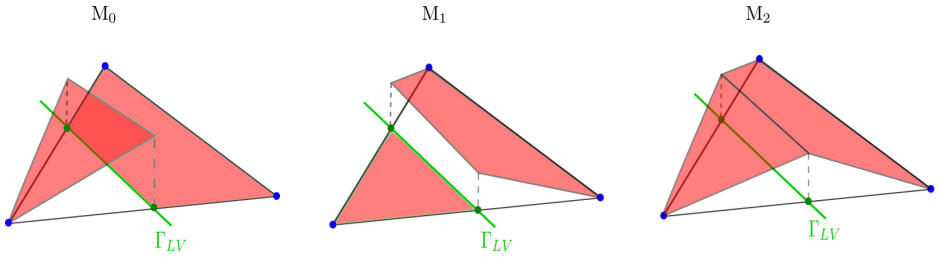

FIGURE 4.2 – Enriched-FEM - The shape functions corresponding to the three added degrees of freedom when element is cut by the interface, M_0 and M_1 are from [19], M_2 from [165]

To grasp the enrichment strategy, the sub-matrix term $\boldsymbol{K}_{enr/enr}$ is explicitly given. This sub-stiffness matrix is built from the term $\sum_{e=1}^{n_el} \int_{\Omega_e} \tau_v^{n+1,i} \nabla p_h^{n+1,i+1} \cdot \nabla q_h \, dV$ from the ASGS stabilisation (Eq. 2.20), only for elements cut by the interface

$$K^{IJ}_{enr/enr} = \int_{\Omega_e} \tau_v^{n+1,i} \nabla M_e^I \cdot \nabla M_e^J \, dV \tag{4.3}$$

with indexes $I, J \in \mathcal{J}_e$. This stabilisation term is the same for Stokes or Navier-Stokes flows. Therefore, enrichment is valid for both cases.

The three added shape functions have a zero value at vertices as it can be seen in Fig. 4.2. Thus, the enriched pressure is written as

$$d\boldsymbol{P}_{enr} = -\boldsymbol{K}^{-1}_{enr/enr} \left(\boldsymbol{K}_{enr/e} d\boldsymbol{U}_e - \boldsymbol{R}_{enr} \right). \tag{4.4}$$

The added degrees of freedom can be condensed in the element as follows

$$\left(\boldsymbol{K}_{e/e} - \boldsymbol{K}_{e/enr} \boldsymbol{K}^{-1}_{enr/enr} \boldsymbol{K}_{enr/e} \right) d\boldsymbol{U}_e = -\boldsymbol{R}_e + \boldsymbol{K}_{e/enr} \boldsymbol{K}^{-1}_{enr/enr} \boldsymbol{R}_{enr} \tag{4.5}$$

A special attention should be paid to the inversion of the matrix $\boldsymbol{K}_{enr/enr}$ for each element cut by the interface. The computational cost is not significant since $\boldsymbol{K}_{enr/enr}$ is only a 3×3 matrix but it may not always be invertible; it is not invertible when the interface Γ_{LV} is parallel to one of the element edges [19]. In that particular case, the shape functions $\mathrm{M}_0 + \mathrm{M}_1$ are proportional to M_2 and then M_0, M_1 and M_2 are no longer linearly independent. The solution from the cited article is to shift the diagonal entries of $\boldsymbol{K}_{enr/enr}$ by adding a small coefficient ϵ when this situation is detected during the computation, *i.e.* $\boldsymbol{K}_{enr/enr} \leftarrow \boldsymbol{K}_{enr/enr} + \epsilon \boldsymbol{I}$. In this work, the third added degree of freedom associated with the M_2 shape function is removed when the interface is parallel to one of the element faces or edges. In practice, this situation is not often detected during a general calculation.

4.1.2 Validation of the implementation

Three cases are investigated, represented in Fig. 4.3 to assess both enrichments to capture strong and weak discontinuities. The first case (A) in Fig. 4.3 presents a pressure jump, whereas the second case (B) has a pressure gradient jump. Finally, the last case (C) presents a jump of both pressure and pressure gradient which holds the same numerical complexity that capillary flow. The first case (a) has a pressure jump at the position $y = y_{jump} = 0.52$. The jump of normal stress across an interface is 0 without surface tension (see Eq. 1.31) and it writes:

$$[\boldsymbol{\sigma} \cdot \boldsymbol{n}] = -[p] \boldsymbol{I} + 2[\mu] \dot{\boldsymbol{\epsilon}}(\boldsymbol{v}) = 0 \tag{4.6}$$

The pressure jump is relative to shear stress at the interface with a change of viscosity. Therefore, a sheared flow presents a pressure jump at the interface when the viscosity is discontinuous. The viscosity ratio is five in this case but the accuracy holds for higher and more realistic ratios

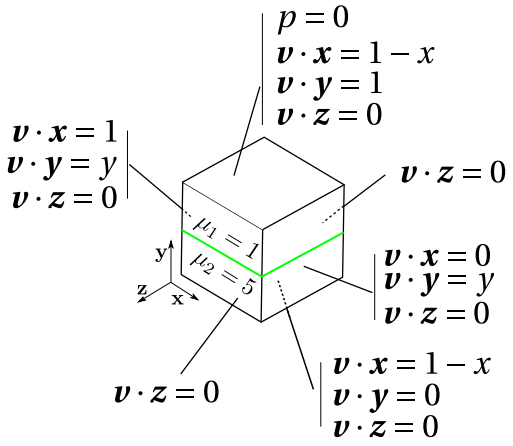

(A) pressure jump

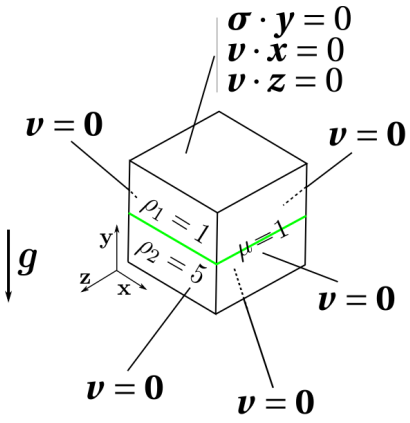

(B) pressure gradient jump

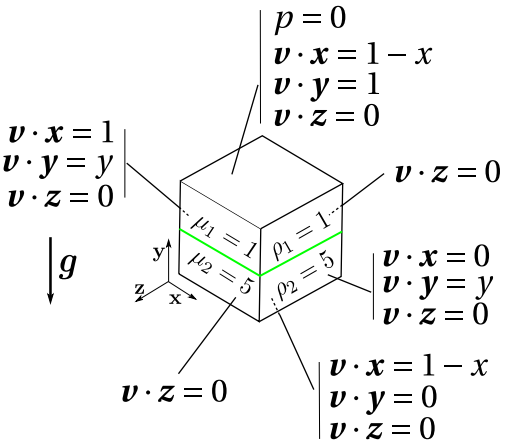

(C) pressure and pressure gradient jumps

FIGURE 4.3 – Enriched-FEM - Boundary conditions for the three cases to assess the discontinuities capturing

like 10^3 or 10^4. The analytical solution of the first case (A) is:

$$\text{velocity} \begin{cases} v_x = 1 - x \\ v_y = y \\ v_z = 0 \end{cases} \qquad (4.7)$$

$$\text{pressure} \begin{cases} p = 2(\mu_2 - \mu_1) \text{ if } y < y_{jump} \\ p = 0 \text{ else} \end{cases}$$

As it can be seen in Fig. 4.4, the pressure for $y > y_{jump}$ is zero and under y_{jump}, the pressure is constant, equal to 8, which are both the theoretical values for the pressure. The velocity field is presented on the right-hand side of the figure. The transparent green at the bottom represents the liquid with the higher density. The pressure field is correctly predicted by the numerical simulation due to the pressure enrichment. In fact, the analytical solution (constant on both sides of the interface) is included in the FE pressure space (piecewise linear with jumps). The interface is here parallel to faces of the cut elements. Therefore the matrix is not invertible as discussed in the previous paragraph. Consequently, the third added degree of freedom [165] is automatically removed. It has been tested that if no enrichment is added, the pressure cannot

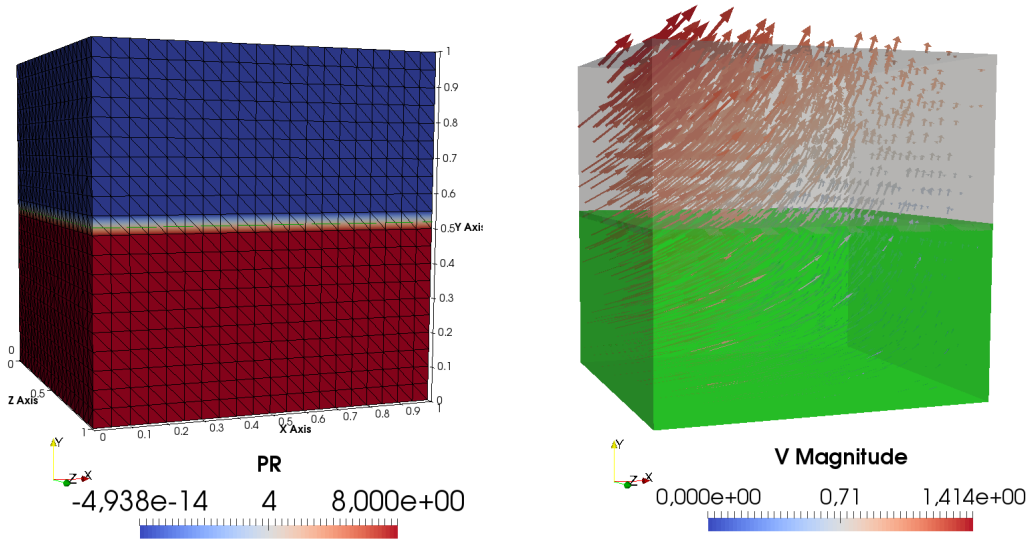

(A) pressure (B) velocity

FIGURE 4.4 – Enriched-FEM - Results with a pressure jump (case (A) Fig. 4.3) in the analytical solution (mesh size $h_e = 1/20$).

be discontinuous across the interface and thus the pressure jump is smoothed over each side of the interface. This first case validates the implementation and the efficiency of the pressure jump capturing technique from Ausas *et al.* [19].

The case (B) in Fig. 4.3 features a jump of pressure gradient, due to a jump in density. Two fluids are inside a container with the heavier fluid at the bottom, like coffee and air in a cup. Gravity is pulling both fluid in the direction $-y$ and $\boldsymbol{g} = (0, -10, 0)$. The analytical solution is

$$\begin{aligned} &\text{velocity } \{\boldsymbol{v} = \boldsymbol{0} \\ &\text{pressure } \begin{cases} p = \rho_1 \|\boldsymbol{g}\| y + \rho_2 \|\boldsymbol{g}\| (1 - y_{jump}) \text{ if } y < y_{jump} \\ p = \rho_2 \|\boldsymbol{g}\| (1 - y) \text{ else} \end{cases} \end{aligned} \tag{4.8}$$

Fig. 4.5 (A) shows the pressure field. The velocity field, presented in the top of Fig. 4.5 (B), has a maximum value in the centre of the domain of 10^{-15}, which is machine zero when using double precision float. Finally, at the bottom in Fig 4.5 (B), the pressure with a linear interpolation profile is plotted at the position $x = 0.5$ and $z = 1$ with an exact match with the theoretical pressure. And again this is expected since the analytical solution is included in the finite elements space.

The case (C) in Fig. 4.3 is the combination of both cases (A) and (B), allowing to assess the robustness of combining both methods. The analytical solution is given by

$$\begin{aligned} &\text{velocity } \begin{cases} v_x = 1 - x \\ v_y = y \\ v_z = 0 \end{cases} \\ &\text{pressure } \begin{cases} p = 2(\mu_2 - \mu_1) + \rho_1 \|\boldsymbol{g}\| y + \rho_2 \|\boldsymbol{g}\| (1 - y_{jump}) \text{ if } y < y_{jump} \\ p = \rho_2 \|\boldsymbol{g}\| (1 - y) \text{ else} \end{cases} \end{aligned} \tag{4.9}$$

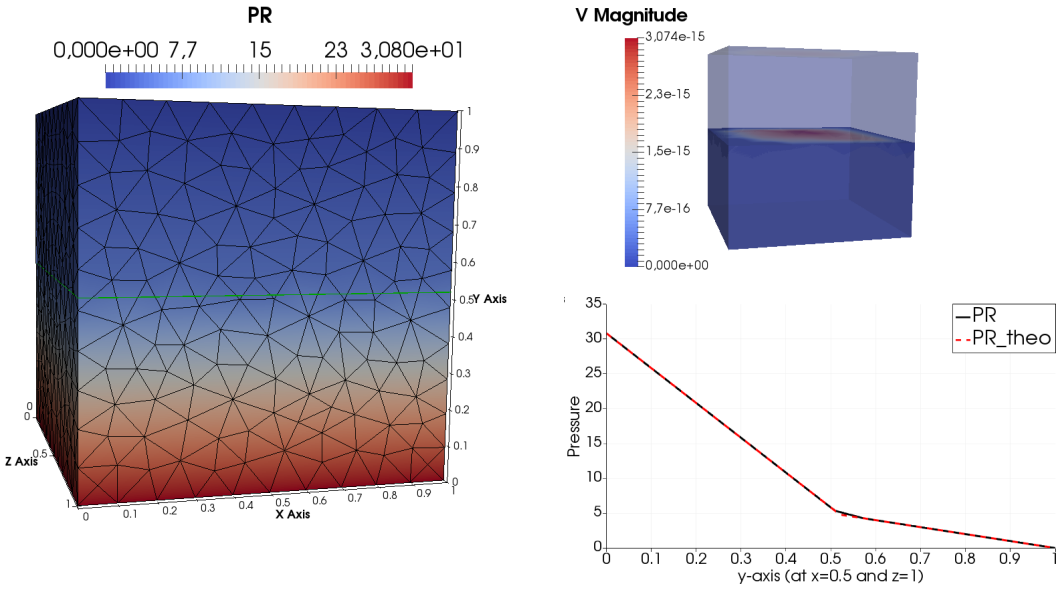

(A) (B)

FIGURE 4.5 – Enriched-FEM - Results with a pressure gradient jump (case (B) Fig. 4.3) in the analytical solution (mesh size $h_e = 1/10$).

The velocity field is plotted in Fig. 4.6 (A). Fig. 4.6 (B) shows the pressure field at the top and

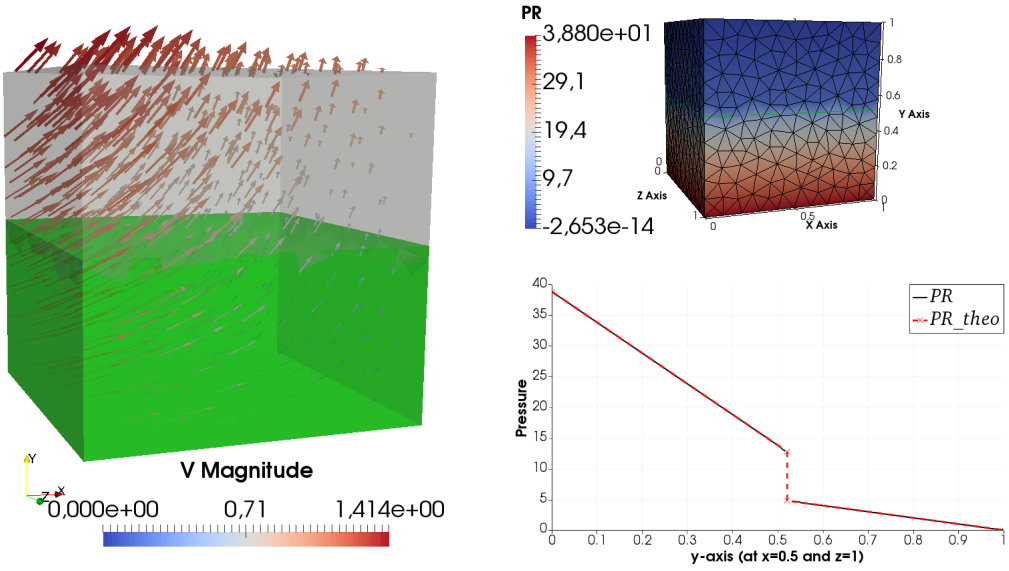

(A) (B)

FIGURE 4.6 – Enriched-FEM - Results with both a pressure and pressure gradient jump (case (C) Fig. 4.3) in the analytical solution.

at the bottom of the figure, the pressure along the y direction at position $x = 0.5$ and $z = 1$. The jump at the interface is recovered by the numerical simulation, even in this case when the discontinuity is inside an element. This last case validates the double enrichment of the pressure field to capture strong and weak discontinuities.

Pressure enrichment is required to capture discontinuities as shown in Fig. 4.7. Without any pressure enrichment both discontinuities are not captured by the simulation. This error in the pressure field is one of the parasitic currents roots in the velocity field at the interface, as it will be discussed in the validation of the implementation section.

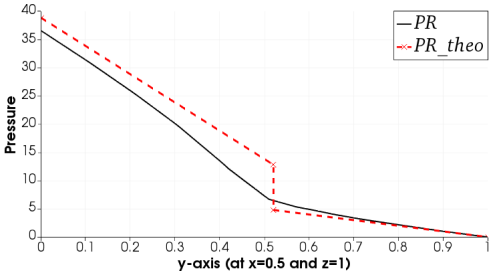

FIGURE 4.7 – Enriched-FEM - Pressure corresponding to the case (C) Fig. 4.3, that is presenting both weak and strong discontinuities. Dashed line: theoritical pressure; Solid line: numerical pressure obtained without enrichment [19] and [165].

4.2 Global FEM formulation for surface tension and surface energies

In a general setting, surface tension is involved at the interface between vapour and liquid phases. Additionally, in presence of a solid substrate (the carbon fibres in our case), surface energies act at the liquid-solid and vapour-solid interfaces. On each of these interfaces, force balance (see Sec.1.2.3), resulting from momentum and angular momentum balances, has to be satisfied. The purpose of this section is to depict a global strategy to include this interface condition in the integral weak FE formulation. Moreover, weakening the regularity required for the solution on the interface enables to see the triple junction equilibrium (Eq. 1.37) as a Neumann condition which appears naturally in the weak formulation.

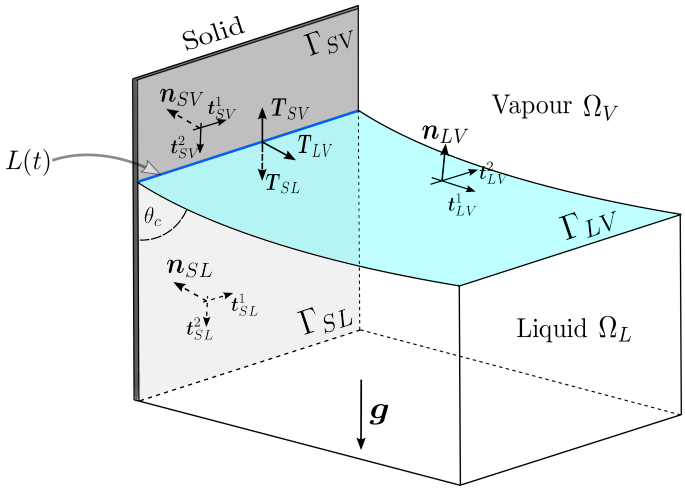

FIGURE 4.8 – Schematic description of notations for a capillary flow - a liquid meniscus against a rigid wall [58]

4.2.1 Relaxed weak formulation

The surface tension and surface energies terms are injected in the integral weak formulation through the stress vector term computed at each boundary $(\partial\Omega_L \cup \partial\Omega_V) \setminus (\Gamma_N)$. Contrary to the case of a single fluid, this time the set $(\partial\Omega_L \cup \partial\Omega_V) \setminus (\Gamma_N)$ is not empty and may be decomposed in the following way:

$$\begin{aligned}&\int_{(\partial\Omega_L\cup\partial\Omega_V)\setminus(\Gamma_N)} \boldsymbol{\sigma}\cdot\boldsymbol{n}\cdot\boldsymbol{w}\,dS\\ &=\int_{\partial\Omega_L\setminus\Gamma_{LV}} \boldsymbol{\sigma}\cdot\boldsymbol{n}_{SL}\cdot\boldsymbol{w}\,dS+\int_{\partial\Omega_V\setminus\Gamma_{LV}} \boldsymbol{\sigma}\cdot\boldsymbol{n}_{SV}\cdot\boldsymbol{w}\,dS-\int_{\Gamma_{LV}} (\boldsymbol{\sigma}_V-\boldsymbol{\sigma}_L)\cdot\boldsymbol{n}_{LV}\cdot\boldsymbol{w}\,dS\end{aligned} \tag{4.10}$$

where the normal are oriented according to Fig. 4.8. The two first terms are Neumann boundary condition for each phase, liquid and vapour. The third and last term is the stress jump at the interface between liquid and vapour phases. Let's remind with the following equation the boundary conditions on the three interfaces Γ_i with $i \in \{LV, SL, SV\}$ and on the triple line $L(t)$:

$$\begin{aligned}&[\boldsymbol{\sigma}\cdot\boldsymbol{n}]_{\Gamma_{LV}} = -\nabla_\alpha(\gamma_{LV}\boldsymbol{t}_{LV}^\alpha) && \text{on } \Gamma_{LV}(t),\\ &\boldsymbol{v}\cdot\boldsymbol{n}_{SL}=0 \quad\text{and}\quad \boldsymbol{\sigma}\cdot\boldsymbol{n}_{SL} = -\beta_{SL}\boldsymbol{v}+\nabla_\alpha(\gamma_{SL}\boldsymbol{t_{SL}}^\alpha) && \text{on } \Gamma_{SL}(t),\\ &\boldsymbol{v}\cdot\boldsymbol{n}_{SV}=0 \quad\text{and}\quad \boldsymbol{\sigma}\cdot\boldsymbol{n}_{SV} = -\beta_{SV}\boldsymbol{v}+\nabla_\alpha(\gamma_{SV}\boldsymbol{t_{SV}}^\alpha) && \text{on } \Gamma_{SV}(t),\\ &\gamma_{SL}\boldsymbol{T}_{SL}+\gamma_{SV}\boldsymbol{T}_{SV}+\gamma_{LV}\boldsymbol{T}_{LV} = R_{\text{solid}}\boldsymbol{n}_s \quad\text{and}\quad \boldsymbol{v}\cdot\boldsymbol{n}_s=0 && \text{on } L(t),\end{aligned} \tag{4.11}$$

For each interfaces, the stress vectors have been substituted with their expression given by the mechanical equilibrium at the interface. The purpose of the derivation is to include the four boundary conditions presented in Eq. 4.11 in the integral weak formulation as the virtual power of external action at the boundary of each subdomain liquid and vapour 4.10. From now on, the subscript for the normal and tangents are omitted but they refer implicitly to the surface over which the integral is performed. The first term in Eq. 4.10 is replaced with the condition on Γ_{SL}, the second term with the condition on Γ_{SV} and the stress jump with the condition on Γ_{LV}. It comes:

$$\begin{aligned}&\int_{(\partial\Omega_L\cup\partial\Omega_V)\setminus(\Gamma_N)} \boldsymbol{\sigma}\cdot\boldsymbol{n}\cdot\boldsymbol{w}\,dS\\ &=\int_{\Gamma_{SL}} (-\beta_{SL}\boldsymbol{v}+\nabla_\alpha(\gamma_{SL}\boldsymbol{t}^\alpha))\cdot\boldsymbol{w}\,dS+\int_{\Gamma_{SV}} (-\beta_{SV}\boldsymbol{v}+\nabla_\alpha(\gamma_{SV}\boldsymbol{t}^\alpha))\cdot\boldsymbol{w}\,dS+\int_{\Gamma_{LV}} \nabla_\alpha(\gamma_{LV}\boldsymbol{t}^\alpha)\cdot\boldsymbol{w}\,dS\end{aligned} \tag{4.12}$$

since $\partial\Omega_j \setminus \Gamma_{LV} = \Gamma_{Sj}$ with $j \in \{L, V\}$ as seen in Fig. 4.8. Recall that in [102], there is an implicit summation on the system coordinate $\alpha = \{1,2\}$ and $\boldsymbol{t}^\alpha$ are the vectors tangent to the surface. The coefficients β_j with $j \in \{L, V\}$ are friction coefficients (see Sec. 1.1.5 cond. (2)) acting on the solid substrate. It is classical in the literature to perform an integration by parts on the term $\nabla_\alpha(\gamma_i\boldsymbol{t}^\alpha)$ [47, 49, 174, 183, 202] in order report the derivatives on the test functions. At first, the integration by parts may be written using the curvilinear abscissa s

$$\int_{\Gamma_i}\frac{d}{ds}(\gamma_i\boldsymbol{t})\cdot\boldsymbol{w}\,dS=\int_{\partial\Gamma_i}\gamma_i\boldsymbol{T}_i\cdot\boldsymbol{w}\,dl-\int_{\Gamma_i}\gamma_i\boldsymbol{t}\cdot\frac{d\boldsymbol{w}}{ds}\,dS \quad \text{with } i\in\{LV,SL,SV\} \tag{4.13}$$

with $\boldsymbol{T}_i$ the tangent at the edge of the interface Γ_i. The same formula may be established in 3D [47], only in that case the term $\gamma_i \boldsymbol{t} \cdot \frac{d\boldsymbol{w}}{ds}$ becomes the surface divergence of the test function $\boldsymbol{w}$. . Therefore, surface tension and surface energy terms are turned into

$$\int_{\Gamma_i} \nabla_\alpha(\gamma_i \boldsymbol{t}^\alpha) \cdot \boldsymbol{w}\, dS = \int_{\partial\Gamma_i} \gamma_i \boldsymbol{T}_i \cdot \boldsymbol{w}\, dl - \int_{\Gamma_i} \gamma_i (\boldsymbol{I} - \boldsymbol{n}\otimes\boldsymbol{n}) : \nabla \boldsymbol{w}\, dS \quad \text{with } i \in \{LV, SL, SV\} \tag{4.14}$$

where the surface divergence is written using the projection operator $\boldsymbol{I} - \boldsymbol{n}\otimes\boldsymbol{n}$ in the tangent directions to the interface. Before the integration by parts, the computation of capillary forces involves the gradient of the tangent vector, that is, the mean curvature. Whereas, now, as it can be seen on the second term of the right-hand side of Eq. 4.14, only the normal vector to the interface is required. The interface should be at least C^1. In that sense, the condition on the regularity of the interface is weakened. The second advantage of doing an integration by parts on the three interfaces is to weakly impose the mechanical equilibrium of the triple line [47]. $\partial\Gamma_i$ represents the boundary of the interface Γ_i, with $i \in \{LV, SL, SV\}$ which is two points in 2D as seen in Fig. 4.9 and a curve in 3D.

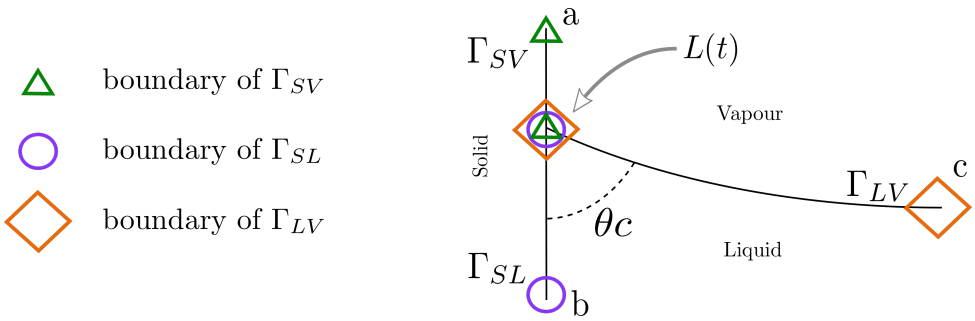

FIGURE 4.9 – Meniscus facing a wall in 2D with visual description of boundaries of each interfaces.

Each term $\int_{\partial\Gamma_i} \gamma_i \boldsymbol{T}_i \cdot \boldsymbol{w}\, dl$ may be decomposed into a contribution at the triple line L(t) and a contribution on the complementary $\partial\Gamma_i \setminus L(t)$. The sum from Eq. 4.12 may be rewritten as

$$\begin{aligned}
&\int_{\partial\Gamma_{SV}} \gamma_{SV}\boldsymbol{T}_{SV}\cdot\boldsymbol{w}\, dl + \int_{\partial\Gamma_{SL}} \gamma_{SL}\boldsymbol{T}_{SL}\cdot\boldsymbol{w}\, dl + \int_{\partial\Gamma_{LV}} \gamma_{LV}\boldsymbol{T}_{LV}\cdot\boldsymbol{w}\, dl \\
&= \underbrace{\int_{L(t)} \underbrace{\left(\gamma_{SV}\boldsymbol{T}_{SV} + \gamma_{SL}\boldsymbol{T}_{SL} + \gamma_{LV}\boldsymbol{T}_{LV}\right)\cdot\boldsymbol{w}}_{=R_{solid}\boldsymbol{n}_s\cdot\boldsymbol{w}}\, dl}_{=0} + \sum_{i\in\{SL,SV,LV\}} \int_{\partial\Gamma_i\setminus L(t)} \gamma_i \boldsymbol{T}_i\cdot\boldsymbol{w}\, dl
\end{aligned} \tag{4.15}$$

The first term of Eq. 4.15 corresponds to the contribution of each interface boundary at the triple line, and the second term is their contribution to the complementary, typically the positions a, b and c in Fig. 4.9 for a 2D case. Let's notice that the term $\int_{\partial\Gamma\setminus L} \gamma \boldsymbol{T}\cdot\boldsymbol{w}\, dl$ may be hard to implement since it is case dependent. By choosing an appropriate condition on velocity at these points, $\boldsymbol{T}_i \cdot \boldsymbol{w} = 0$. In particular, this is the case when $\boldsymbol{v}\cdot\boldsymbol{t}^\alpha$ is enforced equal to zero. As a matter of fact, prescribing the value of tangential velocity $\boldsymbol{v}\cdot\boldsymbol{t}^\alpha$ at $\partial\Gamma_i \setminus L(t)$ with $i \in \{LV, SL, SV\}$ leads to set the tangential component of the test function to zero $\boldsymbol{T}_i\cdot\boldsymbol{w} = 0$, since the velocity and test function belong to the same space $\mathcal{W}$.

In Eq. 4.15, the Young equation at the triple line is verified because the wall is assumed to be rigid ($\boldsymbol{w}\cdot\boldsymbol{n}_S = 0$ on L(t)) and the wall reaction directed in the normal direction. But for soft

solid, this term is mandatory and can even prevail in some circumstances [201]. Here, we thus deliberately neglect elasto-capillarity.

Hence, using expressions 4.15 and 4.14, without including Neumann condition (see condition 3 in Sec. 1.1.5), relation 4.10 can be expressed as

$$\begin{aligned}&\int_{(\partial\Omega_L\cup\partial\Omega_V)\setminus(\Gamma_N)} \boldsymbol{\sigma}\cdot\boldsymbol{n}\cdot\boldsymbol{w}\,dS\\ &=\int_{\Gamma_{solid}}\beta\boldsymbol{v}\cdot\boldsymbol{w}\,dS-\int_{\Gamma}\gamma(\boldsymbol{I}-\boldsymbol{n}\otimes\boldsymbol{n}):\nabla\boldsymbol{w}\,dS+\int_{\partial\Gamma\setminus L}\gamma\boldsymbol{T}\cdot\boldsymbol{w}\,dl\end{aligned} \tag{4.16}$$

with

$$\begin{aligned}&\bullet\quad \int_{\Gamma_{solid}}\beta\boldsymbol{v}\cdot\boldsymbol{w}\,dS=\sum_{j=\{SL,SV\}}\int_{\Gamma_j}\beta_j\boldsymbol{v}\cdot\boldsymbol{w}\,dS\\ &\bullet\quad \int_{\Gamma}\gamma(\boldsymbol{I}-\boldsymbol{n}\otimes\boldsymbol{n}):\nabla\boldsymbol{w}\,dS=\sum_{i\in\{LV,SL,SV\}}\int_{\Gamma_i}\gamma_i(\boldsymbol{I}-\boldsymbol{n}_i\otimes\boldsymbol{n}_i):\nabla\boldsymbol{w}\,dS\\ &\bullet\quad \int_{\partial\Gamma\setminus L}\gamma\boldsymbol{T}\cdot\boldsymbol{w}\,dl=\sum_{i\in\{LV,SL,SV\}}\int_{\partial\Gamma_i\setminus L(t)}\gamma_i\boldsymbol{T}_i\cdot\boldsymbol{w}\,dl.\end{aligned} \tag{4.17}$$

The term acting at position c in Fig. 4.9: $\int_{\partial\Gamma_{LV}\setminus L(t)}\gamma_{LV}\boldsymbol{T}_{LV}\cdot\boldsymbol{w}\,dl$ is naturally canceled when representing a symmetrical boundary condition for the fluid flow $\boldsymbol{v}\cdot\boldsymbol{n}=0$. In that case, it represents the action of a symmetric wall; both flow and capillary action are symmetric.

4.2.2 Semi-implicit time discretisation for the interface terms

The time is sequenced into time increments with the superscript $(\bullet)^n$ denoting the quantity at the n^{th} increment and the time step defined as $\Delta t=t^{n+1}-t^n$. Since an implicit time discretisation is used to solve the Navier-Stokes equations, the surface tension term is required to be computed at the time step t^{n+1}

$$\int_{\Gamma^{n+1}}\gamma(\boldsymbol{I}-\boldsymbol{n}\otimes\boldsymbol{n})\Big|_{n+1}:\nabla\boldsymbol{w}\,dS \tag{4.18}$$

Of course, the three interfaces Γ_{LV}, Γ_{SL} and Γ_{SV} and theirs geometries change over time. To compute the surface tension term presented above, the geometry of the interface has to be known beforehand since the normal to the interface is involved in the surface tension term. In that sense, there is a coupling between the fluid mechanical problem and the interface geometry problem. A distinction may be made between two the interfaces involving a solid and the immersed interface Γ_{LV}.
First, the interfaces Γ_{SL} and Γ_{SV} have a fixed geometry since they are represented by a boundary of the fluid domain which does not change over time. However, the boundary position still depends on time. To remove this first non-linearity, the interface between the solid and one of the fluid is approximated using the previous interface position

$$\int_{\Gamma_j^{n+1}}\gamma_j(\boldsymbol{I}-\boldsymbol{n}\otimes\boldsymbol{n})^{n+1}:\nabla\boldsymbol{w}\,dS\approx\int_{\Gamma_j^{n}}\gamma_j(\boldsymbol{I}-\boldsymbol{n}\otimes\boldsymbol{n})^{n+1}:\nabla\boldsymbol{w}\,dS\quad\forall\, j\in\{SL,SV\}. \tag{4.19}$$

A particular attention have to be paid to the interface between the vapour and liquid phase Γ_{LV} with a changing geometry over time. Oppositely, both the Liquid/Vapour interface position and its geometry are unknown. A first approach consists in using an explicit formulation for the surface tension term

$$\int_{\Gamma_{LV}^{n+1}} \gamma_{LV}(\boldsymbol{I}-\boldsymbol{n}\otimes\boldsymbol{n})^{n+1} : \nabla \boldsymbol{w} dS \approx \int_{\Gamma_{LV}^{n}} \gamma_{LV}(\boldsymbol{I}-\boldsymbol{n}\otimes\boldsymbol{n})^{n} : \nabla \boldsymbol{w} dS \tag{4.20}$$

Brackbill *et al.* [40] have been the first to investigate the stability condition when using a time-explicit discretization for the surface tension term in a bi-fluid flow which reads

$$\Delta t < \Delta t_\gamma := \sqrt{\frac{(\rho_L+\rho_V)h_e^3}{4\pi\gamma_{LV}}} \tag{4.21}$$

This condition comes from the fact that the time step should be small enough to resolve the fastest capillary waves of the problem

$$\frac{c_\gamma \Delta t_\gamma}{h_e} < \frac{1}{2} \tag{4.22}$$

where c_γ is given by the dispersion relation

$$c_\gamma = \sqrt{\frac{\gamma_{LV} k}{\rho_L+\rho_V}} \tag{4.23}$$

Consequently, the condition on the maximum allowable time step is when the maximum dispersion velocity occurs for a wavelength $k = \pi/h_e$ (obtained when recasting Eq. 4.21 and 4.23 in Eq. 4.22). A formal derivation and discussion on a fine tunning of the time step restriction is presented by Sussman *et al.* [203] and Galusinski *et al.* [91]. As noted by Popinet [178], the time step criterion is very restrictive and it is not suited for engineering problems. Furthermore, the restriction on the time step is a consequence of the requirement imposed by the spatiotemporal sampling of capillary waves [73]. Thus, the restriction on the time step due to capillary action is intrinsic to the problem and may not be simply overcome with the use of a small time step. One solution is to damp fast modes rather than resolve them, aiming at using an extended time step. This idea has been first proposed by Bänsch [24] with a Lagrangian finite-element discretisation. Dziuk [83] [84] and Hysing [121] have extended the method to an Eulerian description method, such as the level-set method. The derivation starts from the differential geometry relation [219] stating that the projection operator is equal to the surface gradient of the Lagrangian interface position $id(\boldsymbol{x})$. Then, the unknown position of the interface is approximated based on the previous position plus a predicted increment $\boldsymbol{id}^{n+1} = \boldsymbol{id}^n + \Delta t \boldsymbol{v}^{n+1}$. The complete semi-implicitation derivation may be written as follows

$$\begin{aligned}
\int_{\Gamma_{LV}^{n+1}} \gamma_{LV}(\boldsymbol{I}-\boldsymbol{n}\otimes\boldsymbol{n})^{n+1} : \nabla \boldsymbol{w}\, ds &= \int_{\Gamma_{LV}^{n+1}} \gamma_{LV} \nabla_\Gamma \boldsymbol{id}^{n+1} : \nabla \boldsymbol{w}\, dS \\
&\approx \int_{\Gamma_{LV}^{n}} \gamma_{LV} \nabla_\Gamma (\boldsymbol{id}^n + \Delta t \boldsymbol{v}^{n+1}) : \nabla \boldsymbol{w}\, dS \\
&= \underbrace{\int_{\Gamma_{LV}^{n}} \gamma_{LV}(\boldsymbol{I}-\boldsymbol{n}\otimes\boldsymbol{n})^{n} : \nabla \boldsymbol{w}\, dS}_{a} + \underbrace{\Delta t \int_{\Gamma_{LV}^{n}} \gamma_{LV} \left(\nabla \boldsymbol{v}^{n+1} \cdot (\boldsymbol{I}-\boldsymbol{n}\otimes\boldsymbol{n})^{n}\right) : \nabla \boldsymbol{w}\, dS}_{b}
\end{aligned} \tag{4.24}$$

with ∇_Γ the surface gradient operator. The first term (a in Eq. 4.24) is the surface tension force at the previous time step. The second term (b in Eq. 4.24) is a correction similar to a diffusion operator working in the direction tangential to the interface. Note that if the surface tension term is explicit (only a in Eq. 4.24), then increasing the surface tension coefficient tends to destabilise the system since it increases the external loading with no modification in internal contribution. This counter-intuitive fact does not hold with a semi-implicit treatment of the surface tension term. When increasing the surface tension coefficient, the semi-implicit scheme creates more interface diffusion and then a stiffer system, bringing robustness. According to Popinet [178], the second term will damp fast capillary waves leading to stabilisation. Finally, thanks to an error analysis, Groß *et al.* [103] showed a $O(\sqrt{h_e})$ error bound for the surface tension term when using the semi-implicitation technique.

4.2.3 Validation of the implementation

A circular static bubble in a surrounding fluid is tested in 2D and 3D, without gravity but with a surface tension acting on its contour. First, the 2D case compares the results obtained using the pressure discontinuities capturing technique, and with and without the stabilisation term (b in Eq. 4.24). Whereas, the 3D case assesses the pressure capturing technique efficiency when the semi-implicitation technique is used.

2D bubble

The initial and boundary conditions are depicted in Fig. 4.10. The top boundary condition, prescribing a zero tangential velocity and the normal component of the stress vector lead to impose indirectly the pressure to 10 in the liquid outside the bubble. In 2D, the bubble is a disc with a radius $R = 0.1924$ placed at the centre (0.5,0.5) of the unit domain. The viscosity and the surface tension coefficient are set to 1. Therefore, the jump of pressure due to the curvature of the bubble is $\Delta p = \gamma_{LV}/R \approx 5.20$. The pressure field is represented in Fig. 4.11, where it can be seen that the computed solution is in good agreement with the analytical one.

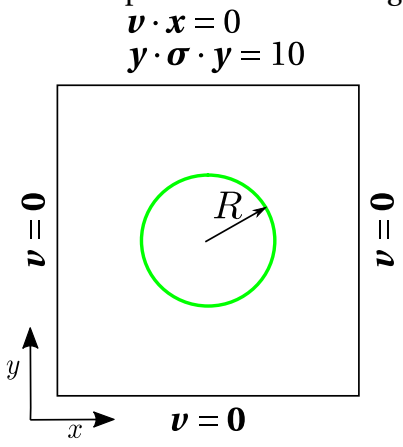

FIGURE 4.10 – Static bubble - Boundary conditions and the initial geometry

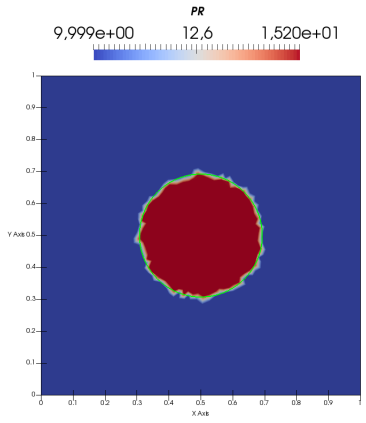

FIGURE 4.11 – Static bubble - Pressure field $h_e = 1/50$

One challenge with numerical simulation of capillary action comes from parasitic currents. The velocity field should be null in the entire domain since the bubble is static. Unfortunately, the discretisation of the interface brings numerical errors when computing the capillary term [2, 86, 92], since a curved interface may not be exactly represented with segments. Typically, those

parasitic currents are located at the interface and may deteriorate the shape of the interface. Low magnitude parasitic currents (compare to the time step) create small local displacements of the interface that initiate capillary waves with short wavelengths (of the order of the mesh size). When the interface starts to oscillate due to the discretisation error, the pressure may change suddenly at one point. This phenomena brings another source of unwanted capillary waves. Those purely numerical capillary waves with short wavelengths are unresolved, creating parasitic currents, which deteriorate the interface by convecting it with unphysical velocities. Parasitic currents are proportional to the ratio γ_{LV}/μ_L [132, 198]. In order to assess the influence of the semi-implicitation technique, a simulation is run from time $t_0 = 1$ to $t_f = 3$ in three regular time increments ($\Delta t = 1$) on a structured grid with a mesh size of 1/50. Fig. 4.12 exhibits parasitic currents around the interface. In the sub-figure (A), the semi-implicitation term

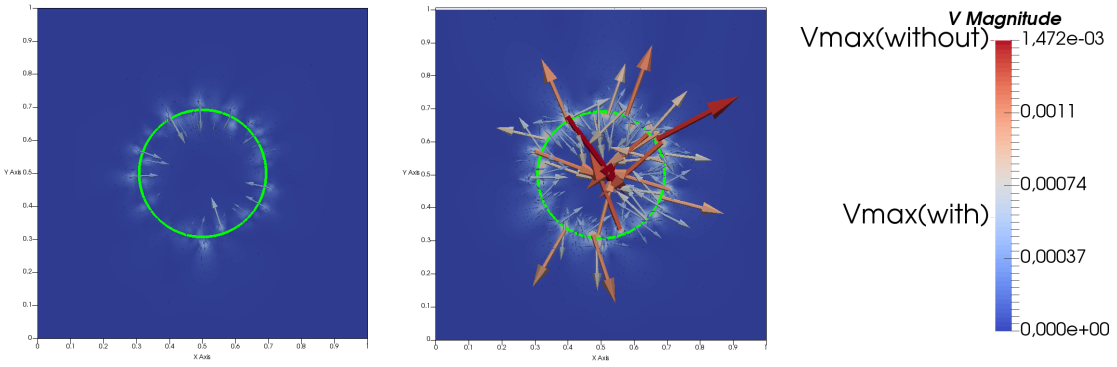

(A) with semi-implicitation (B) without semi-implicitation

FIGURE 4.12 – Static bubble - Parasitic currents (vectors scaled by 200), at beginning of the simulation at time $t = 1$

is used whereas in the sub-figure (B) an explicit scheme is used. The maximum velocity magnitude for the case with the semi-implicitation term is 5.57×10^{-4} and 1.47×10^{-3} without. As expected, the semi-implicitation technique acts as a stabilisation term reducing parasitic currents and allowing the use of a larger time step. After three time steps, unresolved fast modes crumble the interface for the unstabilisated case as it can be seen in Fig. 4.13 (B). On the contrary, thanks to the surface diffusion, the interface remains unchanged with constant parasitic currents around 2.5×10^{-4} (see Fig. 4.13 (A)). The same simulation is run with a smaller time step $\Delta t = 0.1$ in order to reduce the influence of the stabilisation term. The values of the parasitic currents (maximal velocity magnitude) are now: 1.23×10^{-3} with the stabilisation term and 1.47×10^{-3} without. At the end of the simulation after thirty time increments, the interface is unchanged with the semi-implicit term (same order of magnitude for the parasitic current than initially) and distorted otherwise (100 larger parasitic current magnitude than initially) as previously shown with the unitary time step. The stabilisation term not only tends to decrease the value of the parasitic currents but also prevents the parasitic current to increase in time.

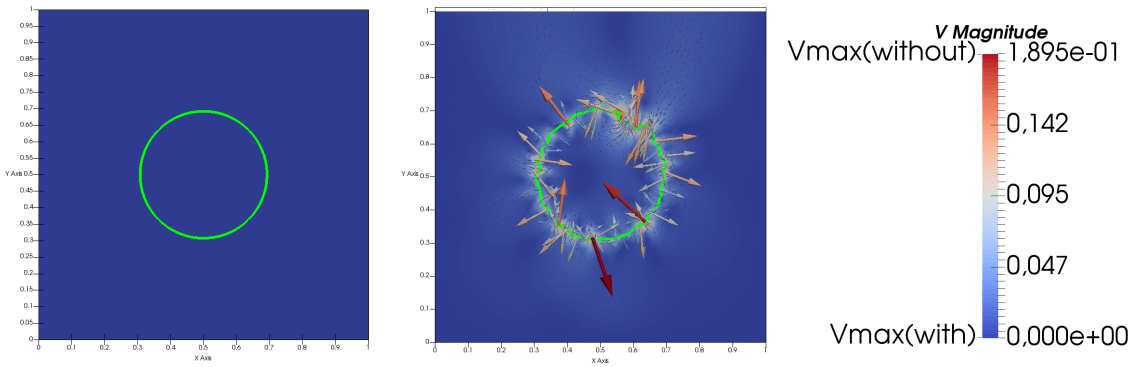

(A) with semi-implicitation (B) without semi-implicitation

FIGURE 4.13 – Static bubble - Parasitic currents (vectors scaled by 1), at the end of the simulation at time $t = 3$

3D bubble

The 3D bubble aims to validate, first, that the pressure enrichment is mandatory for the numerical simulation of capillary effects. And, second, that the pressure enrichment strategy and the semi-impicitation of the surface tension term behave well together. Let us consider a computational domain $\Omega = [0,1]^3$ with the initial setup in Tab. 4.1 and boundary conditions given in Fig. 4.14.

Parameters	Value
Centre of sphere	(0.5,0.5,0.5)
Sphere radius	0.2
Final time	10
Number of time increments	50
Δt	0.2
θ for theta method	0.5
Reinitialisation	False
Filtering function	tanh
Mesh size	$\{0.05, 0.033, 0.025\}$
Surface tension γ_{LV}	1
Viscosity μ	1

TABLE 4.1 – Static 3D bubble - model entries

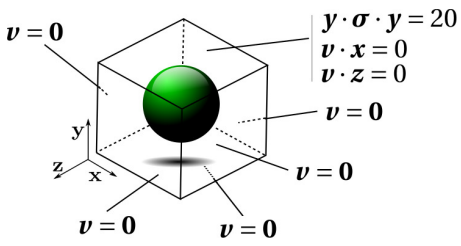

FIGURE 4.14 – Static 3D bubble - Boundary conditions and initial values

The first simulation is executed with a coarse grid (mesh size $h_e = 0.05$) made up of 9620 nodes. The results of the first Stokes computation are represented in Fig. 4.15 at the initial time, before moving the interface. Each subplot of the figure is divided into two parts. On the left-hand side, half of the numerical solution without pressure enrichment is given and on the right-hand side with the three additional degrees of freedom in pressure. The bubble without enrichment is represented in transparent magenta and with the enrichment in transparent green. After the first Stokes computation, the pressure field without enrichment is much diffuse than with enrichment. Indeed, the pressure jump of 10 pressure units is correctly captured by the pressure enrichment but not without. Making an error on the pressure field leads to strong parasitic currents in the velocity field which leads to the complete collapse of the bubble. This may come

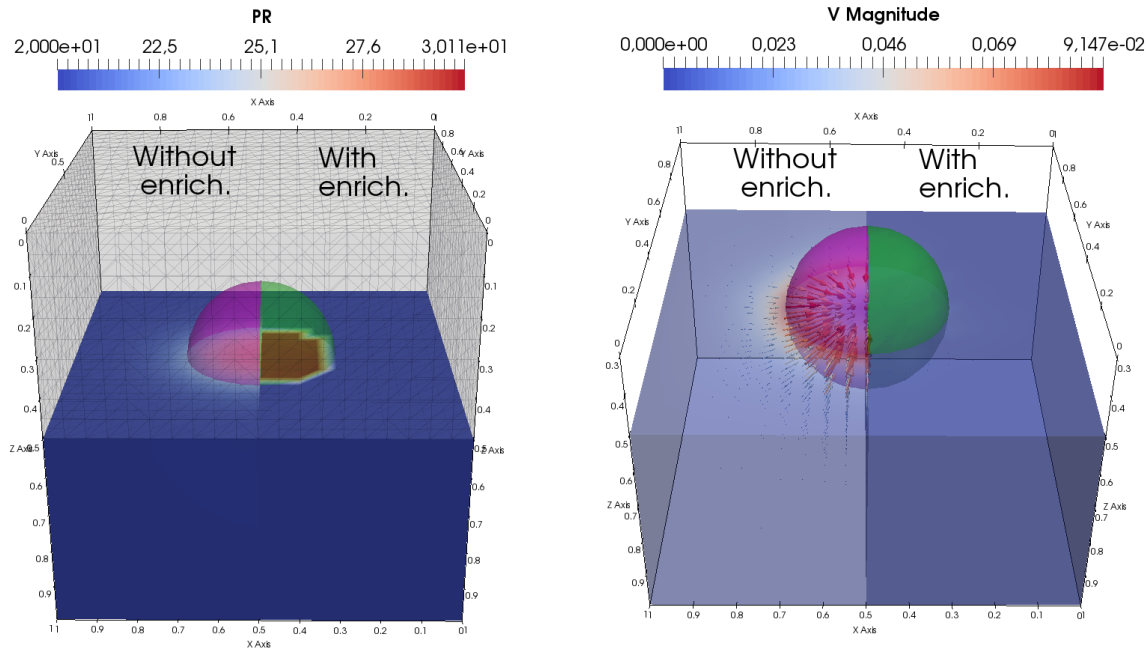

(A) Pressure field

(B) Velocity field

FIGURE 4.15 – 3D static bubble - Comparison with (green) and without (magenta) pressure enrichment

from the error on the estimation of the ASGS stabilisation term $\nabla p \cdot \nabla q$ (see Eq. eq:Navier-Stokes ASGS 2). This term allows some mass to be lost, since it relaxes the mass conservation equation.

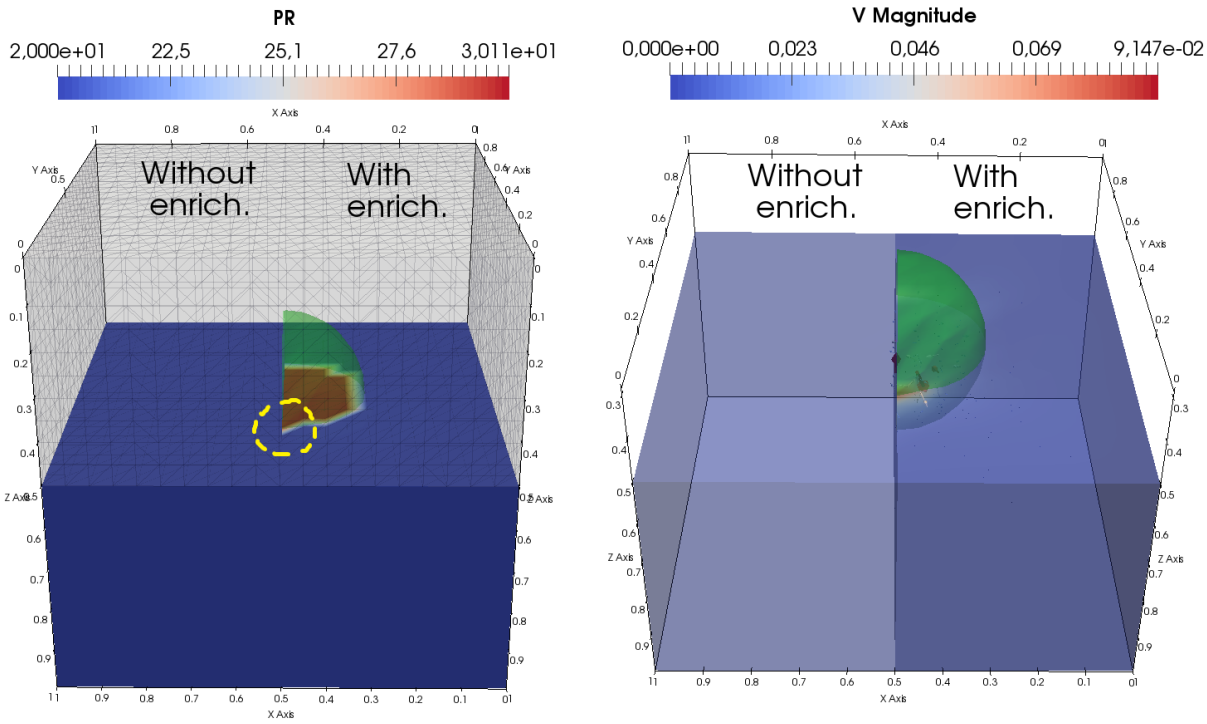

(A) Incr 30

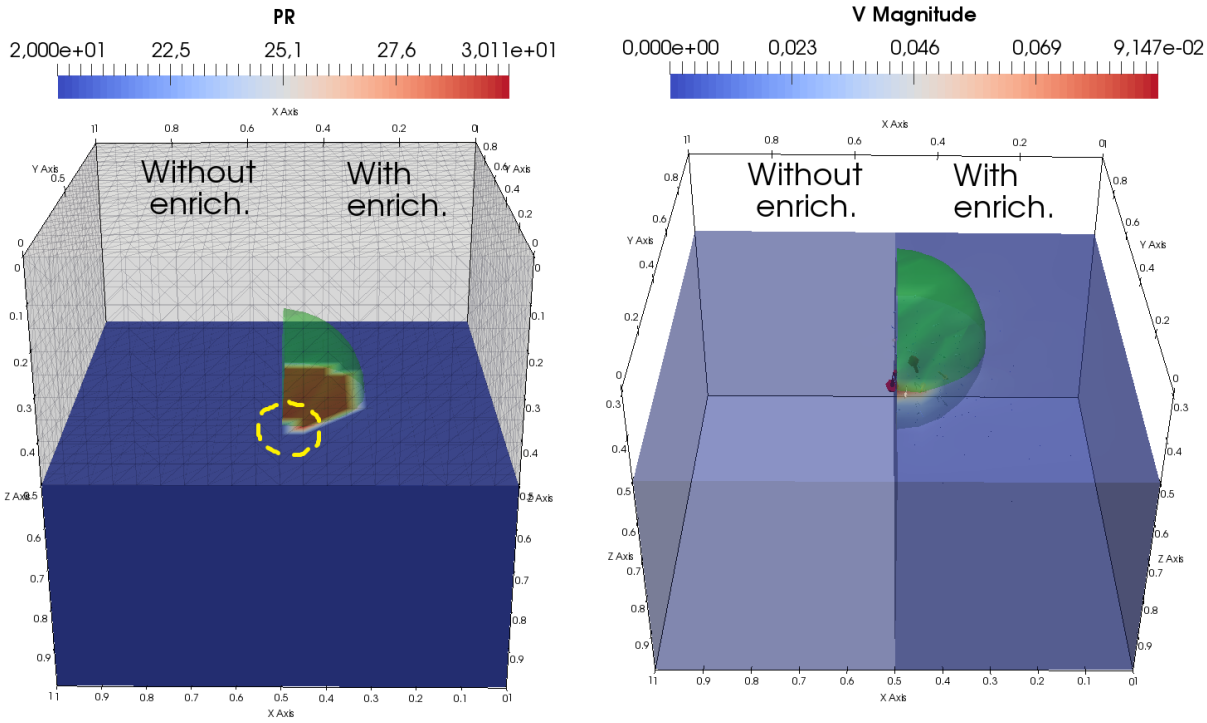

(B) Incr 31

FIGURE 4.16 – 3D static bubble - Parasitic currents left for the case with pressure enrichment

As shown in Fig. 4.16, the bubble without enrichment has totally disappeared after 30 time increments. Nevertheless, the pressure field with stabilisation is oscillating between subplot (*A*) and (*B*), creating parasitic currents. One node is either inside or outside the bubble as shown with the yellow circled region in Fig. 4.16. Fortunately, the semi-implicit term for the capillary

effect adds a surface diffusion to keep spurious velocities as low as possible.
Finally, the mass loss over time with and without using the pressure enrichment technique can be studied. The convergence and comparison study is carried out with three meshes. As can be

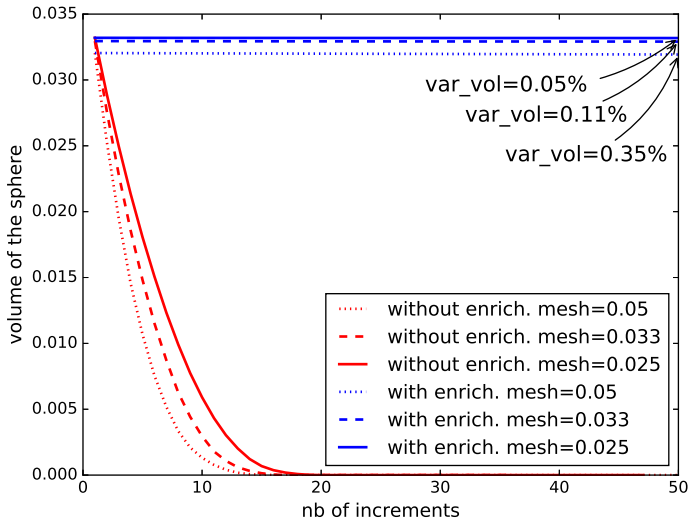

FIGURE 4.17 – 3D static bubble - Mass loss with and without pressure enrichment technique

seen in Fig. 4.17, refining the mesh tends to improve the mass conservation of the bubble by decreasing the parasitic currents. The pressure enrichment is a key element for capillary flow simulation, since it improves significantly the conservation of volume by minimising the parasitic currents. One will notice that the volume at the first time is not exactly the same volume for all the curves; this is due to the better discretisation (polygonalisation) with refined meshes. The volume variation computed at the final time is relative to the initial computed volume and not the theoretical volume. The variation of volume decreases when refining the mesh.

Globally, the two validation cases confirm that parasitic currents originate, first, from the linear discretisation of the interface itself, and second, from the position of the mesh nodes with respect to the interface, *i.e.* nodes close to the interface. It was demonstrated that it is highly profitable to use a pressure enrichment technique to capture the jumps of pressure and pressure gradient. Furthermore, adding the semi-implicit diffusion term at the interface brings robustness to the computation. The semi-implicitation allows to dissociate partially the time step and the mesh size.

4.3 Coupling Fluid and Level-set solvers

Up to this point, each problem (fluid and level-set) has been treated separately. From a general point of view, the level-set problem takes the fluid velocity as an input in order to convect the fluid front. Conversely, the fluid problem depends greatly on the position of fluid front when one comes to integrate the capillary forces. To put it briefly, the global system is non-linear due to the implicit time integration method. This section addresses the coupling strategy to solve this non-linearity. A staggered approach is used to solve recursively one problem after the other.

It is chosen to solve first the fluid flow based on the previous known configuration and then compute the new flow front geometry and position. A second choice is to restrict ourselves to the Stokes equations in order to isolate and deal with only one non-linearity. Still, the strategy developed with the Stokes solver is extensible to Navier-Stokes by adding inertia terms.

4.3.1 Weak coupling

The weak coupling strategy consists in solving the mechanical problem by using the interfaces obtained at the previous time increment. The interfaces are subsequently updated with the computed velocity, and time is incremented. Thus, there is no iteration into a same time increment, and the global solution $(\boldsymbol{v},p,\phi)$ solving simultaneously Stokes and transport equations is reached only for the steady state. The staggered algorithm is given in Algo. 1, the Stokes problem is solved at time t^{n+1} based on an evaluation of the geometry at time t^n.

Algorithm 1 Staggered algorithm for fluid and level-set problems

Require: ϕ_h^0 the initial geometry

for all $t^{n+1} \in]0,T]$ **do**

• **Step 1** find $\boldsymbol{v}_h^{n+1} \in \mathscr{W}_h$ and $p_h^{n+1} \in Q_h$ such that

$$
\begin{aligned}
&-\int_{\Omega_h} p_h^{n+1}\nabla\cdot\boldsymbol{w}_h\,dV+\int_{\Omega_h}\mu^n\nabla\boldsymbol{v}_h^{n+1}:\nabla\boldsymbol{w}_h\,dV-\int_{\Omega_h} q_h\nabla\cdot\boldsymbol{v}_h^{n+1}\,dV+\int_{\Gamma_{\text{solid},h}}\beta\boldsymbol{v}_h^{n+1}\cdot\boldsymbol{w}_h\,dS\\
&+\sum_e\tau_p^{e,n}\int_e\nabla\cdot\boldsymbol{v}_h^{n+1}\nabla\cdot\boldsymbol{w}_h\,dV-\sum_e\tau_v^{e,n}\int_e\nabla p_h^{n+1}\cdot\nabla q_h\,dV+\Delta t\int_{\Gamma_{LV,h}^n}\gamma_{LV}\left(\nabla\boldsymbol{v}_h^{n+1}\cdot(\boldsymbol{I}-\boldsymbol{n}\otimes\boldsymbol{n})^n\right):\nabla\boldsymbol{w}_h\,dS\\
&\quad=\int_{\Omega_h}\rho^n\boldsymbol{g}\cdot\boldsymbol{w}_h\,dV-\int_{\Gamma_h^n}\gamma(\boldsymbol{I}-\boldsymbol{n}\otimes\boldsymbol{n})^n:\nabla\boldsymbol{w}_h\,dS+\int_{\partial\Gamma_h\setminus L}\gamma\boldsymbol{T}\cdot\boldsymbol{w}_h\,dl-\sum_e\tau_v^{e,n}\int_e\rho^n\boldsymbol{g}\cdot\nabla q_h\,dV
\end{aligned}
$$

with $\tau_v=h_e^2/\mu$ and $\tau_p=\mu$, for any test functions $\boldsymbol{w}_h\in\mathscr{W}_h^0$ and $q_h\in\mathscr{Q}_h$.

• **Step 2** find $\phi_h^{n+1}\in\mathscr{S}_h$ such that

$$
\int_{\Omega_h}\frac{\phi_h^{n+1}-\phi_h^n}{\Delta t}\tilde{\phi}_h^*\,dV+\frac{1}{2}\int_{\Omega_h}\boldsymbol{v}_h^{n+1}\cdot\nabla\phi_h^{n+1}\tilde{\phi}_h^*\,dV=-\frac{1}{2}\int_{\Omega_h}\boldsymbol{v}_h^n\cdot\nabla\phi_h^n\tilde{\phi}_h^*\,dV
$$

with $\tilde{\phi}_h^*=\phi_h^*+\tau_k^e\boldsymbol{v}_h^{n+1}\cdot\nabla\phi_h^*$ and $\tau_k^e=\frac{1}{2}\frac{h_e}{||\boldsymbol{v}_{|e}^{n+1}||}$ for any test functions $\phi_h^*\in\mathscr{S}_h^0$.

• **Step 3** Reinitialisation step of the level-set: solve the Halmiton-Jacobi Eq. 3.19 or apply the direct reinitialisation technique 3.1.5.

end for

The geometry of the interface Γ_{LV} has an effect on the computation of the surface tension term but also on each term in the fluid equation except for the pressure gradient term $\int_{\Omega_h} p_h^{n+1}\nabla\cdot\boldsymbol{w}_h\,dV$ and the term from the incompressibility equation $\int_{\Omega_h} q_h\nabla\cdot\boldsymbol{v}_h^{n+1}\,dV$. All these terms are approximated when using the staggered approach what indicates that the integration is performed on the previous geometry *i.e.* $\Omega_L^{n+1}\approx\Omega_L^n$ and $\Omega_V^{n+1}\approx\Omega_V^n$.

4.3.2 Strong coupling

The restriction on the time step (Eq. 4.21) is one of the motivations for using an iterative approach [104], which couples Stokes and transport equations in a stronger way. A second reason for the iterative coupling is to progressively remove the stabilisation term introduced with the semi-implicit scheme. In fact, this purely numerical stabilisation alters the imposition of the triple line equilibrium as Neumann condition. Yet, the stabilisation does not vanish when using a weak coupling, affecting the contact angle. The stabilisation term is proportional to the velocity gradient projected on the interface, which is particularly strong near the triple line. This strong surface diffusion changes the contact angle imposed weakly with a Neumann condition. To address these two issues, an iterative procedure is introduced in this subsection, computing the Stokes problem on the geometry found at the previous iteration. First, the liquid and vapour domains are approximated with $\Omega_V^{n+1,it+1} \approx \Omega_V^{n+1,it}$ and $\Omega_L^{n+1,it+1} \approx \Omega_L^{n+1,it}$. And second, the iterative strategy modifies the semi-implicit scheme of capillary effects [104, 124]. The position of the interface is approximated using the previous iterative geometry rather than the geometry at the previous time step. The change reads

$$\boldsymbol{id}^{n+1,it+1} \approx \boldsymbol{id}^{n+1,it} + \Delta t \delta \boldsymbol{v}^{n+1,it+1} = \boldsymbol{id}^{n+1,it} + \Delta t \left(\boldsymbol{v}^{n+1,it+1} - \boldsymbol{v}^{n+1,it} \right). \tag{4.25}$$

The surface tension force at the moving interface between the vapour and the liquid is transformed using the previous approximation

$$\begin{aligned}
&\int_{\Gamma_{LV}^{n+1,it+1}} \gamma_{LV} (\boldsymbol{I} - \boldsymbol{n} \otimes \boldsymbol{n})^{n+1,it+1} : \nabla \boldsymbol{w} \, ds = \int_{\Gamma_{LV}^{n+1,it+1}} \gamma_{LV} \nabla_\Gamma \boldsymbol{id}^{n+1,it+1} : \nabla \boldsymbol{w} \, dS \\
&\approx \int_{\Gamma_{LV}^{n+1,it}} \gamma_{LV} \nabla_\Gamma \left(\boldsymbol{id}^{n+1,it} + \Delta t \left(\boldsymbol{v}^{n+1,it+1} - \boldsymbol{v}^{n+1,it} \right) \right) : \nabla \boldsymbol{w} \, dS \\
&= \int_{\Gamma_{LV}^{n+1,it}} \gamma_{LV} (\boldsymbol{I} - \boldsymbol{n} \otimes \boldsymbol{n})^{n+1,it} : \nabla \boldsymbol{w} \, dS + \\
&\qquad \underbrace{+ \Delta t \int_{\Gamma_{LV}^{n+1,it}} \gamma_{LV} \left(\left(\nabla \boldsymbol{v}^{n+1,it+1} - \nabla \boldsymbol{v}^{n+1,it} \right) \cdot (\boldsymbol{I} - \boldsymbol{n} \otimes \boldsymbol{n})^{n+1,it} \right) : \nabla \boldsymbol{w} \, dS}_{c}
\end{aligned} \tag{4.26}$$

Compare to an explicit expression of the surface tension term, the additional term named c in Eq. 4.26 brings stabilisation to the computation. Instead of only diffusing the solution like the term b in Eq. 4.24, now the second term, c, depends on the gradient of the incremental unknown. A salient feature of the strong coupling is that the stabilisation term c will progressively vanish when converging during iterations. One can verify that when converging $\| \boldsymbol{v}^{n+1,it+1} - \boldsymbol{v}^{n+1,it} \|_\infty \to 0$, then $c \to 0$. Conversely, when the discrepancy between two successive velocities increases, then the diffusion term c will be larger, creating a more diffusive and robust system.

Algorithm

The complete strong coupling algorithm is presented in Algo. 2. The main difference between the staggered and iterative coupling is the 'while loop' encompassing the Stokes and level-set problems. The fluid problem is modified using Eq. 4.26. The iterative coupling is presented for Stokes but can be extended to Navier-Stokes equations. In that case, the iterations for removing the non-linearity from the inertia term may be incorporated within the iterations

for the surface tension stabilisation (Eq. 4.26). Both non-linearities would be solved at the same time, increasing the complexity of the problem. In this work, the flow is restricted to Stokes flows when using a strong coupling strategy, because the global system features already two non-linearities. The first one is in the Stokes problem since the force depends on the previous iterative velocity (*i.e.* the Stokes problem is not linear in this case). The second non-linearity is global between the fluid and level-set problem, because the level-set convection may change the fluid problem solution.

Convergence criterion

The global system may be put under the form $\boldsymbol{K}(\boldsymbol{U})\boldsymbol{U} = \boldsymbol{F}(\boldsymbol{U})$ with the vector $\boldsymbol{U}$ of unknowns ($\boldsymbol{v}$, p, ϕ). The fixed point method is used to solve the previous equations, and for each iteration the residual has to be null $\boldsymbol{K}(\boldsymbol{U})\boldsymbol{U} - \boldsymbol{F}(\boldsymbol{U}) = \boldsymbol{0}$. Each increment is made of the following steps: compute the vector of unknowns by using a Gauss pivoting strategy or a LU factorization $\boldsymbol{K}(\boldsymbol{U}^{it})\boldsymbol{U}^{it+1} = \boldsymbol{F}(\boldsymbol{U}^{it})$. Then update the stiffness matrix and the external force ($\boldsymbol{K}(\boldsymbol{U}^{it+1})$ and $\boldsymbol{F}(\boldsymbol{U}^{it+1})$) and finally test the conditions if the solution vector verifies the system with the updated stiffness and external force $\boldsymbol{K}(\boldsymbol{U}^{it+1})\boldsymbol{U}^{it+1} = \boldsymbol{F}(\boldsymbol{U}^{it+1})$ or do another iteration. This condition is standard when using a numerical resolution method. In the case of coupling fluid and level-set solvers, this global condition may be tuned. The level-set problem is a linear problem, contrary to the fluid problem which has its external force dependent on the velocity. If the solution of the fluid problem verifies the updated system, therefore the velocity has converged and the updated stiffness for the level-set will not change. That is why, the condition named **CDT1** in Algo. 2, is designed to assess the global convergence of the system by specifically looking at the convergence of the fluid problem. Consequently, the condition **CDT1** is verified if the previous solution verifies the updated (after transport of the level-set) system. The condition is met if the infinity norm $\|\boldsymbol{K}(\boldsymbol{U}^{it+1})\boldsymbol{U}^{it+1} - \boldsymbol{F}(\boldsymbol{U}^{it+1})\|_\infty$ is smaller than a value (ϵ_1 in Algo. 2). Theoretically, the first condition **CDT1** should be sufficient at each time step. However, this condition is not always a suitable choice since parasitic currents may make the solution diverge. When studying the case of a static bubble at equilibrium, parasitic currents appear at the interface. The semi-implicit term (Eq. 4.26) for capillary effects tends to reduce its influence. Indeed, during the iterations, the stabilisation term (c in Eq. 4.26) vanishes when converging, this leads to an increase of the parasitic currents which will increase the stabilisation term back again. To tackle this issue, a more practical convergence parameter may be derived based on the level-set function. The condition **CDT2** is verified if the infinity norm of the increment of unknowns $\phi^{n+1,it+1} - \phi^{n+1,it}$ is lower than an arbitrarily threshold (ϵ_1 in Algo. 2). In general, this second criterion may be not sufficient to ensure the convergence of the whole system. In fact, the solver may be stuck in a local minimum ($\boldsymbol{U}$ is not the solution) but the variation of unknown may be zero. To sum things up, if the condition **CDT1** is true, it implies that **CDT2** is true, but the reverse does not hold. In this work, a regular convergence is assumed when dealing with a simple static interface Γ_{LV} between liquid and vapour phases. In that case, the condition **CDT2** is suitable to control convergence criterion.

Algorithm 2 Iterative algorithm for fluid and level-set problems

Require: ϕ_h^0 the initial geometry

for all $t^{n+1} \in]0, T]$ **do**

$it \leftarrow 0$
CDT1, CDT2 $\leftarrow$ False

while CDT1 or CDT2 is false **do**

• **Step 1** find $\boldsymbol{v}_h^{n+1,it+1} \in \mathscr{W}_h$ and $p_h^{n+1,it+1} \in Q_h$ such that

$$
\begin{aligned}
&-\int_{\Omega_h} p_h^{n+1,i+1} \nabla\cdot \boldsymbol{w}_h \, dV + \int_{\Omega_h} \mu^{n+1,it} \nabla \boldsymbol{v}_h^{n+1,i+1} : \nabla \boldsymbol{w}_h \, dV - \int_{\Omega_h} q_h \nabla\cdot \boldsymbol{v}_h^{n+1,i+1} \, dV \\
&\quad + \sum_e \tau_p^{e,n+1,it} \int_e \nabla\cdot \boldsymbol{v}_h^{n+1,it+1} \nabla\cdot \boldsymbol{w}_h \, dV - \sum_e \tau_v^{e,n+1,it} \int_e \nabla p_h^{n+1,it+1} \cdot \nabla q_h \, dV \\
&\quad + \int_{\Gamma_{\text{solid},h}} \beta^{n+1,it} \boldsymbol{v}_h^{n+1,it+1} \cdot \boldsymbol{w}_h \, dS + \Delta t \int_{\Gamma_{LV}^{n+1,it}} \gamma_{LV} \left(\nabla \boldsymbol{v}^{n+1,it+1} \cdot (\boldsymbol{I} - \boldsymbol{n}\otimes\boldsymbol{n})^{n+1,it} \right) : \nabla \boldsymbol{w} \, dS \\
&= \Delta t \int_{\Gamma_{LV}^{n+1,it}} \gamma_{LV} \left(\nabla \boldsymbol{v}^{n+1,it} \cdot (\boldsymbol{I} - \boldsymbol{n}\otimes\boldsymbol{n})^{n+1,it} \right) : \nabla \boldsymbol{w} \, dS - \int_{\Gamma_h^{n+1,it}} \gamma (\boldsymbol{I} - \boldsymbol{n}\otimes\boldsymbol{n})^{n+1,it} : \nabla \boldsymbol{w}_h \, dS \\
&\qquad + \int_{\Omega_h} \rho^{n+1,it} \boldsymbol{g} \cdot \boldsymbol{w}_h \, dV + \int_{\partial\Gamma_h \setminus L} \gamma \boldsymbol{T}^{n+1,it} \cdot \boldsymbol{w}_h \, dl - \sum_e \tau_v^{e,n+1,it} \int_e \rho^{n+1,it} \boldsymbol{g} \cdot \nabla q_h \, dV
\end{aligned}
$$

with $\tau_v = h_e^2/\mu$ and $\tau_p = \mu$ for any test functions $\boldsymbol{w}_h \in \mathscr{W}_h^0$ and $q_h \in \mathscr{Q}_h$.

• **Step 2** find $\phi_h^{n+1,it+1} \in \mathscr{S}_h$ such that

$$
\int_{\Omega_h} \frac{\phi_h^{n+1,it+1} - \phi_h^n}{\Delta t} \tilde{\phi}_h^* \, dV + \frac{1}{2} \int_{\Omega_h} \boldsymbol{v}_h^{n+1,it+1} \cdot \nabla \phi_h^{n+1,it+1} \tilde{\phi}_h^* \, dV = -\frac{1}{2} \int_{\Omega_h} \boldsymbol{v}_h^n \cdot \nabla \phi_h^n \tilde{\phi}_h^* \, dV
$$

with $\tilde{\phi}_h^* = \phi_h^* + \tau_k^e \boldsymbol{v}_h^{n+1,it+1} \cdot \nabla \phi_h^*$ and $\tau_k^e = \frac{1}{2} \frac{h_e}{||\boldsymbol{v}_{|e}^{n+1}||}$ for any test functions $\phi_h^* \in \mathscr{S}_h^0$.

• **Step 3** Reinitialisation step: solve the Halmiton-Jacobi Eq. 3.19 or apply the direct reinitialisation technique 3.1.5.

if $\|K(U^{n+1,it+1})U^{n+1,it+1} - F(U^{n+1,it+1})\|_\infty < \epsilon_1$ **then**
CDT1 $\leftarrow$ True
end if
if $\|\phi^{n+1,it+1} - \phi^{n+1,it}\|_\infty < \epsilon_2$ **then**
CDT2 $\leftarrow$ True
end if

$it \leftarrow it + 1$
end while
end for

Problem solving marching

When solving the iterative problem coupling level-set and fluid problems, two approaches may be considered. On one hand, the non-linearity on the position of the interface may be solved by approximating the geometry with the previous iteration value ϕ^{it}. The transport problem is then solved using the computed velocity. This first approach is represented in Fig. 4.18 (A) and called 'semi-decoupled approach'. On the other hand, both velocity to transport the interface and geometry to integrate the capillary force can be approximated using the previous ones. As shown in Fig. 4.18 (B), fluid and level-set solvers may be run simultaneously. With this 'fully decoupled approach', the non-linearity is solved using both equations simultaneously. Therefore, the iterations are performed until both solvers have converged.
Few tests have been performed to compare the two approaches. Results tend to indicate that

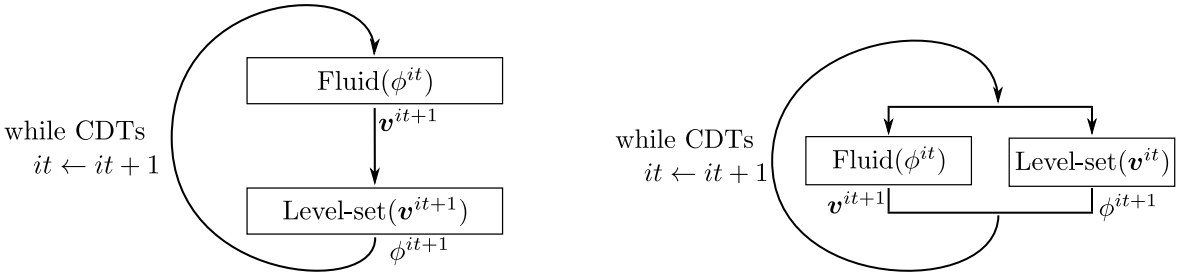

(A) semi-decoupled approach (B) fully decoupled approach

FIGURE 4.18 – Problem solving marching - iterative coupling strategy

the semi-coupled approach (A) is more robust since only the interface geometry in the fluid problem is approximated. Fully decoupled approach (B) makes more iterations than the semi-decoupled approach but fluid and level-set problems may be run simultaneously. The wall clock time spent for each approach seems to depend on the physical problem and no hard rule has been drawn. When looking at the two approaches from a memory optimisation point of view, one can notice that both approaches may be run on two separated machines.
In our case, the robustness of the computation is a crucial feature. Therefore, the semi-decoupled approach has been adopted.

4.4 Numerical experiments

In order to validate the implementation and numerically assess the performance of the model, two cases are investigated. The first one is a drop on a flat surface in two dimensions, and the second case is a drop placed on a sinusoidal surface. Due to the action of gravity, the liquid collapses on the solid. The surface tension and surface energies have been chosen for a case of partial wetting. For both cases the liquid is water and the vapour is air. The properties of the fluids are given in Tab. 4.2 and surface tension coefficients in Tab. 4.3.

	Vapour	Liquid
Viscosity (Pa·s)	1.71×10^{-5}	1.0×10^{-4}
Density (kg·m^{-3})	1.2	1.0×10^{3}

TABLE 4.2 – Drop on surfaces - Fluids properties

	Solid/Vapour - γ_{SV}	Solid/Liquid - γ_{SL}	Liquid/Vapour - γ_{LV}
Surface tension / energies ($N \cdot m^{-1}$)	60.9×10^{-3}	30×10^{-3}	72.8×10^{-3}

TABLE 4.3 – Drop on surfaces - Surface tension coefficients

4.4.1 Drop on flat surface

The first case is a drop spreading on a flat surface pulled down by gravity action ($\boldsymbol{g} = -9.81\boldsymbol{y}\,\mathrm{m\,s^{-2}}$). The interface between air and water is initialised as a quarter of circle with the centre at the origin and a radius of 0.3. The boundary conditions are represented in Fig. 4.19. On the left-hand

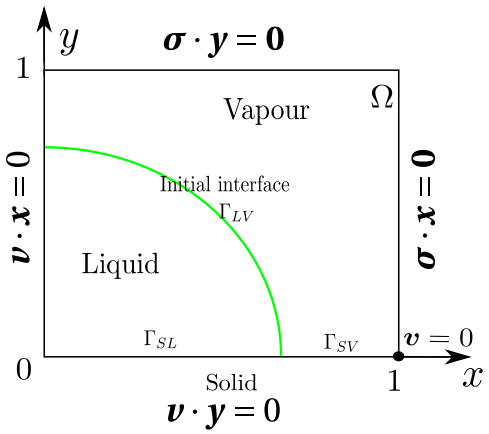

FIGURE 4.19 – Drop on a flat surface - Boundary conditions

side of the figure, the condition on the normal velocity represents a symmetrical plan. The bottom boundary is a solid with also a condition on normal velocity but with two surface energies. On the top and right edges of the domain, a zero traction condition is applied. The bottom right corner has a boundary condition on the velocity in the x-direction in order to cancel the term resulting from the integration by parts $\int_{\partial\Gamma_{SV}\setminus L}\gamma_{SV}\boldsymbol{T}\cdot\boldsymbol{w}_h\,dl$ (see Sec. 4.2.1). The mesh used for this case is an unstructured mesh with a mesh size of 1/50. Ten time increments are run from $t_0 = 1$ to time $t_f = 10$ ($\Delta t = 1$). A comparison on the shape of the drop is obtained with the weak and strong couplings in Fig. 4.20. The interfaces represented at $t = 1$ shows the correction steps done during the iterations. When comparing the three other images in Fig. 4.20, it is clear that the strong coupling reaches the equilibrium position faster compared to the weak coupling. This feature can be seen in Fig. 4.21 by comparing the position of the triple point over time. The strong coupling results drawn with green curves reaches first the equilibrium position. At each simulation time step, the static contact angle is 65° and, in this model, weakly enforced in the simulation. Thanks to the iterations, the first contact angle is 70° rather than 85° for weak coupling. Originally, verifying the contact angle at each time step was what has motivated the development of the iterative method. One can see that the discrepancy is significant when a large time step is used. Nevertheless, when the time step is divided by ten, the result of the weak coupling should tend towards the one generated by the strong coupling.
It can also be noticed in Fig. 4.21 (*B*) that it takes more time increments for the strong coupling strategy to converge to the static contact angle when refining the time step (5 instead of 2). The explanation could lie in the fact that there is no mesh adaptation or refinement and the angle

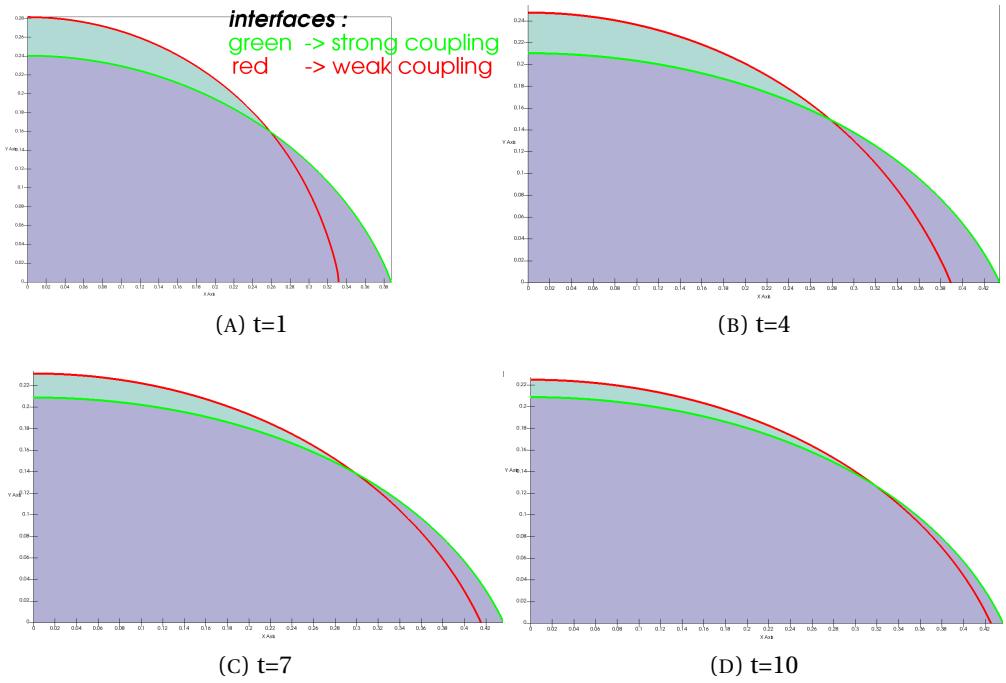

(A) t=1 (B) t=4

(C) t=7 (D) t=10

FIGURE 4.20 – Drop on a flat surface - Comparison of the shape of the drop when using a strong coupling or a weak coupling approach

is limited by the linear interpolation for the interface close to the solid surface. A cross comparison between the two subplots underlines that at first the static contact angle is verified and then the triple line equilibrium position is reached for both coupling strategies. And for every configurations, the strong coupling is quicker than the weak coupling to reach the equilibrium position and the equilibrium contact angle. Imposing the static contact angle instead of a dynamic contact angle tends to decrease the spreading time in good agreement with [135]. Finally, in Fig. 4.21 (*A*) the position of the triple point for the weak coupling has not converged yet. The

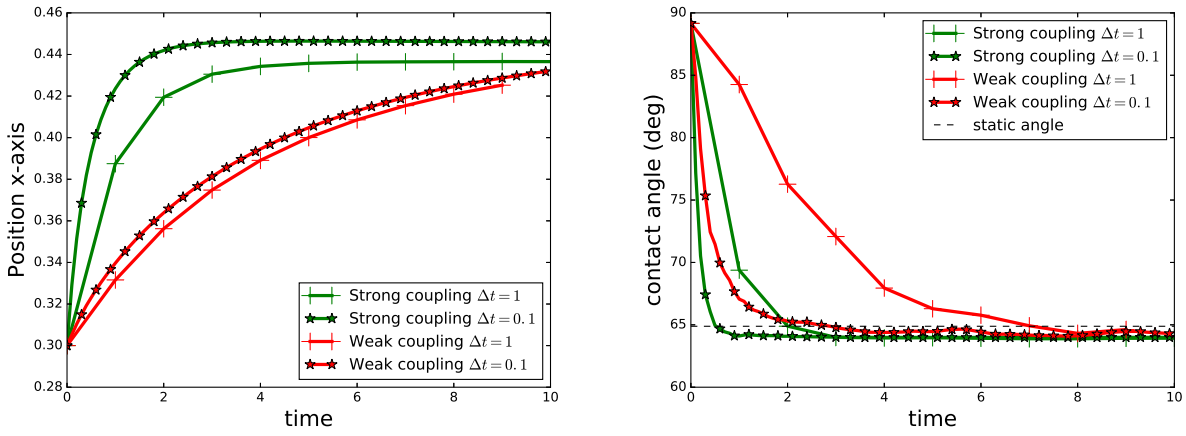

(A) position x of the triple point in time (B) contact angle in time

FIGURE 4.21 – Drop on a flat surface - Comparison between strong and weak coupling when using two time steps 1 and 0.1

discrepancy between the strong coupling with a time step of $\Delta t = 1$ and $\Delta t = 0.1$ on the final

position of the triple point may be due to the volume lost with the larger time step. Actually, during the first time increment, approximatively 60% of the total traveled length by the triple point is covered, whereas the same length is travelled in five time increments with the smaller time step. According to Eq. 3.28, the level-set error is proportional to the square of the time step and the mesh size at power 3/2. With a unitary time step and a mesh size lower than one, the main error is due to the time step. This is consistent with the strong coupling curves where refining the time step improves the conservation of the mass.

Finally, Fig. 4.22 depicts the number of iterations needed to converge, at each time step for the strong coupling. The criterion used to assess the convergence is the maximum absolute variation of the level-set function lower than 1×10^{-4} (CDT2 in Algo. 2) which is 1/200 the mesh size. Fig. 4.22 highlights the trade-off between choosing a larger time step and iterate

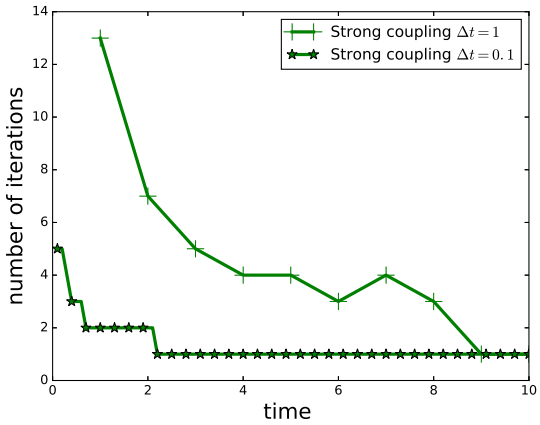

FIGURE 4.22 – Drop on a flat surface - Number of iterations for the strong coupling strategy

many times or to do fewer iterations with a smaller time step. The comparison based on the computational time is possible by assessing the number of Stokes/level-set cycles between the approaches, since the computational cost for one cycle is almost constant between the two approaches. The number of cycles is reported in Tab. 4.4. Systematically, the strong coupling has

	Strong coupling $\Delta t = 1$	Strong coupling $\Delta t = 0.1$	Weak coupling $\Delta t = 1$	Weak coupling $\Delta t = 0.1$
number of Stokes/level-set cycles	45	132	10	100

TABLE 4.4 – Drop on a flat surface - Comparison on the number of Stokes/level-set cycles

more cycles than the weak coupling but the discrepancy between the approaches decreases when refining the time step.

The strong and weak coupling are in principle equivalent. However, when it comes to run the simulation, the minimal time step for converging with only one iteration is not known and depends on the flow obstacle that may arise such as a front of fluid flowing around a fibre. Therefore, the strong coupling has the advantage to automatically iterate if the time step is not small enough, without having to decrease the time step.

4.4.2 Drop on a sinusoidal surface

The case of a drop laying on a sinusoidal solid surface is designed to test the limits of the weak coupling with geometrical changes of the solid interface. The boundary conditions are presented in Fig. 4.23.

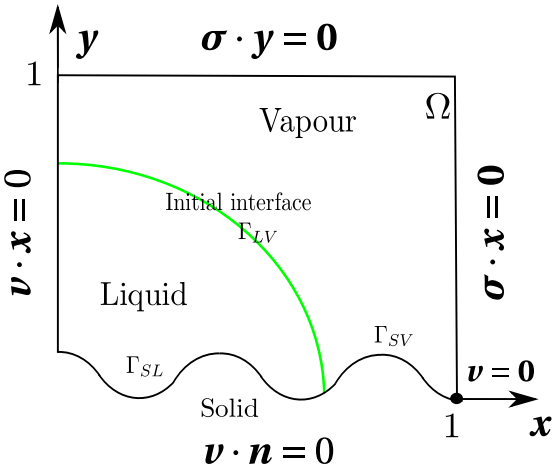

FIGURE 4.23 – Drop on a sinusoidal surface - Boundary conditions

The solid boundary geometry is given by the function $solid$

$$solid(x) = 0.05\cos(10\pi x) \tag{4.27}$$

with the 0.05 the magnitude and 5 the frequency.

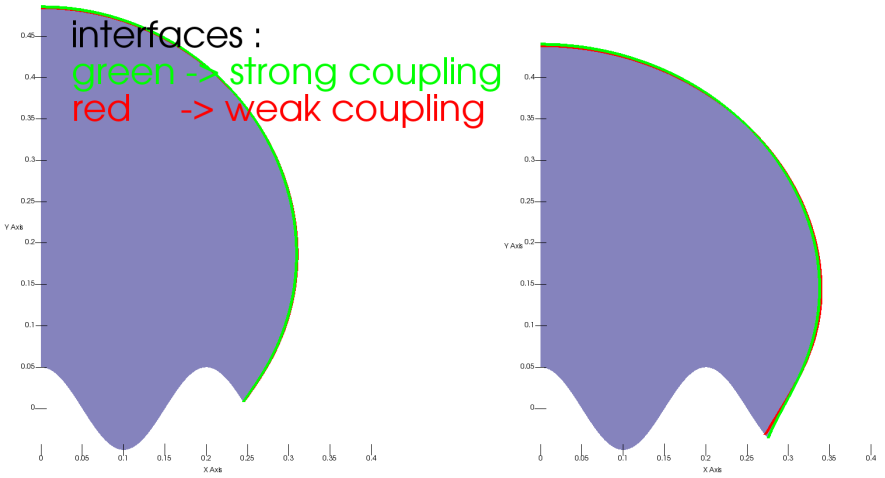

(A) t=0.67 (B) t=3.33

(C) t=4 (D) t=5.33

(E) t=6.67 (F) t=8.67

FIGURE 4.24 – Drop on a sinusoidal surface - Comparison of the shape of the drop when using a strong coupling and a weak coupling approach

The same setup is used as for the case of a drop on a flat surface, but the surface is now sinusoidal. The initial interface is placed on a hill of the sinusoid curve closer than before to the equilibrium static contact angle (*i.e.* $\theta_{init} = 71.54°$ for a static contact angle of 64.8°). Two conditions are used to ensure the convergence of the system and both have to be verified before going to the next time increment. The condition **CDT1**: the relative FE residual (*i.e.* divided by the external force) of the whole system has to be less than $1.e-7$. The second convergence criterion **CDT2**: the minimum admissible level-set variation, has to be less than $1.e-6$. Two time steps are investigated $\Delta t = 0.67$ and $\Delta t = 0.1$. The shape of the drop is presented in Fig. 4.24 for the simulation with $\Delta t = 0.67$. At the triple point, the contact angle has to adapt rapidly due to the change of the vector tangent to the solid surface. A close-up of the subplot (*D*) from Fig. 4.24 is given in Fig. 4.25. It can be seen that the weak coupling strategy has difficulties to adapt to the rapid variation of the solid tangent. It can be seen on this figure that the weak coupling has a contact angle higher than 90° whereas the static contact angle is approximately 64.8°. Physically, a dynamic contact angle is involved but it is not taken into account in our model. This test is a proof of concept and should recover the static contact angle.

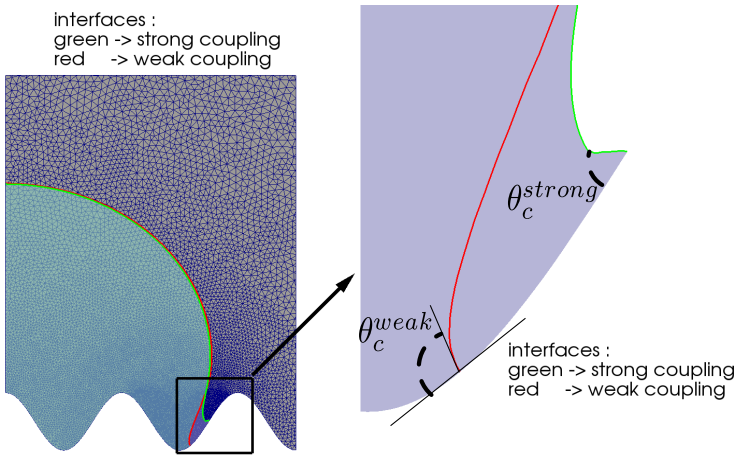

FIGURE 4.25 – Drop on a sinusoidal surface - close-up at $t = 5.33$ for the simulation with the time step of $\Delta t = 0.67$.

In Fig. 4.24 between subplots (*B*) and (*C*) the strong coupling has iterated in order to verify the static contact angle when crossing the minimums of the sinusoid. The weak coupling drop passes the minimum between subplots (*C*) and (*D*) or the close-up Fig. 4.25. At that moment, the contact angle changes suddenly. This characteristic is underpinned by hard evidence as shown in Fig. 4.26 (*B*) for the weak coupling curve with $\Delta t = 0.67$ between $t = 4$ and $t = 5.33$.
The initial contact angle is taken away from the static angle by 10%. Both strong couplings and only the weak coupling with the smaller time step are able to recover the static contact angle for $t \in [0,4]$, as shown in Fig. 4.26 (*B*). Indeed, the weak coupling with the larger time step ($\Delta t = 0.67$) gives a constant overshoot value for the contact angle. When looking at the triple point position in Fig. 4.26 (*A*), all the four simulations give the same position when the drop descends from the hill to the valley of the sinusoid. Quickly after $t = 4$, the drop is climbing the next hill of the sinusoid. Thus, locally at the triple point, the shape of the interface has to change to still verify the contact condition. In Fig. 4.26 (*B*), both strong coupling strategies experience oscillations but are able to describe the contact angle whereas the weak coupling overshoots it. At $t = 10$, according to the subplot (*A*), the position is the same, for all strategies and time steps,

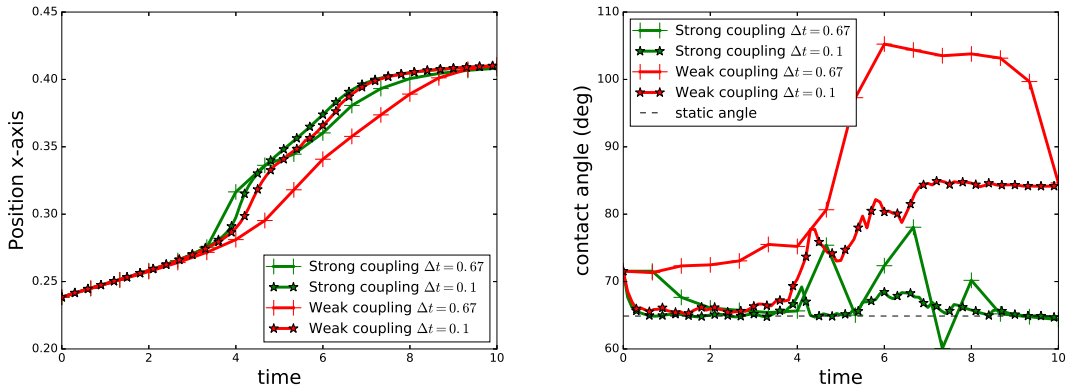

(A) (B)

FIGURE 4.26 – Drop on a sinusoidal surface - Comparison between strong and weak coupling when using different time steps (A) position x of the triple point in time (B) variation of contact angle in time

but the effect of the overshoot is not corrected for the contact angle yet.

The two cases of drop spreading on a solid surface enable to validate the implementation of the surface tension and surface energies. It enlights on the potential improvement of an iterative strategy to couple strongly the problem of capturing interface with the fluid problem.

Conclusion

The numerical strategy presented in this chapter allows performing simulations for flows with capillary effects. The two numerical methods, pressure discontinuities capturing and coupling strategy have been implemented and tested. They were shown to be efficient, and even mandatory to solve the most severe cases. The pressure enrichment is able to deal with pressure and pressure gradient jumps. Furthermore, weak and strong couplings have been discussed, showing their respective advantages and limitations. Robust numerical simulations may be achieved with the weak coupling approach and an enhanced precision especially for the contact angle which may be accessible when using the strong coupling strategy. In the following chapter, numerical experiments will be carried out to validate the model and to improve the understanding of composite manufacturing by Liquid Resin Infusion process.

Résumé en Français : Stratégie numérique pour décrire la capillarité

L'interaction du solveur de la mécanique des fluides et du solveur de capture d'interface, avec l'ajout de deux techniques numériques supplémentaires, permet de décrire la capillarité. Le premier point technique consiste à capter avec précision les discontinuités faibles et fortes du champ de pression. En effet, le changement des paramètres physiques tels que la densité ou viscosité peut générer des sauts de pression et de gradient de pression sur l'interface. La loi de Laplace reliant le saut de pression à la courbure de l'interface est un autre exemple de discontinuité de pression. L'espace d'approximation de la pression étant initialement composé de fonctions continues et linéaires par éléments ne peut par conséquent pas capter ces discontinuités. Pour pallier cette difficulté, trois degrés de liberté ont été ajoutés et condensés avant l'assemblage, sur les éléments traversés par l'interface. Trois cas tests de validation attestent de la capacité de la méthode à décrire les discontinuités du champ de pression. Le second point technique consiste à stabiliser le terme de tension de surface par une semi-implicitation de l'approximation numérique du travail virtuel produit sur l'interface. Cette technique permet de réduire l'intensité des courants parasites au front de fluide. Ces courants parasites proviennent notamment de l'erreur numérique commise lors de la discrétisation linéaire de l'interface. Il a été montré que cette stabilisation, permettant l'utilisation de plus grands pas de temps, relaxe la condition sur l'angle de contact imposé faiblement dans la formulation. Un couplage itératif a été implémenté permettant de trouver à chaque instant l'état d'équilibre quasi-statique du problème global en vitesse, pression et géométrie (décrit par la fonction level-set). Le couplage fort itératif semble indispensable pour prendre en compte les changements topologiques de la surface solide, comme le montre le cas d'une goutte s'étalant sur une surface texturée.

Chapter 5

Numerical experiments

Contents

Introduction

This chapter presents cases, first of validations and then for the study of microstructures. The first part demonstrates the ability of the numerical method to describe cases with surface tension. The numerical solution is compared to either semi-analytical solution, analytical solution, or experiment. The second part of the chapter analyses the behaviour of the flow in microstructures and proposes solutions to extract their physical characteristics. At the scale of the equivalent homogeneous medium, the fibrous medium can be characterised by a fibre volume fraction and a permeability, the flow is then ruled by Darcy's law. Here, two approaches are used to calculate permeabilities by numerical experiments. On one hand, a numerical permeability may be computed based on the Darcy equation written in flow rate. On the other hand, it may also be based on the drag force definition. Once the permeability is evaluated, capillary effects can be added to the Darcy's law by considering a pressure jump at the flow front. The magnitude of this jump is a scalar, called capillary pressure. We propose to determine this quantity by numerical experiments at the fibre scale. More precisely, two strategies are exposed to scale-up the capillary action at the part scale. One method is based on an equivalence with a Darcy's flow in 1D whereas the second method involves an energy equivalence for the same capillary action in a Stokes and associated Darcy domain in Appendix B.

5.1 Validation cases

Validation cases are designed to assess the robustness of the numerical strategy consisting in two coupled solvers (fluid flow and interface tracking) to compute bi-fluid flow with capillary action. Three cases are analysed: the interaction of a meniscus with walls, a bubble rising in a liquid, and a cluster of tubes.

5.1.1 Meniscus and walls

The case of the interaction of a meniscus with walls is subdivided in two cases: a meniscus facing one single wall and a meniscus between two walls. The former has an analytical solution Eq. 5.1, and the latter is compared with two semi-analytical solutions presented in Sec. 1.4.3. The interface position and the contact angle are assessed at equilibrium only. Therefore, the

	Solid/Vapour - γ_{SV}	Solid/Liquid - γ_{SL}	Liquid/Vapour - γ_{LV}
Surface tension / energies ($\mathrm{N\cdot m^{-1}}$)	54.7×10^{-3}	25.9×10^{-3}	50.8×10^{-3}

	Vapour	Liquid
Viscosity ($\mathrm{Pa\cdot s}$)	1.71×10^{-5}	2.76×10^{-3}
Density ($\mathrm{kg\cdot m^{-3}}$)	1.292	3.325×10^{3}

TABLE 5.1 – Input values for the model

friction coefficients applied on the solid are considered as null $\beta_{SL}=\beta_{SV}=0$. The solid is considered to be a cellulose plate, the liquid is diiodomethane and the vapour is air. Surface tension and surface energies correspond to experimental measurements [180] and are summarised in Tab. 5.1. The capillary length representing the distance over which the capillary effects are significant can be computed from the numerical values given in Tab. 5.1, $\kappa^{-1}=\sqrt{\frac{\gamma_{LV}}{\rho_L g}}\approx 0.12\,\mathrm{cm}$. The static contact angle is $\theta_c=\arccos(\frac{\gamma_{SV}-\gamma_{SL}}{\gamma_{LV}})\approx 55.5°$.

Meniscus facing a vertical wall

This first case is a 2D case representing a meniscus facing a vertical infinite wall. The computational domain is the unit square domain presented in Fig. 5.1. The interface is placed horizontally in the middle of the domain at $y=\frac{1}{2}$. On the right-hand side of the domain a homogeneous Dirichlet boundary condition is imposed $\boldsymbol{v}=\mathbf{0}$. Therefore the interface cannot move on this side. This choice does not influence the representation of a meniscus facing a vertical wall since the capillary length, 0.12 cm, is small compared to the length of the domain, 1cm. The fluids (liquid and vapour) can come in and out from the bottom $y=0$ (inlet) and the top $y=1$ (outlet). At both boundaries, the fluid is not sheared since the velocity in the x-direction is set to zero. Therefore the pressure can be imposed through a Neumann boundary condition on the normal stress. Let us choose a zero pressure value at the top of the domain. In order to balance the weight of fluids (liquid and vapour), the pressure at the bottom is equal to the sum of the two hydrostatic pressures in the vapour and liquid phases $\frac{1}{2}g(\rho_L+\rho_V)$. This relation is valid since the gravity is acting in the $-y$ direction. Finally, the left-hand side of the domain represents the solid wall with two surface energies γ_{SL} and γ_{SV}. The interface between liquid and vapour has a constant surface tension γ_{LV} reported in Tab. 5.1.
The term $\int_{\partial\Gamma\setminus L}\gamma\boldsymbol{T}\cdot\boldsymbol{w}\,dl$ (from Eq. 4.15) located at each extremity of each interface may be removed if the tangent velocity is imposed as explained at the end of Chap. 4.2.1. This term arises from the integration by part of the integrals representing surface energies and surface tension. This term vanishes if the velocity is set to $\boldsymbol{v}\cdot\boldsymbol{y}=0$ at the position $(0,1)$ and $(0,0)$ for example, since the tangent $\boldsymbol{T}=\boldsymbol{y}$ at theses points (for the interfaces Γ_{SV} and Γ_{SL}) and the component of

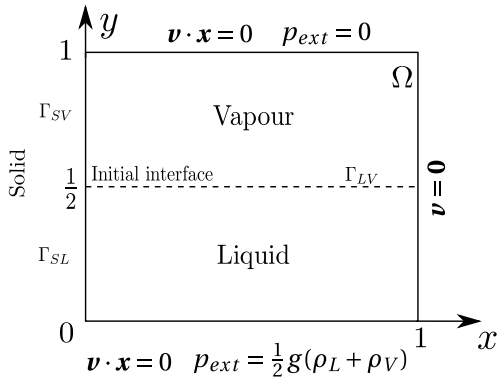

FIGURE 5.1 – Meniscus facing a wall - computational domain and boundary conditions; initially the interface is placed horizontally at $y = \frac{1}{2}$.

the test function $\boldsymbol{w} \cdot \boldsymbol{y}$ is then equal to zero. The static equilibrium of the interface position has an analytical expression [71]

$$x - x_0 = \kappa^{-1} \cosh\left(\frac{2\kappa^{-1}}{y}\right) - 2\kappa^{-1}\left(1 - \frac{y^2}{4\kappa^{-2}}\right)^{1/2} \tag{5.1}$$

where x_0 is the abscissa obtained from Eq.5.1 when $x = 0$ and $y_0 = y(x = 0)$. Note, Eq. 5.1 gives the abscissa as a function of the ordinate. The ordinate of the triple point is given by $y_0 = \sqrt{2}\kappa^{-1}(1 - \sin\theta_c)^{1/2}$, at equilibrium, recalling that θ_c is the static contact angle.

The baseline solution is obtained on a coarse structured mesh made up of 49x49 elements (*i.e.* 2500 nodes). The simulation takes 240 s on a single core processor (CPU speed: 3.7 GHz). 200 increments are performed with a time step Δt =2.5 × 10^{-6} s, so the final time is t_f =5 × 10^{-4} s. It is observed that the equilibrium state is reached at time t_f =5 × 10^{-4} s because the position of

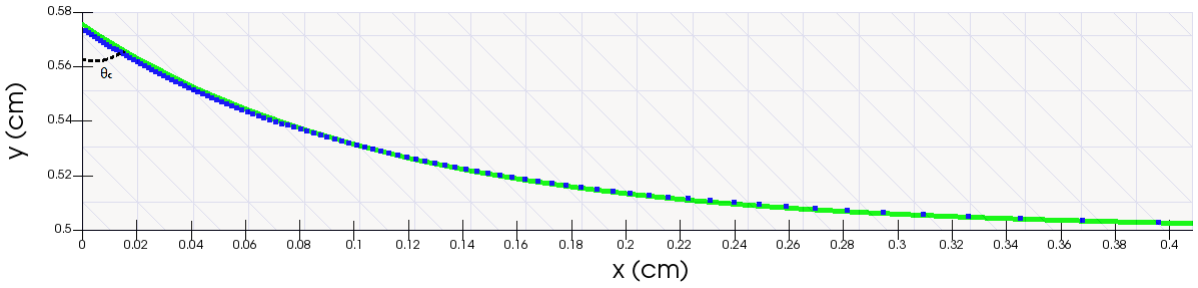

FIGURE 5.2 – Meniscus facing a wall - comparison between the Finite Element solution (green curve) and the analytical solution (blue dots).

the triple point remains unchanged as shown in Fig. 5.6. When the equilibrium state is reached, the computed profile of the interface can be compared with the analytical solution. A good correlation is found between both, as represented in Fig. 5.2. This figure is a close-up presenting half of the domain that includes the triple point. The numerical strategy does not require to impose directly the value of the contact angle but it is done through the triple junction mechanical equilibrium imposed as a Neumann condition in the weak formulation. The corresponding static contact angle is recovered since the computed contact angle is 54.7° for a theoretical contact angle of 55.5° according to the Young's equation. The 1.26° error, *i.e.* 2.9 %, is another parameter reflecting the good correlation between numerical solution and analytical one.

The convergence of the meniscus shape is assessed by looking at the average error for each point in the interval $x \in [0, 0.4]$, further points perfectly match the analytical solution. The abscissa error of the interface position is reported in Tab. 5.2 for a structured mesh (see background of Fig. 5.2). The error decreases with the mesh size. This proves the ability of the method to numerically describe precisely the equilibrium position of an interface in the case of a meniscus facing a vertical wall.

Mesh size (cm)	h=0.02	h=0.01	h=0.005
$\overline{\Delta_x}$ (cm)	4.1×10^{-3}	3.8×10^{-4}	7.6×10^{-5}

TABLE 5.2 – Convergence of the meniscus shape when refining the mesh - mean absolute error $\overline{\Delta_x} = \frac{1}{N}\sum_{i=1}^{N} |x^i_{\text{theo}} - x^i_{\text{num}}|$ with N the number of discretisation points in the interval $x \in [0, 0.4]$.

Globally, the success of simulating problem with capillary effects relies on the approximation of the pressure across the interface, Γ_{LV}. Actually, grasping properly jumps of pressure and pressure gradients is a prime priority. Fig. 5.4 represents pressure profile along the y-axis at three abscissa for the current problem, as shown in black vertical lines in Fig. 5.3. The slope

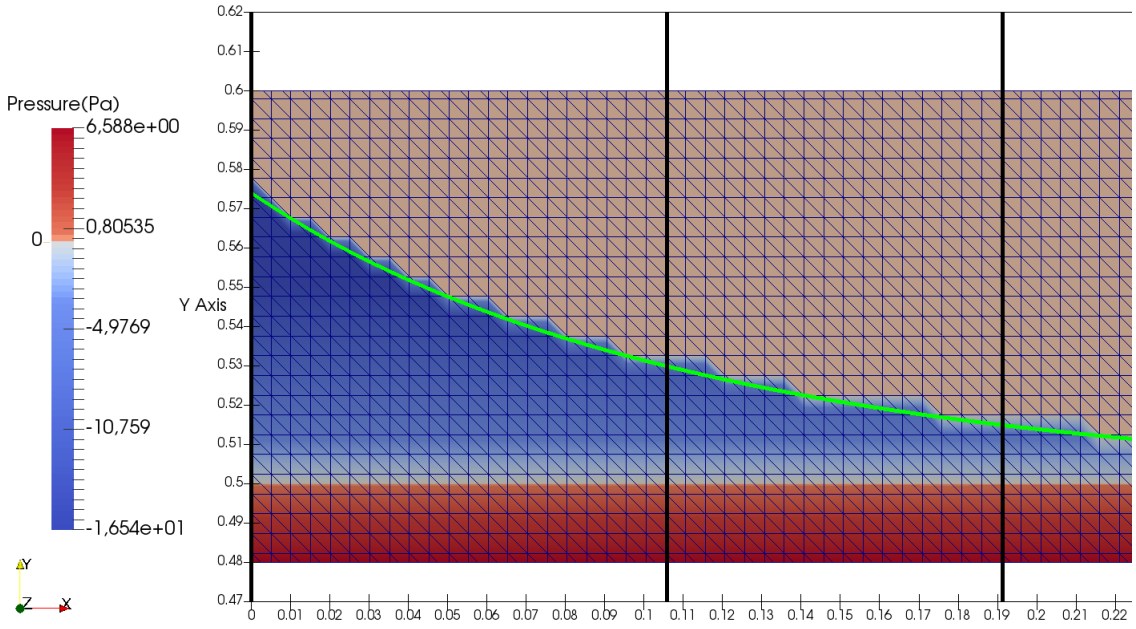

FIGURE 5.3 – Meniscus facing a wall - pressure field [Pa] and profile lines of analysis in black color (199 × 199 mesh).

of the pressure profile is lower above the jump (in air) than under in the liquid. This change of slope operates inside an element cut by the interface. In addition to this pressure gradient jump, the pressure is discontinuous across the interface arising from the curvature or a change of viscosity with a sheared fluid at the interface. The numerical method is able to capture pressure and pressure gradient discontinuities present in this case. Indeed, 98% of the pressure jump is numerically recovered at the triple point on the finest mesh *i.e.* 199 × 199 nodes (95% on the coarse mesh *i.e.* 49 × 49 nodes), which is the point with the highest curvature. This ratio is given only as an indication since it depends greatly on the position of the nodes closest to the interface in the discretisation. In fact, the jump is computed from node closest to the considered

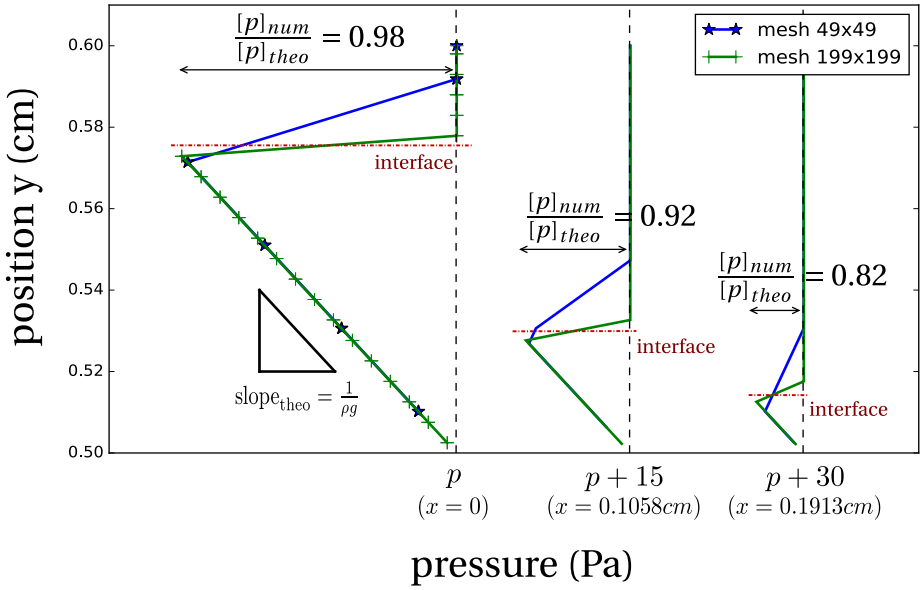

FIGURE 5.4 – Meniscus facing a wall - pressure profile at three x positions (see Fig. 5.3 translated with a pressure $n \times 15$ with $n = 0, 1, 2$.

abscissa on either side of the interface whereas it should be computed at the interface position. Therefore, the method used to compute the error tends to overestimate it. Both jumps are well described due to the enrichments [19] and [165]. The pressure average error is computed throughout the domain and is reported in Tab. 5.3 bringing the proof that the error decreases with the mesh size.

Mesh size (cm)	h=0.02	h=0.01	h=0.005
$\overline{\Delta_{press}}$ (Pa)	4.13×10^{-2}	6.12×10^{-3}	1.42×10^{-3}

TABLE 5.3 – Absolute error on the pressure field as a function of the mesh density - $\overline{\Delta_{press}} = \frac{1}{N_m} \sum_{i=1}^{N_m} |p^i_{\text{theo}} - p^i_{\text{num}}|$ with N_m the number of mesh nodes.

Finally, the velocity at the first increment is plotted in Fig. 5.5 (A). The initial interface is horizontal with a contact angle of 90°. This non-equilibrium at the triple point generates a velocity of magnitude 2.4×10^3 cm$\cdot$s^{-1}, making the meniscus rise in order to verify the contact angle. The Liquid/Vapour interface Γ_{LV} is pressured downwards by the air since the pressure in the liquid is lower, curving the interface. The meniscus continues to go up if the curvature is pronounced enough. The rise stops when the hydrostatic pressure due to the meniscus weight is balanced by the pressure jump from the surface tension action. At equilibrium, the velocities in the domain are associated with parasitic currents. Typically, they are located around the interface (not at the triple point) and are inherent to the linear approximation of the interface [92]. The maximum magnitude in this case is 3 cm$\cdot$s^{-1}, *i.e.* 0.13 % of the initial maximum velocity (2.4×10^3 cm$\cdot$s^{-1}), which can be considered as small and representative of the equilibrium state (see Fig. 5.5 (B)). The spurious velocities are small enough and do not degenerate the interface on the time intervals considered in this kind of simulations.

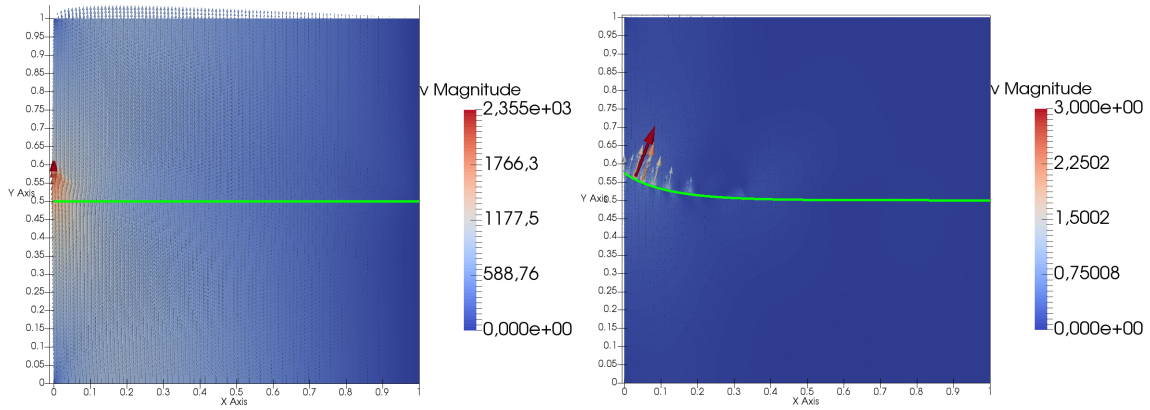

(A) at the first increment (glyph scale factor = 5×10^{-5})

(B) at the last increment (glyph scale factor = 5×10^{-2})

FIGURE 5.5 – Meniscus facing a wall - velocity field magnitude in [cm/s]

In Fig. 5.6, the position (ordinate) of the triple point is plotted over time for various time steps. Decreasing the time step does not change significantly the position and curves are overlaid on each other even during the first increments when the position changes rapidly - see closeup in Fig. 5.6. In that case a staggered algorithm (weak coupling) has been used and is satisfactory. The time at which the equilibrium state is reached depends on the quantity of fluid in

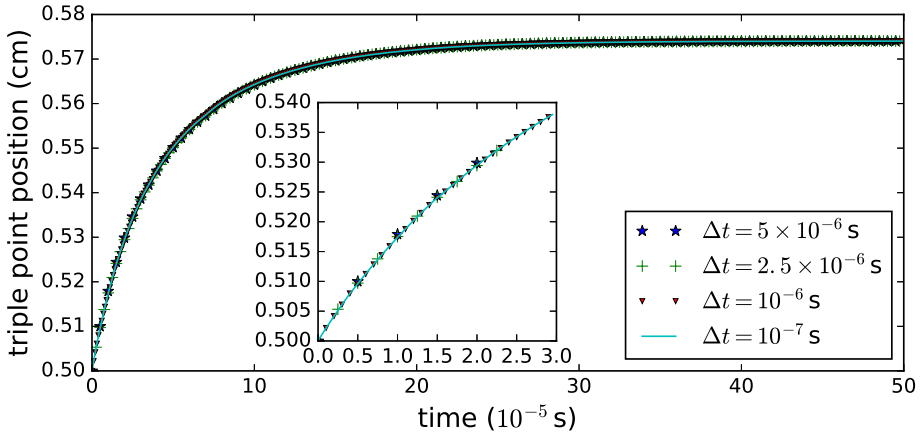

FIGURE 5.6 – Meniscus facing a wall - ordinate of the triple line during time with four different time steps.

the liquid phase. The amount of liquid in the column changes the transition dynamics. It is the reason why the full domain was represented in the PhD thesis of A. Pons [177], for the simulation of a meniscus between two plates to verify the Washburn law giving the height proportional to the square root of time.

Meniscus between two vertical walls

The previous case is extended by placing a second wall on the right-hand side of the domain, see Fig. 5.1. On the second wall, the same boundary conditions are imposed as on the first one: the normal velocity is equal to zero, $\boldsymbol{v} \cdot \boldsymbol{x} = 0$, and two surface energies γ_{SL} and γ_{SV} are considered. The distance between the two walls has to be smaller than the capillary length for

a meniscus to rise in between. That is why, the second wall is placed at the position $x = 0.1\,\text{cm}$. This case is symmetric with respect to the axis $x = 0.05\,\text{cm}$ plan of symmetry. In 2D, the simulation is run on the full domain in order to assess the symmetry of the numerical solution, whereas in 3D, for computational cost reason, the domain is reduced to half of the complete domain with a symmetry boundary condition $\boldsymbol{v} \cdot \boldsymbol{n} = 0$ at $x = 0.05\,\text{cm}$ (see Chap. 1.1.5 boundary condition (4)).

First in 2D, the FE simulation is carried out using a structured mesh, with a mesh size of $2 \times 10^{-3}\,\text{cm}$ in the x-direction and $5 \times 10^{-5}\,\text{m}$ in the y-direction, corresponding to 5,000 nodes. 1,000 increments are performed with a time step $\Delta t = 1 \times 10^{-6}\,\text{s}$. Fig. 5.7 shows a good agreement between FEM solution and semi-analytical solutions based on a minimisation of the energy or on the force equilibrium detailed in Sec. 1.4.3. The blue dotted curve with its ordinate scale on the right-hand side of the figure is the relative error between the FE and the semi-analytical solutions from force balance method. The maximum error corresponds to 0.012 % error on the meniscus height. Like for the case of a meniscus facing a vertical wall, the contact angle is correctly recovered by the FE simulation. The contact angle from the simulation is equal to 56.6° for a targeted theoretical contact angle of 55.5°, which is a 2% error. At the final time $t_f = 1 \times 10^{-3}\,\text{s}$, the system has reached its equilibrium state since the maximum magnitude velocity is $1.4\,\text{cm} \cdot \text{s}^{-1}$, which represents 0.05% of the maximal initial velocity magnitude ($2.8 \times 10^{3}\,\text{cm} \cdot \text{s}^{-1}$).

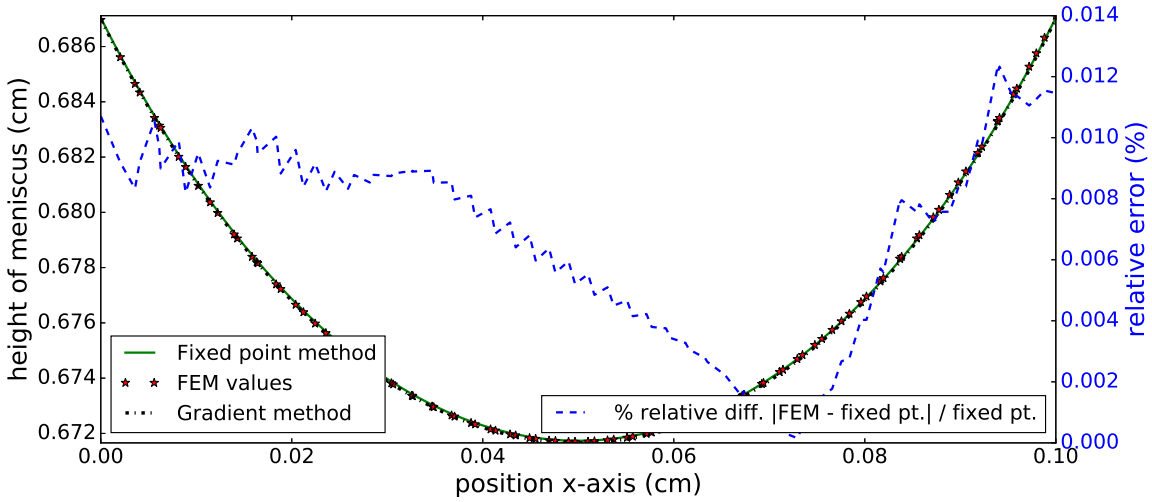

FIGURE 5.7 – Meniscus between two vertical walls 2D - comparison of the shape of the meniscus: FEM solution compared with semi-analytical solutions based on minimisation of energy (minmised with a gradient method) and force balanced (solved with a fixed point method)

Extension to 3D

Even if the case of a meniscus between two vertical walls is a 2D case, the full 3D simulation is run to assess the robustness of the method. The domain is extruded in the z-direction, and the new domain is $\Omega = [0, 0.05] \times [0, 0.5] \times [0, 0.1]$. The initial interface is placed at position $y = 0.15$ since the computational domain is reduced. This influences the boundary condition at the bottom $y = 0$ since the height of the liquid column has changed, $p_{ext} = g(0.15\rho_L + 0.35\rho_V) =$

1.14×10^4 Pa, representing the hydrostatic pressure. 1000 increments are carried out with a time step $\Delta t = 1 \times 10^{-6}$ s, on a unstructured mesh with 32235 nodes. Fig. 5.8 represents the evolution

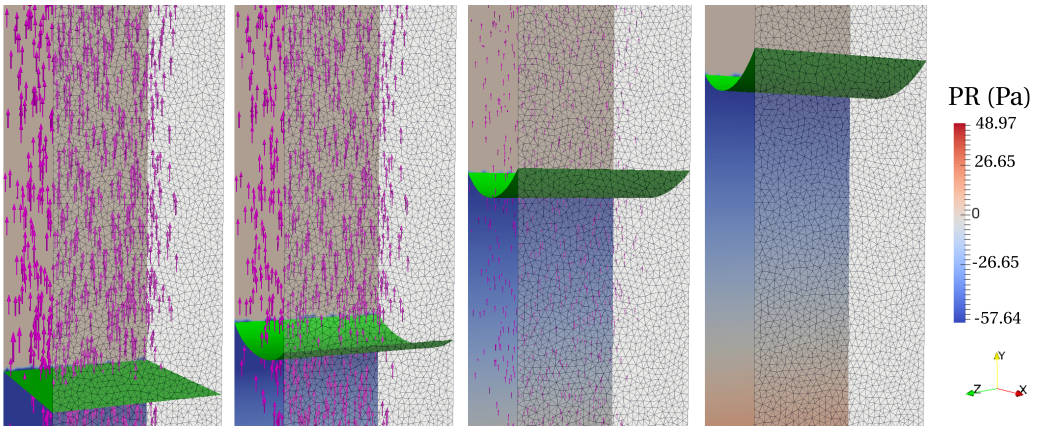

(A) $t = 0s$ (B) $t = 1 \times 10^{-4}$ s (C) $t = 2 \times 10^{-4}$ s (D) $t = 1 \times 10^{-3}$ s

FIGURE 5.8 – Meniscus between two vertical walls 3D - FE solution at 4 times of the simulation. The first wall (foreground) is represented by its mesh and the second wall (background) is opaque with piecewise linear pressure field. The velocity is represented by the magenta arrows ($\|\boldsymbol{v}\|_{max} = 2.6 \times 10^3\,\mathrm{cm \cdot s^{-1}}$ for (A) and $\|\boldsymbol{v}\|_{max} = 6.4\,\mathrm{cm \cdot s^{-1}}$ for (D)) and the liquid-vapour interface is represented by the green surface.

of the velocity and pressure fields during the simulation. Only half of the domain is computed but on the figure, the complete domain with the two walls in reconstructed symmetrically during the post-processing step. The subplot (*A*) is the initial solution to the fluid problem. The velocity is plotted with magenta arrows with a maximum of magnitude equal to $2.6 \times 10^3\,\mathrm{cm \cdot s^{-1}}$. Two intermediate times are presented in subplots (B) and (C), where progressively the magnitude of the velocity field decreases and the meniscus is going up between the walls. The last subplot (D) has a smaller velocity magnitude, $6.4\,\mathrm{cm \cdot s^{-1}}$ (0.2% of the maximum of the initial velocity). The interface represented in green can be considered as steady (in the time interval $[0, 10^{-3}\,\mathrm{s}]$. The piecewise linear pressure is drawn on the opaque background wall. Across the interface, the abrupt change represent the jump of pressure due to the curvature of the meniscus. Under the meniscus, the pressure increases linearly and proportionally to the liquid density.

Following the first 2D analyses, the flow front position can be measured in 3D. Fig. 5.9 presents the computational result obtained in half of the physical domain (a symmetrical boundary condition is placed at $x = 0.05\,\mathrm{cm}$ to represents the second wall placed at position $x = 0.1\,\mathrm{cm}$). The FE simulation of the position (ordinate) of the interface at equilibrium is compared with the two semi-analytical solutions. The absolute error is plotted in dash blue. In 3D the error is larger than in 2D, due to a coarser mesh: the characteristic mesh size is $h_e = 4 \times 10^{-3}\,\mathrm{cm}$ in 3D, while $h_e = 2 \times 10^{-5}\,\mathrm{cm}$ and $h_e = 5 \times 10^{-5}\,\mathrm{cm}$ in respectively the x–and y–directions in 2D. Finally, the static contact angle is recovered: 57.2° for a theoretical angle of 55.5°, representing an error of 3%.

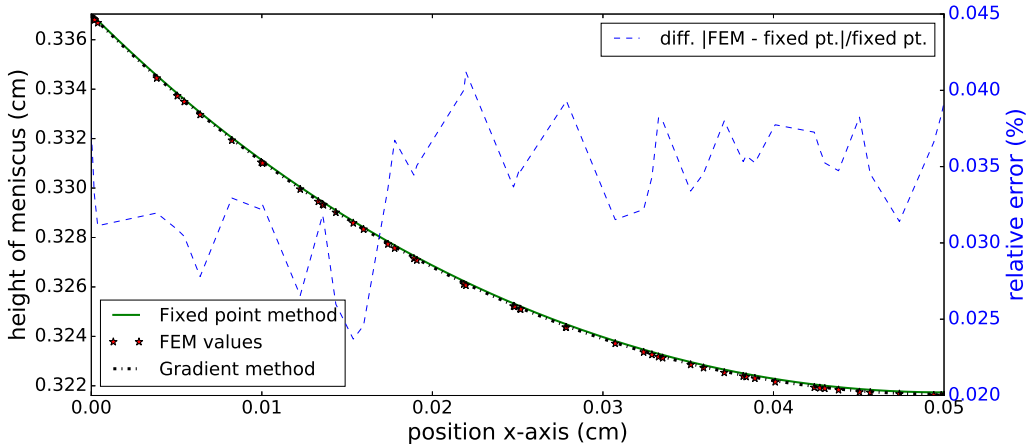

FIGURE 5.9 – Meniscus between two vertical walls 3D - comparison of the shape of the meniscus: FE solution compared with semi-analytical solutions based on minimisation of energy (minimised with a gradient method) and force balanced (solved with a fixed point method)

3D cases are by essence more complex, in terms of configurations possible for the interface when splitting the element, but also for evaluating the integral at the triple junction, since this junction is a point in 2D and a line in 3D. Based on weakly couple fluid and level-set solver, the presented numerical method is able to describe the position of an interface at equilibrium in 2D and 3D, in close agreement with the semi-analytical and analytical solutions.

5.1.2 Benchmark on 2D bubble dynamics

A quantitative 2D numerical benchmark for capillarity is proposed in literature [122]. The benchmark aims to validate and compare interfacial flow codes. Our test case reproduces and compares results with the benchmark. The case is a bubble rising in a liquid due to gravity while the shape of the bubble undergoes deformations driven by capillary action. Note that this case does not exhibit triple junction, since only two phases, liquid and vapour, are present. Both fluids are incompressible. The objective is therefore to test the Stokes and Navier-Stokes solvers with surface tension. A 3D extension is given in [6], whereas similar benchmark are given for diffuse interface model [9] or lattice-Boltzmann / level-set approach [188].
The governing incompressible Navier-Stokes equations are solved incrementally in the space-time domain $\Omega \times [0, t_f]$. A surface tension force is applied between the liquid and vapour subdomain of Ω. The domain and the initial boundary conditions are represented in Fig. 5.10. The pressure is imposed as a Dirichlet boundary condition at the top boundary $y = 2$ to ensure the uniqueness of the solution. The physical parameters and dimensionless numbers of this test case are reported in Tab. 5.4. Both dimensionless numbers (Reynolds and Eötvös numbers

ρ_L	ρ_V	μ_L	μ_V	g	γ_{LV}	$\mathscr{R}e$	Eo	ρ_L/ρ_V	μ_L/μ_V
1000	100	10	1	0.98	24.5	35	10	10	10

TABLE 5.4 – Input data for the simulation of the cluster of tubes

(also called Bond number)) are based on the characteristic length $L = 2r_0$ with r_0 the radius of

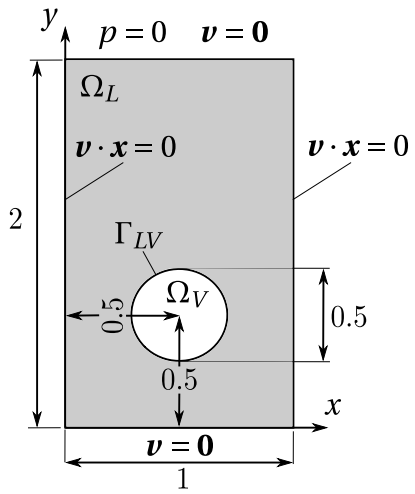

FIGURE 5.10 – Benchmark bubble - computational domain and boundary conditions

the bubble. Also they involve a characteristic velocity, $V = \sqrt{2gr_0}$ the gravitational velocity

$$\mathscr{R}e = \frac{\rho_L V L}{\mu_L}, \qquad Eo = \frac{\rho_L V^2 L}{\gamma_{LV}} \tag{5.2}$$

with numerical values reported in Tab. 5.4. The simulation is run during three units of dimensionless time $t_f = 3$. According to experimental data [60], the bubble should rise in an ellipsoidal regime. The Reynolds number indicates that the full Navier-Stokes equations has to be solved. The Eötvös number points out that capillary effects are higher than gravity effects, leading to no break up of the bubble.
In the purpose of validating the method, four quantities are analyzed:

— Position of the interface at the end of the computation

— Bubble centre of mass position or centroid defined as

$$\boldsymbol{X}_c = (x_c, y_c) = \frac{\int_{\Omega_V} \boldsymbol{x} dV}{\int_{\Omega_V} dV} \tag{5.3}$$

where $\boldsymbol{x}$ is the position. Among many over possibilities the centre of mass position is commonly used [55, 160] to study the position of objects with complex geometry.

— Circularity, defined as the ratio of the perimeter of the area-equivalent circle over the perimeter of the bubble

$$c = \frac{\text{equivalent perimeter}}{\text{perimeter of the bubble}} \tag{5.4}$$

This ratio is derived in 2D from [216].

— Rising velocity computed with the average velocity in the vapour phase

$$\boldsymbol{V}_c = (v_{cx}, v_{cy}) = \frac{\int_{\Omega_V} \boldsymbol{v} dV}{\int_{\Omega_V} dV}. \tag{5.5}$$

This parameter enables to assess the behaviour of the global solution and not only the interface.

As shown in Fig. 5.11, the Stokes solution depicts a bubble rising faster than the Navier-Stokes solution. Actually, inertial effects are taken into account in the latter case tending to slow down the motion at the first times of the rise. Only the Navier-Stokes solution is analysed in more details later for comparison with literature. After departing from its initial position, the bubble takes the shape of a half circle, with the bottom segment bended inside (at $t = 1.5$). Finally, the bubble takes its final "ellipsoidal"-like shape with a constant sign for the curvature (see $t = 2.7$).

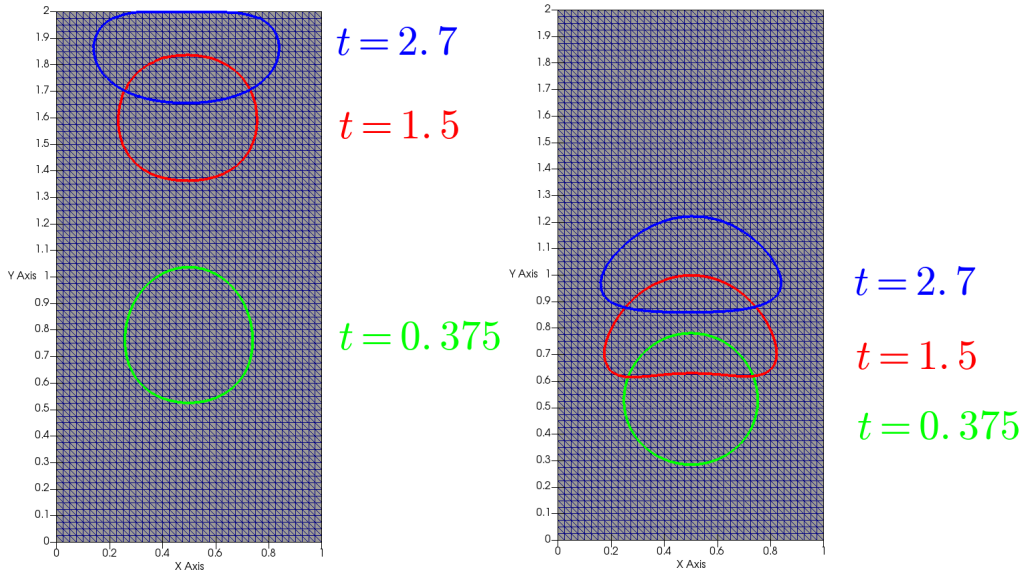

(A) Stokes solution (B) Navier-Stokes solution

FIGURE 5.11 – Benchmark bubble - comparison between Stokes and Navier-Stokes solutions

Reference solutions are extracted manually from the pdf version of benchmark article [122]. Therefore, the comparison with the article data (either TP2D, FreeLife or MooMMD solvers) is given only as an indication since it is not the raw data from the article. 2000 time increments ($\Delta t = 1.5 \times 10^{-3}$) are performed on a structured mesh with a mesh size $h_e = 1/40$ corresponding to the coarser grid of the benchmark [122]. The convergence criterion is 10^{-4} for the relative residual of the Navier-Stokes solver. The level-set is filtered with a filter width equals to three times the mesh size. At $t = t_f$, the final position of the interface is given in the subplot (A) of Fig. 5.12. The solution from the article is superimposed on our computed numerical solution (Zebulon). All the three solvers from the article converge towards a common interface solution when refining the mesh and the time step. Our FE solution on the coarse mesh is compared with the solution on both coarse and the finest grid in the benchmark for assessing the robustness of the method. Obviously, comparison with the finest grid may yield discrepancy.
The average quantities such as the centre of mass of the bubble and the velocity rise are plotted in the sub-figures (B) and (D) respectively. The circularity of our Zebulon FE solution agrees with the converged circularity from the paper during the first half of the simulation. However, a constant discrepancy appears during the second half. It may be due to a variation of mass in our case which increases during the second half of the simulation. Despite increasing, the mass loss stay low at the end of the simulation (3% of mass is loss during the computation). Mass is conserved in the article for the three solvers. Groups TP2D and FreeLife used an interface to

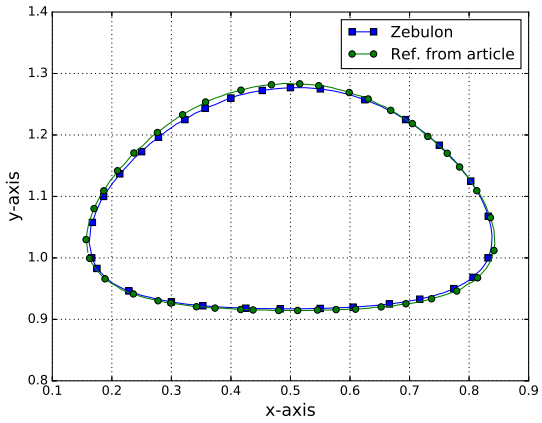

(A) Interface position

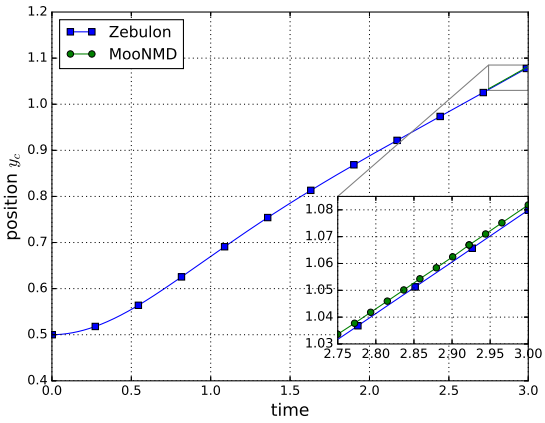

(B) center of mass position

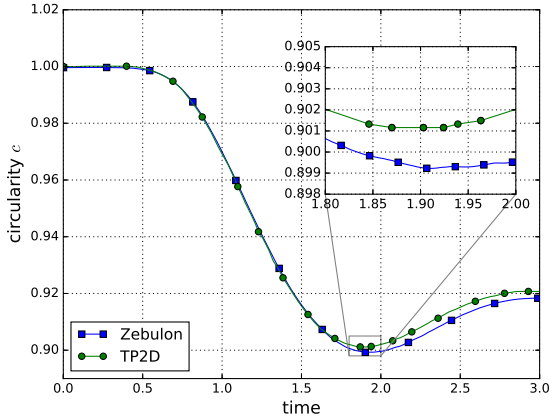

(C) circularity

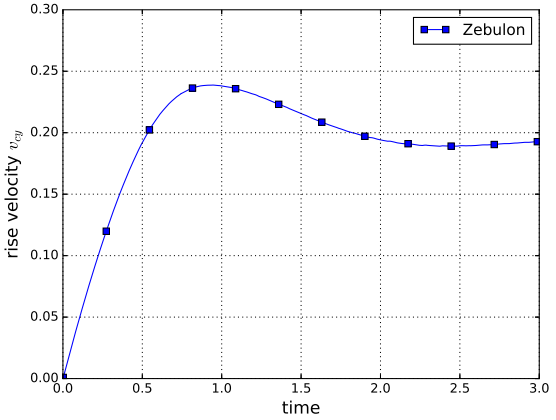

(D) vertical velocity rise

FIGURE 5.12 – Benchmark bubble - data for cross-comparisons

track the position of the bubble and perform a correction step after reinitialisation. The third group, MooNMD uses a fitted mesh in a Lagrangian manner to follow the interface with naturally stable elements. In our case, no such refinements are implemented to keep oriented users method, *i.e.* with as few as possible tunable parameters. Our results may be enhanced when refining the mesh size and time step which will help to conserve the mass.

A quantitative comparison is presented in Tab. 5.5 between the three solvers and our method. All these results are obtained on the coarser mesh $h_e = 1/40$. The minimal value for the circularity is reported in the first line of the table and the time when the minimal circularity is reached, reported in the second line. The maximal y-velocity of the bubble centre is reported in the third line and the corresponding time in the fourth line. Finally, the centroid ordinate is in the last line at the final time $t_f = 3$. The values reflect well that our approach gives results comparable to other methods.

5.1.3 Cluster of tubes

The last validation case is a 3D simulation of a liquid rising inside a cluster of tubes (Fig. 5.13). The cluster is made of ten vertical and parallel glass tubes clamped in an horizontal plate.

TABLE 5.5 – Benchmark bubble - cross-comparison of particular time and values

Group	1 (TP2D)	2 (FreeLIFE)	3 (MooNMD)	us (Zebulon)
c_{min}	0.9016	0.9060	0.9022	0.8982
$t\|_{c=c_{min}}$	1.9234	1.8375	1.8630	1.9095
$v_{cy,max}$	0.2418	0.2427	0.2418	0.2388
$t\|_{v_{cy,max}}$	0.9141	0.9000	0.9236	0.9435
$y_c(t=3)$	1.0818	1.0715	1.0833	1.0798

The tubes are immersed in two fluids, a liquid, at the bottom, and air at the top. Contrary to the case of meniscus between plates, geometry is an obvious challenge. This case is designed to test the model with a complex geometry, with a second curvature on the solid due to the cylindrical shape of the tubes. Input physical parameters in the model are reported in Tab. 5.6. This last case of the subsection has no analytical solution and it embodies a first step towards concluding physical results only based on the simulation.

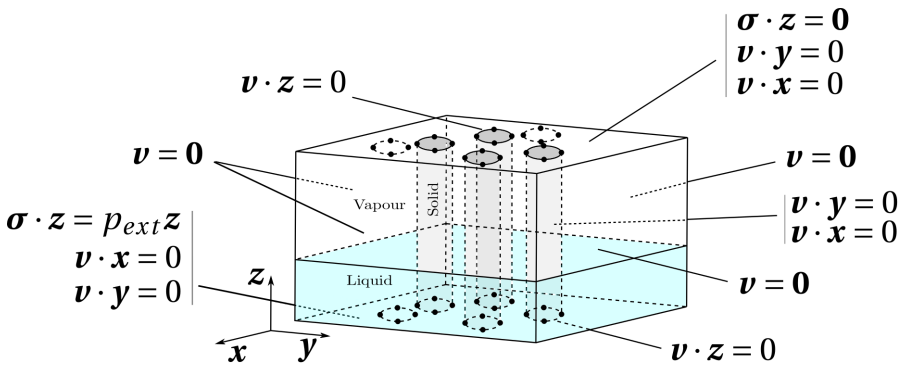

FIGURE 5.13 – Cluster of tubes - computational domain and boundary conditions

	Solid/Vapour - γ_{SV}	Solid/Liquid - γ_{SL}	Liquid/Vapour - γ_{LV}
Surface tension / energies ($\mathrm{N\cdot m^{-1}}$)	60.93×10^{-3}	30.03×10^{-3}	72.8×10^{-3}

	Vapour	Liquid
Viscosity ($\mathrm{Pa\cdot s}$)	1.71×10^{-5}	1×10^{-3}
Density ($\mathrm{kg\cdot m^{-3}}$)	1.292	1×10^{3}

TABLE 5.6 – Input data for the simulation of the cluster of tubes

Fig. 5.13 introduces the boundary conditions. On the lateral faces of the bounding box the velocity is homogeneously imposed with a homogeneous Dirichlet condition $\boldsymbol{v}=\boldsymbol{0}$. This condition has no effect on the solution since the boundary is far enough from the zone of influence of the meniscus. Indeed, the minimum distance from a tube to a side wall is at least tree times the capillary length $\kappa^{-1}\approx 0.27\,\mathrm{cm}$. The velocity is not sheared at the inlet and outlet (bottom and top) since both tangential velocities, $\boldsymbol{v}\cdot\boldsymbol{x}$ and $\boldsymbol{v}\cdot\boldsymbol{y}$ are equal to zero. At each end of the tubes (belonging also to the inlet and outlet boundary), the velocity in the z-direction is set to zero

with a homogeneous Dirichlet condition in order to remove the tangent term appearing when integrating by parts the surface integrals (see Chap. 4.2.1). This choice has no influence on the steady state solution. The velocity on each tube is set to zero in both x and y directions. This condition is a little more restrictive than a simple no-penetration condition $\boldsymbol{v} \cdot \boldsymbol{n} = 0$. Therefore the fluid is slipping only along the z-direction when the meniscus is rising. Those choices make the simulation more robust and have no influence on the steady state solution. Finally, the hydrostatic pressure is imposed at the inlet accounting for the weight of the two fluids. The pressure on the outlet face is set to zero through a Neumann boundary condition.

The mesh shown in Fig. 5.14, has three different refinement regions (denoted 1, 2 and 3 in the figure). The local refinement enables to place a higher number of unknowns around the interface, aiming at the accuracy of the interface representation, especially in regions with a high curvature. To do so, a first computation has been run with a coarse mesh with the refinement number 2 nearby the tubes to extract a rough location of the interface at equilibrium. A refinement has been applied from the rough location (1 and 3) and a the simulation has been recomputed. 100 increments are performed with a time step of $\Delta t = 5 \times 10^{-6}$ s on the mesh from Fig. 5.14 containing 91,701 nodes. For information purposes only, it takes about 16 hours to run this case on a single core desktop processor.

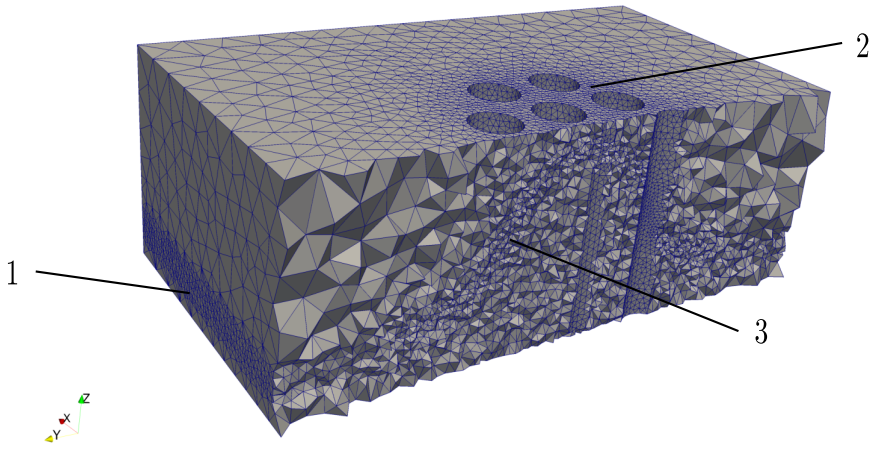

FIGURE 5.14 – Cluster of tubes - mesh

The meniscus at equilibrium is plotted in Fig. 5.15. Glass tubes are represented in transparent gray in the centre and the interface Γ_{LV} is represented in green. The water under the meniscus is colored in light blue. The maximal velocity at the beginning is located at the triple line with a value of 3.3×10^3 cm$\cdot$s^{-1} when at the end of the simulation the maximal value is 2.5×10^2 cm$\cdot$s^{-1} as shown in Fig. 5.16. The meniscus in the centre of the cluster goes up taking advantage of the confined medium with a distance between the tubes lower than the capillary length. On the external fibres of the cluster, a standard meniscus is formed and vanishes on the lateral boundaries.

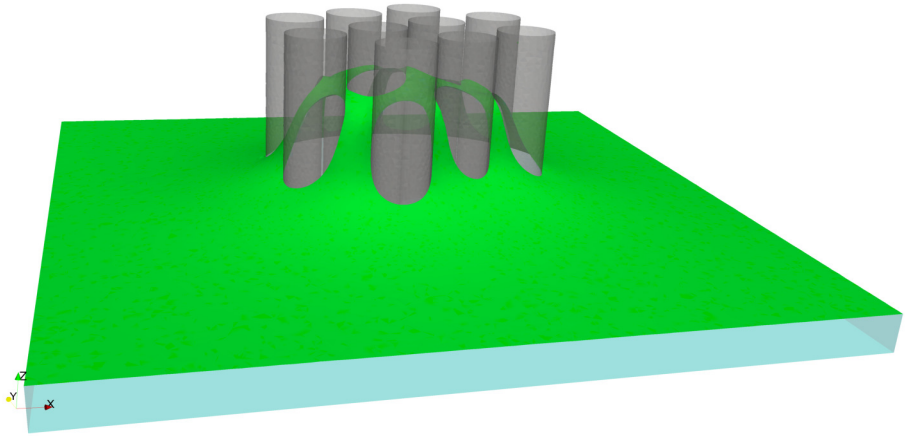

FIGURE 5.15 – Cluster of 10 tubes - equilibrium position of the front of fluid

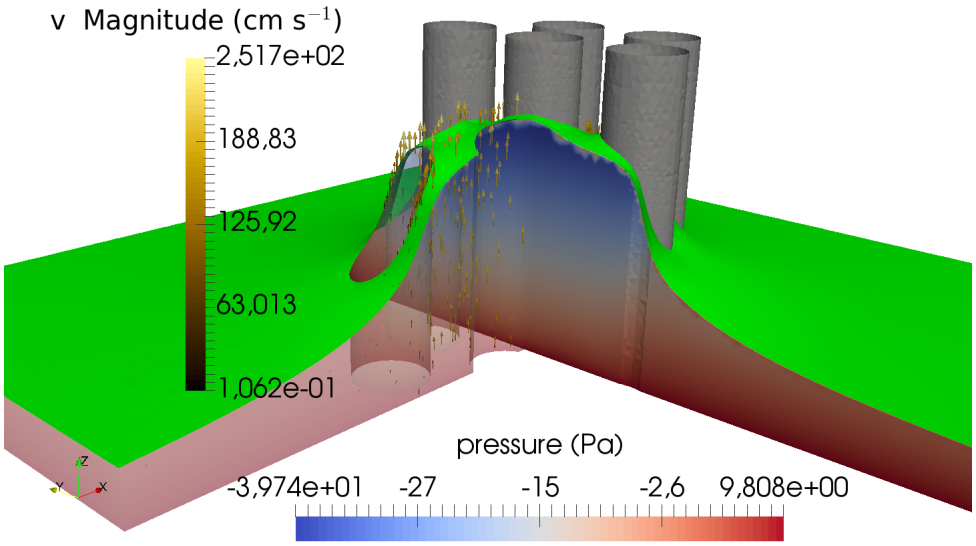

FIGURE 5.16 – Cluster of 10 tubes - velocity and pressure field at $t = t_f$

5.2 Microstructure analysis

After validating the method describing capillary action, the focus is set on the scale-up of permeability and capillary pressure. Firstly, two methods to compute the numerical permeability are derived. The first method is based on the Darcy equation written in flow rate. The second method based on the drag force definition yields an upper bound for the numerical permeability. Secondly, a capillary pressure is computed from the fibre scale to the part scale. Two techniques are presented for the scale-up of the capillary pressure. The first approach assumes that in the same time interval, the same distance is covered by the fluid front with the Stokes and Darcy modellisations. The second method is based on the equality of the work done in Stokes and Darcy by the surface tension forces and capillary pressure respectively.

5.2.1 Numerical permeability

Numerical permeability may be computed from volume averaging in the fluid domain. First, let us present volume averaging equations establishing a link between the Stokes and Darcy equations. The permeability is computed using a saturated flow (*i.e.* with only one phase - the liquid resin).

Volume averaging equations

Let us consider a quantity B defined on a volume $\Omega = \Omega_L \cup \Omega_S$ made up of liquid (resin) and solid (fibres), with $V = \int_\Omega dV$ the total volume and $V_f = \int_{\Omega_L} dV$ the fluid volume. The domain Ω (with characteristic length l_d) belongs to a homogeneous domain of characteristic length l_p, as defined in Fig. 5.17. The following averages represent local information in the homogeneous medium and the condition $l_p \gg l_d$ has to be met. The spatial average of this quantity is defined as

$$< B >= \frac{1}{V} \int_{\Omega_L} B \, dV \tag{5.6}$$

whereas, the same average relative to the fluid volume is

$$< B >^L = \frac{1}{V_L} \int_{\Omega_L} B \, dV. \tag{5.7}$$

The relation between the liquid average and the average in the domain is given through the porosity coefficient $\Phi = V_L/V$ and it reads $< B >= \Phi < B >^L$. Furthermore, the need to interchange differentiation and integration leads to the spatial averaging theorem

$$< \nabla B >= \nabla < B > + \frac{1}{V} \int_{\Gamma_{SL}} \boldsymbol{n}_{LS} B \, dS \tag{5.8}$$

with the normal pointing outside the fluid domain and Γ_{SL} the fibres interfaces embedded in the domain Ω. According to Whitaker [222], this theorem represents a three-dimensional version of the Leibniz rule for interchanging differentiation and integration. The theorem has been proved independently in 1967 [16, 145, 197, 221]. Other derivations have been proposed in literature [78, 100, 115, 181, 220] and the spatial averaging theorem may be generalised to a tensorial quantity $\boldsymbol{B}$

$$< \nabla \cdot \boldsymbol{B} >= \nabla \cdot < \boldsymbol{B} > + \frac{1}{V} \int_{\Gamma_{SL}} \boldsymbol{n}_{LS} \cdot \boldsymbol{B} \, dS \tag{5.9}$$

As shown in Fig. 5.17, the volume average equations homogeneise the subscale flow for a given position x in the homogeneous domain. In order to be clear about the gradient of the average (the second term in Eq. 5.8) the partial derivative of $< B >$ with respect to coordinate x is

$$\frac{\partial < B >}{\partial x} = \lim_{\Delta x \to 0} \left(\frac{< B > [x + \Delta x] - < B > [x]}{\Delta x} \right). \tag{5.10}$$

The spatial derivative is only defined at the homogeneous medium scale. In our case, it may represent the variation of the pressure average in the case of a fibre volume fraction changing along the x-axis in the Darcy medium. The quantity of interest may be averaged in space as presented, but also in time. However, the time average is not needed in the case of a saturated Stokes flow since it is a steady flow.

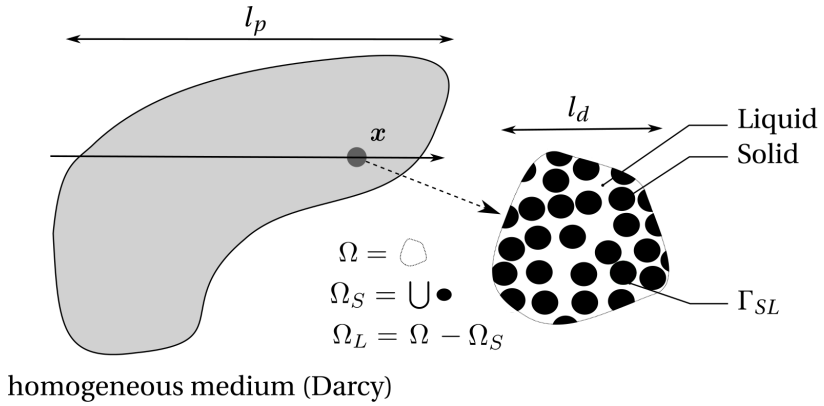

FIGURE 5.17 – Homogeneisation - domain definition

Averaging Stokes equations

Let us begin with the continuity equation, reduced in the case of an incompressible fluid, to the divergence free condition $\nabla \cdot \boldsymbol{v} = 0$. Using the volume averaging theorem Eq. 5.9, it comes

$$\nabla \cdot < \boldsymbol{v} >= -\frac{1}{V} \int_{\Gamma_{SL}} \boldsymbol{n}_{LS} \cdot \boldsymbol{v} \, dS \tag{5.11}$$

where Γ_{SL} represents the boundary with the liquid and all the fibres. The term $\int_{\Gamma_{SL}} \boldsymbol{n}_{LS} \cdot \boldsymbol{v} \, dS$ may take into account a flow at a lower scale such as in the case of a flow at the mesoscale between fibre tows. At the fibre scale, the fibres are impermeable solids, without normal velocity on their contours ($\boldsymbol{v} \cdot \boldsymbol{n} = 0$ condition). The previous equation may be simplified, and it reads

$$\nabla \cdot < \boldsymbol{v} >= 0 \tag{5.12}$$

in the case of impermeable solid fibres.
From the average of momentum balance equation without any external force, it comes

$$\nabla \cdot < \boldsymbol{\sigma} > + \frac{1}{V} \int_{\Gamma_{SL}} \boldsymbol{\sigma} \cdot \boldsymbol{n}_{LS} \, dS = 0 \tag{5.13}$$

The stress tensor may be split into a deviatoric component $2\mu\dot{\boldsymbol{\epsilon}}$ and a spherical component $-p\boldsymbol{I}$. To be consistent with the Darcy's law and experiments, which considers only the fluid pressure, the new unknown is the pressure average in the fluid domain using $< p >= \Phi < p >^L$ with the upper script $\bullet^L$ representing the average relative to the fluid volume as defined in Eq. 5.7. Therefore, Eq. 5.13 leads to

$$\nabla \cdot < 2\mu\dot{\boldsymbol{\epsilon}} > -\Phi \nabla < p >^L + \frac{1}{V} \int_{\Gamma_{SL}} \boldsymbol{\sigma} \cdot \boldsymbol{n}_{LS} \, dS = 0, \tag{5.14}$$

because the gradient of the porosity is supposed to be zero for an homogeneous medium such as in a Darcy volume element with a constant fibre volume fraction *i.e.* $< p >^L \nabla\Phi = 0$. The

deviatoric component of the averaged stress is written as follows

$$< 2\mu\dot{\boldsymbol{\epsilon}} >= \mu \left[\nabla < \boldsymbol{v} > + (\nabla < \boldsymbol{v} >)^T + \frac{1}{V} \underbrace{\int_{\Gamma_{SL}} (\boldsymbol{v} \otimes \boldsymbol{n} + \boldsymbol{n} \otimes \boldsymbol{v}) \, dS}_{=\mathbf{0}} \right] \tag{5.15}$$

since $< (\nabla \boldsymbol{v})^T >= (< \nabla \boldsymbol{v} >)^T$ and no-slip condition is imposed on the fibres. By taking the divergence of the last equation (Eq. 5.15) and recalling $\nabla \cdot (\nabla < \boldsymbol{v} >) = \Delta < \boldsymbol{v} >$ and $\nabla \cdot (\nabla < \boldsymbol{v} >)^T = \nabla (\nabla \cdot < \boldsymbol{v} >)$, it comes

$$\nabla \cdot < 2\mu\dot{\boldsymbol{\epsilon}} >= \mu \Delta < \boldsymbol{v} > \tag{5.16}$$

since the divergence of the average velocity is null for an incompressible fluid. Finally, the averaged momentum equation reads

$$\mu \Delta < \boldsymbol{v} > -\Phi \nabla < p >^L - \boldsymbol{f}_d = 0 \tag{5.17}$$

with $\boldsymbol{f}_d = -\frac{1}{V} \int_{\Gamma_{SL}} \boldsymbol{\sigma} \cdot \boldsymbol{n}_{LS} \, dS$ the normal stress exerted by the fluid on the fibres. According to literature [173, 208], based on the Buckingham π-theorem [142] and a dimensional analysis, the viscous drag force $\boldsymbol{f}_d$ is modelled for solid fibres when neglecting the inertia by

$$\boldsymbol{f}_d = \frac{\Phi \mu}{K} < \boldsymbol{v} > \tag{5.18}$$

where K is the permeability. Therefore, the macroscopic equation becomes

$$\mu \Delta < \boldsymbol{v} > -\Phi \nabla < p >^L - \frac{\Phi \mu}{K} < \boldsymbol{v} >= 0 \tag{5.19}$$

which is well known as the Brinkman's equation [43]. Hypothesising that the viscous term is negligible compared to the drag force from the fibres, leads to the Darcy's equation

$$< \boldsymbol{v} >= -\frac{K}{\mu} \nabla < p >^L \tag{5.20}$$

Permeability computation - method 1

The permeability may be computed from the Darcy's equation based on the flow rate across a surface S, driven by the hydraulic gradient imposed over a domain of length L. The Darcy's equation written in term of flow rate is

$$Q = \frac{K}{\mu} |S| \frac{p_{in} - p_{out}}{L} \tag{5.21}$$

with Q the flow rate across a surface as shown in Fig. 5.18. In case of flows at the fibre scale, the flow rate is computed on the real microstructure in the flow direction using the formula $Q = \int_S \boldsymbol{v} \cdot \boldsymbol{n} \, dS$.

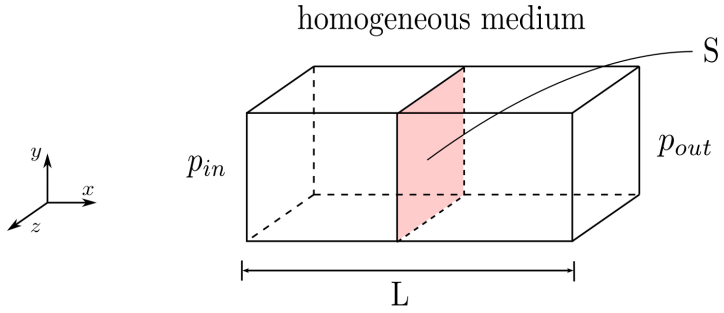

FIGURE 5.18 – Homogeneisation - numerical permeability from Darcy flow rate

Permeability computation - method 2

Darcy's law, applicable at the macroscopic scale, is based on a parameter named permeability, which may be computed from the drag force definition in a porous medium (Eq. 5.18). The assumption is made that the viscous effect is negligible compared to the dissipation due to the drag force. As before, only the hydrostatic part of the fluid stress is of interest, leading to

$$\begin{aligned}\frac{1}{V}\int_{\Gamma_{SL}} \boldsymbol{\sigma}\cdot\boldsymbol{n}\,dS = -\frac{1}{V}\int_{\Gamma_{SL}} p\boldsymbol{n}\,dS = -\frac{1}{V}\int_{\Omega_L}\nabla p\,dV = -<\nabla p> \\ \overset{def}{=} \frac{\Phi\mu}{K}<\boldsymbol{v}>.\end{aligned} \tag{5.22}$$

The permeability is computed using the relation for an unidirectional flow of principal direction i

$$K = -\mu\Phi\frac{<\boldsymbol{v}>_i}{<\nabla p>_i} = -\mu\Phi\frac{\int_{\Omega_L} v_i\,dV}{\int_{\Omega_L}\nabla_i p\,dV} \tag{5.23}$$

Contrary to the previous method based on global parameters (Eq. 5.21) ; this method integrates local variations in the inter-fibre spaces. This is the main difference between the two methods, and that is why it is not expected to recover exactly the same value for the computed permeability. Numerically, it may be verified that $QL \approx \int_\Omega dV <\boldsymbol{v}>_i$ for an incompressible fluid. Therefore, the discrepancy comes from the pressure since numerically it is verified that

$$\frac{p_{in}-p_{out}}{L} \neq \frac{1}{\Phi}\frac{1}{V_L}\int_{\Omega_L}\nabla_i p dV \tag{5.24}$$

Due to its local definition, the second method based on the drag definition is able to capture the pressure field inside the domain. Let us notice that both methods are equivalent when the pressure is linear in the domain. In the case of a fibrous medium, fibres modify the pressure field creating the discrepancy between the two methods. This second method based on the drag definition gives an upper bound for the permeability value. Contrary to the Darcy's equation 5.20, in the second method the gradient of the pressure average is transformed into the average of the pressure gradient. This equivalence is valid if the hydrostatic component of the drag force on the fibres are neglected, *i.e.* $\sum_{j=0}^{\#\text{fibres}}\int_{\text{fibre}_j}\boldsymbol{n}_{LS}p\,dS \approx 0$. Actually, for a flow in the y-direction as it will be investigated, the pressure decreases with y therefore each integral in the sum is positive since the normal is out-going $\frac{1}{V}\int_{\Gamma_{SL}} n_y p\,dS > 0$. Based on Eq. 5.8, the inequality when

switching integral and derivatives is

$$\begin{aligned} \underbrace{\nabla_y < p > + \frac{1}{V}\int_{\Gamma_{SL}} n_y p \, dS}_{=<\nabla_y p>} \quad &> \quad \nabla_y < p > \\ 0 \quad &> \quad \left(< \nabla_y p >\right) \quad > \quad \left(\nabla_y < p >\right) \end{aligned} \tag{5.25}$$

Therefore, inversing the inequality Eq. 5.25 and multiplying by the negative quantity $-\mu\Phi < \boldsymbol{v}\cdot\boldsymbol{y} >$ leads to

$$\underbrace{-\mu\Phi\frac{< \boldsymbol{v}\cdot\boldsymbol{y} >}{< \nabla_y p >}}_{K_{meth.2}} \quad > \quad \underbrace{-\mu\Phi\frac{< \boldsymbol{v}\cdot\boldsymbol{y} >}{\nabla_y < p >}}_{K} \tag{5.26}$$

Finally, in the specific case presented in the following section, the permeability computed based on the drag modelling has a larger value than the one computed from Darcy equation *i.e.* $K_{\text{meth. 2}} > K_{\text{meth. 1}}$. Computing an upper bound for the permeability is still an interesting point since a permeability variability may be observed experimentally [210].

5.2.2 Numerical experiments

Numerical permeability can be computed using one of the two methods presented in the previous paragraph. Both methods need a geometrical description of the microstructure in order to compute the fluid flow (velocity and pressure), from which a numerical permeability is computed. In this subsection, two types of microstructures are generated. The first one has the fibre positions randomly generated for a given volume fraction of fibre and constant radius with a circular shape. The second microstructure is made up of a regular hexagonal packing with the same circular fibre radius.

Randomly generated microstructures

Microstructures have been randomly generated by C. Mattrand based on a Fourier expansion [147] to determine their positions. Two fibre volume fractions τ_f are considered 30% and 45%. The porosity is related to the fibre volume fraction by $\tau_f = 1 - \Phi$. The purpose is first to assess the influence of the domain size on the numerical permeability. The size of a Representative Elementary Volume (VER) for the permeability is the size above which the variation in permeability is only due to statistical fluctuations.
Fibres have a constant radius of $20\bar{x}$, where $\bar{x}$ is the computational unit length. For each five domain sizes ($200\bar{x}$, $400\bar{x}$, $600\bar{x}$, $800\bar{x}$ and $1000\bar{x}$) considered here, 15 fibre placement draws are made for a constant fibre volume fraction. All together, for a given fibre volume fraction $15 \times 5 = 75$ simulations are run. The randomly generated microstructures are periodic, and boundary conditions are given in Fig. 5.19. For each simulation, the numerical permeability is computed in the flow direction. As shown in Fig. 5.20, the flow direction is along the y-axis, from bottom to top. 11 randomly generated streamlines are represented and coloured with the pressure values. Numerical permeabilities are represented in Fig. 5.21. The standard deviation is represented by the blue line and the mean value by a green dot. Both methods have a decreasing standard deviation when increasing the size of the domain in good agreement with results from Narsilio *et al.* [155]. The method based on the drag modelling (*c.f.* Sec. 5.2.1) gives larger

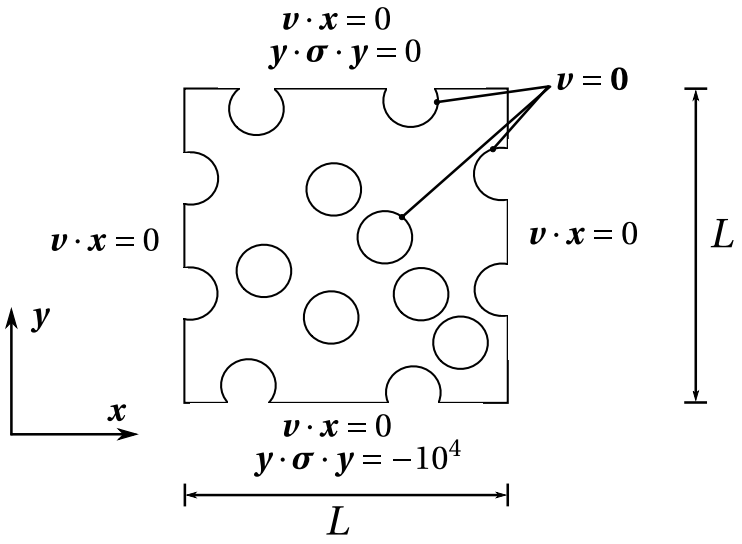

FIGURE 5.19 – Numerical permeability - boundary conditions

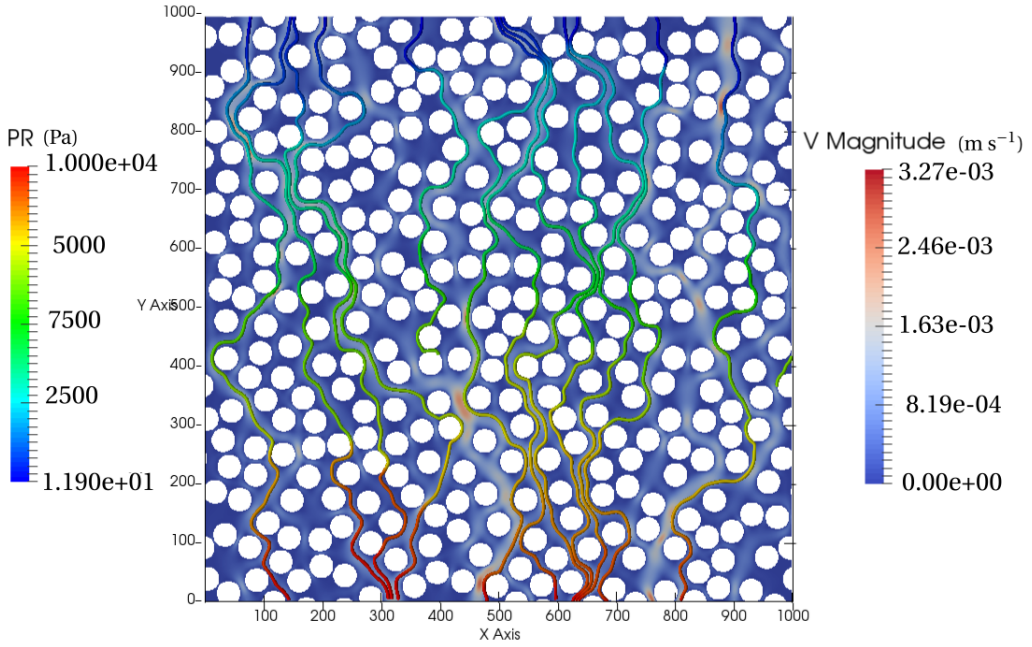

FIGURE 5.20 – Numerical permeability - Flow and streamlines in the domain $\Omega = [0, 1000\bar{x}] \times [0, 1000\bar{x}]$

values as predicted (more than two times higher) than the method based on the flow rate of Darcy equation (*c.f.* Sec.5.2.1).

In the case of fibrous reinforcement, the radius of fibre is around 5 µm. Recalling that the fibres have a radius of $20\bar{x}$, the equality to scale our dimensionless results is $1\overline{x} = 1/4$µm for the spatial scale. For example, the converged permeability for a fibre volume fraction of $\tau_f = 30\%$ is $42\,\bar{x}^2 = 42 \times \left(\frac{1}{4}10^{-6}\right)^2 \mathrm{m}^2 = 2.6 \times 10^{-12}\,\mathrm{m}^2$. Therefore, the converged permeability when increasing the domain size for $\tau_f = 30\%$ is $2.6 \times 10^{-12}\,\mathrm{m}^2$ with method 1 and $6.4 \times 10^{-12}\,\mathrm{m}^2$ with the second method. Furthermore, the mean value for each domain size is a good first approximation. Therefore, to compute a numerical permeability one can either run one simulation on a domain larger than $1000\overline{x}$ or run more than 15 simulations with a smaller domain to homogenise the effect of the fibre positions.

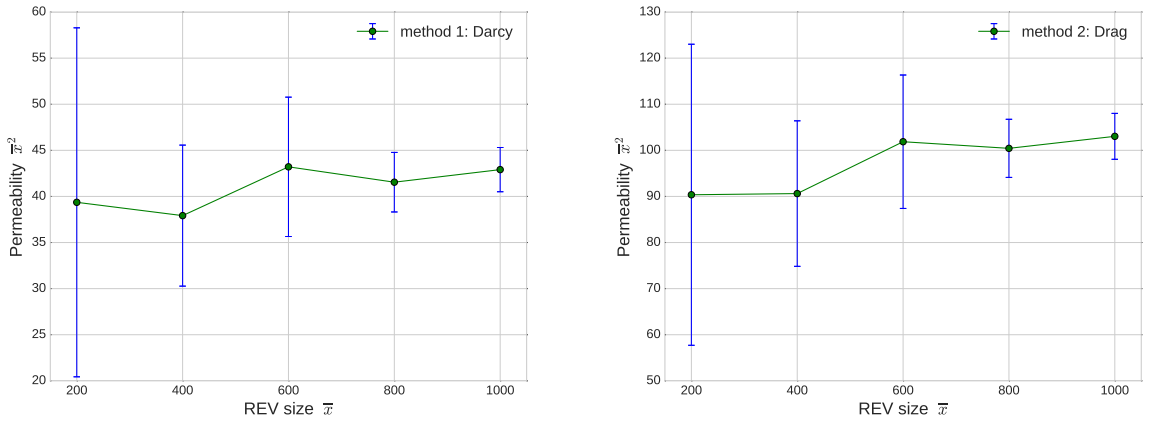

(A) method 1 (B) method 2

FIGURE 5.21 – Numerical permeability - standard deviation and convergence of the numerical permeability against the domain size for $\tau_f = 30\%$

The numerical permeability with a higher volume fraction of $\tau_f = 45\%$ is represented in Fig. 5.22. The standard deviation decreases and the mean value stabilises when increasing the domain size. Again, the second method gives an upper bound estimation for the permeability. Both methods predict approximatively a five times lower permeability when increasing the fibres volume fraction from 30% to 45%. Further cases would be necessary to conclude on this evolution found here.

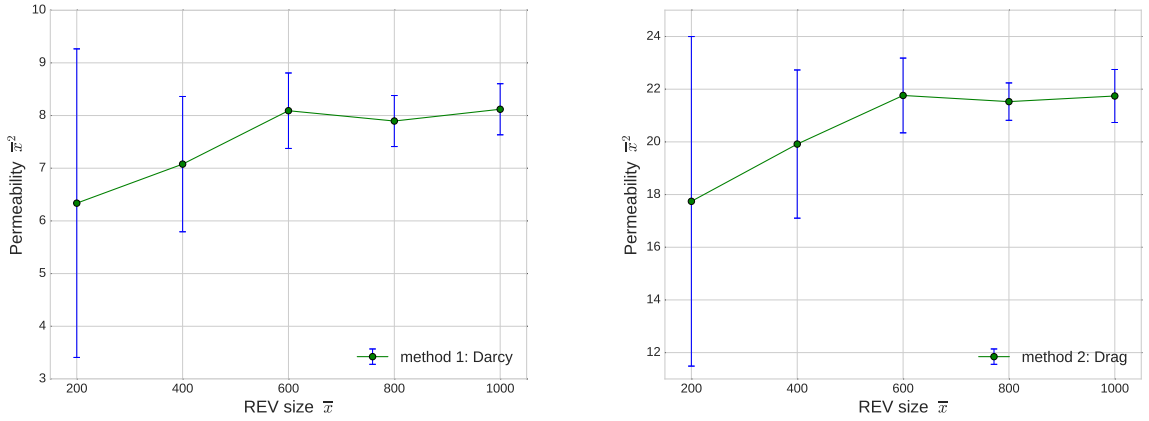

(A) method 1 (B) method 2

FIGURE 5.22 – Numerical permeability - standard deviation and convergence of the numerical permeability against the domain size for $\tau_f = 45\%$

Numerical permeabilities are reported in Tab. 5.7 for a fibre radius of $5\,\mu m$.

τ_f (%)	method 1: Darcy (K [m^2])	method 2: Drag def. (K [m^2])
30	2.6×10^{-12}	6.4×10^{-12}
45	5.1×10^{-13}	1.4×10^{-12}

TABLE 5.7 – Numerical permeability - value summary from random draws

Models from the literature are reported in Tab. 5.8. Four models are given from: Tomadakis and Robertson [207], Davies [79], Chen [80], Kozeny-Carman [29]. The Tomadakis and Robertson model assumes that the fibres are oriented in one direction with a constant radius and a randomly generated position without intersections, an relies on two model parameters chosen in our case $\epsilon_p = 0.33$ and $\alpha = 0.707$ for representing our case (see [207]). Davies [70] derives a formula in a similar context of flow transverse to unidirectional cylindrical fibres when studying fibrous filters to dissociate dust from air. Along with Chen [54], they studied the efficiency of collection and pressure drop due to the filter leading to model the fibrous medium as a homogeneous material with a permeability. Both approaches focus on the flow around a circular cylinder with Reynolds number between 0.2 and 2000. The Kozeny-Carman model [131, 50] based on two articles separated by 10 years, is based on experimental data and a shape factor in order to move from originally spherical particles to any shape of a fibrous medium. The constant used in Kozeny-Carman model is 1/180 [231]. Two other models namely Berdichevski

τ_f (%)	Kozeny-Carman (K [m^2])	Davies (K [m^2])	Chen (K [m^2])	Tomadakis and Robertson (K [m^2])
30	2.1×10^{-12}	3.7×10^{-12}	5.9×10^{-11}	8.3×10^{-12}
45	4.6×10^{-13}	8.5×10^{-13}	1.8×10^{-11}	1.1×10^{-12}

TABLE 5.8 – Numerical permeability - models from the literature

and Cai[31], and Gebart [93], are derived (see Tab. 5.9) for the specific case of a flow transverse to parallel fibres, which correspond to the studied 2D case. The model from Berdichevski and

τ_f (%)	Berdichevski and Cai (K [m^2])	Gebart (K [m^2])	method 1 (K [m^2])	method 2 (K [m^2])
30	3.8×10^{-12}	2.7×10^{-12}	2.6×10^{-12}	6.4×10^{-12}
45	9.4×10^{-13}	6.6×10^{-13}	5.1×10^{-13}	1.4×10^{-12}

TABLE 5.9 – Numerical permeability - models from the literature with flow transverse to parallel fibres and our numerical permeability reported at the end

Cai is based on the self-consistent method which assumes that a basic element representing the microstructure of a heterogeneous medium is embedded in an equivalent homogeneous medium with unknown properties. The permeability is determined by solving the continuity condition between the homogeneous and heterogeneous domains. Finally, Gebart model, like the others, is only based on an approximate analytical solution for a flow transverse to parallel fibres when studying RTM process.

Among the six models from the literature, the method 1 based on Darcy's flow rate gives results close to permeabilities from Kozeny-Carman and Gebart models. The second method, based on the drag definition, predicts a permeability with numerical values falling within the range described by the other models or larger. Therefore, the numerical method presented gives results comparable to models in the literature.

Hexagonal packing

This second microstructure is a regular hexagonal packing 5.23. It is designed to assess the influence of the previous microstructure randomness. Furthermore, the hexagonal packing is a suitable microstructure for a spontaneous capillary rise, as demonstrated in the next section. It also enables to reach a more realistic fibre volume fraction, tending to $\tau_f = 52\%$ when increasing the number of fibres in the stack. Actually, the microstructure (Fig. 5.23) shows a slight

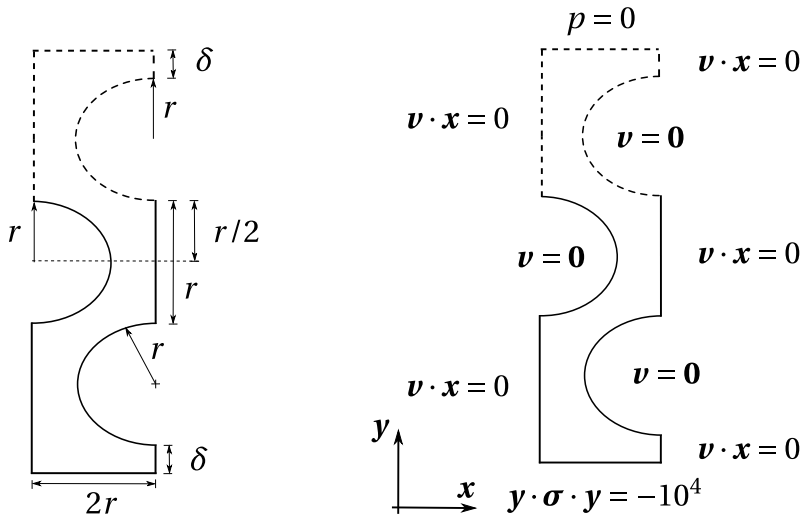

(A) domain geometry

(B) boundary conditions

FIGURE 5.23 – Numerical permeability hexagonal arrangement - geometry and boundary conditions

defect since at the entrance and exit of the domain, a fraction of fibre is lacking. This lacking fibre volume is controlled by the parameter δ and leads to change the fibre volume fraction. Without this lacking fibre, a domain with two quarters of fibres would be enough to compute the permeability as it would represent, with symmetries, a completely regular microstructure. However, the full domain is necessary to compute the capillary pressure, thus the domain in the flow direction is fully represented. As seen in Fig. 5.23 (A), each fibre has a constant radius r with their centres placed periodically (right and left) on two vertical segments spaced by a distance of $2r$, $r = 0.1$ and $\delta = 0.025$. On one segment, two consecutive fibres have their centres separated by a distance of $2r$. Fig. 5.23 (B) exhibits the boundary conditions. The main direction of the flow is in the y-direction since a stress vector is applied at the bottom in this same direction. On the right and left hand sides of the domain, a periodic boundary condition is used for the fluid $\boldsymbol{v} \cdot \boldsymbol{n} = 0$ and the pressure is prescribed directly on the top boundary with $p = 0$ via a Dirichlet condition. No slip is supposed on the fibres, thus the velocity vector is enforced to zero. Finally, the gravity is neglected in this case.

The velocity and pressure fields of the saturated flow are represented in Fig. 5.24. The domain width is enlarged by taking advantage of the symmetries. The velocity magnitude is higher where the space between the fibres is small. The velocity vector is zero at the upper and lower ordinate of every fibre since the flow is supposed periodic and without in-going velocity inside fibres. The pressure field is plotted on the two streamlines in the centre of the figure. Every single particle of fluid flows around the fibres from the bottom to the top boundary with a tortuosity close to 1. The permeability is computed from the velocity and pressure fields based on

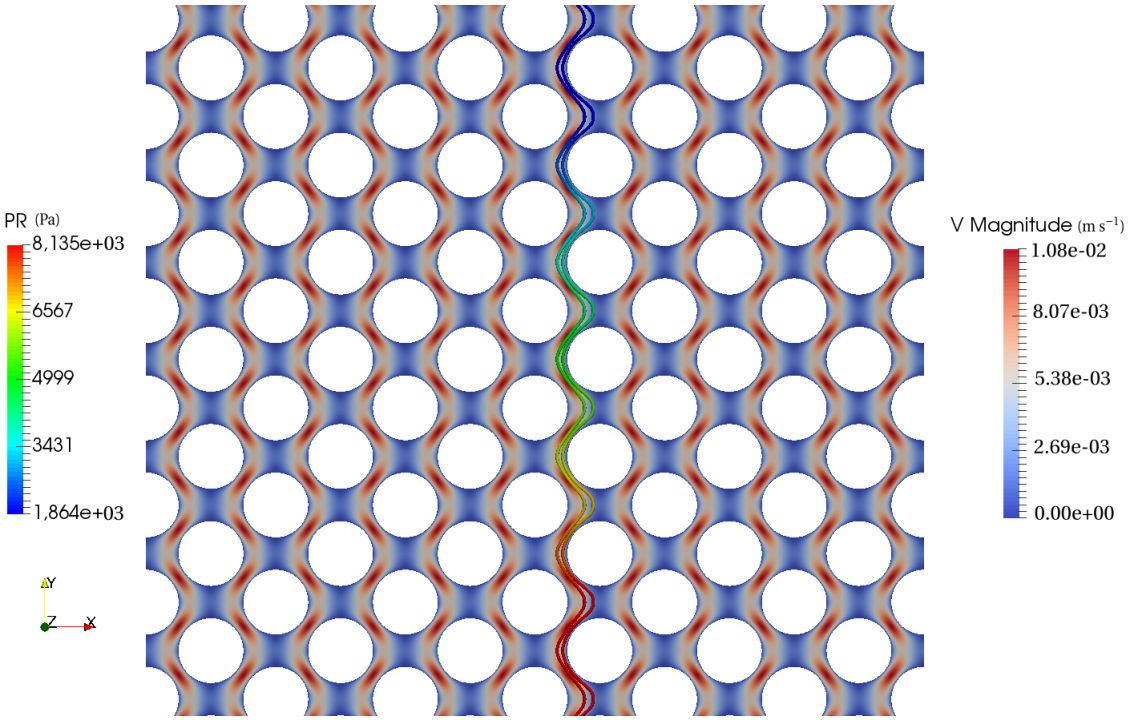

FIGURE 5.24 – Numerical permeability hexagonal arrangement - flow and streamlines in duplicated symmetrical domain, fluid viscosity $\mu_L = 1\,\mathrm{Pa}\cdot\mathrm{s}$

method 1 (extracted from Darcy's equation written with the flow) or method 2 (from the drag definition). The influence of the domain size is evaluated by changing the number of fibres aligned in the flow direction, up to 80 fibres are placed successively. The values are reported in Fig. 5.25. For both methods, the predicted permeability value converges when increasing the size of the domain. The value of the permeability is given in m^2 by fixing the size of the fibre radius $r = 1 \times 10^{-1}\,\bar{x} = 5 \times 10^{-6}\,\mathrm{m}$. Therefore, values of the converged permeability for methods 1 and 2 are $2.3 \times 10^{-13}\,\mathrm{m}^2$ and $5.5 \times 10^{-13}\,\mathrm{m}^2$ respectively. This case of a hexagonal packing corresponds to the case studied by Gebart [93]. He derived a permeability value by approximating an analytical solution for the Stokes equations in a small element representing with symmetries the whole domain. The transverse permeability from Gebart's model is $3.4 \times 10^{-13}\,\mathrm{m}^2$ for a fibre volume fraction of 52% and a fibre radius of 5 µm. Therefore, the numerical method 1 gives a value in the same range that predicted by Gebart. The method 2 describing the upper bound is less than twice the numerical value from method 1. One can conclude that, the computed permeability is correctly predicted with our numerical approach and the upper bound from the second method restricts the uncertainty of the method to a narrow interval. In literature, other numerical permeability [195] yields a lower permeability than the Gebart's model when studying a quadratic fibre packing.

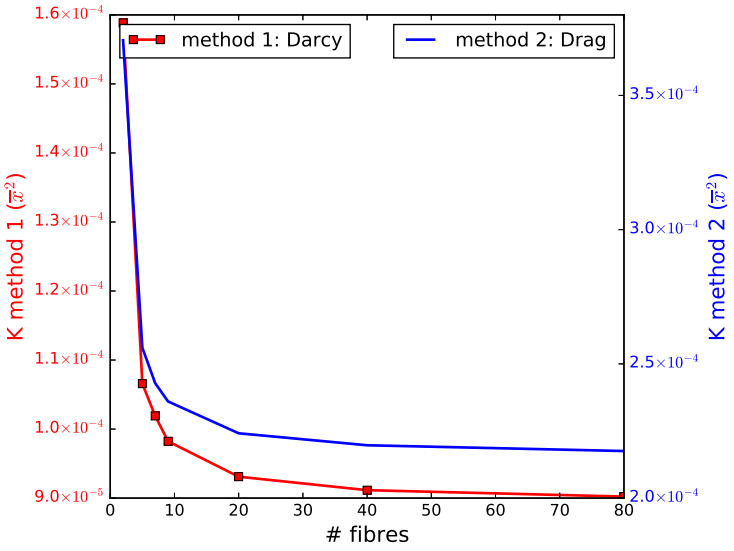

FIGURE 5.25 – Numerical permeability hexagonal arrangement - dimensionless permeability comparison between methods when increasing the number of fibres (# fibres)

Other permeability values from literature are reported in Tab. 5.10, showing a good agreement

τ_f (%)	Kozeny-Carman (K [m^2])	Davies (K [m^2])	Tomadakis and Robertson (K [m^2])	Berdichevski and Cai (K [m^2])	Gebart (K [m^2])	Method 1 (K [m^2])
52	2.3×10^{-13}	4.7×10^{-13}	3.6×10^{-13}	4.8×10^{-13}	3.4×10^{-13}	2.3×10^{-13}

TABLE 5.10 – Numerical permeability - models from the literature with $\tau_f = 52\%$

with method 1 and respecting the upper bound given by method 2. One can notice that the Kozeny-Carman model (with parameter 1/180) [131, 50] predicts the same value than the found numerical value 2.3×10^{-13} m^2.

The tortuosity of the streamlines is larger in the randomly generated case rather than in the hexagonal packing microstructure. Indeed, as seen in Fig. 5.24, the two streamlines have a more regular path than in Fig. 5.20 with a randomly generated microstructure. Therefore, the fluid has a preferential path which has an influence on the permeability. Contrary to models in literature, this versatile approach is able to take into account the effect of tortuosity by spanning from completely regular to 'random' arrangements.

5.2.3 Numerical capillary pressure

Capillary pressure is introduced for modelling the capillary effects at part scale. Indeed, so far in this work, capillary action has been described at the fibre scale by taking into account surface energies/tension on the three different interfaces involved in the problem. However, this local approach can not be used for computing the flow in the entire part during the infusion. Therefore, the flow in the entire part can be described by the Darcy's equation, while a pressure jump at the flow front represents the capillarity effects [17]. The magnitude of this jump

is equal to the capillary pressure, a parameter representing the averaged capillary action at the fibre scale. An extension of the previously presented volume averaging theorem to interfaces and triple line/point may present one possibility to compute the capillary pressure [101]. Yet, in this work we develop a strategy to compute this parameter in two ways: an equivalence with a Darcy's flow in one dimension, and by equaling the work done in a Stokes domain and in a Darcy's domain respectively by the surface tension and by the capillary force. After presenting the two methods, capillary pressure is computed in the randomly generated and hexagonal packing microstructures.

Darcy 1D

A formula for the capillary pressure may be derived from a Darcy's flow in one direction with a pressure jump at the interface located at height $h(t)$ [17]. The pressure at the domain entrance is p_{in} and p_{out} at the outlet (see Fig. 5.26). Assuming that the flow is 1D, then $\boldsymbol{v}$ and p depend

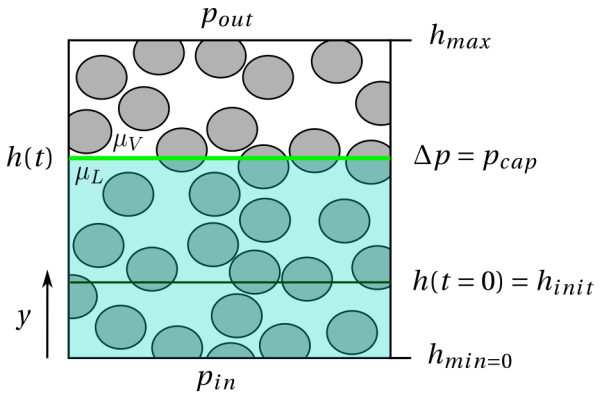

FIGURE 5.26 – Capillary pressure definition from Darcy 1D - Computational domain and boundary conditions

only on y and $\boldsymbol{v}\cdot\boldsymbol{x} = 0$. Substituting the velocity given by the flow equation into the conservation of mass equation leads to a linear pressure for each phase (liquid and vapour)

$$\begin{cases} v_{yj} = -\dfrac{K}{\mu_j}\dfrac{dp_j}{dy} \\ \nabla\cdot\boldsymbol{v}_j = 0 \end{cases} \implies \nabla\cdot\left(-\frac{K}{\mu_j}\frac{dp_j}{dy}\right) = 0 \implies \frac{d^2p_j}{dy^2} = 0 \quad \text{for } j \in \{L,V\}. \tag{5.27}$$

Four coefficients are necessary to solve this equation both in the liquid and vapour phases. These coefficients are determined by considering the following conditions:

$$\begin{aligned} p_L(h_{min}=0) &= p_{in} & p_V(h_{max}) &= p_{out} \\ p_V(h) - p_L(h) &= p_{cap} & v_{yV}(h) &= v_{yL}(h) \end{aligned} \tag{5.28}$$

The two first relations are the boundary conditions prescribed at the inlet and outlet of the domain; the third relation expresses the pressure jump at the fluid front, due to the capillary pressure p_{cap}; the fourth and last relation is the continuity of the normal velocity at the interface,

from the mass conservation. Using the four conditions, the pressure is written

$$p(y,t) = \begin{cases} p_L = \dfrac{p_{out} - p_{in} - p_{cap}}{\frac{\mu_V}{\mu_L} h_{max} - \left(\frac{\mu_V}{\mu_L} - 1\right) h(t)} y + p_{in} & \text{for } y \in [0, h(t)] \\ p_V = \dfrac{p_{out} - p_{in} - p_{cap}}{h_{max} - \left(1 - \frac{\mu_L}{\mu_V}\right) h(t)} \left(y - h_{max}\right) + p_{out} & \text{for } y \in [h(t), h_{max}]. \end{cases} \tag{5.29}$$

Finally, Darcy equation yields the formula for the constant velocity throughout the domain

$$v_y(t) = -\frac{K\left(p_{out} - p_{in} - p_{cap}\right)}{\mu_V h_{max} + \left(\mu_L - \mu_V\right) h(t)}. \tag{5.30}$$

The velocity at the fluid front has the same expression and is equal to the time derivative of the front position $v_y(t) = h'(t)$, leading to the differential equation

$$h'(t) = -\frac{K\left(\Delta p - p_{cap}\right)}{\mu_V h_{max} + \Delta\mu h(t)} \tag{5.31}$$

with $\Delta p = p_{out} - p_{in}$ and $\Delta\mu = \mu_L - \mu_V$. This differential equation has two solutions, only the solution with an increasing height is kept

$$h(t) = \frac{1}{\Delta\mu}\left(\sqrt{-2K\left(\Delta p - p_{cap}\right)\Delta\mu t + \left(\Delta\mu h_{init} + \mu_V h_{max}\right)^2} - \mu_V h_{max}\right) \tag{5.32}$$

For each time $t > 0$, the capillary pressure is computed by inversing the previous formula

$$p_{cap} = \Delta p + \frac{h(t) - h_{init}}{2Kt}\left[\Delta\mu\left(h(t) + h_{init}\right) + 2h_{max}\mu_V\right]. \tag{5.33}$$

The capillary pressure found to be inversely proportional to the permeability. Increasing the fibre volume fraction decreases the permeability and it yields a larger capillary pressure. Changing in topology (such as fibre clustering) may also change the fluid height and increases further the capillary pressure. Furthermore, let us notice that from the Darcy's equation, the height is proportional to the square root of time when the capillary pressure is assumed constant, *c.f.* Eq. 5.32.

One may notice that the permeability has been obtained with no-slip condition prescribed on the fibres, while in the capillary rise a slip condition is considered (otherwise, the triple point cannot rise) and is based on the permeability. It has been numerically assessed that using the same methods, the numerical permeability may vary up to 5 times the reported value when imposing a free slip condition on the fibres in the case of a hexagonal packing. To impose the same boundary conditions when computing the permeability and the capillary pressure, then either the method of calculating permeability must be extended to the case with a slip boundary condition, or the non-slip stress at the triple point must be relaxed only locally to allow the fluid front to advance.

5.2.4 Numerical experiments

A bi-fluid simulation is carried out with the two types of microstructure: the hexagonal fibre packing and the structure generated by a stochastic algorithm. The properties of the interfaces and fluids are reported in Tab. 5.11. The viscosities are those of air for the vapour and water for

	Solid/Vapour - γ_{SV}	Solid/Liquid - γ_{SL}	Liquid/Vapour - γ_{LV}
Surface tension / energies ($\mathrm{N\cdot m^{-1}}$)	60.93×10^{-3}	30.03×10^{-3}	37.03×10^{-3}

	Vapour	Liquid
Viscosity ($\mathrm{Pa\cdot s}$)	1.71×10^{-5}	1×10^{-3}

TABLE 5.11 – Input data for capillary rise in microstructures

the liquid. Resulting from the surface tension and energies, the static contact angle is $\theta_c = 33°$ according to the Young's equation $\gamma_{LV}\cos\theta_c = \gamma_{SV} - \gamma_{SL}$. A low contact angle ensures a high wettability and a better spontaneous impregnation.

Capillary rise in hexagonal arrangement

The geometry considered here is the same as presented in Fig. 5.23 (A). At least three conditions must be met for a spontaneous impregnation to occur:

— (*cdt1*) the length between two fibres has to be much smaller than the capillary length, $2d_2 - 2r \ll \kappa^{-1}$, with d_2 the horizontal distance between fibre centres as shown in Fig. 5.27 and if the centre of the first fibre is located at position $(0,0)$ then the centre of the second fibre is at position $(d_2, d_1 + r)$. This condition is true in our context since $2d_2 - 2r \propto 10\,\mu\mathrm{m}$ and $\kappa^{-1} \propto 1\,\mathrm{cm}$.

— (*cdt2*) The no-penetration condition between fibres has to be verified for the fluid to flow in between. Therefore, the distance between the centres has to be larger than the diameter. In our case with the two first centres at $(0,0)$ and $(d_2, d_1 + r)$, this condition reads: $d_2^2 + (d_1 + r)^2 > 4r^2$ which is automatically verified for $d_2 = 2r$ and $d_1 > 0$, as chosen.

— (*cdt3*) The impregnation stops if the pressure jump Δp across the interface is zero, *i.e.* if the interface is flat [28]. No driving force brings the interface forwards when the contact angle is verified and the interface has reached the state of minimum energy (a straight line) as depicted in Fig. 5.27. In the extreme case where the interface has no curvature and the angle is satisfied, the interface must have reached at least point A in Fig. 5.27, to continue to go up. The ordinate of this point represents the critical distance $d_{1c} = r\sin\alpha = r\sin\left(\frac{\pi}{2} - \theta_c\right) = r\cos\theta_c$. Therefore, the distance d_1 has to be shorter than this critical distance, yielding: $d_1 < d_{1c} = r\cos\theta_c$. For a contact angle $\theta_c = 33°$ indirectly specified through surface tension and surface energies values reported in Tab. 5.11, the third condition for a spontaneous impregnation is $d_1 < 0.85r$ which is verified since the distance is $d_1 = 0.5r$.

Boundary conditions are the same as in Fig. 5.23 (B) for permeability computation, except that a no-penetration condition is prescribed at the fibre contours $\boldsymbol{v}\cdot\boldsymbol{n} = 0$ instead of the no-slip condition. Furthermore, a free normal stress is enforced at the bottom boundary ($y = 0$) to let

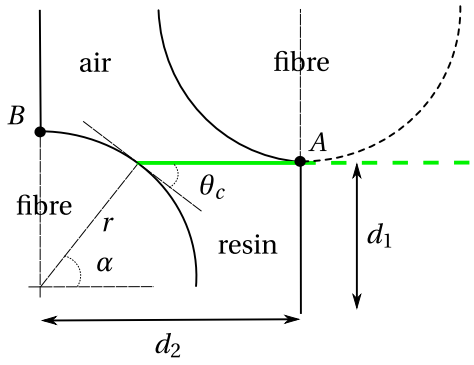

FIGURE 5.27 – Hexagonal packing - Condition for the next fibre to be geometrically accessible

the resin impregnate the fibres by the only action of capillarity.
The impregnation is simulated during $t_f - t_{init} = 0.85\,\text{ms}$ using 35000 time increments. Two time sequences are adopted: between $t_{init} = 0$ and $t = 0.1\,\text{ms}$, 1000 time increments are performed ($\Delta t = 1 \times 10^{-4}\,\text{ms}$), then between $t = 0.1\,\text{ms}$ and $t_f = 0.85\,\text{ms}$, 2500 increments are performed with a larger time step $\Delta t = 3 \times 10^{-4}\,\text{ms}$.

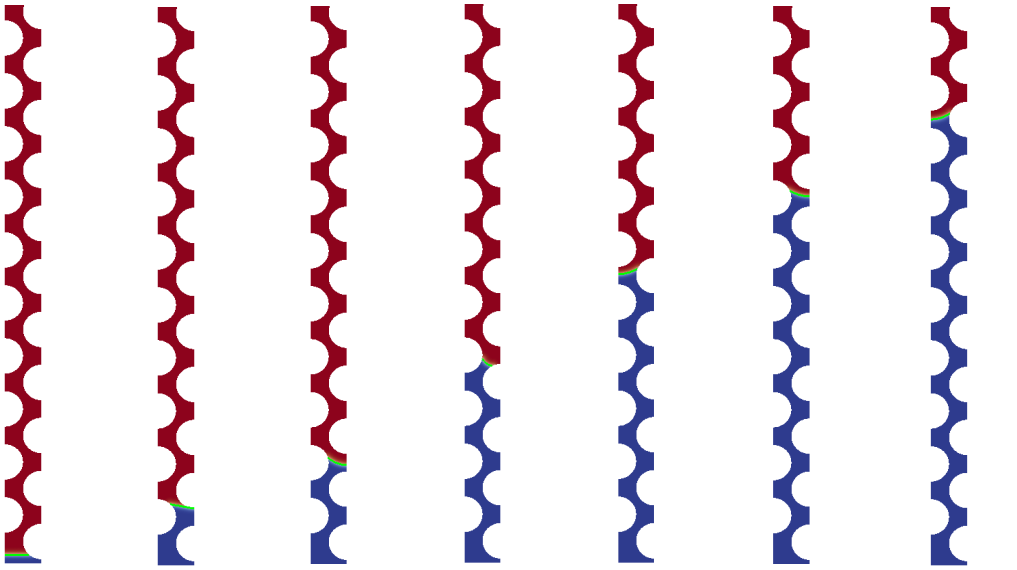

FIGURE 5.28 – Capillary rise in hexagonal packing - Position and shape of meniscus for different times

Fig. 5.28 shows the interface position at seven different times during the capillary rising. The interface is represented by a green curve, the resin below is in blue and air above in red. At each instant, the interface is curved by the capillary action enabling the fluid to impregnate the hexagonal packing microstructure. The arithmetic mean height, $h(t)$ of the interface is computed and plotted in Fig. 5.29 (A). It can be shown that this height behaves like the square root of time. Indeed, the graph of $h^2(t)$, also drawn inside the figure, is a straight line. Therefore, the fluid impregnation velocity decreases in time without any gravity action. The interface slowing down results from the dissipative viscous term $\mu\Delta\boldsymbol{v}$ which acts on an increasing volume of

fluid. This is in good agreement with literature [90, 218], demonstrating that if the surface tension force is constant then the height depends on the square root of time when studying a flow in capillary tubes. This law is known as the Washburn's law. This flow regime is called viscous regime.

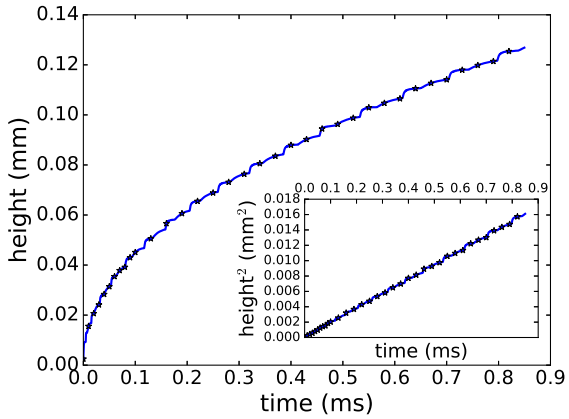

(A) Height of the fluid front over time

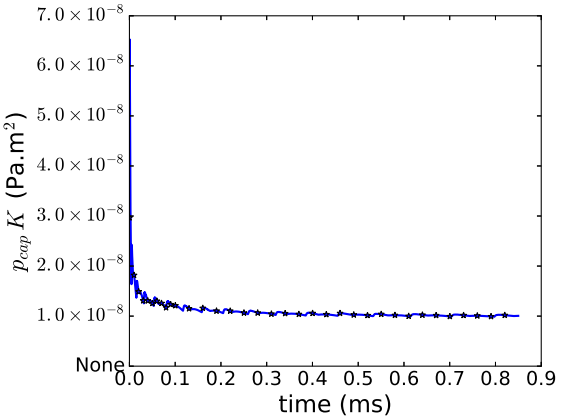

(B) Capillary pressure based on Darcy 1D equivalence

FIGURE 5.29 – Hexagonal packing - Capillary rise and pressure

From the height, the capillary pressure multiplied by permeability is computed using Eq. 5.33 and represented in Fig. 5.29 (B). After 0.1 ms, the value is constant and $p_{cap} \times K \approx 9.7 \times 10^{-9}\,\text{Pa} \cdot \text{m}^2$. The permeability may be known based on previously computed numerical permeability $K_{method1} \approx 2.3 \times 10^{-13}\,\text{m}^2$ and $K_{method2} \approx 5.5 \times 10^{-13}\,\text{m}^2$. Method 1 is based on Darcy's equation expressed with the flow and method 2 gives an upper bound for the permeability *i.e.* a minimal value for the capillary pressure. The capillary pressure has a value of 0.42 bar with the permeability from method 1 and a lower bound of 0.18 bar based on the second method for the permeability computation. This range of value is a good approximation and belongs to common value range [150]. For example, a maximal value of 37 kPa has been measured for woven fabric preforms made of T-300 carbon fibres [7], but also values between 5 and 7 kPa are reported in [12], for glass fibres and epoxy resin. These values are given for information only and not for comparison purposes since capillary pressure depends on the physical properties and geometry of the fibres.

Capillary rise in randomly generated microstructure

The same methodology is applied to compute a capillary pressure in a microstructure with randomly generated fibre positions. Boundary conditions are imposed as presented in Fig. 5.5 on page 115 with some modifications: from now on, only the normal velocity component is set to zero on the fibres contour to enable the fluid to slip.
As presented in the previous paragraph, the same three conditions have to be verified for the resin to impregnate the fibres. The distance between the fibres is smaller than the capillary length since the same fluids are studied and no-penetration between fibres is allowed. However, the third condition is not verified everywhere in the domain. As seen in Fig. 5.30, even for a fibre volume fraction of 45%, there is not always a fibre above to intersect the front of

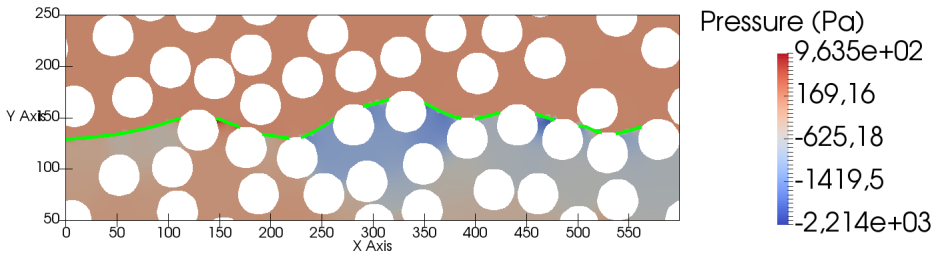

FIGURE 5.30 – Randomly generated microstructure - no spontaneous impregnation without pressure differential

fluid. A complete spontaneous impregnation is not possible in this randomly generated microstructure. Therefore, a pressure gradient is applied between the inlet and outlet of the domain through the condition on the normal component of the stress vector: 2×10^3 Pa on the left-hand side inlet. Thus $\Delta p = -2 \times 10^3$ Pa in Eq. 5.33.
The induced impregnation is simulated during $t_f - t_{init} = 0.891$ ms with 3300 time increments. The simulation has been sequenced using successively two time steps: between $t_{init} = 0$ and $t = 0.0375$ ms, 1000 time increments are performed *i.e.* $\Delta t = 3.75 \times 10^{-5}$ ms, then between $t = 0.0375$ ms and $t_f = 0.891$ ms, 2300 increments are run with a time step $\Delta t = 3.71 \times 10^{-4}$ ms.

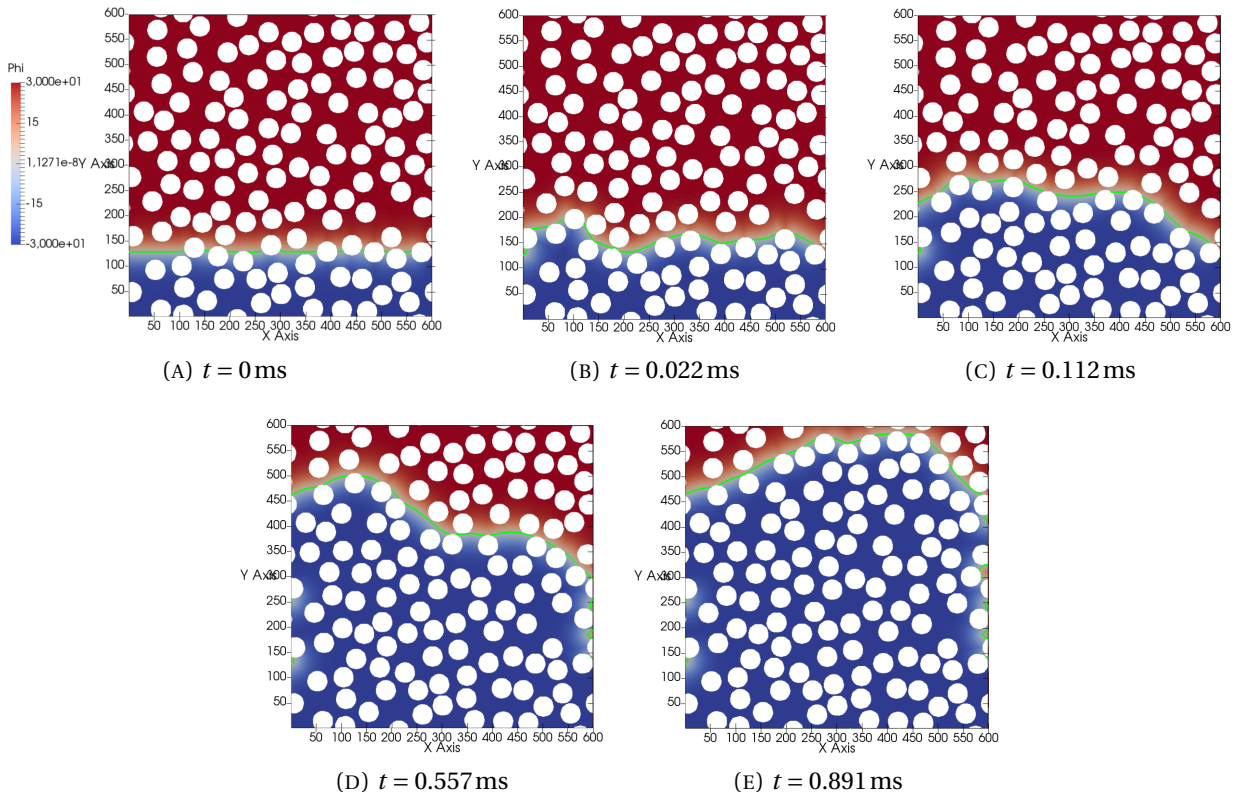

(A) $t = 0$ ms (B) $t = 0.022$ ms (C) $t = 0.112$ ms

(D) $t = 0.557$ ms (E) $t = 0.891$ ms

FIGURE 5.31 – Randomly generated microstructure - Position and shape of meniscus at different instants

The progression of the front of resin is represented at 5 instants in Fig. 5.31. Initially, the interface is a straight line at position $y = 130$ with the resin in blue and the air in red, as shown in Fig. 5.31 (A). The resin starts to flow not in a straight way in the microstructure as it was the

case in the hexagonal packing (subplot (B)). The region under $x < 300$ has a fibre distribution easing the capillary rise than above $x > 300$ for a y-position between 150 and 450: the front of resin moves faster under $x = 300$ as seen in Fig. 5.31 (C) and (D). Oppositely, more fibres are randomly positioned near the top right quarter which helps the front of fluid to move due to capillarity, catching up with the second half.
The size of the REV needed to determine the capillary pressure seems to be larger than the size required to calculate a numerical permeability. At each time step, arithmetic mean value of the y position of the interface is computed and reported in Fig. 5.32 (A). Like in the hexagonal case, the viscous dissipation slows down the fluid front. The fluid position is proportional to the square root of time as pictured in the figure close-up, in good agreement with the theory of the viscous regime [90]. The product of the capillary pressure by the permeability is

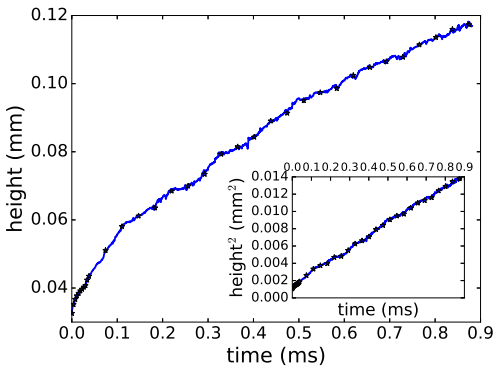

(A) Height of the fluid front in time

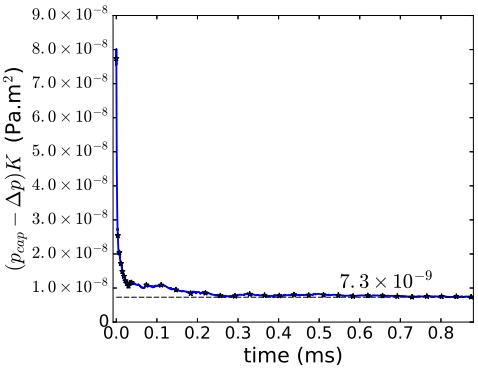

(B) Capillary pressure based on Darcy 1D equivalence

FIGURE 5.32 – Randomly generated microstructure - capillary rise and pressure

computed based on Eq. 5.33 and plotted in Fig. 5.32 (B). The curve reaches a constant value $(p_{cap} - \Delta p)K = 7.3 \times 10^{-9}$ Pa·m^2 for $t > 0.2$ ms. For this microstructure, the numerical permeability is: 5.1×10^{-13} m^2 based on method 1 which is in good agreement with Kozeny-Carman and Gebart models. Recalling that a pressure differential of 2000 Pa is applied between the inlet and outlet, then the capillary pressure is estimated to $p_{cap} = 12.3$ kPa. The capillary pressure lower bound is 3.2 kPa, computed with the second method (giving an upper bound for the permeability).

Even with a fibre volume fraction of 45%, no spontaneous impregnation is possible in this microstructure, and a pressure gradient has to be imposed to set the fluid in motion. This pressure differential may interact with more complexity than just adding up its effects with the capillary pressure as supposed in our interpretation. The influence of the pressure differential on the capillary pressure should be assessed to verify this hypothesis. Finally, the capillary pressure is inversely proportional to the permeability. Therefore, a precise estimation of this microstructure characteristic has to be known prior to compute the capillary pressure.

Conclusion

First, in this chapter, validation cases have been presented and compared with success to analytical and semi analytical solutions. In addition, a good agreement with a benchmark of the literature was found for a bubble rising in a liquid. The last case of a cluster of tubes allowed us to validate the robustness of the approach in a complex 3D geometry. The second part of this chapter analysed two types of microstructure in order to extract a permeability and a capillary pressure, both modelling respectively the capability of a medium to permit a fluid flow through and the average capillary action. One microstructure was a hexagonal packing whereas the other had circular fibres with randomly generated centres. Two methods to compute the permeability were exposed: the first one is based on the Darcy's equation expressed with the flow rate and the other comes from the drag force definition, and provides an upper bound of the numerical permeability. Finally, a method to compute the capillary pressure was derived based on an equivalence of the resin front position between the Stokes flow in the microstructure and a 1D Darcy flow. Both numerical results for the permeability and the capillary pressure are in good agreement with literature. At last, it has been shown that spontaneous capillary rise is only possible when certain geometric conditions are met.
This method may be used to pre-compute permeability and capillary pressure depending on morphological descriptors such as the fibre volume fraction. Then an industrial case of the infusion of a composite part may be simulated, taking into account the capillary action, based on an initial mapping of fibre volume fraction. In parts with complex geometries, a curved region experiences a variation of fibre volume fraction during the forming phase before the infusion as well as during infusion because of the swelling of the preforms for biocomposites. This spatial variation of fibre volume fraction will influence the resin infusion (time and spatial impregnation) through the permeability and the capillary pressure.

Résumé en Français : Éxpériences numériques

Plusieurs cas tests de validation attestent de la fiabilité du modèle prouvant qu'il est capable de décrire la position statique de ménisques contre une plaque et entre deux plaques verticales. De plus, une comparaison avec un benchmark numérique portant sur la capillarité a été réalisée. Une bonne adéquation entre notre solution numérique et celles données par les approches de ce benchmark a été relevée. Enfin, un dernier cas de validation permet de conclure sur la forme plausible d'un ménisque statique dans une microstructure complexe en 3D.
Des écoulements saturés et insaturés sont alors réalisés pour étudier les propriétés de la microstructure. Deux types de microstructures sont considérés : un positionnement hexagonal des fibres et un tirage aléatoire de leurs centres. La perméabilité est calculée grâce à l'équation de Darcy formulée en débit. Une seconde méthode permet de donner une borne supérieure de la perméabilité numérique et repose sur la modélisation de la force de traînée. Enfin, une pression capillaire est extraite de la hauteur du front de fluide en fonction du temps grâce à une équivalence avec un écoulement Darcy 1D. Les valeurs de perméabilités et de pressions capillaires numériques sont comparées aux valeurs de la littérature et montrent une bonne cohérence avec celles-ci. La comparaison entre ces deux types de microstructures montre que la taille du domaine doit être suffisamment grande pour moyenner l'effet du positionnement aléatoire des

fibres. La pression capillaire est calculée en faisant l'hypothèse que cette taille de domaine suffisante pour décrire la perméabilité est également suiffisante pour la pression capillaire. Une équivalence sur la hauteur de fluide avec l'équation de Darcy 1D, permet proposer une valeur numérique de la pression capillaire.

Conclusion

This research work is part of a collaboration between Mines Saint-Étienne and Hexcel Reinforcements to develop numerical methods capable of simulating Liquid Composite Moulding manufacturing processes.
In continuity with previous works, the primary objective of this thesis is to improve the accuracy of the physical model by a local analysis of resin / fibre interactions during the infusion step. Indeed, until now, the fibrous preform has been described by an equivalent homogeneous medium. However, the comparison between simulation and experience, particularly based on preform filling times, indicates that the effects related to capillarity cannot be neglected in the flow regimes met. Describing these local effects is an essential part in modelling the LCM manufacturing processes. A fibre-scale description based on the mechanical balance of the interfaces was adopted. The geometric representation of the interface between air and resin gives to the description a considerable amount of information at the microstructural scale. As a consequence, the secondary objective of this thesis work consists in condensing, in representative global parameters, the information extracted from the study of flows at the fibre scale namely: permeability and capillary pressure. These parameters characterise the flow at the local scale and translate their effects at the global scale of equivalent homogeneous media.

The numerical tool is based on two solvers: one for numerically solving for fluids both momentum balance and conservation of mass equations, and another one for describing an interface representing the moving fluid front through the level-set method. In our study, a bifluid flow is considered. It represents the resin and rarefied air downstream of the fluid front during the infusion process. In this method, a level-set function is used to describe the position of the resin front, separating resin from air during the infusion stage. Both solvers use the finite element method to solve partial differential equations numerically. Each solver was independently tested by verification test cases. The emphasis was placed, for the Navier-Stokes solver, on taking into account the inertial effects requiring to solve a non-linearity in velocity. For the level-set solver, the variations of volume were studied when solving the transport equation.

The fluid mechanics problem has been reformulated by taking into account: the surface tension, surface energies and the mechanical balance of surface tensions at the triple line. In the resulting integral weak form, all these conditions appear to be Neumann conditions. Mathematically, an integration by parts reduces the regularity required for the interface description, avoiding the calculation of the curvature. In all cases, a fixed simplicial mesh was used, with a continuous and linear approximation by element of the unknowns, namely velocity and pressure fields for mechanics and level-set field for capturing the fluid front. However, capillary flows show features that the continuous approximation of pressure cannot take into account. An enhancement of the pressure field approximation has been implemented to describe both

jumps of pressure and pressure gradient. In addition, the linear approximation of the fluid interface can generate parasitic currents. These spurious velocities lead to a degeneration of the interface that can be controlled by a restriction on the time step. To remove this restriction, capillary force stabilization was used to filter parasitic capillary waves. The stabilization introduced as the semi-implicitation of the resin / air interface offers further robustness to the numerical method. It was noted that the stabilization resulting from the semi-implicitation diffuses the condition imposed weakly on the contact angle. Two coupling strategies between the fluid solver and the level-set were then discussed. The main difference between the two couplings is that the strong iterative coupling preserves the contact angle imposed by reducing the stabilization term over the convergence iterations. Also, the main characteristic of the strong iterative coupling is to obtain a solution to the global fluid and level-set problem, which cannot be ensured by the weak coupling.

Menisci at equilibrium against and between vertical walls have been numerically computed. The numerical solutions were successfully compared to analytical and semi-analytical solutions demonstrating the ability of the proposed simulation to reproduce the physics of the problem. The numerical method developed was compared with other methods referenced in a numerical benchmark of the literature. The results obtained are in good agreement with those given by the approaches of this study. Finally, the case of a cluster of tubes is presented, allowing to test the numerical method with interactions between several 3D menisci.
For the purpose of simulating the flow of resin in a part with industrial dimensions, it is essential to consider the preforms as equivalent homogeneous media. Before presenting the upscaling strategy, it was recalled that the Darcy equation may be established from a spatial homogenization of the Stokes equations. Thus the defined permeability reflects the ability of a medium to let a fluid flows through. Permeability is numerically calculated, first, from the Darcy equation formulated in terms of flow rate. A second method defined from the expression of the drag force represents an estimation in excess of the permeability. Finally, capillary effects can be added to the Darcy law by considering a pressure drop at the flow front. The amplitude of this jump is a scalar called capillary pressure that acts in the normal direction on the fluid front. The latter can be determined by assuming an equivalent position of the fluid front between, on the one hand, the Stokes domain and, on the other hand, the position in the homogeneous domain in which the flow is ruled by the Darcy equations in 1D. Both permeability and capillary pressure parameters are in good agreement with the models from literature and the experimentally estimated values.

Several outlooks can be drawn from this work. First in the short run, prospects can be divided into three main areas. A numerical strategy can be developed to gather in an unity model iterations from the Navier-Stokes solver and iterations from the strong coupling when taking into account capillarity. The convergence speed is the parameter to be optimised when developing this model. This improved version could capture in particular the first instants of the wetting when inertial forces are prevailing. The second axis is related to capillarity for taking advantage of the strong iterative coupling with the use of a dynamic angle model. It could be interesting to study the influence of a friction at the triple point on the dynamic angle, with this same friction coefficient extracted from a second analysis at the lower scale by a representation

of the roughness. The third axis is focused on the issue of homogenisation. Numerous precalculated permeabilities depending on representative parameters to be defined would make it possible to create a permeability mapping at the part scale. The capillary pressure resulting also from homogenisation could be calculated from an energy equivalence between a Stokes system and its corresponding Darcy system. A global approach could be developed to jointly compute permeability and capillary pressure.
In the long run, the geometry of the fibres could be extracted from tomographic images. A complete analysis could be conducted to extract morphological criteria representative of the microstructure. The influence of these criteria on the characteristic quantities of capillary flow could also be studied. Finally, the versatility of the approaches could be exploited in many fields, controlled by surface tensions, within structured environments: elasto-capillarity, microfabrication, microfluidics.

This research will be continued as part of the industrial Chair between Mines Saint-Étienne and Hexcel Reinforcements.

Conclusion en Français

Ce travail de recherche s'inscrit dans une collaboration entre Mines Saint-Étienne et l'entreprise Hexcel Reinforcements visant au développement de méthodes numériques simulant les procédés de fabrication par voie liquide. La modélisation puis la simulation numérique des procédés permet de les étudier dans le but de les optimiser.
Dans la continuité des travaux précédents, l'objectif primaire de cette thèse est d'améliorer la finesse du modèle physique par une analyse locale des interactions resine / fibres lors de l'infusion. En effet jusqu'à présent, la préforme fibreuse était décrite par un milieu homogène équivalent. Cependant, la confrontation entre simulation et expérience, notamment basée sur les temps de remplissage de préformes, indique que les effets liés à la capillarité ne peuvent être négligés dans les régimes d'écoulement rencontrés. Décrire ces effets locaux est un élément essentiel de la modélisation des procédés visés. Une description à l'échelle de la fibre se basant sur l'équilibre mécanique des interfaces a été adoptée. La représentation géométrique de l'interface entre l'air et la résine confère à la description une richesse d'information considérable à l'échelle microstructurale. C'est pourquoi, l'objectif secondaire du travail de thèse consiste à condenser, dans des paramètres globaux représentatifs, l'information extraite de l'étude d'écoulements à l'échelle de la fibre : la perméabilité et la pression capillaire. Ces paramètres quantifient l'écoulement à l'échelle locale et permettent de prendre en compte les effets locaux à l'échelle macroscopique d'un milieu homogène équivalent.

L'outil numérique repose sur deux solveurs : l'un permettant de résoudre numériquement les équations de conservation de la quantité de mouvement ainsi que de la masse pour les fluides, l'autre permettant la description d'une interface représentant le front de fluide mobile par la méthode level-set. Dans notre étude, un écoulement bifluide est considéré. Il représente la résine et l'air raréfié en aval du front lors du procédé d'infusion. Dans cette méthode, une fonction level-set permet de décrire la position du front de résine, distinguant la résine de l'air durant l'écoulement. Les deux solveurs se basent sur la méthode des éléments finis pour résoudre numériquement les équations aux dérivées partielles. Chaque solveur a été indépendamment éprouvé par des cas tests de vérification. L'accent a été placé, pour le solveur fluide (Navier-Stokes), sur la prise en compte des effets d'inertie demandant de lever une nonlinéarité en vitesse ; pour le solveur level-set, sur l'étude des variations de volume lors de la résolution de l'équation de transport.

Le problème mécanique fluide a été reformulé en prenant en compte : la tension de surface, les énergies de surface et l'équilibre mécanique des tensions de surface à la ligne triple. Dans la forme faible qui en découle, l'ensemble de ces conditions apparait comme des conditions de Neumann. Mathématiquement, une intégration par partie a permis de diminuer la régularité requise pour la description de l'interface, évitant le calcul de la courbure. Dans tous les cas,

un maillage simplicial fixe a été utilisé, avec une approximation continue et linéaire par élément des inconnues, à savoir des champs de vitesse et de pression pour la mécanique et du champ level-set pour la capture du front de fluide. Cependant, les écoulements capillaires présentent des particularités que l'approximation continue de la pression ne peut pas prendre en compte. Un enrichissement de l'approximation du champ de pression a été implémenté pour décrire les sauts de pression et de gradient de pression. Par ailleurs, l'approximation linéaire de l'interface fluide peut engendrer des courants parasites. Ces derniers conduisent à une dégénérescence de l'interface pouvant être contrôlée par une restriction sur le pas de temps. Pour lever cette restriction, une stabilisation de la force capillaire a été utilisée pour filtrer les ondes capillaires parasites. La stabilisation introduite comme de la semi-implicitation de l'interface résine / air offre, sans nul doute, une robustesse à la méthode numérique. Il a été noté que, la stabilisation issue de la semi-implicitation diffuse la condition imposée faiblement sur l'angle de contact. Deux stratégies de couplage entre le solveur fluide et la level-set ont été ensuite discutées. La principale différence entre les deux couplages porte sur le fait que le couplage fort itératif permet de rétablir l'angle de contact imposé en réduisant le terme de stabilisation au fil les itérations. La caractéristique principale du couplage fort itératif est l'obtention d'une solution au problème global fluide et level-set, qui ne peut être assuré par le couplage faible.

La simulation numérique a permis de calculer les ménisques à l'équilibre contre et entre des murs verticaux. Les solutions numériques ont été comparées avec succès à des solutions analytiques et semi-analytiques démontrant la capacité de la simulation à reproduire la physique du problème. La méthode numérique développée a été confrontée à d'autres méthodes référencées dans un benchmark numérique de la littérature, et les résultats obtenus sont en bonne adéquation avec ceux donnés par les approches de cette étude. Enfin, le cas d'une grappe de tubes est présenté, permettant de tester la méthode numérique avec de fortes interactions entre plusieurs ménisques en 3D.
Dans le but de simuler l'écoulement de résine dans une pièce aux dimensions industrielles, il est indispensable de considérer les préformes comme un milieu homogène équivalent. Dans cette démarche de changement d'échelle, il a été rappelé que l'équation de Darcy est établie à partir d'une homogénéisation spatiale des équations de Stokes. La perméabilité ainsi définie traduit la capacité du milieu à se laisser imprégner par un fluide. La perméabilité est numériquement calculée, d'abord, à partir de l'équation de Darcy formulée en termes de débit. Une seconde méthode définie à partir de l'expression de la force de traînée représente une estimation en excès de la perméabilité calculée. Enfin, les effets capillaires peuvent être ajoutés à la loi de Darcy en considérant un saut de pression au front d'écoulement. L'amplitude de ce saut est un scalaire nommé pression capillaire qui agit normalement au front de fluide. Cette dernière peut être déterminée en faisant l'hypothèse d'une équivalence de la position du front de fluide entre, d'une part le domaine de Stokes et d'autre part, la position dans le domaine homogène équivalent dans lequel l'écoulement est décrit par les équations de Darcy en 1D. Les deux paramètres numériques calculés sont en bon accord avec les modèles issus de la littérature et les valeurs estimées expérimentalement.

Plusieurs perspectives peuvent être tirées de ces travaux. Dans un premier temps, les perspectives à court et moyen terme peuvent se scinder en trois axes. Une stratégie numérique peut

être développée permettant d'intégrer de façon globale les itérations du solveur de Navier-Stokes avec les itérations provenant du couplage fort lors du traitement de la capillarité. La vitesse de convergence étant le paramètre à optimiser lors du développement de cette stratégie. Cette version améliorée pourrait permettre de capter notamment les premiers instants du mouillage où les forces inertielles sont les plus actives. Le second axe de travail sur la capillarité s'inscrit dans la continuité du travail sur le couplage fort itératif avec l'utilisation d'un modèle pour l'angle dynamique. Il pourrait être intéressant d'étudier l'influence d'un frottement au point triple sur l'angle dynamique, ce même frottement pouvant être extrait d'une seconde analyse à l'échelle inférieure par une représentation de la rugosité. Le troisième axe gravite autour de la problématique d'homogénéisation. Une accumulation de perméabilités numériques en fonction de paramètres représentatifs à définir permettrait de créer des cartographies de perméabilité pour des écoulements à l'échelle de la pièce. La pression capillaire issue de l'homogénéisation pourrait être calculée à partir d'une équivalence énergétique entre un écoulement fluide de Stokes et homogénéisé de Darcy. Une approche globale pourrait être développée pour calculer conjointement la perméabilité et la pression capillaire.
À plus long terme, la géométrie des fibres pourrait être extraite d'images tomographiques. Une analyse complète pourrait être menée dans le but d'extraire des critères morphologiques représentatifs de la microstructure et de l'étude de ces paramètres sur les grandeurs caractéristiques de l'écoulement capillaire. Enfin, la versatilité des approches mises en place pourrait être exploitée dans de nombreux domaines où les écoulements forcés ou naturels, contrôlés par les tensions de surface dans notre cas, agissent au sein de milieux structurés : elasto-capillarité, microfabrication, microfluidique.

Ces recherches seront poursuivies dans le cadre de la chaire industrielle entre Mines Saint-Étienne et Hexcel Reinforcements.

Appendix A

Poiseuille flow

Contents

A.1 Flow between two plates

An analytical solution can be derived for the Poiseuille problem of a laminar flow between two plates. The global domain is presented in Fig. A.1 (A) and is simplified in 2D since the solution is constant in the x-direction. Incompressible Stokes equations have to be solved since the

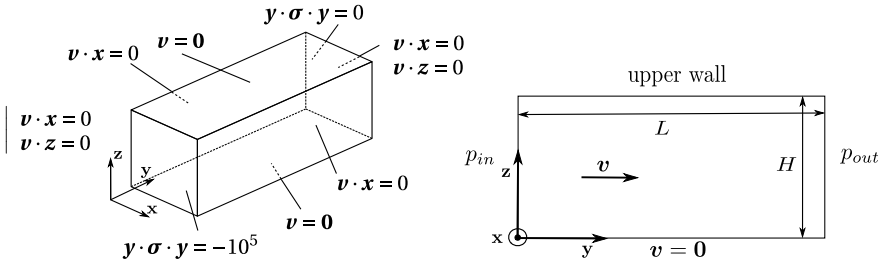

(A) Global domain (B) 2D flow

FIGURE A.1 – Flow between two walls - Global 3D domain (A) and its restriction in 2D (B).

flow is supposed to be laminar:

$$-\mu\boldsymbol{\Delta}\boldsymbol{v}+\nabla p=0 \tag{A.1}$$

$$\nabla\cdot\boldsymbol{v}=0 \tag{A.2}$$

The velocity is supposed to be only in the y-direction and every quantities are constants in the x-direction. From the incompressibility constraint A.2, it comes that the velocity in the y-direction depends only on z such that

$$\boldsymbol{v}=v_y(z)\boldsymbol{y} \tag{A.3}$$

where $\boldsymbol{y}$ is an unit vector in the y-direction.
The conservation of momentum equation A.1 is projected in each directions, and in the z-direction is

$$\frac{\partial p}{\partial z}=0. \tag{A.4}$$

Therefore, the pressure is not changing in the z-direction and may only depend on y: $p = p(y)$. The last projection of the conservation of momentum equation in the y-direction reads

$$\frac{\partial p}{\partial y} = \mu \frac{\partial^2 v_y}{\partial y^2}. \tag{A.5}$$

The left-hand side of the equation depends only on y whereas the right-hand side depends only on z. Thus, $\frac{\partial p}{\partial y} = C$ and the pressure is linear in the y direction

$$p(y) = \underbrace{\frac{p_{out} - p_{in}}{L}}_{C} y + p_{in}. \tag{A.6}$$

The general solution for the velocity is

$$v_y(z) = \frac{1}{2\mu} C z^2 + K_1 z + K_2 \tag{A.7}$$

Boundary conditions have to be used to obtain the analytical solution. The velocity is imposed equal to zero at $\{z = 0\}$, then $K_2 = 0$. For the condition on the upper wall two cases are going to be considered: a slip and no-slip condition.

A.1.1 No-slip condition

This section investigate the case of a no-slip condition on the upper wall as shown in Fig. A.1. The condition reads $v_y(z_H) = 0$ and then the solution of a Poiseuille flow between two plates with no-slip condition on each wall

$$\begin{aligned} v_y &= \frac{C}{2\mu}\left(z^2 - Hz\right) \\ p &= Cy + p_{in} \end{aligned} \tag{A.8}$$

A.1.2 Slip condition

Let's suppose that a slip condition is applied on the upper wall. The Navier condition gives a value for the tangential component of the normal stress

$$\boldsymbol{\sigma} \cdot \boldsymbol{n} - [(\boldsymbol{\sigma} \cdot \boldsymbol{n}) \cdot \boldsymbol{n}]\, \boldsymbol{n} = -\beta \left[\boldsymbol{v} - (\boldsymbol{v} \cdot \boldsymbol{n})\, \boldsymbol{n}\right] \tag{A.9}$$

with β a friction coefficient. In the case of a Newtonian fluid and in this case, the Navier condition may be rewritten as an equality between the shear stress and the tangential velocity weighted by the friction coefficient

$$\mu \frac{\partial v_y}{\partial z} = -\beta v_y \tag{A.10}$$

After replacing Eq. A.7 in the previous Navier condition, the second coefficient K_1 may be expressed as follow

$$K_1 = \frac{1}{\mu + \beta H}\left(-\frac{\beta}{2\mu} C H^2 - CH\right) \tag{A.11}$$

The solution for Poiseuille flow with a no-split boundary condition at the bottom wall and a Navier condition (slip) at the upper wall is

$$\begin{aligned} v_y &= \frac{C}{2\mu} z^2 + \frac{1}{\mu + \beta H} \left(-\frac{\beta}{2\mu} C H^2 - C H \right) z \\ p &= C y + p_{in} \end{aligned} \tag{A.12}$$

When the friction coefficient increases, the solution tends to a no-slip condition.

Appendix B

Capillary pressure based on energy equivalence

Contents

B.1 Stokes/Darcy energy equation

This appendix presents an equivalence between Stokes and Darcy based on the evaluation of the power of external and internal efforts. First, the equation linking internal and external powers is written based on the conservation of momentum without inertia effects. Then, the equation is particularised for Stokes and Darcy cases by choosing the adapted constitutive law. By identification, it is then possible to find a relationship between the terms in Stokes and Darcy systems, accounting for the permeability in the case of a saturated flow. Finally, the same identification is possible in the case of a spontaneous capillary rise between the terms representing the capillarity in both Stokes and Darcy systems.

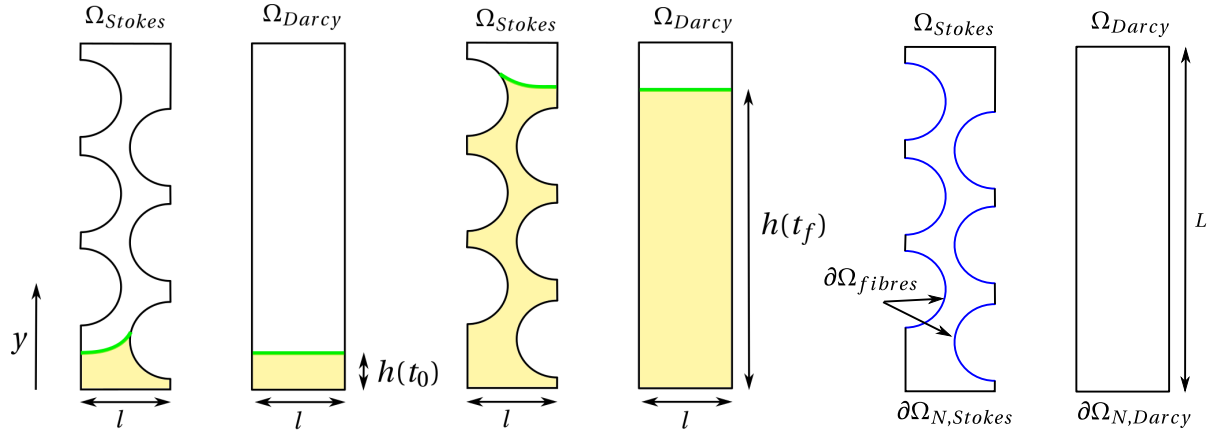

(A) At $t = t_0$ (B) At $t = t_f$ (C) boundary condition

FIGURE B.1 – Energy equivalence between Stokes and Darcy system - Domain definition

B.1.1 Power relationship

Let us consider Ω the computational domain. This domain can be the microstructure described in Fig. B.1 (A) on the left, Ω_{Stokes}, or the equivalent homogeneised medium like in Fig. B.1 (A) on the right, Ω_{Darcy}. In both cases, Ω contains two incompressible Newtonian fluids, one a liquid and the other a gas. Neglecting inertia, the momentum balance equation writes as

$$\nabla \cdot \boldsymbol{\sigma} + \boldsymbol{f} = \boldsymbol{0} \qquad \text{in } \Omega \tag{B.1}$$

with $\boldsymbol{\sigma}$ the stress tensor and $\boldsymbol{f}$ an external force. The power relationship is obtained by integrating this previous equation on the domain Ω after dotting it by the velocity. After integrating the stress term by parts, it comes

$$\underbrace{-\int_\Omega \boldsymbol{\sigma} : \dot{\boldsymbol{\epsilon}}(\boldsymbol{v})\, dV}_{\mathscr{P}^{(int)}} + \underbrace{\underbrace{\int_{\partial\Omega} (\boldsymbol{\sigma}\cdot\boldsymbol{n})\cdot\boldsymbol{v}\, dS}_{\mathscr{P}^{(c)}} + \underbrace{\int_\Omega \boldsymbol{f}\cdot\boldsymbol{v}\, dV}_{\mathscr{P}^{(d)}}}_{\mathscr{P}^{(ext)}} = 0 \tag{B.2}$$

with $\dot{\boldsymbol{\epsilon}}(\boldsymbol{v}) = \frac{1}{2}\left(\nabla\boldsymbol{v} + \nabla\boldsymbol{v}^T\right)$ and:

- $\mathscr{P}^{(ext)}$, the power of external efforts, made of the sum of
  - $\mathscr{P}^{(c)}$, the power of contact efforts
  - $\mathscr{P}^{(d)}$, the power of body forces
- $\mathscr{P}^{(int)}$, the power of internal efforts

The sum of external and internal power yields the variation of kinetic energy.

B.1.2 Constitutive law for Stokes and Darcy equations

The power relationship is applied to Stokes and Darcy in the case of a capillary action without gravity effects. Both equations are derived by choosing the stress ($\boldsymbol{\sigma}$), the normal stress ($\boldsymbol{\sigma}\cdot\boldsymbol{n}$) at the interfaces, and the external forces ($\boldsymbol{f}$).

Stokes

In the case of a Stokes flow, the constitutive law is $\boldsymbol{\sigma} = -p\boldsymbol{I} + 2\mu\dot{\boldsymbol{\epsilon}}(\boldsymbol{v})$, and $\boldsymbol{f} = \boldsymbol{0}$ since gravity is neglected. The contact efforts $\mathscr{P}^{(c)}$ in Eq. B.2 represents the effects of surface tension: $[\![\boldsymbol{\sigma}\cdot\boldsymbol{n}]\!] = \nabla_\alpha\left(\gamma\boldsymbol{t}^\alpha\right)$ on interface Γ_{LV} and considering a Navier friction condition, $\boldsymbol{\sigma}\cdot\boldsymbol{n} = \nabla_\alpha\left(\gamma\boldsymbol{t}^\alpha\right) - \beta(\boldsymbol{v} - (\boldsymbol{v}\cdot\boldsymbol{n})\boldsymbol{n})$ on each interface Γ_k with $k \in \{SL, SV\}$. A last contact condition is applied at the bottom boundary $\partial\Omega_{N,Stokes}$ (see Fig. B.1 (C)), only for a saturated flow: $\boldsymbol{\sigma}\cdot\boldsymbol{n} = -p_{ext}\boldsymbol{n}$.

Darcy

Stress in Darcy is limited to an hydrostatic pressure $\boldsymbol{\sigma} = -p\boldsymbol{I}$. Contrary to Stokes flow, the external force represents a friction proportional to the velocity $\boldsymbol{f} = -\frac{\mu}{K}\boldsymbol{v}$. The effort due to contact represents the capillary pressure $[\![\boldsymbol{\sigma}\cdot\boldsymbol{n}]\!] = -p_{cap}\boldsymbol{n}$ at the only existent interface Γ_{LV} and $\boldsymbol{\sigma}\cdot\boldsymbol{n} = -p_{ext}\boldsymbol{n}$ at the bottom boundary $\partial\Omega_{N,Darcy}$ in Fig. B.1 (C) for a saturated flow.

B.1.3 Energy equivalence for saturated flow (without capillarity)

The relation B.2 is written for both Stokes and Darcy system. Velocity and pressure fields of the Stokes system are denoted with the index $\bullet_S$ and the sum of the power reads

$$-\int_{\Omega_{Stokes}} \left(-p_S\delta_{ij} + 2\mu\dot{\boldsymbol{\epsilon}}(\boldsymbol{v}_S)\right) : \dot{\boldsymbol{\epsilon}}(\boldsymbol{v}_S)\, dV + \int_{\partial\Omega_{fibres}} (\boldsymbol{\sigma}\cdot\boldsymbol{n})\cdot\boldsymbol{v}_S\, dS + \int_{\partial\Omega_{N,Stokes}} (\boldsymbol{\sigma}\cdot\boldsymbol{n})\cdot\boldsymbol{v}_S\, dS = 0 \quad \text{(B.3)}$$

In the case of an incompressible fluid, the pressure term does not work ($\nabla\cdot\boldsymbol{v} = 0$) and after replacing with the boundary values the relation becomes

$$-\int_{\Omega_{Stokes}} 2\mu\dot{\boldsymbol{\epsilon}}(\boldsymbol{v}_S) : \dot{\boldsymbol{\epsilon}}(\boldsymbol{v}_S)\, dV - \int_{\partial\Omega_{fibres}} \beta\boldsymbol{v}_S\cdot\boldsymbol{v}_S\, dS - \int_{\partial\Omega_{N,Stokes}} p_{ext}\boldsymbol{n}\cdot\boldsymbol{v}_S\, dS = 0 \quad \text{(B.4)}$$

because the normal velocity is null on the fibres contours. Also for an incompressible fluid and after replacing the boundary condition, the power equation for Darcy yields

$$-\int_{\Omega_{Darcy}} \frac{\mu}{K}\boldsymbol{v}_D\cdot\boldsymbol{v}_D\, dV - \int_{\partial\Omega_{N,Darcy}} p_{ext}\boldsymbol{n}\cdot\boldsymbol{v}_D\, dS = 0 \quad \text{(B.5)}$$

Assuming that Stokes and Darcy systems carry the same amount of energy, the three terms in Stokes system in Eq. B.4 are equal to the two terms in Darcy system in Eq. B.5. The same constant external pressure p_{ext} is prescribed at the bottom boundary. Therefore, the last term in both system is equal since the flow rate is the same $-\int_{\partial\Omega_{N,Stokes}} p_{ext}\boldsymbol{n}\cdot\boldsymbol{v}_S\, dS = -\int_{\partial\Omega_{N,Darcy}} p_{ext}\boldsymbol{n}\cdot\boldsymbol{v}_D\, dS$. It leads to the identification between power in Darcy and in Stokes systems

$$\int_{\Omega_{Stokes}} 2\mu\dot{\boldsymbol{\epsilon}}(\boldsymbol{v}_S) : \dot{\boldsymbol{\epsilon}}(\boldsymbol{v}_S)\, dV + \int_{\partial\Omega_{fibres}} \beta(\boldsymbol{v}_S - (\boldsymbol{v}_S\cdot\boldsymbol{n})\boldsymbol{n})\cdot\boldsymbol{v}_S\, dS = \int_{\Omega_{Darcy}} \frac{\mu}{K}\boldsymbol{v}_D\cdot\boldsymbol{v}_D\, dV \quad \text{(B.6)}$$

In the Stokes system, the viscous dissipation and friction on the fibres are represented by friction in the Darcy equation. The permeability is unrelated to the fluid viscosity, since the friction in Darcy is proportional to $\frac{\mu}{K}$.
Two cases are now investigated: the no-slip and slip conditions on the fibres.

- No-slip condition $\boldsymbol{v} = \boldsymbol{0}$ on the fibres
  The permeability represents the viscous dissipation in Stokes. Supposing that the viscosity is constant in the fluid, like the permeability in the homogeneised domain then

  $$\int_{\Omega_{Stokes}} 2\dot{\boldsymbol{\epsilon}}(\boldsymbol{v}_S) : \dot{\boldsymbol{\epsilon}}(\boldsymbol{v}_S)\, dV = \frac{1}{K}\int_{\Omega_{Darcy}} \boldsymbol{v}_D\cdot\boldsymbol{v}_D\, dV. \quad \text{(B.7)}$$

  The fluid is set in motion by the gradient of pressure between the inlet ($p = p_{ext}$) and oulet ($p = 0$). The Darcy velocity has an analytical solution for a flow in 1D: a constant velocity $v_D = \frac{K}{\mu}\frac{p_{ext}}{L}$, where L is the domain length (reported in Fig. B.1 (C)). In that case, the permeability could be computed using the formula

  $$K = \frac{2\mu^2 L^2 \int_{\Omega_{Stokes}} \dot{\boldsymbol{\epsilon}}(\boldsymbol{v}_S) : \dot{\boldsymbol{\epsilon}}(\boldsymbol{v}_S)\, dV}{p_{ext}^2 \int_{\Omega_{Darcy}} dV} \quad \text{(B.8)}$$

undependently of the fluid viscosity because the velocity is inversely proportional to the viscosity in Stokes equations $v_S \propto 1/\mu$.

- Slip condition on the fibres (Navier friction)
  Using the same assumption on the Darcy velocity, the formula for the permeability reads

$$K = \frac{\mu L^2 \left(2\mu \int_{\Omega_{Stokes}} \dot{\boldsymbol{\epsilon}}(\boldsymbol{v}_S) : \dot{\boldsymbol{\epsilon}}(\boldsymbol{v}_S)\, dV + \beta \int_{\partial\Omega_{fibres}} \boldsymbol{v}_S \cdot \boldsymbol{v}_S\, dS \right)}{p_{ext}^2 \int_{\Omega_{Darcy}} dV}. \tag{B.9}$$

  In that case, the permeability depends on the fluid and is not a parameter of the microstructure.

B.1.4 Energy equivalence for a bifluid flow

Let us now consider the capillary forces, by assuming that the contribution to the variation of energy in Stokes and Darcy systems between two moments t_0 and $t_f > t_0$, due to capillary effects are equal:

$$\sum_{k \in \{LV,SL,SV\}} \int_{t_0}^{t_f} \left(\int_{\Gamma_{k,Stokes}} \nabla_\alpha \left(\gamma_k \boldsymbol{t}^\alpha \right) \cdot \boldsymbol{v}_S\, dS \right) dt = \int_{t_0}^{t_f} \left(\int_{\Gamma_{LV,Darcy}} p_{cap} \boldsymbol{v}_D \cdot \boldsymbol{n}\, dS \right) dt \tag{B.10}$$

In our case, with impervious fibres $\boldsymbol{v}_S \cdot \boldsymbol{n} = 0$ in Stokes on the fibres contours. Then, with a constant surface tension coefficient, the capillary energy equality becomes

$$\int_{t_0}^{t_f} \left(\int_{\Gamma_{LV,Stokes}} \gamma_{LV} \mathscr{C} \boldsymbol{v}_S \cdot \boldsymbol{n}\, dS \right) dt = \int_{t_0}^{t_f} \left(\int_{\Gamma_{LV,Darcy}} p_{cap} \boldsymbol{v}_D \cdot \boldsymbol{n}\, dS \right) dt \tag{B.11}$$

The right-hand side term of the Darcy domain may be analytically computed by assuming that the Darcy flow is 1D (*i.e.* $\boldsymbol{v}_D \cdot \boldsymbol{n} = \frac{dh}{dt}$) and that the capillary pressure is constant on the interface and over time. The Stokes term on the left-hand side depends on the curvature $\mathscr{C}$ and is numerically computed. Therefore, a precise computation of the curvature is a crucial point. Eq. B.11 is transformed to express the capillary pressure as

$$p_{cap} = \frac{\int_{t_0}^{t_f} \left(\int_{\Gamma_{LV,Stokes}} \gamma_{LV} \mathscr{C} \boldsymbol{v}_S \cdot \boldsymbol{n}\, dS \right) dt}{l \left(h(t_f) - h(t_0) \right)} \tag{B.12}$$

This definition of the capillary pressure has the advantage to be independent of the permeability, contrary to the definition based on the equivalence with Darcy 1D. Note in Eq. B.12 the variation of the liquid height between t_0 and t_f in the Darcy domain, has been taken equal to the one obtained by simulation in the Stokes domain.

B.2 Numerical experiment

Numerical experiments are carried out using the microstructure with a hexagonal packing as described in the Results chapter 5. The first test is for a saturated flow to compute the numerical permeability and the second is a spontaneous impregnation.

B.2.1 Permeability

The results from the numerical permeability using methods 1 and 2 in Fig. 5.25 are compared with the numerical permeability computed from Eq. B.8. The permeability computed with the three methods in reported in Fig. B.3. The method based on the equation of Darcy

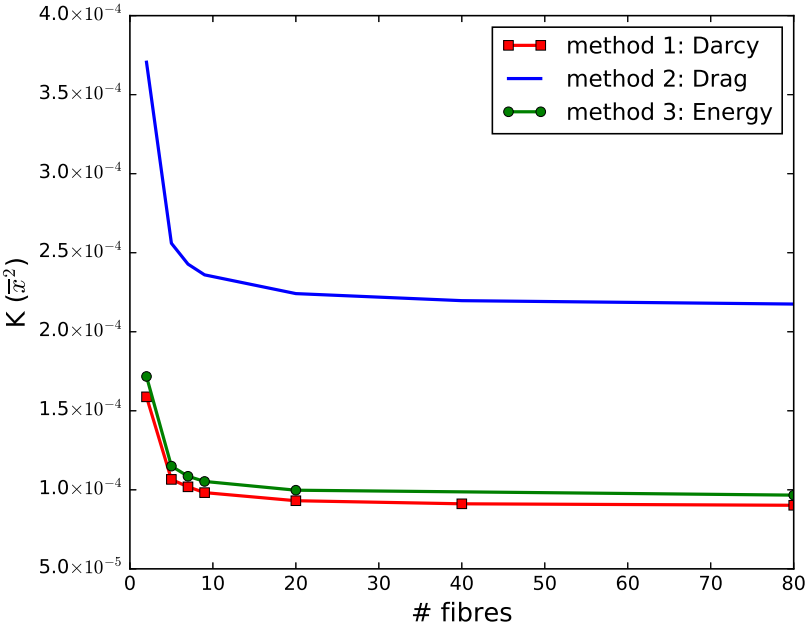

FIGURE B.2 – Saturated flow in hexagonal packing - Numerical permeability

written in terms of flow rate gives close results with the introduced third method based on energy equivalence. The second method gives an estimation with excess for the permeability as mentioned in the thesis.

B.2.2 Capillary pressure

The capillary pressure is computed from Eq. B.11, in the case of a spontaneous capillary rise in a hexagonal fibre packing as presented in the Results section 5 of the thesis. The resin advancing between fibres is represented in Fig. B.3 at different instants and coloured in dark and light blue close to the interface. Time $\tilde{t}$ measures the time after the interface has touched the fibre. The weak coupling seems to struggle with sudden geometry changes. For example, the curvature is inverted between subfigure (C) and (F). Yet, it is of paramount importance to obtain a realistic description of the interface when advancing between two fibres with a high velocity at the triple point since the capillary pressure depends on the curvature as shown in Eq. B.12. The lack of accuracy of the weak coupling has been demonstrated and discussed with the case of a

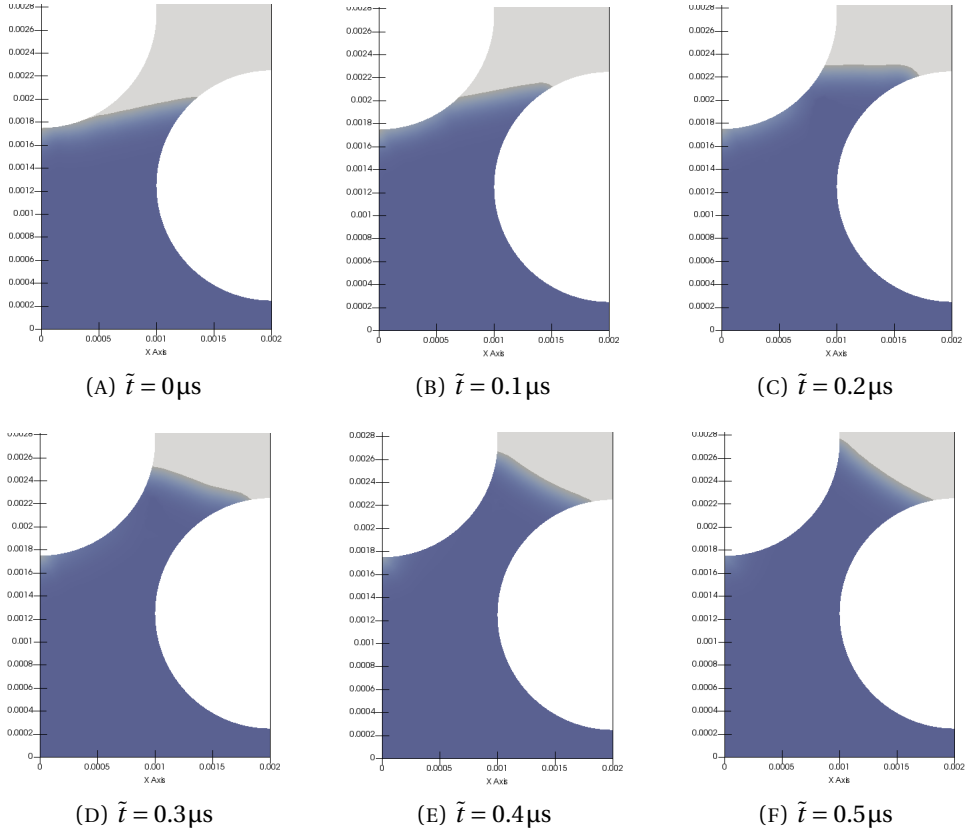

(A) $\tilde{t} = 0\,\mu s$ (B) $\tilde{t} = 0.1\,\mu s$ (C) $\tilde{t} = 0.2\,\mu s$

(D) $\tilde{t} = 0.3\,\mu s$ (E) $\tilde{t} = 0.4\,\mu s$ (F) $\tilde{t} = 0.5\,\mu s$

FIGURE B.3 – Capillary rise in hexagonal packing - Weak coupling

drop spreading on a sinusoidal surface. A strong coupling approach has been tested and the interface position is represented in Fig. B.4. Data have been post-processed with Paraview [8] for numerically integrating along the interface and in time the numerator in Eq. B.12, to compute the capillary pressure.

Due to time constraint, only one test has been performed, resulting in a capillary pressure of 3.6 kPa. In the same hexagonal packing, the method based on Darcy 1D for the computation of the capillary pressure has yielded a value of 42 kPa but with a no-slip condition for the permeability estimation in method 1 associated with. If one wants to compare capillary pressures evaluated with the present energetic method, capillary pressure from the 1D Darcy method should consider a permeability with a free slip boundary condition. In that case, computations yield a five times higher permeability ($1.26 \times 10^{-12}\,m^2$), and so a capillary pressure of 8.4 kPa. Therefore, the capillary pressure computed from the presented energy method gives comparable results with the Darcy 1D method. This encouraging result has to be continued and further tests have to carried out with the strong coupling in both cases.

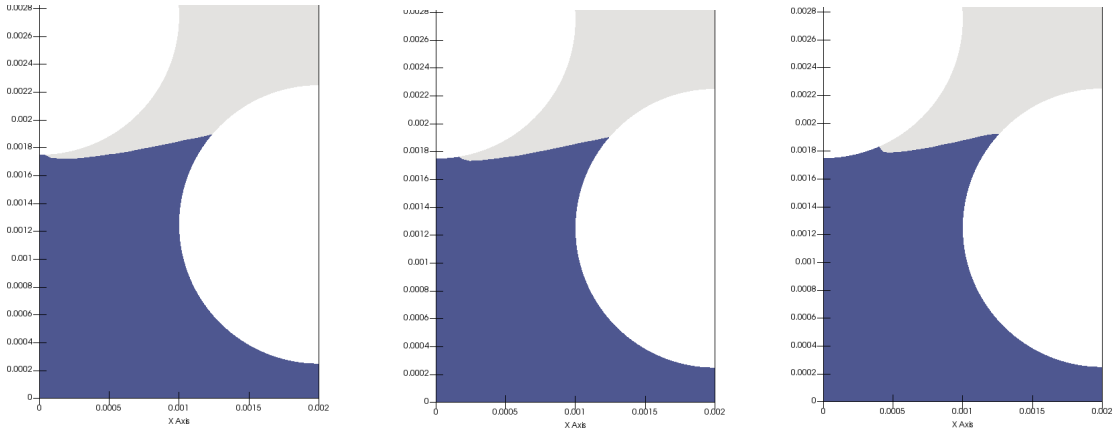

(A) $\tilde{t} = 0\,\mu s$ (B) $\tilde{t} = 0.02\,\mu s$ (C) $\tilde{t} = 0.05\,\mu s$

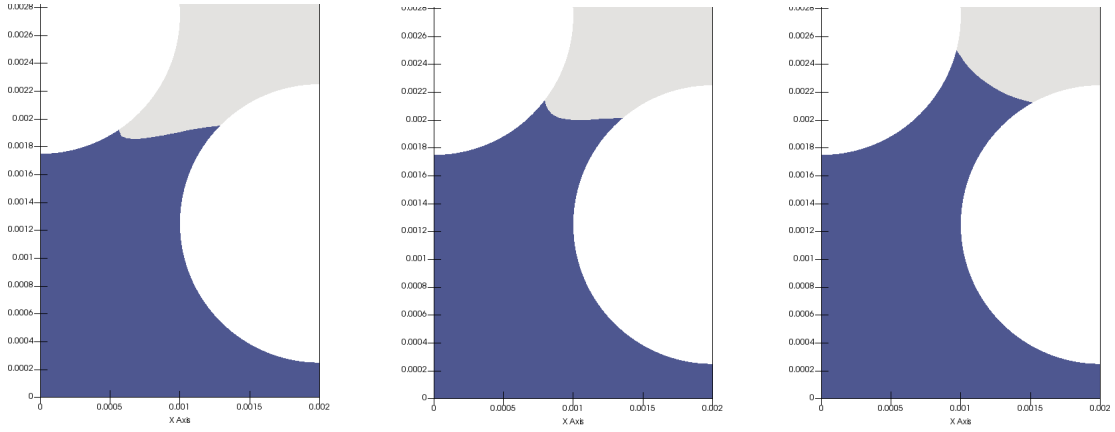

(D) $\tilde{t} = 0.07\,\mu s$ (E) $\tilde{t} = 0.11\,\mu s$ (F) $\tilde{t} = 0.215\,\mu s$

FIGURE B.4 – Capillary rise in hexagonal packing - Strong coupling

List of Figures

List of Tables

Bibliography

[1] J. AARNES and B.-O. HEIMSUND. "Multiscale Discontinuous Galerkin Methods for Elliptic Problems with Multiple Scales". In: *Multiscale Methods in Science and Engineering*. 2005, pp. 1–20.

[2] T. ABADIE, J. AUBIN, and D. LEGENDRE. "On the combined effects of surface tension force calculation and interface advection on spurious currents within Volume of Fluid and Level Set frameworks". In: *Journal of Computational Physics* 297 (2015), pp. 611–636.

[3] L. ABOU ORM. "Variational MultiScale stabilization for Stokes-Darcy coupled flows in porous media undergoing finite deformations: application to infusion-based composite processing." PhD thesis. Ecole Nationale Supérieure des Mines de Saint-Etienne, 2014.

[4] L. ABOUORM, R. TROIAN, S. DRAPIER, J. BRUCHON, and N. MOULIN. "Stokes-Darcy coupling in severe regimes using multiscale stabilisation for mixed finite elements: monolithic approach versus decoupled approach". In: *European Journal of Computational Mechanics* 23.3-4 (2014), pp. 113–137.

[5] A. W. ADAMSON and A. P. GAST. *Physical Chemistry of Surfaces*. 6. 1997. ISBN: 978-0-471-14873-9.

[6] J. ADELSBERGER, P. ESSER, M. GRIEBEL, S. GROSS, M. KLITZ, and A. RUTTGERS. "3D Incompressible Two-Phase Flow Benchmark Computations for Rising Droplets". In: *11th World Congress on Computational Mechanics* l.1401 (2014), p. 14.

[7] K. J. AHN, J. C. SEFERIS, and J. C. BERG. "Simultaneous measurements of permeability and capillary pressure of thermosetting matrices in woven fabric reinforcements". In: *Polymer Composites* 12.3 (1991), pp. 146–152.

[8] J. AHRENS, C. LAW, B. GEVECI, JAMES A., and C. L. B. GEVECI. "Paraview: An end user tool for large data visualization". In: *The visualization handbook* (2005).

[9] S. ALAND and A. VOIGT. "Benchmark computations of diffuse interface models for two-dimensional bubble dynamics". In: *International Journal for Numerical Methods in Fluids* 69.3 (2012), pp. 747–761.

[10] P. R. AMESTOY, I. S. DUFF, J.-Y. L'EXCELLENT, and J. KOSTER. "A Fully Asynchronous Multifrontal Solver Using Distributed Dynamic Scheduling". In: *SIAM Journal on Matrix Analysis and Applications* 23.1 (2001), pp. 15–41.

[11] P. R. AMESTOY, A. GUERMOUCHE, J. Y. L'EXCELLENT, and S. PRALET. "Hybrid scheduling for the parallel solution of linear systems". In: *Parallel Computing* 32.2 (2006), pp. 136–156.

[12] S. AMICO and C. LEKAKOU. "An experimental study of the permeability and capillary pressure in resin-transfer moulding". In: *Composites Science and Technology* 61.13 (2001), pp. 1945–1959.

[13] S. AMICO and C. LEKAKOU. "Mathematical modelling of capillary micro-flow through woven fabrics". In: *Composites Part A: Applied Science and Manufacturing* 31.12 (2000), pp. 1331–1344.

[14] A. AMMAR, E. ABISSET-CHAVANNE, F. CHINESTA, and R. KEUNINGS. "Flow modelling of quasi-Newtonian fluids in two-scale fibrous fabrics: Advanced simulations". In: *International Journal of Material Forming* 10.4 (2017), pp. 547–556.

[15] J. D. ANDERSON. "Governing Equations of Fluid Dynamics". In: *Computational Fluid Dynamics An Introduction*. Ed. by John F WENDT. Springer Berlin Heidelberg, 1992. Chap. 2, pp. 15–51. ISBN: 978-3-540-85056-4.

[16] T. B. ANDERSON and R. JACKSON. "Fluid mechanical description of fluidized beds: Equations of Motion". In: *Industrial and Engineering Chemistry Fundamentals* 6.4 (1967), pp. 527–539.

[17] K. ANDRIAMANANJARA, N. MOULIN, J. BRUCHON, P.-J. LIOTIER, and S. DRAPIER. "Numerical modeling of local capillary effects in porous media as a pressure discontinuity acting on the interface of a transient bi-fluid flow". In: *International Journal of Material Forming* (2018), pp. 1–17.

[18] A. M. ARAGON and A. SIMONE. "The Discontinuity-Enriched Finite Element Method". In: *International Journal for Numerical Methods in Engineering* 112.11 (2017), pp. 1589–1613.

[19] R. F. AUSAS, G. C. BUSCAGLIA, and S. R. IDELSOHN. "A new enrichment space for the treatment of discontinuous pressures in multi-fluid flows". In: *International Journal for Numerical Methods in Fluids* 70.7 (2012), pp. 829–850.

[20] R. F. AUSAS, F. S. SOUSA, and G. C. BUSCAGLIA. "An improved finite element space for discontinuous pressures". In: *Computer Methods in Applied Mechanics and Engineering* 199.17-20 (2010), pp. 1019–1031.

[21] S. BADIA and R. CODINA. "Stokes, Maxwell and Darcy: A single finite element approximation for three model problems". In: *Applied Numerical Mathematics*. Vol. 62. 4. 2012, pp. 246–263.

[22] J. L. BAILLEUL, D. DELAUNAY, and Y. JARNY. "Determination of temperature variable properties of composite materials: Methodology and experimental results". In: *Journal of Reinforced Plastics and Composites* 15.5 (1996), pp. 479–496.

[23] C. BALEY. "Fibres naturelles de renfort pour matériaux composites". In: *Techniques de l'ingénieur* 1 (2013), pp. 1–17.

[24] E. BÄNSCH. "Finite element discretization of the Navier–Stokes equations with a free capillary surface". In: *Numerische Mathematik* 88.2 (2000), pp. 203–235.

[25] J.-J. BARRAU and D. GUEDRA DEGEORGES. "Structures en matériaux composites". In: *Techniques de l'ingénieur* (2004), pp. 1–24.

[26] O. BASSET. "Simulation numérique d écoulements multi-fluides sur grille de calcul". PhD thesis. 2006.

[27] S. BATKAM, J. BRUCHON, and T. COUPEZ. "A Space-Time Discontinuous Galerkin Method for Convection and Diffusion in Injection Moulding". In: *International Journal of Forming Processes* 7 (2004), pp. 11–33.

[28] E. BAYRAMLI and R. L. POWELL. "The normal (transverse) impregnation of liquids into axially oriented fiber bundles". In: *Journal of Colloid And Interface Science* 138.2 (1990), pp. 346–353.

[29] J. BEAR. *Dynamics of Fluids in Porous Media*. Dover Civil and Mechanical Engineering Series. 1988. ISBN: 9780486656755.

[30] N. BEN SALAH, A. SOULAIMANI, and W. G. HABASHI. "A finite element method for magnetohydrodynamics". In: *Computer Methods in Applied Mechanics and Engineering* 190.43-44 (2001), pp. 5867–5892.

[31] A. L. BERDICHEVSKY and Z. CAI. "Preform permeability predictions by self-consistent method and finite element simulation". In: *Polymer Composites* 14.2 (1993), pp. 132–143.

[32] J. D. BERRY, M. J. NEESON, R. R. DAGASTINE, D. Y. C. CHAN, and R. F. TABOR. "Measurement of surface and interfacial tension using pendant drop tensiometry". In: *Journal of Colloid and Interface Science* 454 (2015), pp. 226–237.

[33] J. M. BERTHELOT. *Matériaux composites: comportement mécanique et analyse des structures*. Enseignement de la physique. Masson, 1992.

[34] J. BESSON and R. FOERCH. "Large scale object-oriented finite element code design". In: *Computer Methods in Applied Mechanics and Engineering* 142.1-2 (1997), pp. 165–187.

[35] C. BINETRUY, B. HILAIRE, and J. PABIOT. "Tow impregnation model and void formation mechanisms during RTM". In: *Journal of Composite Materials* 32.3 (1998), pp. 223–245.

[36] M. BLAIS. "Modélisation et suivi du procédé par infusion de résine sur une nouvelle génération de renforts structuraux pour l'aéronautique". PhD thesis. Ecole Nationale Supérieure des Mines de Saint-Etienne, 2016.

[37] T. D. BLAKE. "The physics of moving wetting lines". In: *Journal of Colloid and Interface Science* 299.1 (2006), pp. 1–13.

[38] T. D. BLAKE and J. M. HAYNES. "Kinetics of liquidliquid displacement". In: *Journal of Colloid and Interface Science* 30.3 (1969), pp. 421–423.

[39] D. BONN, J. EGGERS, J. INDEKEU, and J. MEUNIER. "Wetting and spreading". In: *Reviews of Modern Physics* 81.2 (2009), pp. 739–805.

[40] J. U. BRACKBILL, D. B. KOTHE, and C. ZEMECH. "A continuum method for modeling surface tension". In: *Journal of Computational Physics* 100.2 (1992), pp. 335–354.

[41] F. BREZZI and M. FORTIN. *Mixed and Hybrid Finite Element Methods*. Vol. 15. 1991, p. 350.

[42] F. BREZZI, L. P. FRANCA, T. J. R. HUGHES, and A. RUSSO. "$b = \int g$". In: *Computer Methods in Applied Mechanics and Engineering* 145.3-4 (1997), pp. 329–339.

[43] H. C. BRINKMAN. "Experimental data on the viscous force exerted by a flowing fluid on a dense swarm of particles". In: *Applied Scientific Research* 2.1 (1951), pp. 155–161.

[44] A. N. BROOKS and T. J. R. HUGHES. "Streamline upwind/Petrov-Galerkin formulations for convection dominated flows with particular emphasis on the incompressible Navier-Stokes equations". In: *Computer Methods in Applied Mechanics and Engineering* 32.1-3 (1982), pp. 199–259.

[45] J. BRUCHON. "Study of the formation of a foam structure by direct simulation of the expansion of bubbles in a polymeric liquid matrix". Theses. École Nationale Supérieure des Mines de Paris, 2004.

[46] J. BRUCHON, S. DRAPIER, and F. VALDIVIESO. "3D finite element simulation of the matter flow by surface diffusion using a level set method". In: *International Journal for Numerical Methods in Engineering* 86.7 (2011), pp. 845–861.

[47] J. BRUCHON, Y. LIU, and N. MOULIN. "Finite element setting for fluid flow simulations with natural enforcement of the triple junction equilibrium". In: *Computers and Fluids* 171 (2018), pp. 103–121.

[48] E. BURMAN. "Consistent SUPG-method for transient transport problems: Stability and convergence". In: *Computer Methods in Applied Mechanics and Engineering* 199.17-20 (2010), pp. 1114–1123.

[49] G. C. BUSCAGLIA and R. F. AUSAS. "Variational formulations for surface tension, capillarity and wetting". In: *Computer Methods in Applied Mechanics and Engineering* 200.45-46 (2011), pp. 3011–3025.

[50] P. C. CARMAN. "Fluid flow through granular beds". In: *Transactions of the Institution of Chemical Engineers* 15 (1937), pp. 155–166.

[51] P. CELLE, S. DRAPIER, and J. M. BERGHEAU. "Numerical modelling of liquid infusion into fibrous media undergoing compaction". In: *European Journal of Mechanics, A/Solids* 27.4 (2008), pp. 647–661.

[52] A. W. CHAN and R. J. MORGAN. "Tow impregnation during resin transfer molding of bi-directional nonwoven fabrics". In: *Polymer Composites* 14.4 (1993), pp. 335–340.

[53] M. CHATAIN. "Matériaux composites : présentation générale". In: *Techniques de l'ingénieur Matériaux composites : présentation et renforts* (2001), pp. 1–11.

[54] C. Y. CHEN. "Filtration of Aerosols by Fibrous Media". In: *Chemical Reviews* 55.3 (1955), pp. 595–623.

[55] L. CHEN, S. V. GARIMELLA, J. A. REIZES, and E. LEONARDI. "The development of a bubble rising in a viscous liquid". In: *Journal of Fluid Mechanics* 387 (1999), pp. 61–96.

[56] J. CHESSA and T. BELYTSCHKO. "An enriched finite element method and level sets for axisymmetric two-phase flow with surface tension". In: *International Journal for Numerical Methods in Engineering* 58.13 (2003), pp. 2041–2064.

[57] J. CHESSA and T. BELYTSCHKO. "An extended finite element method for two-phase fluids". In: *Journal of Applied Mechanics* 70.1 (2003), pp. 10–17.

[58] L. CHEVALIER, J. BRUCHON, N. MOULIN, P.-J. LIOTIER, and S. DRAPIER. *Accounting for local capillary effects in two-phase flows with relaxed surface tension formulation in enriched finite elements*. 2018.

[59] F. CHINESTA, A. AMMAR, A. LEYGUE, and R. KEUNINGS. "An overview of the proper generalized decomposition with applications in computational rheology". In: *Journal of Non-Newtonian Fluid Mechanics* 166.11 (2011), pp. 578–592.

[60] R. CLIFT, J. R. GRACE, and M. E. E. WEBER. *Bubbles, Drops and Particles*. 1978, p. 795. ISBN: 978-0486445809.

[61] R. CODINA. "A discontinuity-capturing crosswind-dissipation for the finite element solution of the convection-diffusion equation". In: *Computer Methods in Applied Mechanics and Engineering* 110 (1992), pp. 325–342.

[62] R. CODINA. "A stabilized finite element method for generalized stationary incompressible flows". In: *Computer Methods in Applied Mechanics and Engineering* 190.20-21 (2001), pp. 2681–2706.

[63] R. CODINA. "Stabilized finite element approximation of transient incompressible flows using orthogonal subscales". In: *Computer Methods in Applied Mechanics and Engineering* 191.39-40 (2002), pp. 4295–4321.

[64] R. CODINA, J. PRINCIPE, O. GUASCH, and S. BADIA. "Time dependent subscales in the stabilized finite element approximation of incompressible flow problems". In: *Computer Methods in Applied Mechanics and Engineering* 196.21-24 (2007), pp. 2413–2430.

[65] Ramon. CODINA. "A finite Element Model for Incompressible Flow Problems". PhD thesis. Universitat Politècnica de Catalunya, Barcelona, 1992.

[66] R. G. COX. "The dynamics of the spreading of liquids on a solid-surface. Part 1. Viscous-flow". In: *Journal of Fluid Mechanics* 168 (1986), pp. 169–194.

[67] R. G. COX. "The dynamics of the spreading of liquids on a solid surface. Part 2. Surfactants". In: *Journal of Fluid Mechanics* 168 (1986), pp. 195–220.

[68] B. J. DALY and W. E. PRACHT. "Numerical Study of Density-Current Surges". In: *Physics of Fluids* 11 (1968), p. 15. ISSN: 71.

[69] H. DARCY. "Les fontaines publiques de la ville de Dijon". In: *Recherche* (1856), p. 647.

[70] C. N. DAVIES. "The Separation of Airborne Dust and Particles". In: *Proceedings of the Institution of Mechanical Engineers, Part B: Management and engineering manufacture* 1.1-12 (1953), pp. 185–213.

[71] P.-G. DE GENNES, F. BROCHARD-WYART, and D. QUÉRÉ. *Capillarity and Wetting Phenomena - Drops, Bubbles, Pearls, Waves*. 2002. ISBN: 978-0-387-00592-8.

[72] B. DE PARSCAU DU PLESSIX, S. LE CORRE, F. JACQUEMIN, P. LEFEBURE, and V. SOBOTKA. "Improved simplified approach for the prediction of porosity growth during the curing of composites parts". In: *Composites Part A: Applied Science and Manufacturing* 90 (2016), pp. 549–558.

[73] F. DENNER and B. G. M. van WACHEM. "Numerical time-step restrictions as a result of capillary waves". In: *Journal of Computational Physics* 285 (2015), pp. 24–40.

[74] A. DEREIMS. "Simulation industrielle des procédés d'élaboration de pièces composites par infusion de résine : couplage fluide / solide poreux très faiblement perméable en grandes déformations". PhD thesis. Ecole Nationale Supérieure des Mines de Saint-Etienne, 2013.

[75] C. DEVALVE and R. PITCHUMANI. "Simulation of void formation in liquid composite molding processes". In: *Composites Part A: Applied Science and Manufacturing* 51 (2013), pp. 22–32.

[76] L. DING, C. SHIH, Z. LIANG, C. ZHANG, and B. WANG. "In situ measurement and monitoring of whole-field permeability profile of fiber preform for liquid composite molding processes". In: *Composites Part A: Applied Science and Manufacturing* 34.8 (2003), pp. 779–789.

[77] M. DISCACCIATI, D. HACKER, A. QUARTERONI, S. QUINODOZ, S. TISSOT, and F. M. WURM. "Numerical simulation of orbitally shaken viscous fluids with free surface". In: *International Journal for Numerical Methods in Fluids* 71.3 (2013), pp. 294–315.

[78] D. A. DREW. "Averaged Field Equations for Two-Phase Media". In: *Studies in Applied Mathematics* 1.2 (1971), pp. 133–166.

[79] F. A. L. DULLIEN. "Selected Operations Involving Transport of a Single Fluid Phase through a Porous Medium". In: *Porous Media*. Second Edition. San Diego: Academic Press, 1992. Chap. 5, pp. 235–249. ISBN: 978-0-12-223650-1.

[80] F. A. L. DULLIEN. "Single-Phase Transport Phenomena in Porous Media". In: *Porous Media*. Second Edition. Academic Press, 1979. Chap. 4, pp. 157–234. ISBN: 978-0-12-223650-1.

[81] E. DUSSAN and S. DAVIS. "On the motion of a fluid-fluid interface along a solid surface". In: *Journal of Fluid Mechanics* 65.1 (1974), pp. 71–95.

[82] E. B. DUSSAN. "On the Spreading of Liquids on Solid Surfaces: Static and Dynamic Contact Lines". In: *Annual Review of Fluid Mechanics* 11.1 (1979), pp. 371–400.

[83] G. DZIUK. "An algorithm for evolutionary surfaces". In: *Numerische Mathematik* 58.1 (1990), pp. 603–611.

[84] G. DZIUK and C. M. ELLIOTT. "Finite elements on evolving surfaces". In: *IMA Journal of Numerical Analysis* 27.2 (2007), pp. 262–292.

[85] M. EL-KAMALI, J. S. SCHOTTÉ, and R. OHAYON. "Computation of the equilibrium position of a liquid with surface tension inside a tank of complex geometry and extension to sloshing dynamic cases". In: *Computational Mechanics* 46.1 (2010), pp. 169–184.

[86] M. FEBRES and D. LEGENDRE. "Enhancement of a 2D front-tracking algorithm with a non-uniform distribution of Lagrangian markers". In: *Journal of Computational Physics* 358.1 (2018), pp. 173–200.

[87] U. FEY, M. KÖNIG, and H. ECKELMANN. "A new Strouhal-Reynolds-number relationship for the circular cylinder in the range $47 < Re < 2 \times 10^5$". In: *Physics of Fluids* 10.7 (1998), pp. 1547–1549.

[88] M. FORTIN. "Old and new finite elements for incompressible flows". In: *International Journal for Numerical Methods in Fluids* 1.4 (1981), pp. 347–364.

[89] E. FRIED and M. E. GURTIN. "A unified treatment of evolving interfaces accounting for small deformations and atomic transport with emphasis on grain-boundaries and epitaxy". In: *Advances in applied mechanics* 40.4 (2004), pp. 1–177.

[90] N. FRIES. *Capillary transport processes in porous materials - Experiment and Model*. 2010, p. 167. ISBN: 978-3869555072.

[91] C. GALUSINSKI and P. VIGNEAUX. "On stability condition for bifluid flows with surface tension: Application to microfluidics". In: *Journal of Computational Physics* 227.12 (2008), pp. 6140–6164.

[92] S. GANESAN, G. MATTHIES, and L. TOBISKA. "On spurious velocities in incompressible flow problems with interfaces". In: *Computer Methods in Applied Mechanics and Engineering* 196.7 (2007), pp. 1193–1202.

[93] B. R. GEBART. "Permeability of Unidirectional Reinforcements for RTM". In: *Journal of Composite Materials* 26.8 (1992), pp. 1100–1133.

[94] P. G. de GENNES. "Wetting: statics and dynamics". In: *Reviews of Modern Physics* 57.3 (1985), pp. 827–863.

[95] C. GEUZAINE and J. F. REMACLE. "Gmsh: A 3-D finite element mesh generator with built-in pre- and post-processing facilities". In: *International Journal for Numerical Methods in Engineering* 79.11 (2009), pp. 1309–1331.

[96] A. GIAVARAS and E. BOATENG. "Transient filling modelling at meso-level for RTM process using a single phase LSM". In: *International Journal of Material Forming* 8.2 (2014), pp. 197–210.

[97] J. W. GIBBS. "On the equilibrium of heterogeneous substances". In: *American Journal of Science* 3.96 (1878), pp. 441–458.

[98] V. GRAVEMEIER. *The variational multiscale method for laminar and turbulent flow*. 2006.

[99] V. GRAVEMEIER. "The variational multiscale method for laminar and turbulent incompressible flow". PhD thesis. University of Stuttgart, 2003.

[100] W. G. GRAY and P. C.Y. LEE. "On the theorems for local volume averaging of multiphase systems". In: *International Journal of Multiphase Flow* 3.4 (1977), pp. 333–340.

[101] W. G. GRAY and C. T. MILLER. "A generalization of averaging theorems for porous medium analysis". In: *Advances in Water Resources* 62 (2013), pp. 227–237.

[102] S. GROSS and A. REUSKEN. "An extended pressure finite element space for two-phase incompressible flows with surface tension". In: *Journal of Computational Physics* 224.1 (2007), pp. 40–58.

[103] S. GROSS and A. REUSKEN. "Finite element discretization error analysis of a surface tension force in two-phase incompressible flows". In: *SIAM Journal on Numerical Analysis* 45.4 (2007), pp. 1679–1700.

[104] S. GROSS and A. REUSKEN. *Numerical Methods for Two-phase Incompressible Flows*. 1st ed. Springer-Verlag Berlin Heidelberg, 2011, p. 482. ISBN: 978-3-642-19685-0.

[105] C. GRUAU and T. COUPEZ. "3D tetrahedral, unstructured and anisotropic mesh generation with adaptation to natural and multidomain metric". In: *Computer Methods in Applied Mechanics and Engineering* 194.48-49 (2005), pp. 4951–4976.

[106] E. HACHEM. "Stabilized finite element method for heat transfer and turbulent flows inside industrial furnaces". PhD thesis. Mines ParisTech, 2009.

[107] E. HACHEM, M. KHALLOUFI, J. BRUCHON, R. VALETTE, and Y. MESRI. "Unified adaptive Variational MultiScale method for two phase compressible-incompressible flows". In: *Computer Methods in Applied Mechanics and Engineering* 308 (2016), pp. 238–255.

[108] Y. K. HAMIDI, L. AKTAS, and M. C. ALTAN. "Three-dimensional features of void morphology in resin transfer molded composites". In: *Composites Science and Technology* 65 (2005), pp. 1306–1320.

[109] F. H. HARLOW and J. E. WELCH. "Numerical Calculation of Time-Dependent Viscous Incompressible Flow of Fluid with Free Surface". In: *Physics of Fluids* 8.12 (1965), pp. 2182–2189.

[110] G. HAUKE and T. J. R. HUGHES. "A comparative study of different sets of variables for solving compressible and incompressible flows". In: *Computer Methods in Applied Mechanics and Engineering* 153.1-2 (1998), pp. 1–44.

[111] G. HAUKE and T. J. R. HUGHES. "A unified approach to compressible and incompressible flows". In: *Computer Methods in Applied Mechanics and Engineering* 113.3-4 (1994), pp. 389–395.

[112] D. HENDRIANA and K. J. BATHE. "On upwind methods for parabolic finite elements in incompressible flows". In: *International Journal for Numerical Methods in Engineering* 47.1-3 (2000), pp. 317–340.

[113] C. W. HIRT and B. D. NICHOLS. "Volume of fluid (VOF) method for the dynamics of free boundaries". In: *Journal of Computational Physics* 39.1 (1981), pp. 201–225.

[114] R. L. HOFFMAN. "A study of the advancing interface. I. Interface shape in liquid-gas systems". In: *Journal of Colloid And Interface Science* 50.2 (1975), pp. 228–241.

[115] F. A. HOWES and S. WHITAKER. "The spatial averaging theorem revisited". In: *Chemical Engineering Science* 40.8 (1985), pp. 1387–1392.

[116] T. J. R. HUGHES. "Multiscale phenomena: Green's functions, the Dirichlet-to-Neumann formulation, subgrid scale models, bubbles and the origins of stabilized methods". In: *Computer Methods in Applied Mechanics and Engineering* 127.1-4 (1995), pp. 387–401.

[117] T. J. R. HUGHES, G. R. FEIJOO, L. MAZZEI, and J. B. QUINCY. "The variational multiscale method - a paradigm for computational mechanics". In: *Computer Methods in Applied Mechanics and Engineering* 166.1-2 (1998), pp. 3–24.

[118] T. J. R. HUGHES, L. P. FRANCA, and G. M. HULBERT. "A new finite element formulation for computational fluid dynamics: VIII. The galerkin/least-squares method for advective-diffusive equations". In: *Computer Methods in Applied Mechanics and Engineering* 73.2 (1989), pp. 173–189.

[119] T. J. R. HUGHES, M. MALLET, and M. AKIRA. "A new finite element formulation for computational fluid dynamics: II. Beyond SUPG". In: *Computer Methods in Applied Mechanics and Engineering* 54.3 (1986), pp. 341–355.

[120] C. HUH and L. E. SCRIVEN. "Hydrodynamic model of steady movement of a solid/liquid/fluid contact line". In: *Journal of Colloid And Interface Science* 35.1 (1971), pp. 85–101.

[121] S. HYSING. "A new implicit surface tension implementation for interfacial flows". In: *International Journal for Numerical Methods in Fluids* 51.6 (2006), pp. 659–672.

[122] S. HYSING, S. TUREK, D. KUZMIN, N. PAROLINI, E. BURMAN, S. GANESAN, and L. TOBISKA. "Quantitative benchmark computations of two-dimensional bubble dynamics". In: *International Journal for Numerical Methods in Fluids* 60.11 (2009), pp. 1259–1288.

[123] S. R. IDELSOHN, J. M. GIMENEZ, J. MARTI, and N. M. NIGRO. "Elemental enriched spaces for the treatment of weak and strong discontinuous fields". In: *Computer Methods in Applied Mechanics and Engineering* 313 (2017), pp. 535–559.

[124] A. JARAUTA, P. RYZHAKOV, J. PONS-PRATS, and M. SECANELL. "An implicit surface tension model for the analysis of droplet dynamics". In: *Journal of Computational Physics* 374 (2018), pp. 1196–1218.

[125] H. JI and Q. ZHANG. "A simple finite element method for Stokes flows with surface tension using unfitted meshes". In: *International Journal for Numerical Methods in Fluids* 81.2 (2016), pp. 87–103.

[126] M. R. KAMAL and S. SOUROUR. "Kinetics and thermal characterization of thermoset cure". In: *Polymer Engineering and Science* 13.1 (1973), pp. 59–64.

[127] M. K. KANG, W. I. LEE, and H. T. HAHN. "Formation of microvoids during resin-transfer molding process". In: *Composites Science and Technology* 60 (2000), pp. 2427–2434.

[128] P. I. KARKANAS and I. K. PARTRIDGE. "Cure modeling and monitoring of epoxy/amine resin systems. II. Network formation and chemoviscosity modeling". In: *Journal of Applied Polymer Science* 77.10 (2000), pp. 2178–2188.

[129] C. E. KEES, I. AKKERMAN, M. W. FARTHING, and Y. BAZILEVS. "A conservative level set method suitable for variable-order approximations and unstructured meshes". In: *Journal of Computational Physics* 230.12 (2011), pp. 4536–4558.

[130] M. KHALLOUFI, Y. MESRI, R. VALETTE, E. MASSONI, and E. HACHEM. "High fidelity anisotropic adaptive variational multiscale method for multiphase flows with surface tension". In: *Computer Methods in Applied Mechanics and Engineering* 307 (2016), pp. 44–67.

[131] J. KOZENY. "Über kapillare leitung des wassers im boden". In: *Akad. Wiss.Wien* 136.2 (1927), pp. 271–306.

[132] B. LAFAURIE, C. NARDONE, R. SCARDOVELLI, S. ZALESKI, and G. ZANETTI. "Modelling Merging and Fragmentation in Multiphase Flows with SURFER". In: *Journal of Computational Physics* 113.1 (1994), pp. 134–147.

[133] P. LAMBERT. *Surface Tension in Microsystems: Engineering Below the Capillary Length*. Microtechnology and MEMS. Springer Berlin Heidelberg, 2013. ISBN: 978-3-642-37551-4.

[134] Y. LEE, Y. JHAN, C. CHUNG, and Y. HSU. "A Prediction Method for In-Plane Permeability and Manufacturing Applications in the VARTM Process". In: *Engineering* 3 (2011), pp. 691–699.

[135] D. LEGENDRE and M. MAGLIO. "Comparison between numerical models for the simulation of moving contact lines". In: *Computers and Fluids* 113 (2014), pp. 2–13.

[136] C. LEKAKOU and M. G. BADER. "Mathematical modelling of macro- and micro-infiltration in resin transfer moulding (RTM)". In: *Composites Part A: Applied Science and Manufacturing* 29.1-2 (1998), pp. 29–37.

[137] R. J. LENHARD, J. H. DANE, and M. OOSTROM. "Immiscible fluids". In: *Encyclopedia of Soils in the Environment*. 2005, pp. 239–247. ISBN: 978-0-12-348530-4.

[138] C. LI. "Simulation numérique de la fabrication de composites à renfort fibreux 3D par le procédé d'infusion". PhD thesis. Institut Universitaire de Technologie de Tarbes, 2018.

[139] T. S. LUNDSTRÖM and B. R. GEBART. "Influence from process parameters on void formation in resin transfer molding". In: *Polymer Composites* 15.1 (1994), pp. 25–33.

[140] T. S. LUNDSTRÖM, B. R. GEBART, and C. Y. LUNDEMO. "Void Formation in RTM". In: *Journal of Reinforced Plastics and Composites* 12.12 (1993), pp. 1339–1349.

[141] J. LUO, X. Y. HU, and N. A. ADAMS. "A conservative sharp interface method for incompressible multiphase flows". In: *Journal of Computational Physics* 284 (2015), pp. 547–565.

[142] L. E. MALVERN. *Introduction to the mechanics of a continuous medium*. 1969. ISBN: 978-0134876030.

[143] C. MARANGONI. "On the expansion of a drop of liquid floating on the surface of another liquid". In: *Tipographia dei fratelli Fusi, Pavia* (1865).

[144] A. MARCHAND, S. DAS, J. H. SNOEIJER, and B. ANDREOTTI. "Contact angles on a soft solid: From Young's law to Neumann's law". In: *Physical Review Letters* 109.23 (2012), p. 236101.

[145] C. M. MARLE. "Ecoulements monophasique en milieu poreux". In: *Revue de l'Institut français du pétrole* 22.10 (1967), pp. 1471–1509.

[146] A. MASUD and A. A. AL-NASEEM. "Variationally derived discontinuity capturing methods: Fine scale models with embedded weak and strong discontinuities". In: *Computer Methods in Applied Mechanics and Engineering* 340 (2018), pp. 1102–1134.

[147] C. MATTRAND, A. BÉAKOU, and K. CHARLET. "Numerical modeling of the flax fiber morphology variability". In: *Composites Part A: Applied Science and Manufacturing* 63 (2014), pp. 10–20.

[148] J. C. MAXWELL. "On Stresses in Rarefied Gases Arising from Inequalities of Temperature. [Abstract]". In: *Proceedings of the Royal Society of London* 27 (1878), pp. 304–308.

[149] M. MCLEAN, E. D. HONDROS, and K. C. MILLS. *Marangoni and Interfacial Phenomena in Materials Procesessing: Originating from Contributions to a Discussion of the Royal Society of London*. Matsci. Maney Publishing, 1998. ISBN: 9781861250568.

[150] V. MICHAUD. "A Review of Non-saturated Resin Flow in Liquid Composite Moulding processes". In: *Transport in Porous Media* 115.3 (2016), pp. 581–601.

[151] P. D. MINEV, T. CHEN, and K. NANDAKUMAR. "A finite element technique for multifluid incompressible flow using Eulerian grids". In: *Journal of Computational Physics* 187.1 (2003), pp. 255–273.

[152] S. E. MOUSAVI, J. E. PASK, and N. SUKUMAR. "Efficient adaptive integration of functions with sharp gradients and cusps in n-dimensional parallelepipeds". In: *International Journal for Numerical Methods in Engineering* 91.4 (2012), pp. 343–357.

[153] N. K. NAIK, M. SIRISHA, and A. INANI. "Permeability characterization of polymer matrix composites by RTM/VARTM". In: *Progress in Aerospace Sciences* 65 (2014), pp. 22–40.

[154] T. NAKAMURA, S. KANEKO, F. INADA, M. KATO, K. ISHIHARA, T. NISHIHARA, N. W. MUREITHI, and M. A. LANGTHJEM. *Flow-Induced Vibrations: Classifications and Lessons from Practical Experiences*. Elsevier Science, 2014. ISBN: 9780080449548.

[155] Guillermo A. NARSILIO, Olivier BUZZI, Stephen FITYUS, Tae Sup YUN, and David W. SMITH. "Upscaling of Navier-Stokes equations in porous media: Theoretical, numerical and experimental approach". In: *Computers and Geotechnics* 36.7 (2009), pp. 1200–1206.

[156] T. T. NATARAJAN and N. EL-KADDAH. "Finite element analysis of electromagnetic and fluid flow phenomena in rotary electromagnetic stirring of steel". In: *Applied Mathematical Modelling* 28.1 (2004), pp. 47–61.

[157] C. L. M. H. NAVIER. "Mémoire sur les lois du mouvement des fluids". In: *Mémoire de l'Académie Royale des Sciences de l'Institut de France* 6 (1823), pp. 389–416.

[158] L. C. NGO and H. G. CHOI. "Efficient direct re-initialization approach of a level set method for unstructured meshes". In: *Computers and Fluids* 154 (2017), pp. 167–183.

[159] V. T. NGUYEN, J. PERAIRE, B. C. KHOO, and P. O. PERSSON. "A discontinuous Galerkin front tracking method for two-phase flows with surface tension". In: *Computers and Fluids* 39.1 (2010), pp. 1–14.

[160] C. E. NORMAN and M. J. MIKSIS. "Gas bubble with a moving contact line rising in an inclined channel at finite Reynolds number". In: *Physica D: Nonlinear Phenomena* 209.1-4 (2005), pp. 191–204.

[161] S. OSHER and R. FEDKIW. *Level Set Methods and Dynamic Implicit Surfaces*. 2004. ISBN: 978-0-387-95482-0.

[162] S. OSHER and R. P. FEDKIW. "Level Set Methods: An Overview and Some Recent Results". In: *Journal of Computational Physics* 169.2 (2001), pp. 463–502.

[163] S. OSHER and J. A. SETHIAN. "Fronts propagating with curvature-dependent speed: Algorithms based on Hamilton-Jacobi formulations". In: *Journal of Computational Physics* 79.1 (1988), pp. 12–49.

[164] H.-C. OWEN. "A Finite Element Model for Free Surface and Two Fluid Flows on Fixed Meshes". PhD thesis. Universitat Politècnica de Catalunya, 2009.

[165] H. C. OWEN and R. CODINA. "Improving Eulerian two-phase flow finite element approximation with discontinuous gradient pressure shape functions". In: *International Journal for Numerical Methods in Fluids* 49.12 (2005), pp. 1287–1304.

[166] G. PACQUAUT. "Couplage Stokes/Darcy dans un cadre Level-set en grandes déformations pour la simulation des procédés d'élaboration par infusion de résine". PhD thesis. Ecole Nationale Supérieure des Mines de Saint-Etienne, 2010.

[167] C. H. PARK, A. LEBEL, A. SAOUAB, J. BRÉARD, and W. I. LEE. "Modeling and simulation of voids and saturation in liquid composite molding processes". In: *Composites Part A: Applied Science and Manufacturing* 42.6 (2011), pp. 658–668.

[168] V. A. PATEL. "Kármán vortex street behind a circular cylinder by the series truncation method". In: *Journal of Computational Physics* 28.1 (1978), pp. 14–42.

[169] D. PENG, B. MERRIMAN, S. OSHER, H. ZHAO, and M. KANG. "A PDE-Based Fast Local Level Set Method". In: *Journal of Computational Physics* 155.2 (1999), pp. 410–438.

[170] P.-O. PERSSON and J. PERAIRE. "Sub-Cell Shock Capturing for Discontinuous Galerkin Methods". In: *44th AIAA Aerospace Sciences Meeting and Exhibit*. 2006.

[171] C. S. PESKIN. "Flow patterns around heart valves: a digital computer method for solving the equations of motion". PhD thesis. Yeshiva University, 1972.

[172] P. G. PETROV and J. G. PETROV. "A Combined Molecular-Hydrodynamic Approach to Wetting Kinetics". In: *Langmuir* 8.7 (1992), pp. 1762–1767.

[173] K. M. PILLAI. "Governing equations for unsaturated flow through woven fiber mats. Part 1. Isothermal flows". In: *Composites Part A: Applied Science and Manufacturing* 33.7 (2002), pp. 1007–1019.

[174] D. PINO MUÑOZ, J. BRUCHON, S. DRAPIER, and F. VALDIVIESO. "A finite element-based level set method for fluid-elastic solid interaction with surface tension". In: *International Journal for Numerical Methods in Engineering* 93.9 (2013), pp. 919–941.

[175] D. H. PINO MUNOZ. "High-performance computing of sintering process at particle scale". PhD thesis. Ecole Nationale Supérieure des Mines de Saint-Etienne, 2012, p. 180.

[176] R. POMEROY, S. GROVE, J. SUMMERSCALES, Y. WANG, and A. HARPER. "Measurement of permeability of continuous filament mat glass-fibre reinforcements by saturated radial airflow". In: *Composites Part A: Applied Science and Manufacturing* 38.5 (2007), pp. 1439–1443.

[177] A. PONS. "Simulation numérique de la montée capillaire en espace confiné, en vue de l'application à des procédés d'élaboration de matériaux composites par imprégnation non-réactive ou réactive". PhD thesis. Université de Bordeaux, 2017.

[178] S. POPINET. "Numerical Models of Surface Tension". In: *Annual Review of Fluid Mechanics* 50 (2018), pp. 49–75.

[179] G. PUAUX. "Simulation numérique des écoulements aux échelles microscopique et mésoscopique dans le proécé RTM". PhD thesis. Ecole Nationale Supérieure des Mines de Paris, 2012.

[180] M. F. PUCCI, P.-J. LIOTIER, and S. DRAPIER. "Tensiometric method to reliably assess wetting properties of single fibers with resins: Validation on cellulosic reinforcements for composites". In: *Colloids and Surfaces A: Physicochemical and Engineering Aspects* 512 (2017), pp. 26–33.

[181] M. QUINTARD and S. WHITAKER. "Transport in ordered and disordered porous media IV: Computer generated porous media for three-dimensional systems". In: *Transport in Porous Media* 15.1 (1994), pp. 51–70.

[182] A. REUSKEN and E. LOCH. "On the accuracy of the level set supg method for approximation interfaces". In: *IGPM preprint* (2013), pp. 1–17.

[183] A. REUSKEN, X. XU, and L. ZHANG. "Finite element methods for a class of continuum models for immiscible flows with moving contact lines". In: *International Journal for Numerical Methods in Fluids* 84.5 (2017), pp. 268–291.

[184] O. REYNOLDS. "An Experimental Investigation of the Circumstances Which Determine Whether the Motion of Water Shall Be Direct or Sinuous, and of the Law of Resistance in Parallel Channels". In: *Philosophical Transactions of the Royal Society of London* 35 (1883), pp. 84–99.

[185] F. RISPOLI, A. CORSINI, and T. E. TEZDUYAR. "Finite element computation of turbulent flows with the discontinuity-capturing directional dissipation (DCDD)". In: *Computers and Fluids* 36.1 (2007), pp. 121–126.

[186] M. P. ROBICHAUD, P. A. TANGUY, and M. FORTIN. "An iterative implementation of the Uzawa algorithm for 3D fluid flow problems". In: *International Journal for Numerical Methods in Fluids* 10.4 (1990), pp. 429–442.

[187] E. RYSSEL and P. O. BRUNN. "Comparison of a quasi-Newtonian fluid with a viscoelastic fluid in planar contraction flow". In: *Journal of Non-Newtonian Fluid Mechanics* 86.3 (1999), pp. 309–335.

[188] M. A. SAFI, N. PRASIANAKIS, and S. TUREK. "Benchmark computations for 3D two-phase flows: A coupled lattice Boltzmann-level set study". In: *Computers and Mathematics with Applications* 73.3 (2017), pp. 520–536.

[189] P. H. SAKSONO and D. PERIĆ. "On finite element modelling of surface tension Variational formulation and applications - Part I: Quasistatic problems". In: *Computational Mechanics* 38.3 (2006), pp. 265–281.

[190] P. H. SAKSONO and D. PERIĆ. "On finite element modelling of surface tension: Variational formulation and applications - Part II: Dynamic problems". In: *Computational Mechanics* 38.3 (2006), pp. 251–263.

[191] H. SAUERLAND and T. P. FRIES. "The Stable XFEM for two phase flows". In: *Computers and Fluids* 87 (2012), pp. 41–49.

[192] H. SCHLICHTING. *Boundary layer theory*. 1979, p. 799. ISBN: 978-3-662-52919-5.

[193] M. SHAKOOR, B. SCHOLTES, P. O. BOUCHARD, and M. BERNACKI. "An efficient and parallel level set reinitialization method - Application to micromechanics and microstructural evolutions". In: *Applied Mathematical Modelling* 39.23-24 (2014), pp. 7291–7302.

[194] Y. D. SHIKHMURZAEV. "Singularities at the moving contact line. Mathematical, physical and computational aspects". In: *Physica D: Nonlinear Phenomena* 217.2 (2006), pp. 121–133.

[195] L. SILVA, G. PUAUX, M. VINCENT, and P. LAURE. "A monolithic finite element approach to compute permeability at microscopic scales in LCM processes". In: *International Journal of Material Forming* 3 (2010), pp. 619–622.

[196] A. A. SKORDOS, C. MONROY ACEVES, and M. P. F. SUTCLIFFE. "A simplified rate dependent model of forming and wrinkling of pre-impregnated woven composites". In: *Composites Part A: Applied Science and Manufacturing* 38.5 (2007), pp. 1318–1330.

[197] J. C. SLATTERY. "Multiphase viscoelastic flow through porous media". In: *AIChE Journal* 14.1 (1968), pp. 50–56.

[198] A. SMOLIANSKI. "Finite-element/level-set/operator-splitting (FELSOS) approach for computing two-fluid unsteady flows with free moving interfaces". In: *International Journal for Numerical Methods in Fluids* 48.3 (2005), pp. 231–269.

[199] S. SOGHRATI, A. M. ARAGÓN, C. ARMANDO DUARTE, and P. H. GEUBELLE. "An interface-enriched generalized FEM for problems with discontinuous gradient fields". In: *International Journal for Numerical Methods in Engineering* 89.8 (2012), pp. 991–1008.

[200] J. E. SPRITTLES and Y. D. SHIKHMURZAEV. "Finite element simulation of dynamic wetting flows as an interface formation process". In: *Journal of Computational Physics* 233.1 (2013), pp. 34–65.

[201] R. W. STYLE, R. BOLTYANSKIY, Y. CHE, J. S. WETTLAUFER, L. A. WILEN, and E. R. DUFRESNE. "Universal deformation of soft substrates near a contact line and the direct measurement of solid surface stresses". In: *Physical Review Letters* 110.6 (2013), p. 066103.

[202] Y. SUI, H. DING, and P. SPELT. "Numerical Simulations of Flows with Moving Contact Lines". In: *Annual Review of Fluid Mechanics* 46 (2014), pp. 97–119.

[203] M. SUSSMAN and M. OHTA. "A Stable and Efficient Method for Treating Surface Tension in Incompressible Two-Phase Flow". In: *SIAM Journal on Scientific Computing* 31.4 (2009), pp. 2447–2471.

[204] M. SUSSMAN, P. SMEREKA, and S. OSHER. "A Level Set Approach for Computing Solutions to Incompressible Two-Phase Flow". In: *Journal of Computational Physics* 114.1 (1994), pp. 146–159.

[205] L. H. TANNER. "The spreading of silicone oil drops on horizontal surfaces". In: *Journal of Physics D: Applied Physics* 12.9 (1979), pp. 1473–1484.

[206] T. E. TEZDUYAR and Y. J. PARK. "Discontinuity-capturing finite element formulations for nonlinear convection-diffusion-reaction equations". In: *Computer Methods in Applied Mechanics and Engineering* 59.3 (1986), pp. 307–325.

[207] M. M. TOMADAKIS and T. J. ROBERTSON. "Viscous permeability of random fiber structures: Comparison of electrical and diffusional estimates with experimental and analytical results". In: *Journal of Composite Materials* 39.2 (2005), pp. 163–188.

[208] C.L. TUCKER III and R.B. DESSENBERGER. "Governing equations for flow through stationary fiber beds". In: *Flow and Rheology in Polymer Composites Manufacturing*. 1994. Chap. 8. ISBN: 9780444893475.

[209] M. TUTAR and A. E. HOLD. "Computational modelling of flow around a circular cylinder in sub-critical flow regime with various turbulence models". In: *International Journal for Numerical Methods in Fluids* 35.7 (2001), pp. 763–784.

[210] N. VERNET, E. RUIZ, S. ADVANI, J. B. ALMS, M. AUBERT, M. BARBURSKI, B. BARARI, J. M. BERAUD, D. C. BERG, N. CORREIA, M. DANZI, T. DELAVIÈRE, M. DICKERT, C. DI FRATTA, A. ENDRUWEIT, P. ERMANNI, G. FRANCUCCI, J. A. GARCIA, A. GEORGE, C. HAHN, F. KLUNKER, S. V. LOMOV, A. LONG, B. LOUIS, J. MALDONADO, R. MEIER, V. MICHAUD, H. PERRIN, K. PILLAI, E. RODRIGUEZ, F. TROCHU, S. VERHEYDEN, M. WEITGREFE, W. XIONG, S. ZAREMBA, and G. ZIEGMANN. "Experimental determination of the permeability of engineering textiles: Benchmark II". In: *Composites Part A: Applied Science and Manufacturing* 61 (2014), pp. 172–184.

[211] P. VIGNEAUX. “Méthodes Level Set pour des problèmes d’interface en microfluidique”. In: (2008).

[212] L. VILLE, L. SILVA, and T. COUPEZ. “Convected level set method for the numerical simulation of fluid buckling”. In: *International Journal for Numerical Methods in Fluids* 66.3 (2011), pp. 324–344.

[213] O. V. VOINOV. “Hydrodynamics of wetting”. In: *Fluid Dynamics* 11.5 (1976), pp. 714–721.

[214] C. D. VOLPE and S. SIBONI. “The Wilhelmy method: A critical and practical review”. In: *Surface Innovations* 6.3 (2018), pp. 120–132.

[215] T. VON KÁRMÁN and L. EDSON. *The Wind and Beyond: Theodore Von Kármán, Pioneer in Aviation and Pathfinder in Space*. The Wind and Beyond: Theodore Von Kármán, Pioneer in Aviation and Pathfinder in Space. Little, Brown, 1967.

[216] Hakon WADELL. “Sphericity and Roundness of Rock Particles”. In: *The Journal of Geology* 41.3 (1933), pp. 310–331.

[217] P. WANG, S. DRAPIER, J. MOLIMARD, A. VAUTRIN, and J. C. MINNI. “Numerical and experimental analyses of resin infusion manufacturing processes of composite materials”. In: *Journal of Composite Materials* 46.13 (2012), pp. 1617–1631.

[218] E. W. WASHBURN. “The dynamics of capillary flow”. In: *Physical Review* 18.3 (1921), pp. 273–283.

[219] C. E. WEATHERBURN. *Differential Geometry of Three Dimensions*. Cambridge, UK: Cambridge Univ. Press, 1927. ISBN: 9781316606957.

[220] S. WHITAKER. “A Simple Geometrical Derivation of the Spatial Averaging Theorem”. In: *Chemical Engineering Education* 19 (1985), pp. 18–21, 50–52.

[221] S. WHITAKER. “Diffusion and dispersion in porous media”. In: *AIChE Journal* 13.3 (1967), pp. 420–427.

[222] S. WHITAKER. *The Method of Volume Averaging*. Springer Netherlands, 1999. ISBN: 978-0-7923-5486-4.

[223] Y. WIELHORSKI, A. BEN ABDELWAHED, E. ARQUIS, S. GLOCKNER, and J. BRÉARD. “Numerical Simulation of Bubble Formation and Transport in Cross-Flowing Streams”. In: *The Journal of Computational Multiphase Flows* 6 (2014), pp. 299–312.

[224] L. WILHELMY. “Uber die Abhängigkeit der Capillaritäts-Constanten des Alkohols von Substanz und Gestalt des benetzten festen Körpers”. In: *Annalen der Physik* 195.6 (1863), pp. 177–217.

[225] M.W. WILLIAMS, D.B. KOTHE, and E.G. PUCKETT. “Accuracy and convergence of continuum surface tension models”. In: *Fluid Dynamics at Interfaces* (1998), pp. 294–305.

[226] C H K WILLIAMSON. “Vortex Dynamics in the Cylinder Wake”. In: *Annual Review of Fluid Mechanics* 28.1 (1996), pp. 477–539.

[227] C. H. K. WILLIAMSON and G. L. BROWN. “A series in $1/\sqrt{Re}$ to represent the Strouhal-Reynolds number relationship of the cylinder wake”. In: *Journal of Fluids and Structures* 12.8 (1998), pp. 1073–1085.

[228] M. WINTER, B. SCHOTT, A. MASSING, and W. A. WALL. "A Nitsche cut finite element method for the Oseen problem with general Navier boundary conditions". In: *Computer Methods in Applied Mechanics and Engineering* 330 (2018), pp. 220–252.

[229] T. YOUNG. "An Essay on the Cohesion of Fluids". In: *Philosophical Transactions of the Royal Society of London* 95 (1805), pp. 65–87.

[230] S. T. ZALESAK. "Fully multidimensional flux-corrected transport algorithms for fluids". In: *Journal of Computational Physics* 31.3 (1979), pp. 335–362.

[231] M. A. F. ZARANDI, K. M. PILLAI, and B. BARARI. "Flow along and across glass-fiber wicks: Testing of permeability models through experiments and simulations". In: *AIChE Journal* 64.9 (2018), pp. 3491–3501.

[232] O. C. ZIENKIEWICZ, R. L. TAYLOR, S. J. SHERWIN, and J. PEIRÓ. "On discontinuous Galerkin methods". In: *International Journal for Numerical Methods in Engineering* 58.8 (2003), pp. 1119–1148.

École Nationale Supérieure des Mines
de Saint-Étienne

NNT: *2019LYSEM008*

Loïc CHEVALIER

ACCOUNTING FOR CAPILLARY EFFECTS IN LEVEL-SET BASED FINITE ELEMENTS MODELLING OF IMPREGNATION IN FIBROUS MEDIA

Speciality: Mechanics and Engineering

Keywords: Capillarity, stabilised FE, bi-fluid flow, level-set, discontinuities capturing, surface tension, fibrous composites, numerical permeability, capillary pressure

Abstract:

Accounting for surface tension effects is of major interest in many fields in engineering. More specifically, in the field of LCM composite processing, surface tension driven phenomena control the impregnation of liquid resin into fibrous preforms. In the work described here, a numerical method able to deal with a general bi-fluid model integrating capillary actions is developed and implemented. Firstly, the method relies on a precise computation of the surface tension force. Considering a mathematical transformation of the surface tension virtual work, the regularity required for the solution on the evolving curved interface is weakened, and the mechanical equilibrium of the triple line can be enforced as a natural condition. Consequently, contact angles of the liquid over the solid phase result from this equilibrium. Secondly, for an exhaustive capillary action representation, pressure and pressure gradient jumps across the interface must be accounted for. A pressure enrichment strategy is used to properly compute the discontinuities in both pressure and gradient fields. On top of that, a strong coupling strategy is shown to yield physically sound solutions even for complex solid surfaces. The resulting method is shown to predict accurately static contact angles for several test cases and is evaluated in complex 3D cases. Owing to this methodology, capillary pressure and permeability can be extracted, upscaled from flows computed in both model and more realistic microstructures.

École Nationale Supérieure des Mines
de Saint-Étienne

NNT : *2019LYSEM008*

Loïc CHEVALIER

PRISE EN COMPTE DES EFFETS CAPILLAIRES DANS LA MODÉLISATION PAR ÉLÉMENTS FINIS ET LEVEL-SET DE L'IMPRÉGNATION DANS LES MILIEUX FIBREUX

Spécialité : Mécanique et Ingénierie

Mots clefs : Capillarité, EF stabilisés, écoulement bi-fluide, level-set, capture des discontinuités, tension de surface, composites fibreux, perméabilité numérique, pression capillaire

Résumé :

La prise en compte des effets liés à la tension superficielle est d'une importance majeure dans l'élaboration de composites par procédés LCM où ils influencent l'imprégnation de la résine liquide dans les préformes fibreuses, et donc la santé matière finale. Dans ce travail, une méthode numérique capable de traiter un modèle général bi-fluide intégrant des actions capillaires est développée et mise en œuvre. La méthode repose d'abord sur le calcul précis de la force de tension superficielle. Considérant une transformation mathématique du travail virtuel de la tension superficielle, la contrainte de régularité requise pour la solution sur l'interface courbe en mouvement est réduite, et l'équilibre mécanique de la ligne triple peut être imposé comme une condition naturelle. Par conséquent, les angles de contact du liquide sur la phase solide résultent de cet équilibre. Ensuite, pour une représentation exhaustive des actions capillaires, les sauts de pression et de gradient de pression à travers l'interface doivent être pris en compte. Une stratégie d'enrichissement de la pression est utilisée pour calculer correctement les discontinuités dans les champs de pression et de gradient. De plus, une stratégie de couplage fort itératif permet d'obtenir des solutions physiquement acceptables, même pour des surfaces solides complexes. La méthode qui en résulte permet de prédire correctement des angles de contact statiques pour plusieurs cas tests, elle est également évaluée sur des cas 3D complexes. Grâce à cette méthodologie, il est possible d'extraire la pression capillaire et la perméabilité à partir de moyennes des flux calculés dans des microstructures d'abord modèles puis plus réalistes.